Master's thesis and Internship : Thermal modelling and experimental measures of a French-type masonry stove for Low-Tech heating applications

Auteur : Renouprez, Loïc
Promoteur(s) : Lemort, Vincent
Faculté : Faculté des Sciences appliquées
Diplôme : Master : ingénieur civil en génie de l'énergie à finalité spécialisée en Energy Conversion
Année académique : 2025-2026
URI/URL : http://hdl.handle.net/2268.2/25228

University of Liège
Faculty of Applied Science

Thermal modelling and experimental measures of a French-type masonry stove for Low-Tech heating applications

Author:
Renouprez Loïc

Promotor:
Lemort Vincent

Jury Members:
Lemort Vincent
Gendebien Samuel
Dewallef Pierre

Master thesis submitted in partial fulfillment of the requirements for the Master's degree in Energy Engineering with specialized purpose in Energy Conversion

Academic year 2025-2026

Acknowledgements

This work marks the end of my studies as an engineer. I would like to express my gratitude to all the friends, professors, and classmates who have been part of this journey. Their guidance, rigor and kindness have constantly motivated me to give my best, helping me succeed through both the challenging and the good moments.

First, I would like to thank my supervisor, Vincent Lemort, for his trust, support, and guidance throughout the realization of this work.

I would also like to thank my internship supervisor at the non-profit organisation *Low-Tech Liège*, Kim Maréchal, for his trust and support during my months with the organization, as well as my colleagues Aurélien Bouhon, Simon Fontaine, and Romane Pirson. I am particularly grateful to Aurélien Bouhon for sharing his knowledge of masonry stoves and for providing access to his stove for this project.

Special thanks are also due to the masonry stove brand *UZUME* and the French Association for Artisanal Masonry Stoves (AFPMA) for making the required data available for this study.

Finally, I am deeply grateful to my family, including my brother and sisters, and especially to my parents, whose constant support has been essential. Without them, completing these years would have been even more challenging.

Abstract

Household energy consumption plays a significant role in climate change, and reducing both energy use and greenhouse gases from this sector is a major challenge. The European Union has defined ambitious targets for 2030 and 2050 to mitigate climate change and emissions. In line with these objectives, Wallonia has developed the RENOBATEX funding mechanism to support housing renovation projects promoting energy efficiency and energy sobriety. One of the supported initiatives is the *RenoLow* project, carried out by the non-profit organisation *LowTech Liège*, which promotes low-tech renovation strategies. Household heating is a central element of this project, notably through French-type masonry stoves manufactured by *UZUME*, a French masonry stove manufacturer. This thesis focuses on this type of masonry stove, which provides heat from wood combustion in an efficient and relatively low-emission way.

The main objective is to develop a transient numerical model of a French-type masonry stove. The model can then be used by *LowTech Liège* to generate quantitative results on thermal comfort and energy consumption, supporting end users' understanding and acceptance of this heating solution. After a short review of masonry stoves and thermal modelling approaches, the thesis introduces a numerical model that predicts the temporal evolution of temperatures throughout nearly all parts of the stove, using a discretised representation of the masonry structure. This model relies on user-defined inputs, which are directly accessible to stove users or designers. It represents the masonry stove physics in two stages: a simplified model of the time-varying heat released by batch wood combustion, and a detailed modelling of the heat transfer processes within the stove and with its environment using a resistance–capacitance (RC) network approach. The resulting system of equations is implemented and solved in *Python*. Several numerical schemes are tested before retaining a Backward Differentiation Formula (BDF) method as a good compromise between robustness and computation time.

The second part of the thesis presents the experimental setup used to collect, in situ, external surface temperatures measurement on the four side walls of on an *UZUME* masonry stove under two operating conditions, corresponding to summer and winter use. These experimental data are then used to perform a parametric study of combustion and mass flow rate evolution parameters, allowing the identification of realistic and robust ranges of values.

Finally, the numerical predictions are compared with the experimental measurements to assess the ability of the model to reproduce the thermal behaviour of the stove. The results show that the model captures the main transient thermal behaviour of the masonry stove, with simulated temperature profiles closely matching the experimental trends. The absolute root mean square error between experimental and simulated data is approximately 8 °C for both experimental campaigns, corresponding to a mean absolute error of about 6.5 °C. Given the experimental uncertainties, the external surface temperatures ranging from 20 °C to about 130 °C, and the simplifying assumptions adopted, this level of agreement is considered satisfactory for a first-generation numerical model and provides a solid basis for further research and future evaluations of the impact of masonry stoves on household energy performance.

Contents

1 Introduction **1**
- 1.1 Context . . . 1
- 1.2 Problem statement and thesis objectives . . . 3
- 1.3 Structure of the report . . . 4

2 Review of literature **6**
- 2.1 The masonry stove . . . 6
  - 2.1.1 Biomass as a renewable source of energy . . . 6
  - 2.1.2 Description of a masonry stove . . . 7
  - 2.1.3 History of masonry stoves . . . 9
  - 2.1.4 Masonry stove as a final solution . . . 11
- 2.2 Thermal modelling . . . 13
  - 2.2.1 Fundamentals of thermal behaviour . . . 13
  - 2.2.2 RC network . . . 16
  - 2.2.3 Numerical solvers . . . 17

3 Masonry stove model **19**
- 3.1 Software used . . . 19
- 3.2 Modelling methodology . . . 19
- 3.3 Discretization . . . 20
  - 3.3.1 Accumulator discretization in control volumes . . . 20
  - 3.3.2 Wall discretization . . . 23
  - 3.3.3 Global discretization . . . 23
- 3.4 Masonry stove model setup . . . 24
  - 3.4.1 Assumptions . . . 24
  - 3.4.2 Inputs . . . 25
  - 3.4.3 Preprocessing computations . . . 27
  - 3.4.4 Wall data structure . . . 29
- 3.5 Combustion modelling . . . 30
  - 3.5.1 Assumptions . . . 31
  - 3.5.2 Inputs . . . 31
  - 3.5.3 Adiabatic combustion chamber . . . 31
  - 3.5.4 Time-dependent combustion temperature profile . . . 33
- 3.6 Thermal storage and heat release modelling . . . 35
  - 3.6.1 Assumptions . . . 36
  - 3.6.2 Inputs . . . 36
  - 3.6.3 Flue gas mass flow rate evolution . . . 37
  - 3.6.4 Heat transfer mechanisms and governing equation . . . 38
  - 3.6.5 Discretized gas temperature evolution . . . 39
  - 3.6.6 Discretized wall temperature evolution . . . 41

3.7 Numerical solvers and implementation . . . 48
3.7.1 Forward Euler . . . 49
3.7.2 Runge–Kutta (RK45) . . . 49
3.7.3 Backward Euler . . . 50
3.7.4 Backward Differentiation Formula (BDF) . . . 52
3.7.5 Stability criterion . . . 53
3.8 Simulation results . . . 56
3.8.1 Model setup and input parameters . . . 56
3.8.2 Stability analysis and optimal time step . . . 58
3.8.3 Effect of wall discretization . . . 62
3.8.4 Combustion submodel results . . . 64
3.8.5 Integrated stove simulation results . . . 65
3.9 Final numerical solver selection . . . 71

4 Experimental data measurement **72**
4.1 Experimental setup . . . 72
4.2 Measuring instruments . . . 73
4.3 Pre-test data collection . . . 75
4.4 Measurement procedure during stove operation . . . 75
4.5 Experimental results . . . 77

5 Numerical model vs experimental data **81**
5.1 Model configuration for comparison with experiments . . . 81
5.2 Parametric study and model calibration . . . 82
5.2.1 Calibration of combustion intensity factor . . . 82
5.2.2 Sensitivity analysis of mass-flow ramp parameters . . . 84
5.3 Final comparison with experimental data . . . 86

6 Conclusion and perspectives **90**
6.1 Conclusion . . . 90
6.2 Limitations . . . 91
6.3 Future work . . . 92

A Appendix: Combustion **93**
A.1 Stoichiometric fuel-to-air-ratio computation . . . 93

B Appendix: Heat transfer modelling **94**
B.1 Correlations for Nusselt number . . . 94
B.2 Nusselt numbers for laminar flow in rectangular ducts . . . 96
B.3 Wall surface resistance effect . . . 96
B.4 Linearisation of radiative heat transfers . . . 98

C Appendix: *B14 V5* masonry stove data **100**
C.1 Inputs for *B14 V5* masonry stove simulation . . . 100
C.2 Detailed geometry inputs . . . 102
C.3 *B14 V5* masonry stove datasheet . . . 105

D Appendix: Experimental results **106**
D.1 Infrared thermal images . . . 106

E Appendix: Comparison of experimental and numerical results **108**
E.1 Combined sensitivity analysis of mass-flow ramp parameters 108
E.2 Supplementary error analysis between experimental and simulation data 109

F Appendix: Review of literature of thermal comfort **111**
F.1 General review of literature 111
F.2 Typical metabolic heat generations 132

List of Figures

1.1 Final energy consumption per sector in EU in 2023 2
1.2 Energy consumption in households in EU in 2022 3

2.1 Schematic of the main components of a masonry stove 7
2.2 Schematic of venturi opening of a masonry stove. 8
2.3 *Grundofen* and *Kachelofen* masonry stoves 10
2.4 Traditional cuboid Russian oven. 10
2.5 *kakelugn* and modern *pönttöuuni* masonry stoves. 11
2.6 Evolution of convective heat transfer rate with surface temperature. 14
2.7 Evolution of radiative heat transfer rate with surface temperature 15
2.8 Evolution of total heat transfer rate from a surface with surface temperature . . . 16

3.1 Schematic of the main steps, outputs and inputs of the numerical model. 20
3.2 Illustration of the gas domain discretization at a change of flow direction. 21
3.3 Wall sub-element discretization within a single gas segment. 22
3.4 Wall discretization for different numbers of temperature nodes. 23
3.5 Simplified global discretization of the masonry stove 24
3.6 Illustration of the neglected wall regions for thermal behaviour. 25
3.7 Schematic of the adiabatic combustion chamber model. 32
3.8 Combustion chamber flue gas temperature evolution during combustion 35
3.9 RC network representation of heat-transfer mechanisms associated with a single gas segment. 38
3.10 Heat-transfer mechanisms affecting a discretized gas segment 39
3.11 Local RC representation of gas-to-wall heat transfer. 42
3.12 Local RC representation of conductive heat transfer between refractory and casing walls. 44
3.13 Convective and radiative heat transfer between an external casing wall and ambient air. 45
3.14 Radiative heat exchange between the internal walls of a gas channel 46
3.15 RC representation of the internal one-dimensional conductive heat-transfer within a wall 47
3.16 Sketch of the *B14 V5 in kit Medi Batchblock* masonry stove. 56
3.17 Flue gas path in the *B14 V4* masonry stove and gas segment discretization of this stove. 57
3.18 Discretization in gas segments and wall sub-elements of the *B14 V4* masonry stove. 57
3.19 Effect of the maximum time step on solution accuracy and computational efficiency for the BDF solver 60
3.20 Effect of the maximum time step on solution accuracy and computational efficiency for the RK solver 61
3.21 Flue gas temperature profile during combustion period for the *B14 V5* masonry stove simulation. 64

3.22 Evolution of flue gas temperature. 66
3.23 Mean temperature evolution of refractory wall 67
3.24 Mean temperature evolution of casing wall 68
3.25 Surface temperature evolution of casing walls 69
3.26 Instantaneous stove heat power and cumulative energy released. 70
3.27 Evolution of gas temperature in the third discretized gas segment for the RK and BDF schemes. 71

4.1 Masonry stove used for the experimental measurements. 72
4.2 Measuring instruments for experimental measurements. 73
4.3 Probe installation with aluminium tape on stove surfaces. 74
4.4 Measurement points for experimental data gathering 76
4.5 Surface temperature evolution of the masonry stove during the summer and winter test campaigns. 77
4.6 Thermal images of the stove's four sides at 1 h 42 min after ignition 78

5.1 Global relative RMSE vs. combustion factor λ_c. 83
5.2 RMSE vs. mass flow-rate ramp-up duration parameter 84
5.3 RMSE vs. mass flow-rate ramp-down duration parameter 85
5.4 Back and left faces: model vs. experimental temperature evolution. 88

C.1 Technical data sheet of *B14 V5* masonry stove. 105

D.1 Thermal images of the stove's four sides at 3 h 10 min after ignition 106
D.2 Thermal images of the stove's four sides at 6 h 02 min after ignition 107

E.1 Sensitivity maps of global RMSE vs. ramp-up and ramp-down durations flow rate parameters. 108
E.2 Front and right faces: model vs. experimental temperature evolution. 110

F.1 Diagram of autonomic and behavioural human temperature regulation 113
F.2 Thermal interaction between a human body and its environment. 118
F.3 Evolution of operative temperature with air temperature for different mean radiant temperatures 121
F.4 Evolution of the PPD with variation of the PMV. 124
F.5 Correlation between comfort temperature and monthly mean outdoor temperature. 127
F.6 Evolution of comfort temperature with monthly mean outdoor temperature from a static model and an adaptive model for air-conditioned and naturally ventilated buildings 128

List of Tables

2.1 Thermal properties of different materials used in stoves. 9
2.2 Basic thermal resistance and capacitance formulas. 17

3.1 Attributes of the *Wall Python* Class. 30
3.2 Input parameters for the combustion modelling. 31
3.3 Values of the parameters for combustion chamber flue gas temperature profile. . . 34
3.4 Input parameters for thermal storage and heat release modelling. 37
3.5 RC network stability ratios for node types in the masonry stove. 55
3.6 Summary of stability criteria for the four solvers. 55
3.7 Simulation results comparison for 2, 3, 4 and 5 wall nodes. 63
3.8 Results of the adiabatic combustion chamber model for the *B14 V5* masonry stove simulation. 64

4.1 Summary of instruments used in the summer and winter test campaigns. 74
4.2 Pre-test experimental data measured prior to the combustion 75
4.3 Comparison of point and area-averaged surface temperatures from IR camera and laser thermometer 79

5.1 Input parameters modified for experimental data comparison. 81
5.2 Error metrics for the summer test campaign 87

B.1 Nusselt numbers for laminar flow in rectangular ducts. 96
B.2 RMSE between simplified and reference models (with/without wall surface nodes) 98

C.1 Input values for model setup of the *B14 V5 in-kit Medi Batchblock* masonry stove. 100
C.2 Input values for combustion simulation in the *B14 V5 in-kit Medi Batchblock* masonry stove 101
C.3 Input values for thermal storage and heat-release simulations of the *B14 V5 in-kit Medi Batchblock* masonry stove. 101
C.4 Dimensions of the *B14 V5 Medi Batchblock* masonry stove 104

E.1 Error metrics for the winter test campaign 109

F.1 Equations for Convection Heat Transfer Coefficient in thermal comfort 114
F.2 Garment Insulation Values. 119
F.3 Thermal sensation scale according to Bedford and ASHRAE 120
F.4 Adaptive algorithms for comfort temperature computation 129
F.5 Thermal comfort categories used in norms ISO 7730 and EN 16798 130
F.6 Comfort categories according to EN ISO 7730 131
F.7 Comfort categories for mechanically ventilated buildings 131
F.8 Adaptive model comfort categories for naturally ventilated buildings 131
F.9 Typical Metabolic Heat Generation for Various Activities. 132

Nomenclature

List of abbreviations and acronyms

AFPMA	*Association Française du Poêle Maçonné Artisanal*
AR6	Sixth Assessment Report
ASHRAE	American Society of Heating, Refrigerating and Air-Conditioning Engineers
BDF	Backward differentiation formula
CEB	Compressed earth blocks
CEN	European Committee for Standardization
CFL	Courant–Friedrichs–Lewy limit
CO	Carbon monoxide
CO_2	Carbon dioxide
EU	European Union
GWP	Global warming potential
IEQ	Indoor Environmental Quality
IPCC	Intergovernmental Panel on Climate Change
ISO	International Organization for Standardization
LCA	Life cycle assessment
MAE	Mean absolute error
MIT	Massachusetts Institute of Technology
NDCs	Nationally Determined Contributions
NO_x	Nitrogen oxides
ODE	Ordinary differential equation
O_2	Oxygen
PM_1	Particulate matter with diameter $\leq$ 1 micrometer
$PM_{2.5}$	Particulate matter with diameter $\leq$ 2.5 micrometer
PM_{10}	Particulate matter with diameter $\leq$ 10 micrometer
PRW	*Plan de Relance de la Wallonie*
RC	Resistance-capacitance model
RK	Runge-Kutta
RMSE	Root mean square error
SCATs	Smart Controls and Thermal Comfort
SPW	*Service Public de Wallonie*
VOCs	Volatile Organic Compounds

List of symbols

A	Area [m^2]
C	Thermal capacitance [J/K]
c_p	Specific heat capacity [J/kgK]
D	Diameter [m]
E	Emissive power [W/m^2]
e	Thickness [m]
ET	Effective temperature [°C]
ET^*	Corrected effective temperature [°C]
ex	Excess of air [-]
F	View factor [-]
f	Area factor or fuel-to-air ratio [-]
G	Thermal conductance [W/K]
g	Sigmoid function [-]
Gz	Graetz number [-]
H	Height [m]
h	Convective heat transfer coefficient [W/m^2K]
I	Insulation [clo]
k	Thermal conductivity [W/mK]
L	Length [m]
LHV	Lower heating value [J/kg]
LR	Lewis ratio [-]
M	Metabolic energy [met]
m	Mass [kg]
$\dot{m}$	Mass flow rate [kg/s]
M_X	Molar mass of element x [g/mol]
n_{nodes}	Number of wall temperature nodes [-]
Nu	Nusselt number [-]
n_X	Number of moles of x [mol]
p	Water vapor pressure [Pa]
PMV	Predicted Mean Vote [-]
PPD	Predicted Percentage Dissatisfied [%]
Pr	Prandtl number [-]
$\dot{Q}$	Heat transfer rate [W]
q''	Heat flux [W/m^2]
R	Thermal resistance [W/K]
Ra	Rayleigh number [-]
Re	Reynolds number [-]
RH	Relative humidity [-]
RQ	Respiratory quotient [-]
R_u	Universal gas constant [J/molK]
S	Rate of heat storage [W/m^2]
s	Steepness coefficient [-]
SF	safety factor [-]
T	Temperature [K]
t	Time [s]
u	Mean velocity [m/s]

$\dot{V}$	Volumetric flow rate [m^3/s]
W	Mechanical work for muscles [met]
w	Width [m]
wt	Mass fraction of moisture on a wet basis [-]
σ	Stefan-Boltzmann constant [W/m^2K^4]
ϵ	Emissivity [-]
ω	Wettedness [-]
α	Fraction of body mass [-]
ρ	Density [kg/m^3]
θ	Amplitude parameter [-]

List of subscripts

a	Air
abs	Absorbed
ad	Adiabatic
amb	Ambient
av	Average
b	Blackbody
c	Convection
cl	Clothing
cng	Casing
$comb$	Combustion
$comf$	Comfort
$cond$	Conduction
cr	Core
$cross$	Cross-sectional
D	Dubois or diameter
e	Evaporative
eff	Effective
ext	External
f	Fluid
fd	fully-developed
fg	Fluid to gas
g	Black globe
h	Hydraulic
i	Indoor
$init$	Initial
lam	Laminar
m	Moisture
max	Maximum
mr	Mean radiant
mth	Monthly
nom	Nominal
o	Operative
out	Outside
r	Radiation
ref	Reference
res	Respiratory
$restit$	Restitution
rfr	Refractory
rm	Running mean
rsw	Regulatory sweating
s	Surface
sk	Skin
st	Stoichiometric
su	Supply
sur	Surrounding
$surf$	Surface
$turb$	Turbulent

"All models are wrong, but some are useful."

—George E. P. Box (1976)

Chapter 1
Introduction

1.1 Context

An assessment of the state of the environment, biodiversity and more globally the world has imposed itself: living in the current mode of development is leading and will continue to lead to severe climate changes and resources depletion. This crisis faced by humanity is widely recognized and discussed across various domains including public debate, media discourse, and scientific literature. These last years, the Intergovernmental Panel on Climate Change (IPCC) wrote different reports alerting the world and policymakers. With its Sixth Assessment Report (AR6) released in 2023, this group of expert scientifics confirms that, principally through emissions of greenhouse gases, human activities have unequivocally caused global warming. This warming is already leading, and will continue to lead, to numerous hazards including weather extremes intensification, food and water insecurity, economic damages across various sectors and growing risks for ecosystems [1].

With these warning signs, policies and laws addressing mitigation have consistently expanded, like the European Green Deal proposed by the European Commission targetting to achieve net-zero greenhouse gas emissions within the EU by 2050 [2]. Nevertheless, despite these efforts, there are still huge gaps between projected emissions from implemented policies and the reduction targets stated in countries' Nationally Determined Contributions (NDCs). The IPCC states that it is likely that warming will exceed 1.5°C since pre-industrial levels during the 21st century and it will be almost impossible to limit warming well below 2°C, the long-term objective announced at the Paris Agreement [3].

In response to the growing mismatch between human activities and their living environments, and to the lack of sufficiently rapid political action, new approaches and concepts appear to try to recreate harmony between humans and their planet. One of them that can be cited is the low-tech approach. Its basic principle is to create technologies with low environmental impact and limited resources. However, it goes even further than that having sometimes organizational, systemic, cultural and even political and philosophical dimensions. This description aligns with the definition given by the French engineer, Arthur Keller : «*It is an approach, a method, a vision, a philosophy, almost a culture, largely exceeding the strict technological question. A global approach that allows us to return to compliance with planetary limits, i.e. not to consume more energy, materials and resources than the Earth can sustainably provide.*» [4]. It integrates technologies in society following four main principles [5]:

1. Sustainability: the low-tech must be eco-designed, recyclable and limiting in term of resources consumption.

2. Accessibility: the low-tech must be appropriable by the greatest number, simple to produce, use and repair and its cost adapted to all classes of society.

3. Usefulness: the low-tech approach first encourages sobriety before using technologies. If needed, it responds to essential needs of the individual or the collective. It contributes to make healthy and relevant lifestyles and modes of productions and consumptions in various essential fields as energy, food, water, waste management, materials, housing, transport, hygiene or even health.

4. Social links: the low-tech approach wants to recreate social links and promote living together.

This system approach is adopted by the non-profit organization *Low-Tech Liège*, which initiated the research presented in this thesis. This non-profit organization is one of the many low-tech communities emerging across France and beyond, notably through the *Low-tech Labs* established in numerous French cities.

Among the various domains in which low-tech principles can be applied, housing stands out as a particularly relevant field. It affects directly everyday life while accounting for a significant share of energy consumption and greenhouse gas emissions. Households therefore represent a critical opportunity for implementing low-tech solutions that reduce environmental impacts while promoting accessible and sustainable lifestyles. In Europe, households accounted for 26% of final energy consumption in 2023 (Figure 1.1).

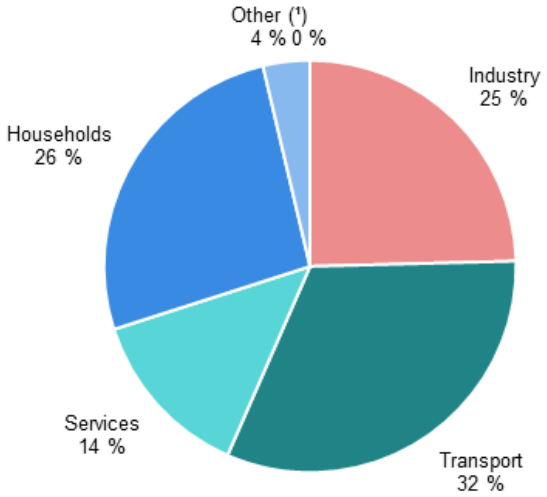

Figure 1.1: Final energy consumption per sector in EU in 2023 [6].

Recognizing the key role of housing in the energy transition, the Belgian government has also taken action through the public service of Wallonia (SPW). In March 2023, the SPW launched a call for projects, named RENOBATEX, as part of the Wallonia Recovery Plan (PRW). This funding scheme financially supports innovative projects with the aim of facilitating energy renovation and encouraging energy sobriety. The non-profit organization *LowTech Liège* responded to the call for projects and managed to be financed

for their project named *Renolow*, which promotes the renovation of dwellings in accordance with low-tech principles.

1.2 Problem statement and thesis objectives

Within building renovation projects, space heating plays a critical role. In the European Union, it contributed to 63.5% of household energy consumption in 2022 (Figure 1.2). Beyond its energy impact, the ability to heat one's home and maintain acceptable thermal comfort is also a fundamental requirement for occupants and a key criterion in the perceived quality of a dwelling. For these reasons, space heating is one of the main areas of focus in the *Renolow* project. Among the heating solutions considered, the masonry stove has been selected by the project team as a promising low-tech technology for space heating due to its simplicity, ease of repair, and sustainability.

One of the first objectives of *LowTech Liège* is to be able to provide quantitative information on the energy consumption and thermal comfort delivered by masonry stoves, in order to support households, builders and designers in their decision-making process. Potential users often expect robust and understandable data before adopting a heating system, particularly in the context of renovation. Thermal comfort is a critical aspect in this regard: apart from aesthetic considerations, buildings are primarily assessed on the comfort they provide to occupants, with direct implications for health, well-being and productivity. Furthermore, a proper assessment of this comfort makes it possible to explore strategies that reduce energy and material use while remaining within acceptable comfort ranges, which depend not only on indoor air temperature but also on radiative heat exchanges with the masonry stove.

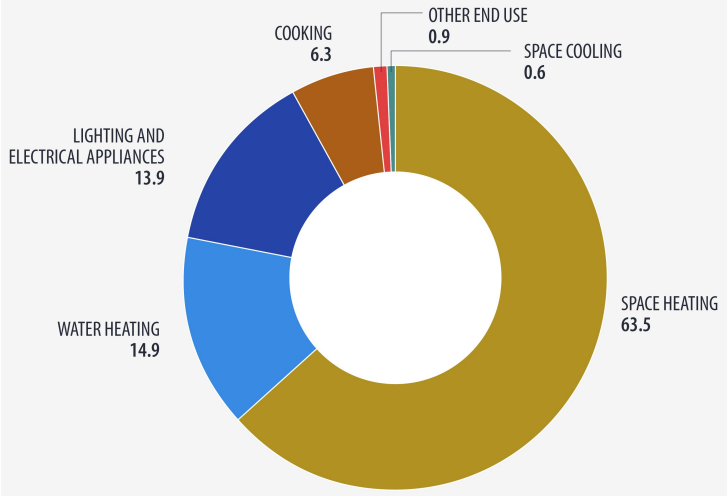

Figure 1.2: Energy consumption in households in EU in 2022 [7].

However, discussions with the members of the *Renolow* project highlighted a significant lack of scientific documentation and experimental studies on the new generation of French-type masonry stoves developed in some Western European countries, particularly in France and Belgium. Although masonry stoves have existed for several centuries in some

regions, their recent development and renewed interest in these countries, partly driven by the low-tech movement, remain insufficiently documented from a numerical modelling perspective. For these type of more recent masonry stoves, some simple calculation tools are available, mainly intended to estimate nominal heat power output depending on room size or to support stove sizing procedures, such as those developed by the AFPMA or the Austrian Tiled Stove Association [8, 9]. However, these tools are not designed to represent the transient internal and external thermal behaviour of the stove. As a result, there is very limited work on numerical models capable of describing the detailed thermal dynamics required for thermal comfort evaluation provided by the French-type masonry stove.

In this context, **the main objective** of this thesis is to develop a detailed open source transient numerical model of a French-type masonry stove, with a particular focus on stoves manufactured by the French company *UZUME*. The model aims to describe the transient thermal behaviour of the stove and to predict temperature evolution throughout the stove and flue gas path using a discretized representation. To support and assess the relevance of the model, experimental temperature measurements are carried out in situ on a real masonry stove. These data are used to compare model predictions with measured behaviour and to evaluate the model's ability to reproduce the main thermal dynamics of the system.

Beyond its intrinsic modelling interest, the developed model is intended to serve subsequently as a tool for *LowTech Liège* to generate quantitative results related to energy consumption and thermal comfort. To support this application, a comprehensive review of thermal comfort indicators and calculation methods is therefore presented in the appendix F of this thesis, forming a methodological basis that can later be combined with model outputs.

1.3 Structure of the report

This thesis is organised into 6 chapters:

- **Chapter 1**: The first chapter consists of the introduction to the work. It presents the global context, the problem statement to which the report responds and the different objectives of the thesis.
- **Chapter 2**: This chapter presents the state of the art of low-tech heating technologies, with a particular focus on masonry stoves, as well as existing approaches for modelling their thermal behaviour. In addition, another review of the literature on thermal comfort is provided in Appendix F. This review may be used for further analysis if required[1].
- **Chapter 3**: The third chapter focuses on a model of the French-type masonry stove. It explains the different hypotheses, equations and mathematical methods used to model the combustion process and the heat transfers occurring in the masonry stove, and to solve the numerical model. First results of the model are also analysed.

[1] In particular, it may serve the organisation *LowTech Liège* to reach their final goal of quantifying thermal comfort based on the results of the masonry stove model developed in this thesis

- **Chapter 4**: The fourth chapter is dedicated to experimental data measured in situ. The experimental setup as well as the experimental results obtained during two test campaigns are provided and analysed.
- **Chapter 5**: The fifth chapter uses experimental data to perform a parametric study of parameters requiring calibration or sensitivity analysis, followed by a comparison between experimental and simulation results to evaluate the validity of the developed numerical model.
- **Chapter 6**: In the last chapter, conclusions are drawn and some perspectives to improve the work are proposed.

Chapter 2
Review of literature

This chapter develops the available literature necessary for solving the problem presented. It starts by presenting the basics of a masonry stove. Then, it develops the thermal behaviour of this stove as well as some approaches developed to model and solve thermal problems numerically.

2.1 The masonry stove

This section proposes an overview of the scientific literature available on masonry stoves. It begins with an overview of biomass as an energy source since it is the source of energy used in masonry stoves. Then, it is followed by an examination of the scientific literature on masonry stoves, highlighting the behaviour of the technology, its historical development, as well as its known advantages and limitations.

2.1.1 Biomass as a renewable source of energy

Biomass refers to organic matter of biological origin present in the biosphere, including plant and animal material, as well as substances derived from their natural or artificial transformation processes [10]. It primarily originates from recent photosynthesis activity, either directly (e.g., wood, crops) or indirectly (e.g., agricultural residues, animal waste). Biomass includes traditional forms such as firewood and charcoal for cooking and heating and modern bioenergy sources such as biofuels, biogas, and industrial biomass for electricity generation. Its variable composition and moisture content significantly influence its combustion behaviour and energy conversion efficiency [11].

Despite being one of the oldest energy sources, biomass remains a major component of the global and national energy mix. In 2022, it accounted for 66% of the renewable share of Belgium's total energy supply [12]. Worldwide, it represented 30.8% of energy consumption for heating buildings in 2021 [13].

Biomass offers several advantages that support its continued relevance as an energy source. It is often considered carbon neutral, as the carbon dioxide (CO_2) absorbed during growth through photosynthesis is theoretically offset by the CO_2 released during combustion, resulting in a net-zero CO_2 balance. Compared to fossil fuels, biomass thus presents a lower global warming potential (GWP) and reduced greenhouse gas emissions [14]. In addition, its availability, especially in rural areas, and easy harvesting enable localized energy production and greater energy autonomy for local communities. It is a significant advantage in a context of increasing scarcity and extraction challenges for fossil resources.

Unlike other renewable sources such as wind or solar energy, biomass can provide constant energy, unaffected by weather or seasonal variability [15]. Furthermore, its price is generally more stable than that of gas or electricity, both of which are highly exposed to international market fluctuations. As a result, wood heating can be more cost-effective over the long term [16].

However, biomass heating has also limitations. To maintain carbon neutrality, harvesting rates must match regrowth rates,allowing sufficient time for CO_2 reabsorption [17]. Moreover, indirect greenhouse gas emissions occur throughout the biomass supply chain: forestry operations, processing and transport. Unsustainable biomass extraction can also have negative impacts on food security and land use. Sustainable woodland management practices, such as using forest residues and green waste, can help mitigate these effects. Nevertheless, excessive residue removal may reduce soil carbon sequestration, deplete nutrients, and degrade forest biodiversity and habitats [14]. Additionally, among the main concerns surrounding biomass use is its potential to degrade air quality through the release of fine particulate matter (PM_1, $PM_{2,5}$ and PM_{10}), heavy metals and other hazardous compounds during combustion. These emissions contribute to poor air quality and can pose risks to human health [18].

2.1.2 Description of a masonry stove

A masonry stove, also named a mass stove, is a central heating system that uses biomass, specifically firewood, as energy source. It operates on the principle of accumulating heat at high temperatures during combustion and progressively releasing it at heating temperatures over time. Figure 2.1 presents a schematic representation of such a device, highlighting its four main components :

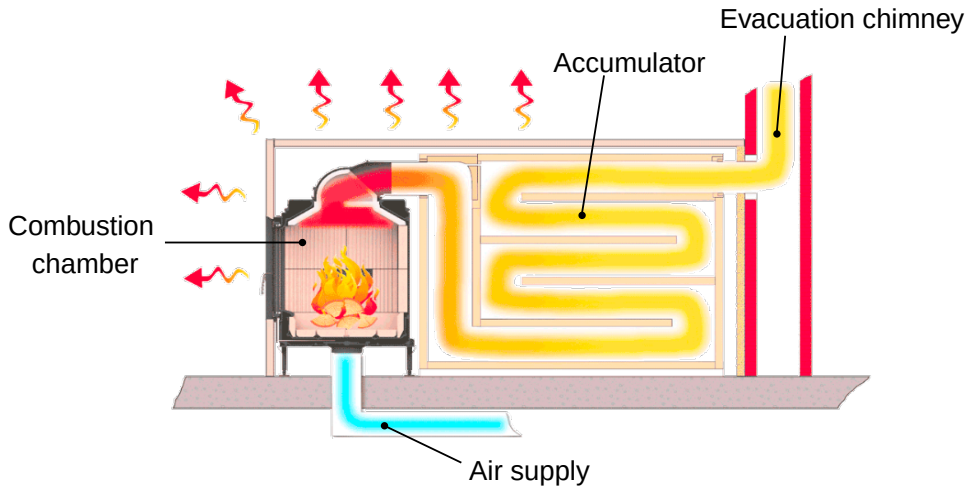

Figure 2.1: Schematic of the main components of a masonry stove [19].

- **The combustion chamber**: This is where wood combustion occurs, producing high-temperature combustion gases. Combustion occurs in a batch mode, with the wood loaded at once and burned over a given period without additional fuel input. The chamber is typically built from refractory bricks and equipped with a metal loading door, which may be glazed.

- **The air supply**: This component channels external air into the combustion chamber to support combustion. The air usually enters from beneath the stove, requiring an appropriate preliminary installation before building the stove itself.
- **The accumulator**: This part of the stove stores the heat produced during combustion and gradually releases it to the ambient environment. It is composed of an internal channel system that slows the movement of combustion gases to optimize heat exchange. These channels are made from refractory materials with high thermal resistance and inertia, allowing for an efficient and progressive heat restitution. Additionally, the channel network enables a second and complete combustion of the fumes at high temperatures, reducing emissions of unburned gases and enhancing overall efficiency.
- **The evacuation chimney**: This flue system, usually constructed of steel, ensures the proper expulsion of combustion gases to the exterior of the building.

In some cases, a decorative external finish, made from brick, stone, tiles, mineral coating, compressed earth blocks (CEB) or another type of refractory bricks, is applied on the external side of the stove. These materials are added not only to enhance aesthetic appeal but also to enhance thermal inertia and maintain high emissivity which is advantageous for heat radiation.

Furthermore, in the analysed French-type masonry stoves, a narrow throat, named the venturi opening, is placed just after the combustion chamber and before the accumulator channels (see Figure 2.2). This constriction produces a Venturi effect: as the flue gases pass through the reduced cross-section, their velocity increases and the static pressure drops. This pressure drop stabilizes the draft and reduces the risk of smoke backflow. In addition, the increased velocity and resulting turbulence promote the entrainment of secondary air into the combustion zone, enhancing mixing and facilitating complete combustion. Notably, this supports secondary combustion of the flue gases in the first part of the accumulator immediately after the combustion chamber.

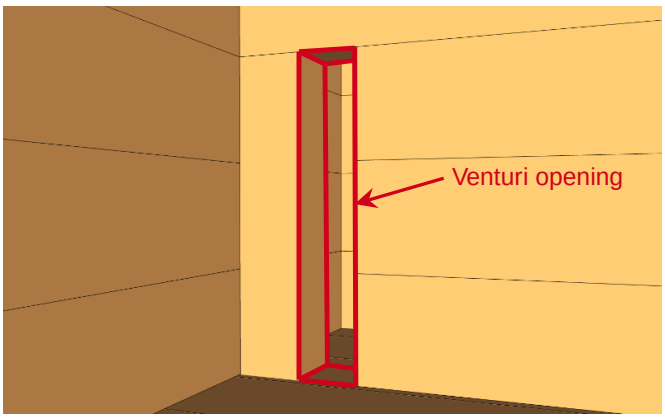

Figure 2.2: Throat opening between combustion chamber and accumulator channel from a French masonry stove of the company *UZUME*.

The accumulator and the combustion chamber are composed of materials selected for their high thermal resistance, high specific heat capacity, c_p, and moderate thermal conductivity, k, to ensure resistance to high temperatures (thanks to thermal resistance), effective accumulation of a big quantity of heat and gradual release of it (thanks to high c_p). Among the most used materials, there are concrete bricks (limited use only for the accumulator due to lower temperature resistance), stones as soapstone, and refractory bricks made from refractory clay and grog. Table 2.1 presents the thermal properties of these three materials with the range of variation depending on the density and composition, as well as metals (stainless steel and cast iron) commonly used in classical wood-burning stoves. Compared to these metals, masonry materials combine high heat capacity and relatively low thermal conductivity, making them well suited for masonry stove applications. Due to their lower temperature resistance, concrete bricks and stones are suitable for the accumulator, while refractory bricks can be used for both the combustion chamber and the accumulator. [20]

Material	**Max Temp (°C)**	**c_p (J/kg·K)**	**k (W/m·K)**
Concrete brick	$\sim$ 450	$\sim$ 900	0.5–2
Stones (soapstone)	600–1000	800–1000	5–6
Refractory brick	1200–1700	900–1100	1.0–1.5
Stainless steel	800–900	400-500	$\sim$15
Cast iron	600–700	460–550	30–55

Table 2.1: Thermal properties of different materials used in stoves.

Thanks to their thermal properties, the masonry materials used in the stove enable rapid and high temperature combustion of a single wood load. This combustion typically lasts 1.5 to 2 hours and is enough to release progressively heat over 12 to 24 hours. The amount of wood necessary as well as the dimensions of the combustion chamber and the accumulator are defined depending on the volume to be heated and the period between 2 wood reloads [21]. Many artisanal stove builders are skilled in making these dimensioning calculations. Therefore, this thesis focuses on the modelling of the stove operation rather than the dimensioning process.

2.1.3 History of masonry stoves

The use of thermal mass to store and radiate heat from a fire is not a recent innovation. One of the earliest known systems based on radiant heating is the Roman central heating system, named the hypocaust, used in thermal baths, particularly in the *Caldarium*, where heated floors and walls emitted stored warmth. [22]

After the Romans, the next use of accumulation heating stoves were only developed later in colder regions of Europe. The first stove, the *Grundofen*, closely resembling the modern masonry heater, appeared around the 12th century in Austria, one of the most developed country in terms of masonry stoves. This masonry stove featured a combustion chamber not fully enclosed by the accumulator's channels (Figure 2.3). Its cladding was typically composed of materials with excellent thermal properties - firebrick slabs, high density blocks, similar to magnesite bricks, specialized ceramics or cob. The *Grundofen* was a relatively simple and efficient stove, making it accessible and popular in rural Austrian

areas [23, 24, 25]. Later, during the 15th and 16th centuries, an aesthetic evolution of the *Grundofen*, the *kachelofen*, appeared in Austria. This stove was clad in glazed ceramic tiles, resulting in a higher surface temperature and a more decorative design (Figure 2.3). Both models remain in use in Austria today, but in modernized versions, as Austria has some of the most restrictive emission regulations for wood-burning heaters in Europe [26, 27, 28].

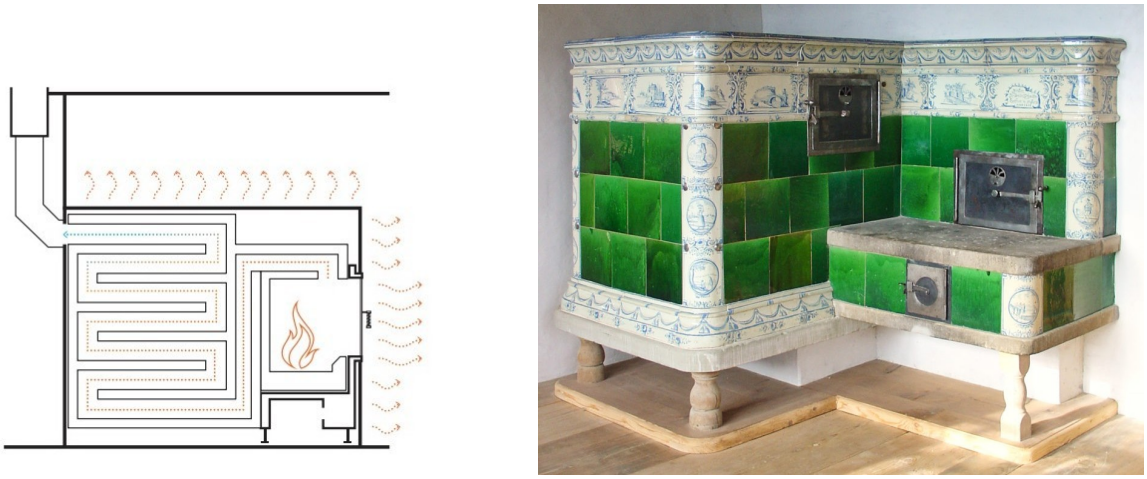

Figure 2.3: Schematic of *Grundofen* masonry stove (left) and typical *Kachelofen* masonry stove from 1816 (right)[23, 29].

Around the same period, in the late 15th-century in Russia, another type of stove was developed: the Russian oven. These stoves were made of clay sometimes reinforced with chopped straw. They served multiple functions: heating, cooking and even sleeping. It was built as a large and cuboid thermal mass featured with a tunnel-shaped vaulted cooking chamber and, thanks to a multitude of layers, a surface at a relevant temperature to sleep on it during harsh winters. Russian ovens are still found in some traditional homes today. [30]

Figure 2.4: Traditional cuboid Russian oven [31].

Later, in the end of 18th century, innovations emerged in Scandinavia. At that time, Sweden was experiencing a shortage of wood under high demands from the glass production industry and domestic heating. In order to cope with this energy crisis, the king Gustave III entrusted two talented designers, F. Wrede, a general, and C.J. Cronstedt, an architect, with the task of redesigning the traditional Austrian *Kachelofen*. They retained the tiled surface but introduced a contraflow system, using both upward and downward flue channels while the previous Austrian model only used upward flue channels (Figure 2.5). This system gave more resistance to the flue gas making them last longer in the channels and improving heat retention in the accumulator before exiting through the chimney. This new design was called the *kakelugn* [22, 32]. Then, in the late 19th century, Finland adapted the Swedish model to develop its own model, the *pönttöuuni*. Based on the

same contraflow principle, it featured symmetrical flue gas channels along the sides but differed in its external finish: instead of ceramic tiles, the Finns opted for a sheet metal cladding (Figure 2.5). This innovation made the stoves easier to build and maintain and reduced smoke leaks, while maintaining high thermal efficiency. Modern versions of these traditional stoves still exist today. A notable example is *Tulikivi*, a Finnish manufacturer that builds masonry heaters from soapstone, a material known for its exceptional thermal performances (see Table 2.1). *Tulikivi* stoves continue to use the contraflow principle and design derived from the *pönttöuuni*. [25]

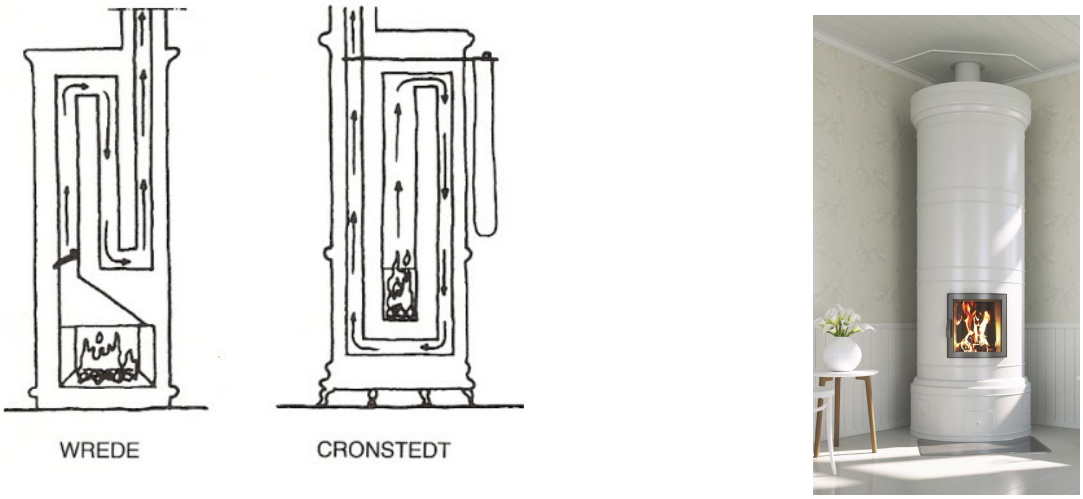

Figure 2.5: Contraflow principle of the *kakelugn* developed by Wrede and Cronstedt (left) and modern version of the metal-sheet cladded *pönttöuuni* (right) [22, 33].

More recently, from the late 20th century to early 21st century, a renewed interest in masonry stoves has emerged in France, notably through the low-tech approach. This includes the creation of the AFPMA, French association of the artisanal masonry stove, in 2008 and the adoption of adapted old versions of masonry stoves by ecological and low-tech communities. Unlike other countries that favor standardized designs, France has embraced more flexible and artisanal approaches. These stoves are often custom-built using local materials and inspired by a mix of traditional European designs. It is precisely this type of artisanal masonry stove that is analysed in this report, focusing on a model developed by the French company *UZUME*, which is active in low-tech communities, including *LowTech Liège*. A more detailed description of this stove is provided in later chapters.

2.1.4 Masonry stove as a final solution

Various low-tech space heating options exists, primarily using solar energy and biomass renewable sources of energy. These sources are favoured by low-tech communities due to their accessibility, sustainability and compatibility with simple technologies. In some regions, use passive solar heating, through well-oriented windows combined with effective insulation, provides sufficient warmth. In other cases, solar air heating technology, which relies on a solar collector, offers an additional solution. In this system, cool indoor air is drawn into the collector and heated by solar radiation. The resulting temperature increase causes a decrease in air density, generating a natural upward airflow that

recirculates the warmed air back into the interior space. However, in areas with limited sunlight, such as Belgium, these methods do not provide adequate heating during winter, necessitating additional heating solutions. It is in this case that biomass-based low-tech technologies appear. [34]

Among biomass-based alternatives, there are the classical wood-burning stove based on convection heat transfer, the rocket stove (same principle as the classical wood-burning stove but with an optimized and more efficient combustion) and the masonry stove. The masonry stove stands out as the final low-tech solution compared to others due to its multiple advantages:

- **Accessibility:** The design principles of masonry stoves are straightforward, making them easy to understand, maintain and repair in case of problem. The possibility of buying mountable kits make them widely accessible and constructible by the greatest number.
- **Reduced operational effort:** Compared to classical wood stoves, masonry stoves are less time-consuming. One combustion enables to have a long-lasting heat restitution thanks to the highly inertial materials, reducing the frequency of refuelling.
- **Enhanced thermal comfort:** The large, hot radiative surfaces of a masonry stove contribute to a comfortable thermal environment. Temperatures within the room tend to be reasonably balanced from floor to ceiling, and radiant heat allows occupants to feel comfortable even if the air temperature is moderate. Research at MIT (Massachusetts Institute of Technology) has shown that people often prefer rooms with cooler air but warm surfaces, rather than warmer air with cold surfaces [98]. This emphasizes the importance of radiant heating in maintaining comfort efficiently, potentially reducing the need to overheat the room and lowering energy consumption.
- **High efficiency and low emissions:** The secondary combustion of fumes within the internal channels ensures higher efficiency and lower pollutant emissions than classical stoves. The efficiency of modern high-efficiency traditional wood stoves goes rarely above 70-80% while optimized masonry stoves can reach efficiencies of 90 to 95%. This higher efficiency allowing for a lower consumption of wood for the same quantity of heat delivered. [16, 21]
- **Environmental benefits:** The Life Cycle Assessment (LCA) of the masonry stove shows a low Global Warming Potential (GWP) of 0.0381 $kg_{CO_2,eq}$/kWh, compared, for example, to 0.0879 $kg_{CO_2,eq}$/kWh for heat pumps and 0.2833 $kg_{CO_2,eq}$/kWh for gas boilers [20].
- **Energy independence:** In a world that is increasingly moving towards electrification, biomass provides a sustainable alternative to reduce stress on the electricity demand and electrical grid, while waiting for it to be strengthened.
- **Adaptability and multifunctionality:** Depending on the models, a masonry stove can include features for heating water or cooking by, for example, adding an oven inside its canals or cooking plates on top of it. Nevertheless, care must be taken that these additional elements does not perturb the combustion process at risk of incomplete combustion and increased pollutant emissions.

Nonetheless, there are also drawbacks that must not be forgotten :

- **High mass:** Units often exceed 1 tonne and can reach until 6 tonnes for the biggest one, requiring structural reinforcement of the supporting floor [26].
- **Initial cost:** The initial cost is relatively costly compared to other heating systems, ranging between 6000€ and 15000€ depending on the size and power needed [35]. However, this cost is partially offset over time by the fuel savings it generates and can be mitigated by government subsidies or self-construction using kits that are cheaper.
- **Slow heat-up:** Due to its high thermal inertia, it has a slow-heat up. It requires pre-scheduling of combustion to have a good thermal comfort at the moment wanted.
- **Operational sensitivity:** Improper operation (e.g., insufficient fire, disrupted combustion) can reduce efficiency, damage components and increase the emissions of greenhouse gases.
- **Air pollutant emissions:** Masonry and traditional stoves release high levels of air pollutants (Particulate Matter (PM), Volatile Organic Compounds (VOCs), nitrogen oxides (NO_x)), significantly impacting air quality. An LCA results indicate that approximately 10^4 m^3 of equivalent air would be theoretically required to dilute or neutralize the pollutants emitted per kWh of energy produced by a masonry stove, compared to 10^1 m^3/kWh for heat pumps and gas boilers [20]. This highlights that air pollution is one of the most critical disadvantages of masonry stoves.

2.2 Thermal modelling

This section first reviews the fundamental heat transfers mechanisms occurring in a masonry stove. Then, develops how these exchanges could be modelled and how the resulting equations can be solved numerically.

2.2.1 Fundamentals of thermal behaviour

The following overview of heat transfers mechanisms in masonry stoves is based on the textbook by Incropera and al. [36], the energy factsheet on masonry stoves from the Brussels Institute for Environmental Management [21] and the course on Heat transfers by P. Dewallef and V. Terrapon [37].

Heat is transferred via three well-known mechanisms: conduction, convection and radiation. A masonry stove uses all three of them, tough to varying extents. **Conduction** is the transfer of thermal energy through molecular vibrations and collisions within a material or across materials in contact. This physical phenomenon, driven by temperature gradients, occurs within the bricks of the combustion chamber and the accumulator, as heat is transferred from the hot combustion gases into the solid materials and eventually to the ambient air. Mathematically, the heat flux transferred by conduction in a material of thermal conductivity, k [W/mK], and from a point a to a point b separated by a distance dx is computed:

$$q''_{cond} = k \frac{(T_a - T_b)}{dx} \tag{2.1}$$

Convection is the heat transfer between a surface and a fluid in motion, combining molecular diffusion and bulk fluid motion (advection). Convection heat transfer can be classified by flow type. If the flow is caused by external means, it is named forced convection. On the other hand, natural or free convection occurs as warmer air, heated by contact of a hot surface, becomes less dense and rises. It is this type of convection that occurs at the outside of masonry stoves and radiators. The heat flux transferred by convection is expressed by the Newton's law of cooling :

$$q_c'' = h(T_s - T_f) \tag{2.2}$$

where h is the convection heat transfer coefficient [W/m^{2}K], T_s is the surface temperature [K] and T_f is the fluid temperature [K]. The value of the convective heat transfer coefficient typically depends on: the boundary layer, the nature of the fluid motion, fluid thermodynamic and transport properties. It is computed based on these condition through different formulas. For free convection on vertical surfaces, h can be approximated as a typical order of magnitude of 4 W/m^2K, depending on the fluid properties and temperature difference. Using this approximation and a constant convective heat transfer coefficient, Figure 2.6 illustrates the increase in convective heat flux with surface temperature. This is an interesting property since masonry stoves have surfaces at relatively high temperatures. Nevertheless, convection accounts only for a small portion of the total heat transfer from a masonry stove. The main heat transfers occur through the third mechanisms: radiation.

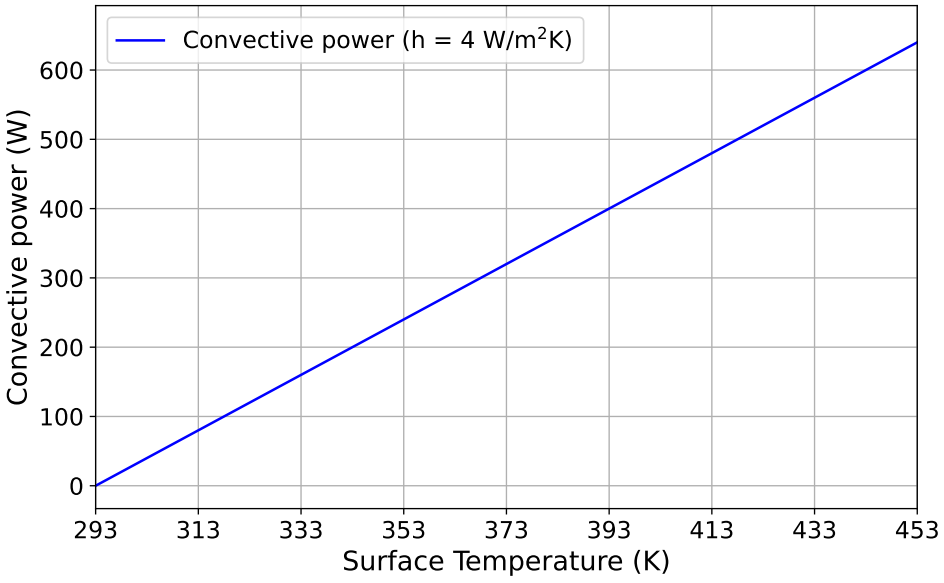

Figure 2.6: Evolution of convective heat transfer rate [W] with variation of the surface temperature ($T_f = 293.15$ K and surface of 1 m^2).

Radiation is energy emitted by matter at non-zero temperature. This energy is transported by electromagnetic waves. Therefore, this exchange happens between two surfaces, one emitting and the other receiving. A surface, at a certain temperature, is able to emit power through radiation. Nevertheless, it can never emit power higher than a certain limit which is defined by the power emitted by a blackbody at this temperature. This limit, is defined by the emissive power of a blackbody, E_b, and is given by the Stefan-Boltzmann

law:

$$E_b = \sigma T_s^4 \tag{2.3}$$

where σ is the Stefan-Boltzmann constant: $\sigma = 5.67 \times 10^{-8}$ [W/m^{2}K^4].

Real surfaces, they emit less than blackbodies. This is accounted by using a property of the material's surface: the emissivity, ϵ ($0 < \epsilon < 1$). In addition to emissivity, the portion of radiation absorbed by a surface must be considered to calculate the net radiative heat flux. This absorbed radiation is:

$$G_{abs} = \alpha G \tag{2.4}$$

where α is the absorptivity, how much incident radiation is absorbed ($0 < \alpha < 1$), and G is the irradiation [W/m^2].

In the special case of a radiation exchange between a small surface at T_s and a much larger isothermal surface, that completely surrounds the smaller one, the irradiation of the surrounding surface may be approximated by that of a blackbody at T_{sur}: $G = \sigma T_{sur}^4$. This applies for masonry stove walls, the small surfaces exchanging radiation with the much larger room walls. If the surface is assumed to be a gray surface ($\alpha = \epsilon$), the net radiative heat flux becomes and can finally be expressed:

$$q_r'' = \epsilon E_b - \epsilon \sigma T_{sur}^4 = \epsilon \sigma (T_s^4 - T_{sur}^4) \tag{2.5}$$

This radiation phenomenon shows that masonry stoves must be placed in clear and open spaces, free from obstructive objects, to maximize radiative heat transfer by letting electromagnetic waves reach walls and people. Figure 2.7 shows the dependence of radiative heat power on surface temperature. Similar to convection, the strong increase of radiative heat transfer with surface temperature is advantageous for masonry stoves, which have surfaces at relatively high temperatures.

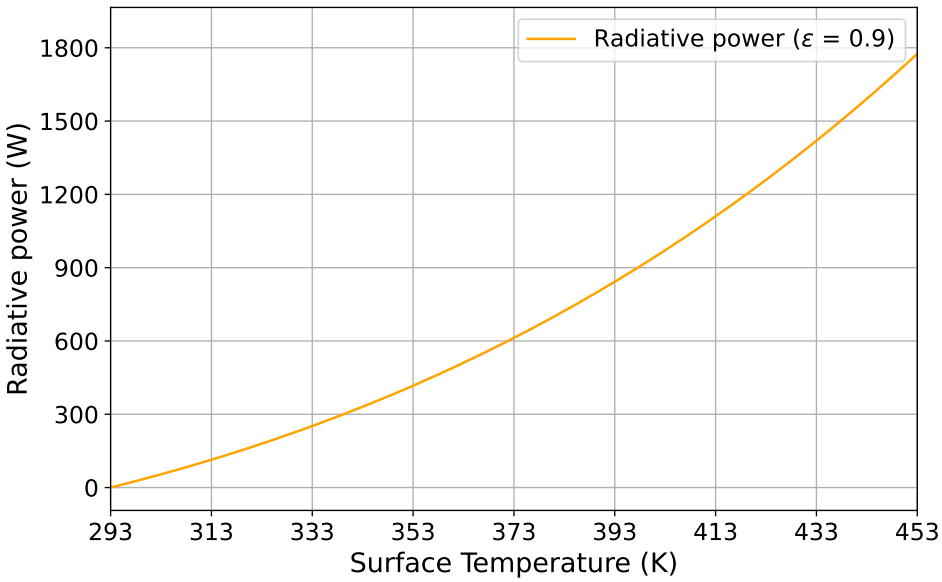

Figure 2.7: Evolution of radiative heat transfer rate [W] with variation of the surface temperature ($T_{sur} = 293.15$ K and surface of 1 m^2).

Finally, the total heat transfer rate transmitted to the ambient air combines both radiation and convection as shown in Figure 2.8. This figure presenting the variation of this total heat transfer rate with the surface temperature, confirms that for typical masonry stove surface temperatures that can approximately reach up to 130°C (403.15 K), radiation is the dominant heat transfer mode.

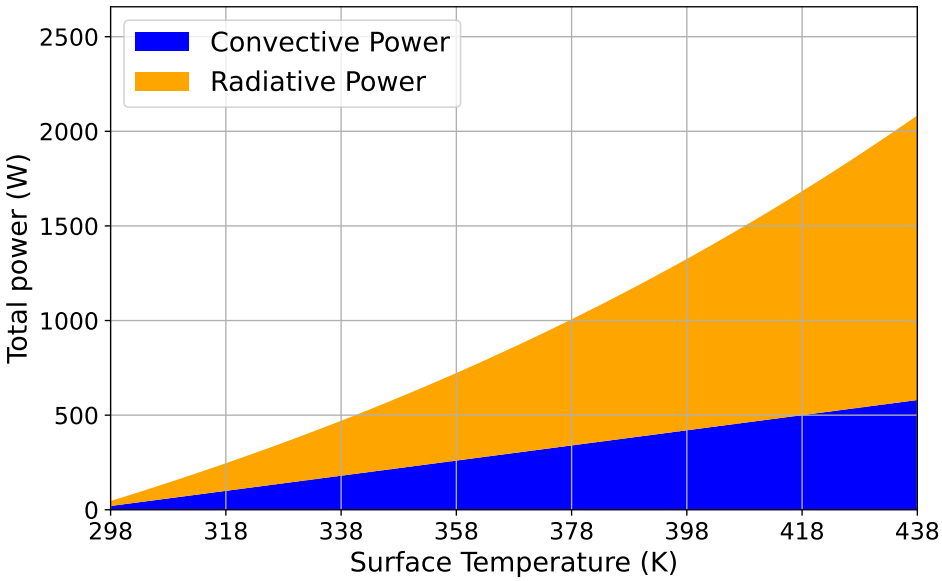

Figure 2.8: Evolution of total (radiation + convection) heat transfer rate from a surface [W] with variation of the surface temperature.

2.2.2 RC network

In thermal system modelling, these three mechanisms of heat transfer can be represented using an equivalent electrical analogy known as the resistance–capacitance (RC) network model. RC network models are widely used to represent transient heat transfer in buildings and thermal systems due to their low computational cost and ease of coupling with system-level models. In this approach, thermal resistances, R [K/W], represent the opposition to heat flow, analogous to electrical resistances in a circuit, while thermal capacitances, C [J/K], model the ability of materials to store thermal energy, analogous to capacitors. When applied to a control volume with lumped properties (properties, like temperature or heat capacity, that are uniform throughout the region or component), the heat balance can be expressed as a first-order ordinary differential equation (first-order ODE). For example, for a wall temperature node at temperature $T(t)$ that exchanges heat with the ambient environment and receives a time-dependent heat input, the balance is:

$$C\frac{dT(t)}{dt} + \frac{T(t) - T_\infty}{R} = \dot{Q}_{\text{in}}(t) \tag{2.6}$$

where:

- $T(t)$ is the node temperature (e.g., an internal wall node),
- T_∞ is the ambient or boundary temperature,
- $\dot{Q}_{\text{in}}(t)$ is the time-dependent heat input [W].

The thermal resistances and capacitance can be computed using the equations listed in Table 2.2. When multiple resistances or capacitances are present, they may be combined to obtain equivalent parameters. Thermal resistances can be combined following the same rules as electrical resistances: they add up when in series and follow reciprocal addition when in parallel. Thermal capacitances, by contrast, add directly when the corresponding elements are assumed to share a common temperature node, corresponding to a parallel configuration in a lumped-parameter thermal model. [36, 37, 41]

Type	**Formula**	**Variables**
Conduction (flat wall)	$R = \frac{L}{kA}$	L: thickness, k: conductivity, A: area
Convection (surface)	$R = \frac{1}{hA}$	h: convective coefficient, A: area
Radiation	$R = \frac{1}{h_{\text{rad}}A}$	h_{rad}: radiative heat transfer coefficient for linearised radiation
Thermal Capacitance	$C = \rho V c_p$ or $C = m c_p$	ρ: density, V: volume, c_p: specific heat

Table 2.2: Basic thermal resistance and capacitance formulas.

2.2.3 Numerical solvers

Once the thermal behaviour is represented by an RC network, the governing equations can be written as a system of coupled ordinary differential equations (ODEs), such as that given in Eq. (2.6). These ODEs generally cannot be solved analytically and require numerical time-integration schemes. Numerous time-integration schemes exist in the literature about numerical modelling to solve these systems.

Explicit methods, such as the Forward Euler scheme and Runge–Kutta methods, are widely used due to their simplicity and ease of implementation [38, 39]. However, for stiff problems, such as those arising from strongly coupled RC thermal networks, explicit schemes generally require very small time steps to maintain numerical stability [40].

To overcome this limitation, implicit methods, including the Backward Euler and Backward Differentiation Formula (BDF) schemes, are preferred for stiff thermal problems. These methods are unconditionally stable for linear systems and allow larger time steps while maintaining accuracy [41, 42, 43]. Both explicit and implicit methods have already

been applied in thermal simulations and lumped-parameter thermal models to handle strong thermal coupling and long-time integration [41, 44].

Time-integration schemes are further subject to stability and accuracy constraints. Explicit methods require time steps small enough to satisfy Courant–Friedrichs–Lewy (CFL) conditions for advective transport, as well as stability limits related to the resistances and capacitances of the RC network. Implicit methods relax these stability restrictions for linear systems and are generally independent of the RC network parameters. Nevertheless, when advective heat transport is present, CFL-type constraints remain relevant as practical guidelines to ensure physically meaningful propagation of thermal energy, even with implicit schemes. [45, 46, 47, 48, 49]

Chapter 3

Masonry stove model

This chapter constitutes the main part of this work. It details the modelling of the French-type masonry stoves developed by *UZUME*, including the assumptions, inputs, governing equations, discretization, numerical solvers, and preliminary simulation results.

3.1 Software used

The model has been entirely developed using the programming language *Python*. This language was chosen due to its widespread use in both academia and industry. It is a simple and readable language with a syntax that closely resembles natural human language. It is open source and offers a vast ecosystem of libraries that significantly reduce development time and enable powerful functionality with minimal code.

The 3D modelling software, *SketchUp*, was also used to create visual representations of the masonry stove under study. The French company, *UZUME*, which supplies the masonry stoves for the *Renolow* project, provided stove sketches through this software.

3.2 Modelling methodology

To model the masonry stove, the problem was divided into several stages represented in Figure 3.1. The first step is to set up the stove configuration. This includes performing pre-processing computations and initializing all relevant model inputs, such as the discretized stove geometry, material properties, and initial temperature values. This setup phase serves as the foundation for the subsequent time-dependent modelling process.

Once the configuration is initialized, the model computes the stove's thermal evolution in two main stages:

- **Combustion modelling**: The combustion occurring in the combustion chamber is modelled using an adiabatic combustion chamber model (Step 2 in Figure 3.1). This model outputs the adiabatic flame temperature resulting from the combustion process. This temperature is then used as a reference to reconstruct the flue gas temperature profile during the combustion, based on typical combustion flue gas temperature trends. This reconstructed flue gas temperature profile is prescribed as a time-dependent thermal boundary condition in the combustion chamber and acts as the driving source for heat transfer within the stove. It represents, in a simplified manner, the heat released by the batch wood combustion process.

- **Heat storage and release dynamics**: In the second part of the modelling (Step 3 in Figure 3.1), the flue gas temperature profile is used as an input to simulate the transient thermal behaviour of the masonry stove. The model computes the temporal evolution of temperatures at the discrete locations defined by the spatial discretization. It accounts for the main physical phenomena governing the stove operation, including heat transfer and thermal energy storage, over both the combustion (or accumulation) phase and the restitution phase, during which the stove gradually releases the stored heat.

In summary, the model takes as input the stove configuration, initial temperatures, and basic combustion data. It then computes the temperature evolution at all discretized nodes, with each node representing the average temperature of its corresponding discretised control volume.

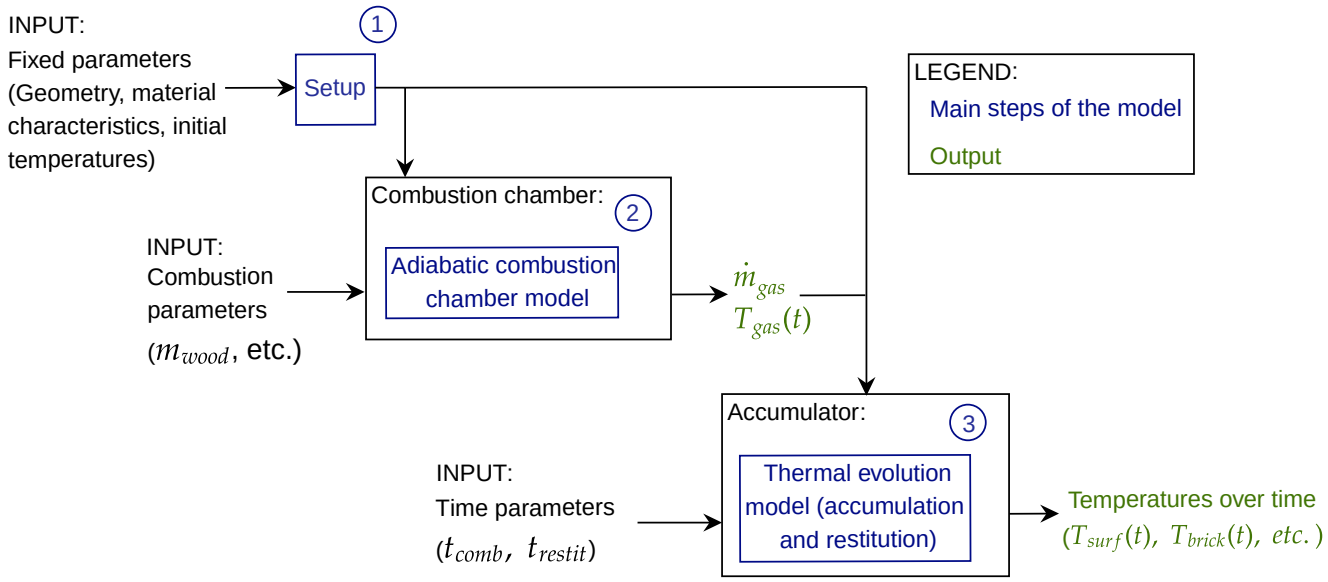

Figure 3.1: Schematic of the main steps, outputs and inputs of the numerical model.

3.3 Discretization

As just seen in the modelling methodology, before running the model, the user must define the discretization of the masonry stove modelled to give it as an input. It consists of two choices: dividing the accumulator's internal flue-gas circuit into control volumes along the flow path and specifying the discretization within each wall. Each flue-gas control volume is represented by a single temperature node, whose value corresponds to the average temperature over the control volume. Similarly, each wall surrounding a gas control volume is discretized into n_{nodes} volume elements, each represented by its own temperature node.

3.3.1 Accumulator discretization in control volumes

The discretization enables the model to accommodate diverse stove geometries. Strict rules are enforced for the discretization to ensure that the segment-level energy

balances computed by the model remain valid and consistent. For illustration, Figure 3.2 shows the discretization of a part of the accumulator flue gas domain visible into six segments (control volumes bounded by stove walls).

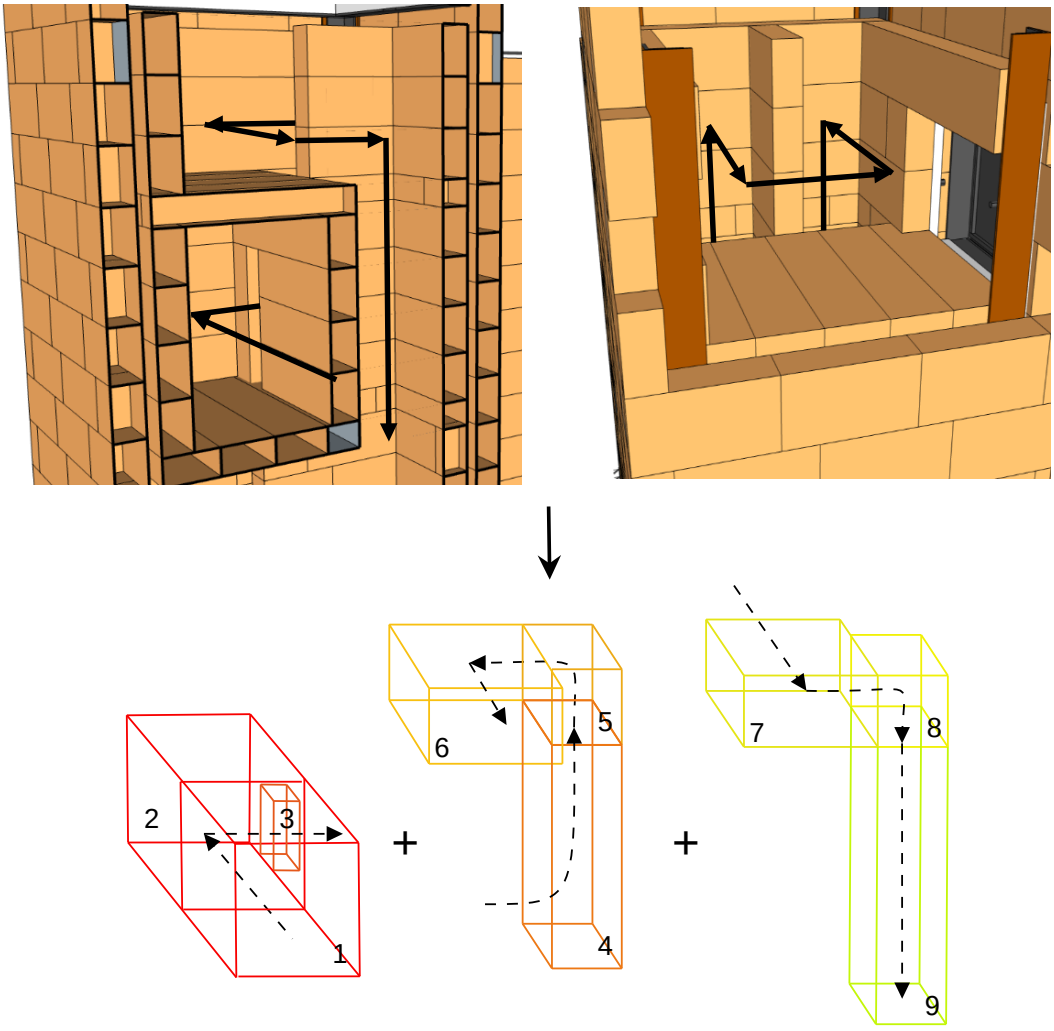

Figure 3.2: Illustration of the gas domain discretization into control volumes at a change of flow direction in the stove's flue-gas circuit.

The discretization follows a set of fundamental rules that must be applied in all cases. A new gas segment is created whenever:

- the cross-sectional area perpendicular to the gas flow changes;
- the gas flow direction changes (e.g., between segments 5 and 6 or 7 and 8);
- the surrounding wall materials differ on any side of the control volume. For instance, segments 4 and 5 share three walls (right, back and front sides) but differ on the left side, where segment 4 has a wall while segment 5 is open to the adjacent gas segment.
- a wall of a gas segment is in contact, on its opposite face, with more than one gas segment. For example, segments 1 and 2 are split because they follow the separation of their right wall that adjoins two distinct segments (4 and 9). As a result, to

preserve consistency of the wall–gas heat exchange, segments 6 and 7 are also split, as their bottom walls are in contact with segments 1 and 2 that just have been splitted.

The rules described above govern the discretization of the gas domain along the flue gas flow direction in the channels. In most cases, the walls forming the channels and surrounding a discretized gas segment follow the same discretization as the gas domain, meaning that each surrounding wall is divided at the same locations as the gas segments.

A specific situation arises when a wall of a discretized gas segment is in contact, on its opposite face, with two discretized gas segments in which the flow directions are perpendicular to the flow direction in the original segment. In this case, the gas region remains a single gas segment characterized by a uniform gas temperature. However, to correctly account for heat exchange with adjacent regions having different flow orientations and being separated, the surrounding walls are subdivided accordingly. This subdivision of the wall envelope is referred to here as a *wall sub-element*. Each physical wall within a sub-element is discretized independently through its thickness and is associated with its own set of temperature nodes, as detailed in the next section.

This subdivision allows the wall discretization to match the adjacent gas segments and ensures an accurate representation of heat fluxes at the interfaces. Consequently, the wall discretization may be finer than the gas discretization. In the following sections, the total numbers of gas segments and wall sub-elements are denoted by M and N, respectively.

As an example, Figure 3.3 shows segments 1 and 2, two discretized gas segments divided transversely. These segments share their left wall with the right wall of the single gas segment 4, whose flow direction is perpendicular to that of segments 1 and 2. Since the opposite face of segment 4's right wall adjoins the two divided gas segments, all walls surrounding segment 4 are subdivided into two wall sub-elements, following the separation in segments 1 and 2 (separated by the dotted lines on the figure). Segment 4 itself remains a single gas segment with a uniform gas temperature, but is thermally coupled to multiple wall sub-elements with distinct wall temperature fields. Thus, the model represents a single discretized gas region while resolving heat transfer through finer discretized wall sub-regions to preserve accurate heat exchange.

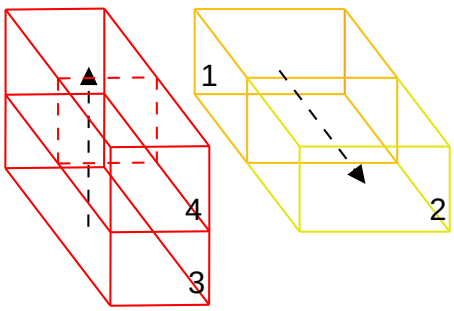

Figure 3.3: Wall sub-element discretization within a single gas segment.

3.3.2 Wall discretization

After discretizing the gas domain into gas segments and the subdivision of walls into wall sub-elements (along their length), each wall within a wall sub-element is also discretized as a one-dimensional domain along its thickness, e. Each wall is divided into n_{nodes} discrete elements, each associated with a centered temperature node Figure 3.4 shows this discretization and the associated thermal resistances. The number of nodes controls the spatial resolution of heat conduction within a wall layer: a higher number of nodes improves accuracy but increases computational cost. The optimal choice of this number of nodes is defined in section 3.8.3.

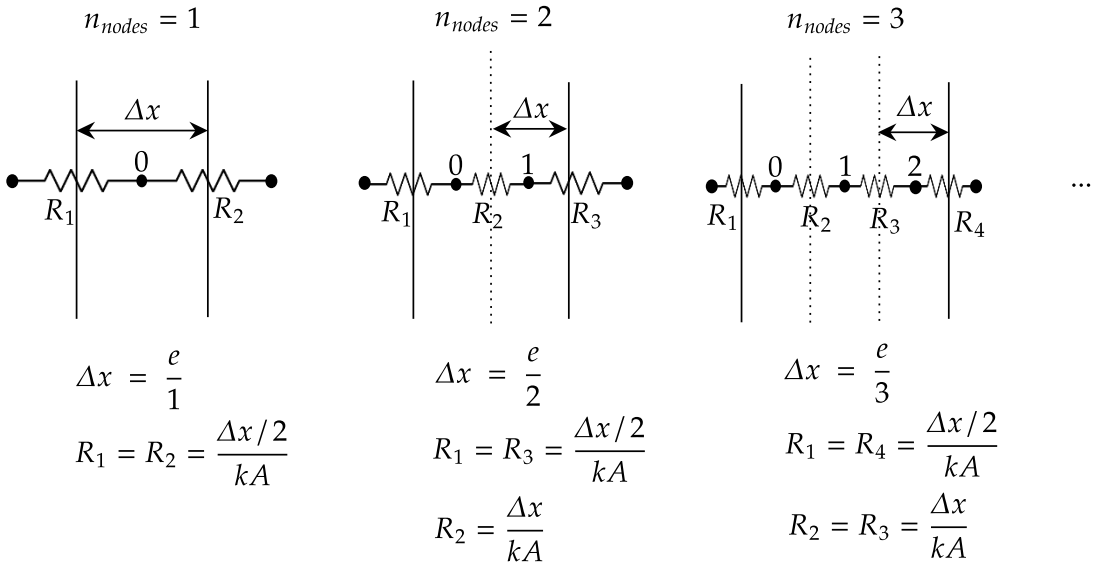

Figure 3.4: Wall discretization for different numbers of temperature nodes.

3.3.3 Global discretization

After the discretization of the gas domain into gas segments and the subdivision of walls into wall sub-elements along their length and thickness, the full stove domain can be represented in a consistent, global indexing system. The flue-gas circuit is divided into M gas segments and thus M gas temperature nodes, indexed from 0 to $M-1$. Each gas segment may be associated with one or more wall sub-elements, which are indexed from 0 to $N-1$. Each wall sub-element is bounded by up to five individual walls (most of the time four), and each of these walls is further discretized along its thickness into n_{nodes} temperature nodes, indexed from 0 to $n-1$. It is worth noting that, although temperatures are updated based on heat transfer between discrete nodes, each node represents the average temperature of its associated control volume.

Figure 3.5 illustrates a simplified 1D straight representation of this discretization structure, where only two walls per sub-element are shown and no subdivision of gas segments into wall sub-elements is considered ($M = N$). In this representation, each wall temperature is identified by three indices, $T_{\text{wall},i,j,k}$, defined as follows:

- i: index of the wall sub-element (equal to the gas-segment index in this simplified case), $0 \leq i \leq M-1$,
- j: wall side within the segment (Left (j=0), Right (j=1), Top (j=2), Bottom (j=3), Back (j=4) or Front (j=5)),
- k: through-thickness node index, $0 \leq k \leq n_{nodes} - 1$.

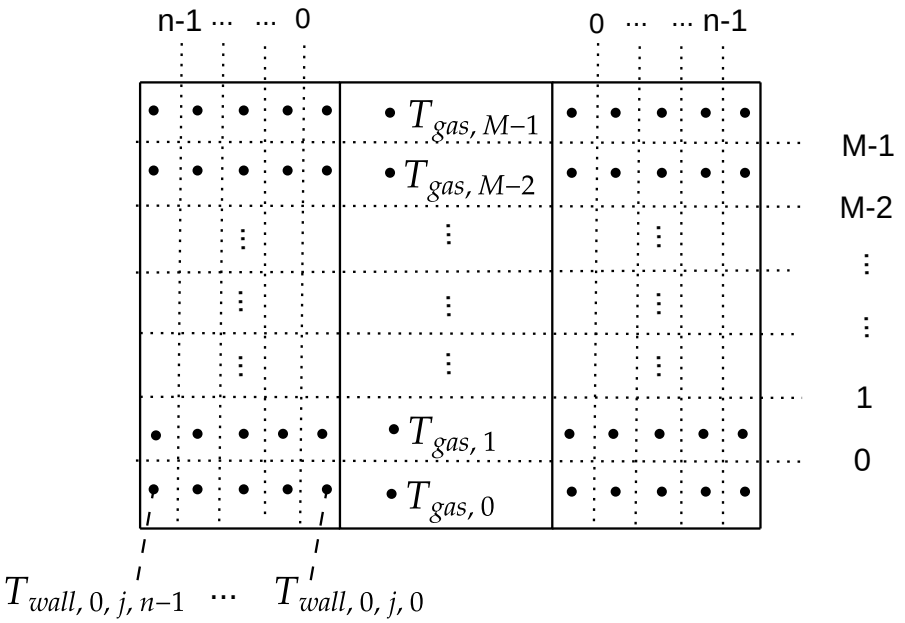

Figure 3.5: Simplified 1D representation of the discretization of the masonry stove (only two walls per gas segments are shown).

3.4 Masonry stove model setup

As described in the literature review, the masonry stove consists of a combustion chamber and an accumulator through which the flue gas circulates. The internal walls of the masonry stove are made of refractory materials, while the external walls, in contact with the ambient environment, are often composed of two layers to increase inertia: a refractory material and an outer casing. Once discretized, this configuration is provided to the computer model and stored as a constant throughout the time-dependent simulation. This initial stage of the model, referred to as the setup, also performs preprocessing computations of thermal properties and parameters that remain constant during the simulation. In this section, the assumptions and user inputs required for the setup are first described, followed by the computations and wall-element initialization performed during this stage of the model.

3.4.1 Assumptions

The following hypotheses are made for the pre-computations of the stove configuration, geometry and flue gas properties:

- The majority of thermal properties (e.g., conductivity, capacity, density) of the walls are assumed to be temperature-independent.
- The heat transfers are supposed unidirectional across each wall. As a consequence, no heat transfer is occurring within the corners where two walls meet and these corners surface areas are not taken into account for exchanges with the ambient. Figure 3.6 shows in black a schematic example of the regions excluded from the model geometry using this assumption. However, while there are no heat transfers through these regions, their mass is still taken into account in the capacities of the walls to have an accurate representation of the inertia of the entire stove.

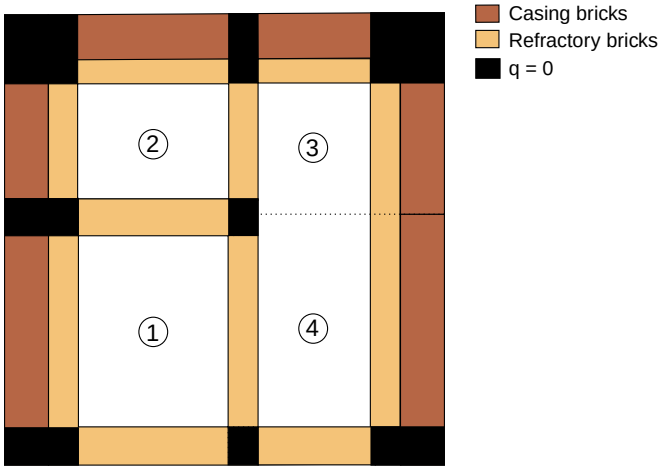

Figure 3.6: Illustration of the neglected wall regions for thermal behaviour.

- The wood is approximated as a generic hardwood with an empirical elemental composition of $C_1H_{1.43}O_{0.66}$. This approximation is representative of typical hardwood species commonly burned in masonry stoves in Belgium, and is consistent with the type of wood used in the experimental measurements.[2]
- Complete combustion: all carbon is converted into CO_2, with no CO formation. Even if this is a big assumption, it is justified by the presence of secondary combustion of gases in masonry stoves, as outlined in Section 2.1.4. However, it is important to mention that this assumption is valid when the combustion is done in good conditions (enough air supply, etc.).
- Flue gas considered at standard pressure of 1 bar.
- Dry-air assumption (no Argon), with air composition (molar) given by:

$$\mathrm{O_2} : 0.2095, \quad \mathrm{N_2} : 0.7905$$

so that:

$$\frac{n_{\mathrm{N_2}}}{n_{\mathrm{O_2}}} \approx 3.76.$$

3.4.2 Inputs

Once the user has defined the stove discretization, the following inputs must be specified for the setup stage. These inputs are used for pre-processing computations and retained throughout the time-dependent simulation:

[2]The molecular formula, $C_1H_{1.43}O_{0.66}$, has been obtained from the mass percentages of carbon (50%), hydrogen (6%) and oxygen (44%) present in dry hard firewoods [50, 51, 52]. From these percentages, assuming 100 g of dry wood, the corresponding moles of each component are obtained: C: $\frac{m_C}{M_c} = \frac{50}{12.01} = 4.16$, H: $\frac{m_H}{M_H} = \frac{6}{1.008} = 5.95$ and O: $\frac{m_O}{M_O} = \frac{44}{16.00} = 2.75$. By normalizing with respect to carbon, the molecular formula is obtained: H: $\frac{5.95}{4.16} = 1.43$ and O: $\frac{2.75}{4.16} = 0.66$.

Discretized geometry and configuration inputs:

- Two tables, one for gas segments and the other for wall sub-elements (sizes M and N), listing the length, L [m] (perpendicular to the stove door dimension), height, H [m] (vertical dimension) and width, w [m] (parallel to the stove door dimension) of each gas segment and wall sub-element. As noted in the previous section 3.3.1, a single gas segment may correspond to multiple wall sub-elements.
- A boolean matrix indicating the presence (1) or absence (0) of a refractory wall layer and/or a casing wall layer for each side of each wall sub-element. The matrix has N columns (one per wall sub-element) and 6 rows (one per side: left, top, right, bottom, back and front). The side's order is defined in a coordinate system where the observer stands in front of the masonry stove door. For example, on Figure 3.6, imagining that the door is parallel to the sheet, segment 2 has its left and top sides composed of two layers while his bottom and right sides are only composed of a refractory wall and its front and back sides have no closure. Analysing in this way the four segments present in the Figure, the following matrices would be given:

$$\mathrm{rfr}_{\mathrm{walls}} = \begin{bmatrix} 1 & 1 & 1 & 1 & 0 & 0 \\ 1 & 1 & 1 & 1 & 0 & 0 \\ 1 & 1 & 1 & 1 & 0 & 0 \\ 1 & 1 & 1 & 1 & 0 & 0 \end{bmatrix} \qquad \mathrm{cng}_{\mathrm{walls}} = \begin{bmatrix} 1 & 0 & 0 & 0 & 0 & 0 \\ 1 & 1 & 0 & 0 & 0 & 0 \\ 0 & 1 & 1 & 0 & 0 & 0 \\ 0 & 0 & 1 & 0 & 0 & 0 \end{bmatrix} \tag{3.1}$$

- A table to define pair walls that are shared between two or more wall sub-elements. Analysing again Figure 3.6, for which for example the top wall of segment 1 is shared with the bottom wall of segment 2, the matrix would be ((a, b): a=wall sub-element and b=side of the wall considered in the wall sub-element):

$$\mathrm{shared}_{\mathrm{rfr,walls}} = \begin{bmatrix} (1, \text{'TOP'}), & (2, \text{'BOTTOM'}) \\ (1, \text{'RIGHT'}), & (4, \text{'LEFT'}) \\ (2, \text{'RIGHT'}), & (3, \text{'LEFT'}) \end{bmatrix} \tag{3.2}$$

- A table indicating the direction (front, back, left, right, up or down) of the flue gas flow in each discretized gas segment (table of size M). Assuming the gas flow is going inside the sheet in section 1 and out of the sheet for others sections of Figure 3.6, this matrix would be:

$$\mathrm{directions} = \big[front, \quad back, \quad back, \quad back,\big] \tag{3.3}$$

- A table describing which gas segments are divided in several wall sub-elements. From Figure 3.3, gas segment 4 would be divided into two wall sub-elements 4 and 5, which would give for that simplified example the table:

$$\mathrm{div}_{gas,seg} = \big[4 : [4, 5]\big] \tag{3.4}$$

Thermophysical properties inputs:

- Thickness of each wall type (refractory and casing), e [m];
- Densities of gas and both wall types, ρ [kg/m^3];
- Thermal conductivity of both wall types, k [W/mK];
- Specific heat capacity of both wall types, c_p [J/kgK];
- Initial temperature of walls, $T_{init,walls}$ [K];
- Number of temperature nodes desired inside a wall, n_{nodes} [-]

3.4.3 Preprocessing computations

Before solving the time-dependent thermal problem, the set of preprocessing computations is performed to initialize all quantities that remain constant throughout the simulation. These include the masses of the refractory and casing walls for each wall sub-element, the mass and thermophysical properties of the flue gas in each gas segment, and the radiative view factors between walls within the accumulator. Since material properties are assumed to be temperature-independent, all these quantities are computed once during the setup phase and stored for use in the transient model.

3.4.3.1 Mass calculations

Each wall's mass is calculated from its dimensions and density. For example, considering a wall sub-element i, the masses of the refractory (rfr) and casing (cng) walls located on its left and top sides are computed using the geometrical dimensions defined in the inputs section:

$$m_{rfr,i,left} = L_i \times H_i \times e_{rfr} \times \rho_{rfr} \tag{3.5}$$

$$m_{cng,i,left} = L_i \times H_i \times e_{cng} \times \rho_{cng} \tag{3.6}$$

$$m_{rfr,i,top} = L_i \times w_i \times e_{rfr} \times \rho_{rfr} \tag{3.7}$$

The mass of flue gases in a gas segment of index k is also calculated based on the volume of this segment but this time using the flue gas density of the corresponding gas segment:

$$m_{gas,k} = L_k \times w_k \times H_k \times \rho_{gas,k} \tag{3.8}$$

At the end of these computations, the model stores a table of size $N \times 6$ (number of wall sub-element $\times$ number of wall sides per sub-element) for all wall masses and a table of size M of gas control volume masses.

3.4.3.2 Combustion flue gas thermophysical properties

The properties of the flue gas depend on its composition, which itself is determined by the type of wood burned. In this section, the flue gas composition and properties are derived from the elemental composition of dry wood, represented as $\mathrm{C_xH_yO_z}$. To determine the resulting flue gas species, the general form of the complete combustion reaction, accounting for fuel moisture and excess air, ex, is given by:

$$\begin{aligned}\mathrm{C_xH_yO_z} \;+\; n_{\mathrm{H_2O,m}}\,\mathrm{H_2O} + (1+\mathrm{ex})\,\nu_{\mathrm{O_2,stoich}}\big(\mathrm{O_2} + 3.76\,\mathrm{N_2}\big) \\ \longrightarrow\; x\,\mathrm{CO_2} \;+\; \Big(\frac{y}{2} + n_{\mathrm{H_2O,m}}\Big)\,\mathrm{H_2O} \;+\; \mathrm{ex}\,\nu_{\mathrm{O_2,stoich}}\,\mathrm{O_2} \\ +\; (1+\mathrm{ex})\,\nu_{\mathrm{O_2,stoich}}\,3.76\,\mathrm{N_2}.\end{aligned} \tag{3.9}$$

with:

- $\nu_{\mathrm{O_2,stoich}}$: stoichiometric $\mathrm{O_2}$ requirement per mole of dry fuel (obtained from the combustion reaction with $ex = 0$ and $n_{H_2O,m}$ =0):

$$\nu_{\mathrm{O_2,stoich}} \;=\; x + \frac{y}{4} - \frac{z}{2}$$

- $n_{\mathrm{H_2O,m}}$: moles of water carried by the wet fuel per mole of dry fuel, for a moisture mass fraction on a wet basis wt:

$$n_{\mathrm{H_2O,m}} \;=\; \frac{\dfrac{wt}{1-wt}\,M_{\mathrm{dry}}}{18} \quad \text{with} \quad M_{\mathrm{dry}} = 12x + y + 16z$$

From the preceding reaction, the molar amounts of the flue gas components are then:

$$n_{CO_2} = x, \qquad n_{H_2O} = \frac{y}{2} + n_{H_2O,m}, \quad n_{O_2} = ex \times \nu_{O_2,stoich}, \quad n_{N_2} = (1+ex)\,\nu_{O_2,stoich}\,3.76$$

The corresponding mole fraction of each species is:

$$x_i = \frac{n_i}{n_{sum}} \quad \text{for} \quad i \in \{CO_2, H_2O, O_2, N_2\} \tag{3.10}$$

where $n_{sum} = n_{CO_2} + n_{H_2O} + n_{O_2} + n_{N_2}$ is the total number of moles.

Once the flue gas composition is fully defined through these mole fractions, they are combined with temperature and pressure and used as input to the *Python* library *CoolProp* to evaluate the mixture properties of the flue gas: specific heat $c_{p,mix,kg}$ (in mass basis), thermal conductivity k_{mix}, density ρ_{mix}, kinematic viscosity ν_{mix} and thermal diffusivity α_{mix}. These properties are computed separately for each gas segment using a representative flue-gas temperature of that segment. Pure-species properties are evaluated using *CoolProp*, and mixture properties are then obtained using mole or mass fraction-weighted mixing rules depending on the units in which the pure-species properties are output:

$$c_{p,mix,mol}(T) = \sum_i x_i\, c_{p,i}(T) \qquad \Rightarrow \qquad c_{p,mix,kg}(T) = \frac{c_{p,mix,mol}}{M_{mix}} \qquad [\mathrm{J/kgK}] \tag{3.11}$$

$$k_{mix}(T) = \sum_i w_i\, k_i(T) \qquad [\mathrm{W/mK}] \tag{3.12}$$

$$\mu_{mix}(T) = \sum_i w_i\, \mu_i(T) \qquad [\mathrm{Pa.s}] \tag{3.13}$$

$$\frac{1}{\rho_{mix}(T)} = \sum_i \frac{w_i}{\rho_i(T)} \qquad \Rightarrow \qquad \rho_{mix}(T) = \left(\sum_i \frac{w_i}{\rho_i(T)}\right)^{-1} \qquad [\mathrm{kg/m^3}] \tag{3.14}$$

$$\alpha_{mix}(T) = \frac{k_{mix}(T)}{\rho_{mix}(T)\, c_{p,mix}(T)} \qquad [\mathrm{m^2/s}] \tag{3.15}$$

$$\nu_{mix}(T) = \frac{\mu_{mix}(T)}{\rho_{mix}(T)} \qquad [\mathrm{m^2/s}] \tag{3.16}$$

where

- M_i = molar mass of species i
- $M_{mix} = \sum_i x_i\, M_i$: molar mass of the flue gas mixture
- $w_i = \frac{M_i}{M_{mix}}$: mass fraction of species i.

3.4.3.3 View factors

View factors account for radiation exchange within the rectangular channels of the masonry stove accumulator. These channels being parallelepiped rectangles, the relevant geometries for which view factors are computed are aligned parallel rectangles (for opposite channel walls) and perpendicular rectangles sharing a common edge (for adjacent channel

walls). These view factors are computed using the approximate analytical formulas from *Incropera and DeWitt's Principles of Heat and Mass Transfer* textbook [36]:

$$F_{\parallel}(X,Y) = \frac{2}{\pi XY}\left[\left(\ln\left(\frac{(1+X^2)(1+Y^2)}{1+X^2+Y^2}\right)\right)^{\frac{1}{2}}\right.$$
$$+ X\sqrt{1+Y^2}\,\arctan\left(\frac{X}{\sqrt{1+Y^2}}\right)$$
$$\left.+ Y\sqrt{1+X^2}\,\arctan\left(\frac{Y}{\sqrt{1+X^2}}\right) - X\arctan(X) - Y\arctan(Y)\right] \tag{3.17}$$

where $X = L/d$ and $Y = l/d$ with $L > l$ the rectangle dimensions and d the distance between the two parallel walls.

$$F_{\perp}(H,W) = \frac{1}{\pi W}\left[W\arctan\left(\frac{1}{W}\right) + H\arctan\left(\frac{1}{H}\right)\right.$$
$$- \sqrt{H^2+W^2}\,\arctan\left(\frac{1}{\sqrt{H^2+W^2}}\right)$$
$$+ \frac{1}{4}\ln\left(\frac{(1+W^2)(1+H^2)}{1+W^2+H^2}\left(\frac{W^2(1+W^2+H^2)}{(1+W^2)(W^2+H^2)}\right)^{W^2}\right.$$
$$\left.\left.times\left(\frac{H^2(1+H^2+W^2)}{(1+H^2)(H^2+W^2)}\right)^{H^2}\right)\right] \tag{3.18}$$

where $H = Z/U$ and $W = V/U$ with U the common edge length, Z and V the smallest and biggest adjacent edge lengths.

Additionally, once several view factors are computed, reciprocity equation can be used to obtain the others factors:

$$F_{j,i} = F_{i,j}\,\frac{A_i}{A_j}. \tag{3.19}$$

Finally, since equations (3.17) and (3.18) are approximations, the view factors are normalized to satisfy the summation rule to 1:

$$F_{i,j} = \frac{F_{i,j}}{\sum_j F_{i,j}} \tag{3.20}$$

All view factors are computed and stored for each wall sub-element and used as constant inputs in the subsequent time-dependent thermal model.

3.4.4 Wall data structure

The final task of the setup phase is to store all wall-related information required by the thermal model. Each wall of each discretized wall sub-element is therefore represented as a *Python* object instantiated from a class named *Wall*. This class defines a template from which individual wall objects are created and accessed throughout the code. Table

3.1 summarizes the attributes of the *Wall* class. In this table, the expressions for the thermal resistances between internal nodes and between the outermost node and the surface depend on the number of nodes, as illustrated in Figure 3.4.

This object-oriented structure allows physical walls that are shared between two gas segments (i.e. exposed to gas on both sides) to be represented by a single *Wall* object. In such cases, both gas segments reference the same wall instance and therefore share the same temperature array in memory. Consequently, any update of a wall temperature node due to heat exchange on one side of the gas channel is immediately reflected on the opposite side. For example, using the matrix of shared walls defined in equation 3.2, the temperature nodes of `Wall[(2,'BOTTOM')]` reference those of `Wall[(1,'TOP')]`. Thus, when the gas in segment 2 exchanges heat with its bottom wall, the resulting temperature change is automatically accounted for as the top wall of segment 1, since both correspond to the same physical wall.

Attribute	**Description**	**Unit / Value**
`type`	Type of wall (refractory or casing)	[-]
`n_nodes`	Number of discretized nodes in the wall	[-] (default = 3)
`T`	Array of temperatures at each node	[K] (initialized to `T_init`)
`A`	Surface area of the wall	[m]
`cp`	Specific heat capacity	[J/kg·K]
`thickness`	Wall thickness	[m]
`rho`	Density of the wall material	[kg/m^3]
`k`	Thermal conductivity	[W/m·K]
`R`	Nodal thermal resistance	[K/W]
`R_surf`	Thermal resistance between surface and node	[K/W]
`C_node`	Nodal heat capacity	[J/K]

Table 3.1: Attributes of the *Wall Python* Class.

3.5 Combustion modelling

Once all fixed parameters have been defined and the spatial discretization is established, the next step in the simulation consists in combustion modelling. Modelling the combustion is essential since it is the source of energy for all the stove. It corresponds to simulating the wood combustion occurring in the combustion chamber. Combustion in masonry stoves is a batch process, in which a single fuel load is burned without reloading. In this thesis, the combustion is modelled in two main stages. First, the adiabatic flue-gas temperature $T_{\text{gas,ad}}$ and the flue gas mass flow rate, $\dot{m}_{gas}$, are computed using an adiabatic combustion-chamber model. The adiabatic gas temperature is then used to prescribe the time evolution of the flue-gas temperature over the entire combustion period. The present section describes the assumptions and inputs used and the modelling steps adopted for these two stages.

3.5.1 Assumptions

The following assumptions are applied both in the adiabatic combustion chamber model and in the derivation of the flue-gas temperature profile:

- For the computation of the adiabatic gas temperature, the combustion chamber is assumed adiabatic: no heat is exchanged between the combustion chamber and its surroundings, and the system is considered perfectly insulated.
- All assumptions listed in Section 3.4.1 for the computation of flue-gas properties remain valid. Among these, the main ones are complete combustion and the use of hardwood with chemical formula $C_1H_{1.43}O_{0.66}$.

3.5.2 Inputs

All input parameters of the combustion model, that the user must give additionally to the one for the setup, are related to the wood combustion process. They are summarized in Table 3.2. They mainly describe the fuel and operating conditions required to perform the combustion calculation. Some of them, if not given, are put to optimal or basic literature based values.

Parameter	**Description**	**Unit**
ex	Excess of air fraction	[-] (default: 1.1 [55])
wt	Fuel moisture content (between 0 and 1)	[-] (default: 0.2 [53, 54])
LHV_{fuel}	Lower heating value of the fuel	[J/kg]
m_{fuel}	Mass of fuel (wood) burned	[kg]
$c_{p,fuel}$	Specific heat capacity of the fuel	[J/kgK]
t_{comb}	Combustion duration	[s]
$T_{init,gas}$	Initial temperature of the gases in the channels of the stove before combustion [3]	[K] (default: 293.15K)
$T_{a,su}$	Supply air temperature	[K] (default: 293.15K)
$T_{fuel,su}$	Supply fuel temperature	[K] (default: 293.15K)

Table 3.2: Input parameters for the combustion modelling.

3.5.3 Adiabatic combustion chamber

Before applying the adiabatic combustion chamber model, the fuel–to-air ratio must be determined:

$$f = \frac{f_{st}}{1 + ex} \tag{3.21}$$

where f_{st} is the stoichiometric fuel-to-air ratio (corresponding to $ex = 0$).

[3] This temperature can exceed ambient temperature if a previous combustion was performed and the stove has not yet returned to its initial temperature.

The stoichiometric ratio is derived from the complete combustion reaction of the generic fuel $C_xH_yO_z$, leading to (see Appendix A.1 for details):

$$f_{st} = \frac{12.01x + 1.008y + 16z}{28.85\left(x + \frac{y}{4} - \frac{z}{2}\right) 4.76} \tag{3.22}$$

For the developed model, hardwood is considered as fuel, represented by $C_1H_{1.43}O_{0.66}$ ($x = 1$, $y = 1.43$, $z = 0.66$).

Once this ratio is computed, the adiabatic combustion chamber model is applied. It is derived from the course on Cooling and Low-Temperature Heating Systems by V. Lemort [56]. It is based on a chemical equilibrium computation that yields the adiabatic combustion gas temperature, denoted $T_{gas,ad}$. In addition, the model provides the flue gas mass flow rate, $\dot{m}_{gas}$, which is required for subsequent heat transfers between the flue gas and masonry walls as well as for flue gas advection between gas segments. Figure 3.7 illustrates the heat exchanges involved in this model.

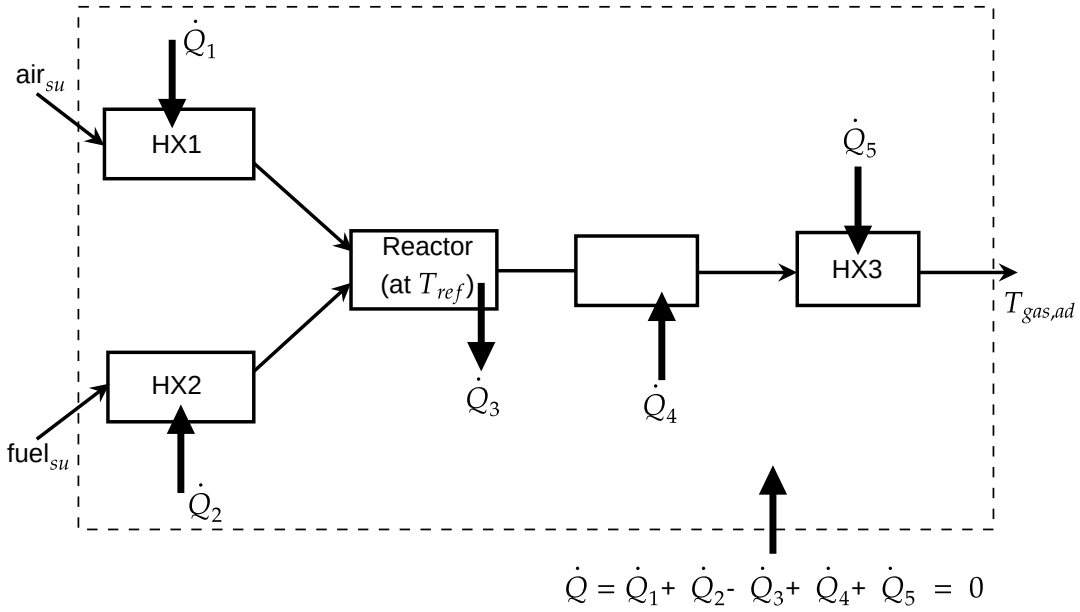

Figure 3.7: Schematic of the adiabatic combustion chamber model.

In this model, the combustion reaction is assumed to occur at a reference temperature, T_{ref}, set by default at 293.15 K. The first two heat exchanges, HX1 and HX2, correspond to the sensible energy needed to heat the incoming air and fuel from their respective supply temperatures to the reference temperature:

$$\dot{Q}_1 = \dot{m}_a c_{p,a}(T_{ref} - T_{a,su}) \tag{3.23}$$

$$\dot{Q}_2 = \dot{m}_{fuel} c_{p,fuel}(T_{ref} - T_{fuel,su}) \tag{3.24}$$

with:

- $\dot{m}_{fuel}$: fuel mass flow rate: $\dot{m}_{fuel} = \frac{m_{fuel}}{t_{comb}}$ [kg/s]
- $\dot{m}_a$: air mass flow rate: $\dot{m}_a = \frac{\dot{m}_{fuel}}{f}$ [kg/s]

With these definitions of the inlet mass flow rates, the total flue gas mass flow rate can be written as:

$$\dot{m}_{gas} = \dot{m}_{fuel} + \dot{m}_{air} \tag{3.25}$$

The combustion reaction then releases heat, $\dot{Q}_3$, along with the formation of flue gases. This released heat is evaluated from the lower heating value (LHV) of the fuel:

$$\dot{Q}_3 = LHV_{fuel}\dot{m}_{fuel} \tag{3.26}$$

In case of incomplete combustion, part of the fuel may be converted into CO instead of CO_2, resulting in an additional heat loss expressed as:

$$\dot{Q}_4 = \dot{m}_{fuel}LHV_{CO} \tag{3.27}$$

In the present model, complete combustion is assumed, so $\dot{Q}_4 = 0$.

The last heat transfer, HX3, accounts for the energy required to raise the flue gases from the reference temperature, T_{ref}, to the adiabatic gas temperature, $T_{gas,ad}$. This quantity can be computed:

$$\dot{Q}_5 = \dot{m}_{gas}c_{p,gas}(T_{gas,ad} - T_{ref}) \tag{3.28}$$

Finally, by performing a global energy balance over the adiabatic combustion chamber:

$$\dot{Q}_1 + \dot{Q}_2 - \dot{Q}_3 + \dot{Q}_5 = 0 \tag{3.29}$$

The adiabatic gas temperature is obtained as:

$$T_{gas,ad} = \frac{-\dot{Q}_1 - \dot{Q}_2 + \dot{Q}_3 + \dot{m}_{gas}c_{p,g}T_{ref}}{\dot{m}_{gas}c_{p,gas}} \tag{3.30}$$

3.5.4 Time-dependent combustion temperature profile

In practice, the flue gas temperature in the combustion chamber does not remain constant at the adiabatic gas temperature throughout the whole combustion process. Initially, the temperature starts at ambient temperature, then increases rapidly and reaches a value close to the adiabatic flame temperature under near-ideal conditions. After the fuel is depleted, the gas temperature gradually decreases as combustion slowly ceases.

This behaviour leads to a typical three-phase temperature profile for batch-mode combustion, as encountered in masonry stoves: a sharp rise (moisture-driven start-up), a plateau or near-plateau (during intense volatile combustion phase), and a gradual decline associated with char burnout [57]. Several transient CFD studies reproduce this characteristic evolution of the flue gas temperature, showing a rapid rise followed by a pronounced peak close to the adiabatic temperature and a slower cooling phase [58, 59, 60].

To represent this behaviour in the present model, a combination of sigmoid functions, denoted g, is used to approximate the temperature rise and fall. Sigmoid functions are well-suited for such modelling due to their smoothness, continuity, and ability to represent gradual transitional behaviours. Due to their continuous, differentiable S-shaped response, they are a standard mathematical tool commonly used in engineering systems representing smooth rising and falling responses between baseline and plateau values [61, 62, 63, 64]. Therefore, adopting a combination of sigmoid functions in the present combustion model

provides a practical and flexible approximation of the rise, peak, and decay of the flue gas temperature during batch combustion, consistent with literature-reported batch-mode combustion flue gas temperature evolutions. The following relationships are adopted:

$$g_{rise} = \frac{1}{1 + exp(-s_1(t - t_{rise}))} \tag{3.31}$$

$$g_{fall} = \frac{1}{1 + exp(-s_2(t - t_{fall}))} \tag{3.32}$$

$$g = g_{rise}(1 - \theta g_{fall}) \tag{3.33}$$

$$T = T_{init} + (T_{max} - T_{init})\, g \tag{3.34}$$

where:

- T_{init}: initial temperature in the combustion chamber (=$T_{init,gas}$ input of Table 3.2),
- T_{max}: adiabatic gas temperature reached during the peak combustion phase obtained from the adiabatic combustion chamber model,
- s_1, s_2: steepness coefficients for the rising and falling parts of the curve, respectively,
- $t_{\text{rise}}, t_{\text{fall}}$: characteristic times describing the onset of the main combustion phase and the start of the cooling phase,
- θ: amplitude parameter controlling the magnitude of the decay after peak combustion and shaping the tail of the curve.

This formulation provides sufficient flexibility to adjust the temperature evolution so that it matches measured flue gas temperature profiles of masonry stoves. In particular, the rise is typically steeper than the decay, which can be represented by choosing $s_1 > s_2$, while t_{rise} and t_{fall} allow the timing of the peak to be shifted.

The values of these shape parameters could not be directly measured in this study. Therefore, since no experimental data on the flue gas temperature evolution within the stove were available to calibrate the model, the parameters have been set to correspond to typical profiles reported in the literature for batch-mode masonry stoves [57, 59, 60, 58]. This approach provides a representative approximation of the combustion phases. The fixed values used in the numerical model are summarized in Table 3.3.

Parameter	**Value**	**Unit**
T_{init}	293.15	[K]
t_{rise}	300	[s]
t_{fall}	5400	[s]
s_1	0.01	[-]
s_2	0.002	[-]
θ	0.4	[-]

Table 3.3: Values of the parameters for combustion chamber flue gas temperature profile.

Figure 3.8 shows the flue gas temperature evolution in the combustion chamber obtained using the fixed parameter, s_1, s_2, θ, t_{fall} and t_{rise} given in Table 3.3, with a maximum temperature T_{max} of 1318.2 K and a combustion duration $t_{comb} = 7200$ s. The resulting curve provides a good approximation of the expected combustion temperature trend, with an initial rise (section 1) followed by a quasi-plateau at $T_{max} = 1318.2$ K (section 2) and a subsequent gradual decline (section 3).

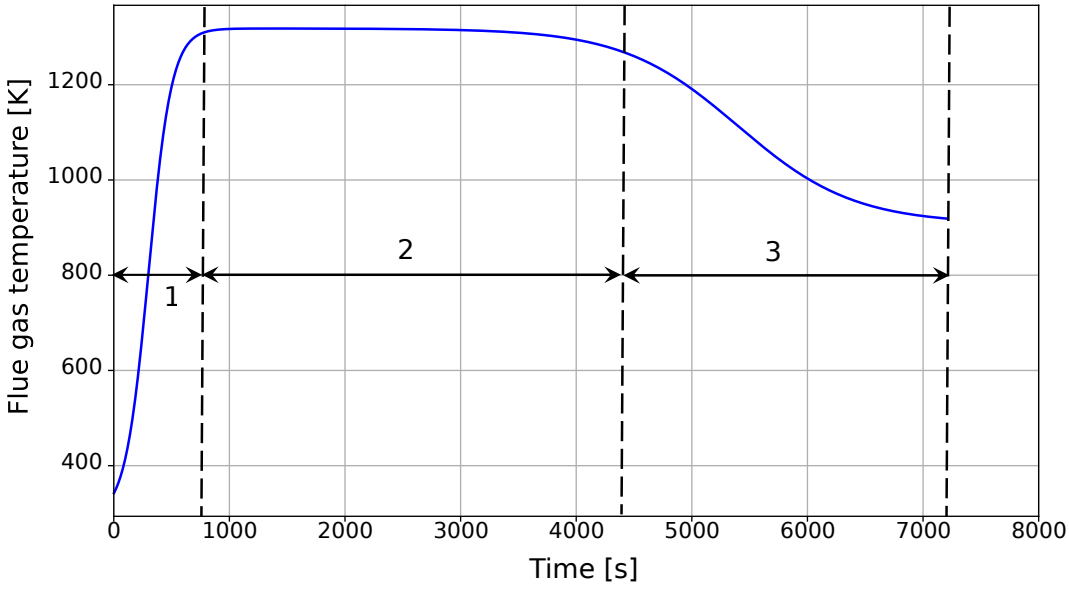

Figure 3.8: Combustion chamber flue gas temperature evolution profile during combustion using the parameter values from Table 3.3.

3.6 Thermal storage and heat release modelling

The final step to model the masonry stove consists of simulating the time evolution of temperatures and heat transfers within the system (see step 3 of Figure 3.1). As highlighted in the literature review, the operation of a masonry stove can be divided into two mains periods. During combustion, heat is accumulated in the stove: the thermal energy generated by wood combustion is transferred from the flue gas to the internal masonry, where it is stored. Then, once the burn is complete, two manual closure dampers (at the air inlet and at the chimney outlet) are closed in order to confine the hot flue gases inside the stove, and the stored heat is gradually released to the surrounding environment. During this second phase, the stove temperature progressively decreases.

This section first introduces the assumptions and input parameters used to model these thermal phenomena. It then presents the physical models and equations used to compute the different heat transfer mechanisms and to update over time the temperatures fields as well as the flue gas flow rate.

3.6.1 Assumptions

The following assumptions are adopted in the model developed to simulate the heat storage and release:

- The temperature field inside the stove walls is discretized on a set of lumped nodes located at the centres of control volumes. Heat transfer is only computed between these neighbouring nodes, and each node represents one cell assumed to be at a uniform temperature.
- The ambient air in the room is assumed to be perfectly mixed; consequently, the room air temperature is spatially uniform. Furthermore, it is supposed constant in time. In the same way, the outside temperature is supposed constant.
- The flue gas is assumed to be perfectly mixed within each discretized gas segment.
- Thermophysical properties (e.g., specific heat capacities, thermal conductivities) are taken as constant with temperature.
- Radiative heat exchange between the external surface of the stove and the room is modelled using the Stefan–Boltzmann law, assuming the environment behaves as a large isothermal enclosure and walls behave as diffuse-gray surfaces. View factors between the stove surfaces and surrounding walls are not explicitly considered, and a unit view factor, $F = 1$, is assumed. This is a reasonable approximation for an object (the masonry stove) radiating towards a large surrounding environment (a room) whose surfaces are approximately at the room air temperature.
- A sufficiently strong natural draft is assumed during combustion to ensure the required air supply (according to the specified excess air) and effective circulation of hot flue gases within the stove. This draft is considered to be ensured by proper chimney sizing and air inlet design by the manufacturer and is not explicitly modelled.
- Heat conduction in the masonry walls is assumed unidirectional going from hot flue gas segments to the ambient. This simplification is justified by the dominance of heat flow paths in one direction, from the gas to the outer casing.
- Advection of energy between gas segments is discretized using a first-order upwind scheme, assuming an unidirectional mass flow from segment $i - 1$ to segment i.
- At the end of combustion, at time t_{comb}, the two manual dampers are closed and after a short transient, the flue gas mass flow rate is assumed to be zero. Consequently, after that time, each gas control volume is treated as stagnant, and no further advection of gas (and energy) occurs between neighbouring gas segments.

3.6.2 Inputs

This part of the model uses, as inputs, most of the outputs from the geometry/setup and combustion submodels defined previously. The only additional parameters that must be specified by the user are listed in Table 3.4. Together with the input parameters defined in the setup section (Section 3.4.2) and the combustion modelling one (Table 3.2), this table completes the list of data that must be provided by the user to run the numerical simulation of a specific masonry stove configuration.

Parameter	Description	Unit
ϵ_{walls}	Emissivity of the stove's walls (between 0 and 1)	[-]
ϵ_{gas}	Emissivity of the flue gas (typically between 0.1 and 0.3 depending on the wood burned [65, 66])	[-] (default: 0.2)
T_{out}	Temperature of the outside of the house/building	[K] (default: 283.15K (mean yearly temperature in Liège [67]))
$t_{release}$	Duration of the post-combustion heat release period over which results are computed	[s]

Table 3.4: Input parameters for thermal storage and heat release modelling.

3.6.3 Flue gas mass flow rate evolution

Similarly to the flue gas temperature in the combustion chamber, the flue gas mass flow rate, $\dot{m}_{gas}$, does not instantaneously reach the nominal value computed from the adiabatic combustion chamber model. At the beginning of the combustion, the flue gas mass flow rate is assumed to start from zero and then increase to the nominal value as the natural draft establishes. At the end of combustion, at time t_{comb}, the two dampers are closed to isolate the accumulator from the chimney and the air inlet. The gas circulation then decreases and eventually stops, but with a finite delay.

Like for the flue gas temperature profile, since it was not possible to gather experimental data inside the stove itself, the temporal evolution of the flue gas mass flow rate has been parametrised. To represent it, two characteristic times are introduced: the ramp-up time, $t_{\text{ramp,up}}$, which defines the duration of the linear increase of the mass flow rate from zero to its nominal value, and the ramp-down time, $t_{\text{ramp,down}}$, which defines the duration of the linear decrease from the nominal value back to zero. The resulting piecewise definition of $\dot{m}_{gas}(t)$ assumes a linear increase and a linear decrease:

$$\dot{m}_{gas}(t) = \begin{cases} \dot{m}_{nom} \frac{t}{t_{\text{ramp,up}}}, & 0 \leq t < t_{\text{ramp,up}} \\ \dot{m}_{nom}, & t_{\text{ramp,up}} < t \leq t_{comb} \\ \dot{m}_{nom} \left(1 - \dfrac{t - t_{comb}}{t_{\text{ramp,down}}}\right), & t_{comb} < t < t_{comb} + t_{\text{ramp,down}} \\ 0, & t \geq t_{comb} + t_{\text{ramp,down}} \end{cases}$$

The time-dependent flue gas mass flow rate $\dot{m}_{gas}(t)$ directly influences the convective heat transfer coefficients in each gas channel segment, and therefore the transient heat transfer to the masonry. The two parameters, $t_{\text{ramp,up}}$ and $t_{\text{ramp,down}}$, are explored in a subsequent sensitivity analysis (section 5.2.2) to investigate their influence on the wall temperature evolution and determine a reasonable range of values.

3.6.4 Heat transfer mechanisms and governing equation

As discussed in the literature review, a resistance–capacitance (RC) network model is used to represent heat transfer within the masonry stove. Figure 3.9 illustrates the RC network associated with a single discretized gas segment, surrounded by three refractory and two casing wall elements. Each bullet in the figure represents a lumped temperature node, corresponding to a thermal capacitance. The network includes thermal resistances, thermal capacitances, and heat-transfer interactions $\dot{Q}$ [W] between:

- the flue gas and the refractory wall (gas–rfr),
- the flue gas and the casing wall (gas–cng),
- the refractory and casing walls (rfr–cng),
- the casing wall and the ambient environment (cng–a).

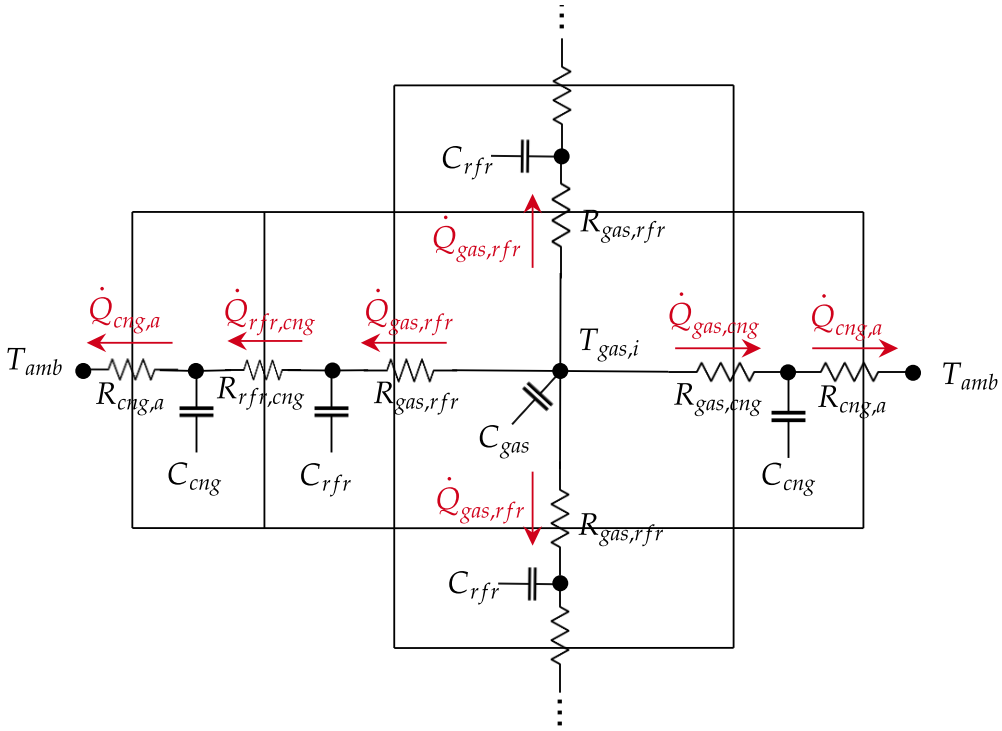

Figure 3.9: RC network representation of heat-transfer mechanisms associated with a single gas segment (• = temperature node).

The figure shows a simplified representation. In the numerical model, each wall contains more than one temperature node (at least two), and additional interactions, omitted for better understanding of the picture, exist. These interactions are the radiative exchange between internal walls and the advective enthalpy transport between adjacent gas segments. These additional mechanisms are described in the following sections. All the described interactions could occur in each of the M discretized gas segments, depending on the configuration.

The governing equation for representing such an RC model is a first-order differential equation. For a thermal node with temperature $T(t)$, thermal capacitance C [J/K],

thermal resistance R [K/W], and heat entering and leaving the node, $\dot{Q}_{\text{in}}(t)$ and $\dot{Q}_{\text{out}}(t)$, the energy balance is written as:

$$C\frac{dT(t)}{dt} = \dot{Q}_{\text{in}}(t) - \dot{Q}_{out}(t) \tag{3.35}$$

Here, $\dot{Q}_{\text{in}}$ and $\dot{Q}_{\text{out}}$ represent all contributions of heat entering and leaving the node, including convective, conductive, and radiative exchanges with connected nodes or the environment. These fluxes depend on the thermal resistances connecting the node to others and on the temperatures of those nodes or surfaces. Equation (3.35) provides the generalized energy balance that forms the basis for modelling all heat transfer phenomena between nodes in the masonry stove.

3.6.5 Discretized gas temperature evolution

Each discretized gas segment is associated with a gas temperature node subject to two primary effects:

1. Advective enthalpy transport from segment $i-1$ to i, and from i to $i+1$,
2. Heat exchanges with surrounding walls, computed using the RC network.

These interactions are sketched in Figure 3.10, which is a simplified two-dimensional representation. In the actual model, more than two walls may be adjacent to a given gas segment and each wall is discretized into multiple temperature nodes.

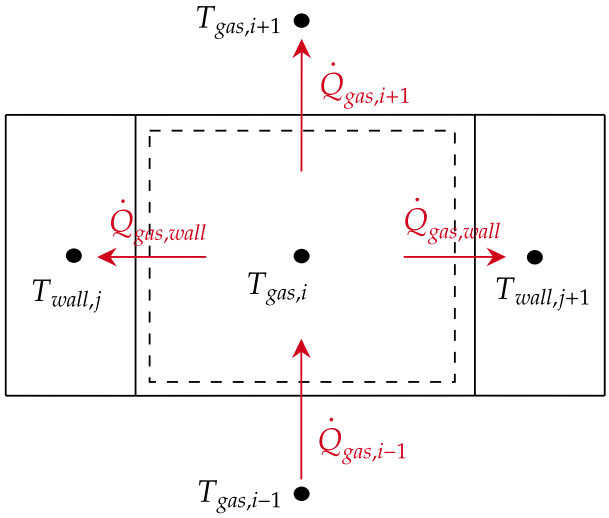

Figure 3.10: Heat-transfer mechanisms affecting a discretized gas segment: wall exchanges, and advective enthalpy transport.

3.6.5.1 Gas energy balance

For a generic internal gas segment i, the energy balance based on equation (3.35) is expressed as:

$$C_{gas,i}\frac{dT_{gas,i}(t)}{dt} = \dot{Q}_{gas,i-1}(t) - \dot{Q}_{gas,i+1}(t) - \sum_{walls}\dot{Q}_{gas,wall}(t) \tag{3.36}$$

$$= \dot{m}_{gas}(t)c_{p,gas,i}\big(T_{gas,i-1}(t) - T_{gas,i}(t)\big) - \sum_{walls}\dot{Q}_{gas,wall}(t) \tag{3.37}$$

where:

- The advective term $\dot{m}c_p\,(T_{i-1} - T_i)$ represents the net enthalpy flux into and out of segment i due to advection,, combining the incoming flux from the upstream segment $i-1$ and the outgoing flux to the downstream segment $i+1$. Using a first-order upwind discretization, these fluxes are written as:

$$\begin{aligned} \text{inflow from } i-1: &\quad \dot{Q}_{\text{gas},\,i-1} = \dot{m}c_p T_{i-1}, \\ \text{outflow to } i+1: &\quad \dot{Q}_{\text{gas},\,i+1} = \dot{m}c_p T_i. \end{aligned}$$

  This term becomes zero when the dampers are closed, i.e, when $\dot{m}_{gas} = 0$.

- $C_{gas,i} = m_{gas,i}c_{p,gas,i}$ is the heat capacity of the gas in segment i.

- $\sum_{walls} \dot{Q}_{gas,wall}(t)$ denotes the total heat transfer rate between the gas and the walls of segment i and is derived in Section 3.6.6.1 below.

3.6.5.2 Special treatment of the first and last gas segment

The first gas segment, representing the combustion chamber, has no upstream gas segment and is directly influenced by the combustion process. During the combustion phase, the gas temperature in this segment is prescribed by the flue-gas temperature profile, $T_{flue}(t)$, which represents the energy provided by the burning fuel, as introduced in Section 3.5.4.

As combustion nears its end, the defined flue-gas temperature profile decreases and the surrounding walls of the combustion chamber may reach temperatures comparable to or hotter than the prescribed flue-gas temperature. At this stage, the combustion chamber is no longer an active heat source: the energy released by the fuel has diminished. Imposing T_{flue} at this point would override the actual energy exchanges with the walls, neglecting heat flowing from the masonry to the gas. To handle this, the first segment transitions to a regime where its temperature is governed by the local energy balance with the surrounding walls and by advective outflow to the next gas segment, without enforcing the flue-gas temperature any more.

To obtain a smooth transition between these two regimes, a symmetric threshold $\dot{Q}_{\text{thresh}}$ is introduced. When the net heat flux of the first gas segment to its surrounding walls exceeds $\dot{Q}_{\text{thresh}}$, the gas temperature is fully imposed by T_{flue} ($w = 1$). When the net flux is below $-\dot{Q}_{\text{thresh}}$, it means the walls provide heat to the gas segment and the combustion source is switched off ($w = 0$), leading to the first gas segment being only governed by its local energy balance. For intermediate values, w varies linearly between 0 and 1. The updated temperature of the first gas segment is then computed as:

$$T_{\text{gas},0}(t + \Delta t) = w\,T_{\text{flue}}(t) + (1 - w)\,T_{\text{gas,loss},0}(t + \Delta t) \tag{3.38}$$

where:

- The weight w is defined from the net heat exchange with the walls:

$$w = \begin{cases} 1, & \text{if } \sum_{walls} \dot{Q}_{gas,wall}(t) \geq \dot{Q}_{\text{thresh}}, \\ \dfrac{\sum_{walls} \dot{Q}_{gas_0,wall}(t)}{2\,\dot{Q}_{\text{thresh}}} + \dfrac{1}{2}, & \text{if } -\dot{Q}_{\text{thresh}} < \sum_{walls} \dot{Q}_{gas,wall}(t) < \dot{Q}_{\text{thresh}}, \\ 0, & \text{if } \sum_{walls} \dot{Q}_{gas,wall}(t) \leq -\dot{Q}_{\text{thresh}} \end{cases} \tag{3.39}$$

- $T_{gas,loss,0}$ is obtained by integrating the energy balance of segment 0, considering only wall interactions and advective outflow to the next segment:

$$C_{gas,0}\frac{dT_{gas,0}(t)}{dt} = -\dot{m}_{gas}(t)c_{p,gas,0}T_{gas,0}(t) - \sum_{walls}\dot{Q}_{gas,wall}(t) \tag{3.40}$$

$$\Leftrightarrow \quad T_{gas,loss,0}(t+\Delta t) = T_{gas,0}(t) - \frac{\sum_{walls}\dot{Q}_{gas,wall}(t)dt}{C_{gas,0}} - \frac{\dot{m}_{gas}(t)c_{p,gas,0}T_{gas,0}(t)dt}{C_{gas,0}}$$

The last gas segment has also two regimes. Before the dampers are closed, its outflow, $\dot{m}_{gas}c_{p,gas}T_{gas,i}$, is lost to the ambient. After the dampers are closed, the advective outflow vanishes, and the segment evolves only according to wall interactions.

3.6.6 Discretized wall temperature evolution

The previous section introduced the discretized gas temperature evolution. In parallel, the temperature evolution of the surrounding walls must be computed, as these govern the thermal storage and release within the stove. Most wall interactions are already represented in the global RC network (Figure 3.9), except for radiative exchanges between internal walls of the same channel, which need to be added explicitly. This section details the formulation of all these wall heat-transfer contributions from which the general energy balance for a generic wall node T_{wall_x} can be expressed as:

$$C_{wall_x}\frac{dT_{wall_x}}{dt} = \dot{Q}_{gas,wall_x} + \dot{Q}_{rfr,cng} - \dot{Q}_{wall_x,a} + \sum_{walls \neq wall_x}\dot{Q}_{rad,wall} \tag{3.41}$$

where the terms on the right-hand side correspond to heat exchange with the gas, adjacent walls, the ambient, and radiative exchange with other internal walls. Depending on the node's location and wall type, some of these terms may vanish.

In the following subsections, each term in equation (3.41) is described in detail, starting with the heat transfer between the gas and the wall. This provides the foundation for understanding how wall nodes interact thermally with both the gas and surrounding environment.

3.6.6.1 Gas–wall heat transfer term $\dot{Q}_{\text{gas,wall}}$

Figure 3.11 illustrates the local RC representation of the interaction for a gas–refractory wall segment, showing the wall discretized into three control volumes (nodes), each with

thermal capacitance $C_{\text{rfr}} = \rho_{\text{rfr}} A c_{p,\text{rfr}} \Delta x$. Only the wall node adjacent to the gas (node 0) directly exchanges heat with the gas segment i:

$$\dot{Q}_{gas,rfr}(t) = \frac{T_{gas,i}(t) - T_{rfr,0}(t)}{R_{gas,rfr}} \tag{3.42}$$

In this expression, $R_{\text{gas,rfr}}$ represents the total thermal resistance between the gas and the first wall node, including convective and radiative contributions from the gas side in h_{gas} and the conduction resistance through the wall surface in R_{surf}:

$$\begin{aligned} R_{gas,rfr} &= \frac{1}{h_{gas}(T_{surf,rfr}(t), \dot{m}_{gas}(t), T_{gas,i}(t))} + R_{surf,rfr} \\ &= \frac{1}{h_{gas}(T_{surf,rfr}(t), \dot{m}_{gas}(t), T_{gas,i}(t))} + \frac{\Delta x_{rfr}/2}{k_{rfr}\, A} \end{aligned} \tag{3.43}$$

where A is the gas–wall exchange area and $\Delta x_{\text{rfr}} = e_{\text{rfr}}/n_{\text{nodes}}$. The same formulation applies to a casing wall by replacing rfr indices with cng.

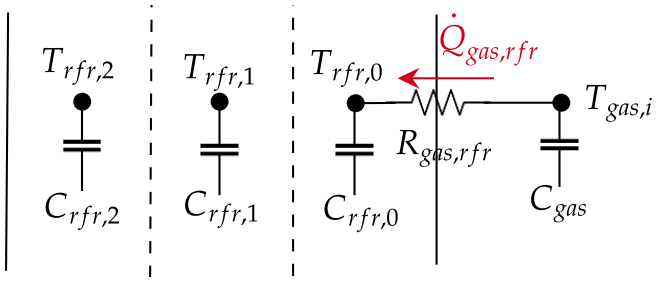

Figure 3.11: Local RC representation of gas-to-wall heat transfer.

The gas–wall heat flux is governed by the effective heat-transfer coefficient h_{gas}, which accounts for both convective and radiative heat transfer from the flue gas to the wall. Radiative transfer in combustion gases arises primarily from radiatively active species such as CO_2, H_2O or soot at high temperatures. In the present configuration, the contribution of gas radiation remains moderate due to the relatively short characteristic path lengths in the channels and limited gas optical thickness. Most of the correlations used below to compute the effective heat-transfer coefficient are primarily taken from the heat and mass transfer textbook written by Frank P. Incropera and al [36]. The expression of h_{gas} depends on whether a mass flow rate is present in the gas segment.

When gas is flowing ($\dot{m}_{\text{gas}} > 0$), heat transfer between the gas and the wall is dominated by forced convection and radiation. In that case, the effective coefficient is written as a sum of a convective and a linearised radiative contribution:

$$\begin{aligned} h_{\text{gas}} &= h_{\text{conv,gas}}\big(\dot{m}_{\text{gas}},\, k_{\text{gas}},\, \nu_{\text{gas}},\, \alpha_{\text{gas}},\, \rho_{gas}\big) + h_{rad,gas} \\ &= h_{\text{conv,gas}}\big(\dot{m}_{\text{gas}},\, k_{\text{gas}},\, \nu_{\text{gas}},\, \alpha_{\text{gas}},\, \rho_{gas}\big) + 4\,\epsilon_{gas}\,\sigma\,T_m^3 \end{aligned} \tag{3.44}$$

where $T_m = \frac{T_{gas,i}+T_{surf,wall}}{2}$ is the mean absolute temperature, the thermophysical gas properties are evaluated according to equation (3.11)-(3.16) and ϵ_{gas} is the flue gas emissivity whose range of values is given in Table 3.4. The radiation linearisation enables it to be incorporated within the resistance-based formulation of the gas–wall exchange.

When the gas is stagnant ($\dot{m}_{\text{gas}} = 0$, i.e., with closed dampers), there is no bulk motion and the forced convection term vanishes. Under these conditions, each discretized gas segment is assumed trapped within its control volume, and heat transfer occurs by molecular diffusion across the gas layer. Although conduction in gases exists physically, in the context of the applied assumption of a perfectly mixed segment (no gradient of temperature inside a gas segment) its effect is already captured implicitly in the uniform segment temperature and is therefore neglected in the model. The effective heat transfer coefficient then only represents the radiative contribution, which remains unaffected by the absence of bulk motion. However, its magnitude progressively decreases as combustion stops and the gas temperature approaches that of the surrounding internal walls. This finally gives, for stagnant gas, the effective gas–wall heat-transfer coefficient that reduces to:

$$\begin{aligned} h_{\text{gas}} &= h_{rad,gas} \\ &= 4\,\epsilon_{gas}\,\sigma\,T_m^3 \end{aligned} \tag{3.45}$$

The remaining coefficient to evaluate is the convective heat-transfer coefficient, $h_{\text{conv,gas}}$, of equation (3.44). It is computed from the Nusselt number, the hydraulic diameter, and the gas thermal conductivity, k_{gas}:

$$h_{conv,gas} = \frac{Nu_D\,k_{gas}}{D_h} \tag{3.46}$$

where $D_h = 4A_{cross}/P$ is the hydraulic diameter of the rectangular channels with $A_{\text{cross}} = l \times H$ the cross-sectional area and $P = 2(l + H)$ the wetted perimeter of a specific discretized channel.

The Nusselt number depends on the flow regime, which is characterised by the Reynolds number (function of the mean velocity u), Re, and Prandtl number, Pr:

$$Re = \frac{u\,D_h}{\nu_{gas}}, \qquad u = \frac{\dot{V}_{gas}}{A_{cross}}, \qquad Pr = \frac{\nu_{gas}}{\alpha_{gas}} \tag{3.47}$$

Depending on Re and Pr numbers, different correlations are applied for laminar (highly ordered flow), transitional, or turbulent (highly irregular three-dimensional motion) flow. Since the stove's channels create an internal flow, and the ratio of the flow path length to the hydraulic diameter L/D_h is much smaller than 10 ($\frac{L}{D_h} << 10$), the flow remains in the thermal entry region. Therefore, correlations for thermally developing internal flow in the entry region are used. All correlations that are employed in the numerical model for computing the Nusselt number are detailed in Appendix B.1.

3.6.6.2 Refractory–casing wall heat transfer term $\dot{Q}_{\text{rfr,cng}}$

Figure 3.12 illustrates the conductive heat transfer between a refractory and a casing wall. For the case of a three-node discretization in each wall, the heat transfer $\dot{Q}_{\text{rfr,cng}}$ occurs between the refractory node $T_{\text{rfr},2}$ and casing node $T_{\text{cng},0}$:

$$\dot{Q}_{rfr,cng}(t) = \frac{T_{rfr,2}(t) - T_{cng,0}(t)}{R_{rfr,cng}} \tag{3.48}$$

The thermal resistance between these nodes takes into account surface resistances and the contact resistance between the walls, R_c:

$$\begin{aligned} R_{\text{rfr,cng}} &= R_{\text{surf,rfr}} + \frac{R_c}{A} + R_{\text{surf,cng}} \\ &= \frac{\Delta x_{\text{rfr}}/2}{k_{\text{rfr}}\,A} + \frac{R_c}{A} + \frac{\Delta x_{\text{cng}}/2}{k_{\text{cng}}\,A}. \end{aligned} \tag{3.49}$$

The thermal contact resistance, R_c, represents the imperfect mechanical contact between the refractory and casing bricks. Due to surface roughness and the presence of small air gaps (no applied pressure between bricks), reported values of thermal contact resistance for brick–brick interfaces typically range from 10^{-4} to 10^{-2} m^{2}K/W [69, 70]. In the absence of temperature measurements at the refractory–casing interface, R_c is set to a fixed value corresponding to the mid-range of reported values: $R_c = 5 \times 10^{-3}$ m^{2}K/W. A rapid sensitivity analysis showed that reasonable variations of R_c within this range have a limited effect on the predicted wall temperatures, confirming the robustness of this modelling choice.

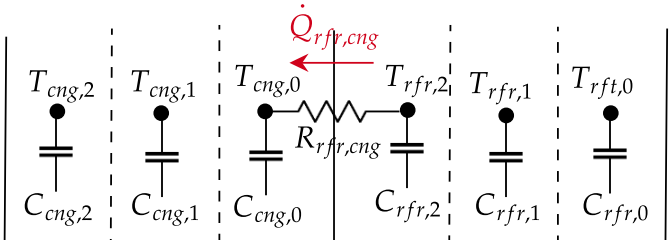

Figure 3.12: Local RC representation of conductive heat transfer between refractory and casing walls.

3.6.6.3 Wall–ambient heat transfer term $\dot{Q}_{\mathbf{wall,a}}$

Figure 3.13 shows the heat transfer between the external wall node and ambient air and is a close-up of the left casing wall in Figure 3.9. The heat transfer between the external wall node and the ambient air, $\dot{Q}_{\mathrm{cng,a}}$, is decomposed into a convective contribution between the wall node and the ambient and a radiative contribution between the wall surface and the surrounding:

$$\begin{aligned} \dot{Q}_{cng,a} &= \dot{Q}_{conv} + \dot{Q}_{rad} \\ &= \frac{T_{cng,2} - T_{amb}}{R_{cng,a}} + \epsilon\sigma A(T^4_{surf,cng} - T^4_{amb}) \end{aligned} \tag{3.50}$$

where:

- A is the exchange area between the discretized wall and the ambient.
- $R_{\mathrm{cng,a}}$ is the total thermal resistance between the ambient air and the external wall node:

$$\begin{aligned} R_{\mathrm{cng,a}} &= \frac{1}{A\, h_{\mathrm{conv}}(T_{\mathrm{surf,cng}}(t), T_{\mathrm{amb}})} + R_{\mathrm{surf,cng}} \\ &= \frac{1}{A\, h_{\mathrm{conv}}(T_{\mathrm{surf,cng}}(t), T_{\mathrm{amb}})} + \frac{\Delta x_{\mathrm{cng}}/2}{k_{\mathrm{cng}}\, A} \end{aligned} \tag{3.51}$$

- $T_{\mathrm{surf,cng}}$ is the wall surface temperature, estimated by linear extrapolation from the two nodes closest to the surface:

$$T_{\mathrm{surf,cng}} = T_{\mathrm{cng},2} + \tfrac{1}{2}\big(T_{\mathrm{cng},2} - T_{\mathrm{cng},1}\big). \tag{3.52}$$

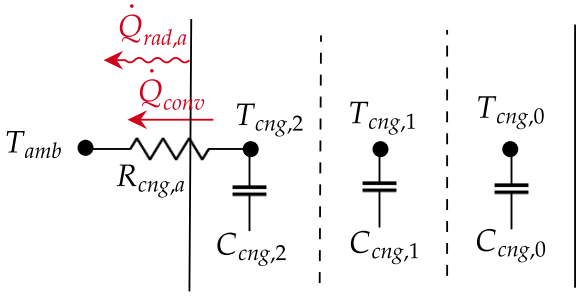

Figure 3.13: Convective and radiative heat transfer between an external casing wall and ambient air.

In reality, the convective and radiative heat fluxes act at the wall surface, not at the center of the first wall control volume. For convection, this is accounted for by including the surface conduction resistance $R_{\text{surf,cng}}$ between the wall surface and the first node as done in equation (3.51). In contrast, radiation cannot be represented as a simple linear resistance without introducing significant approximation errors because radiative heat flux varies non-linearly with temperature according to the Stefan–Boltzmann law. Strictly speaking, an additional wall node should be added at the wall surface. Its temperature would be updated based on radiative heat transfer, and the first centered node would then be updated using the heat transfer between it and this surface node through the surface resistance. To avoid this, the model assumes that the radiative flux acts directly on the first centered node, effectively neglecting the surface conduction resistance for the radiation term. This simplification has been examined and validated in Appendix B.3, showing that it reduces computational cost while maintaining accuracy.

The remaining unknown to close $\dot{Q}_{\text{wall,a}}$ is the convective heat-transfer coefficient h_{conv}, defined as:

$$h_{conv} = \frac{Nu_D}{k_a\, L} \tag{3.53}$$

The Nusselt number is obtained from the Churchill and Chu correlation for free convection on a vertical plate, as reported in Incroperas textbook [36].This correlation is valid over the full range of Rayleigh numbers, Ra_L:

$$Nu_D = \left[\frac{0.825 + 0.387\, Ra_L^{1/6}}{\left(1 + \left(\frac{0.492}{Pr}\right)^{9/16}\right)^{8/27}} \right]^2 \tag{3.54}$$

with the Rayleigh number:

$$Ra_L = \frac{g\,\beta\,|T_{surf,wall} - T_{amb}|\,L^3}{\nu_a \alpha_a}\, Pr \tag{3.55}$$

where:

- $\beta = \left(\frac{T_{amb}+T_{surf,wall}}{2}\right)^{-1}$
- L is the characteristic length of the geometry
- $g = 9.81$ m/s^2 is the gravitational acceleration

Ambient air properties are evaluated at 350 K. This approximation is justified since their temperature dependence is limited in the range of interest, and 350 K is representative of the mean film temperature $\frac{T_{\text{amb}}+T_{\text{surf,wall}}}{2}$ during operating conditions. The adopted values are:

$$k_a = 30.0 \times 10^{-3}\ \text{W m}^{-1}\text{K}^{-1}, \qquad \nu_a = 20.92 \times 10^{-6}\ \text{m}^2/\text{s}, \qquad \alpha_a = 29.9 \times 10^{-6}\ \text{m}^2/\text{s}.$$

3.6.6.4 Radiative exchange between internal walls $\dot{Q}_{\text{rad,wall}}$

The last wall heat-transfer contribution is the radiative exchange between the internal walls forming a gas channel. Figure 3.14 illustrates, for a given gas segment, the radiative heat received by wall 0 from the three other internal walls (the full model applies the same calculation for each wall in the segment). As for wall–ambient radiation, the fluxes should strictly apply at the wall surfaces, but they are applied at the first wall node in the model, neglecting R_{surf} (see Appendix B.3 for validation). The walls are assumed to behave as diffuse–gray surfaces, which allows the use of standard radiative exchange relations between surfaces. Radiation absorption by the flue gas between walls is neglected, since the gas optical thickness is small, while gas-to-wall radiation is already accounted for in Section 3.6.6.1.

As an example, the net radiative heat flux from the other walls j to wall 0 is:

$$\sum_j \dot{Q}_{\text{rad},j\to 0}(t) = A_0 \sum_j \left[\frac{\left(T_{\text{surf},j}(t)^4 - T_{\text{surf},0}(t)^4\right)}{\dfrac{1-\epsilon_0}{\epsilon_0} + \dfrac{1}{F_{j0}} + \dfrac{1-\epsilon_j}{\epsilon_j}} \right], \quad j = 1,2,3, \tag{3.56}$$

where:

- A_0 is the surface area of wall 0.
- ϵ_i is the hemispherical emissivity of wall i.
- F_{j0} is the view factor from wall j to wall 0 (computed in Section 3.4.3.3).

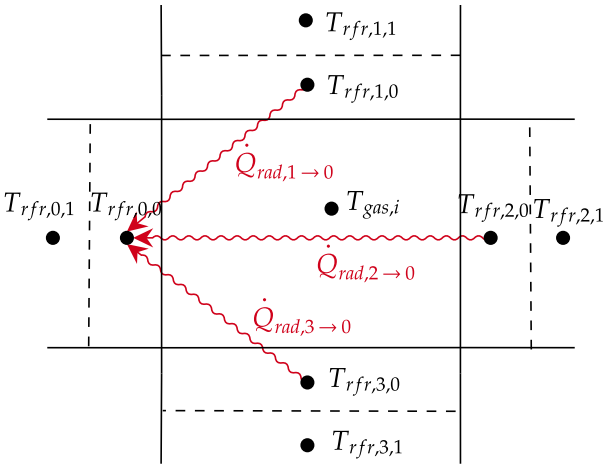

Figure 3.14: Radiative heat exchange between the internal walls of a gas channel; example of the net radiation received by wall 0 from walls 1 to 3.

3.6.6.5 Internal conduction within wall elements

In addition to the gas–wall exchanges and the external wall heat-transfer mechanisms presented above, each wall undergoes internal conductive heat transfer between its discretized nodes. Figure 3.15 illustrates this mechanism for a wall discretized into three nodes ($n_{nodes} = 3$). For any wall node located between two neighbouring nodes (i.e., an interior node), the transient energy balance is:

$$\begin{aligned} C_{node}\frac{dT_1(t)}{dt} &= \dot{Q}_{0\to1}(t) - \dot{Q}_{1\to2}(t) \\ &= \frac{T_0(t) - T_1(t)}{R_{in}} - \frac{T_1(t) - T_2(t)}{R_{in}} \end{aligned} \tag{3.57}$$

where:

- $C_{\text{node}} = \rho A c_p \Delta x$ is the thermal capacitance of a wall control volume associated with density and specific heat capacity depending on the material of the wall,
- $R_{\text{in}} = \dfrac{\Delta x}{kA}$ is the internal conduction resistance between two adjacent casing nodes with thermal conductivity depending on the material of the wall.

In contrast, extreme nodes, i.e., those adjacent to the wall surfaces, have only one internal neighbour for conduction but are also influenced by external heat-transfer mechanisms described previously. For them, the equations below describe only the contribution from internal conduction to their energy balances:

$$\begin{aligned} C_{node}\frac{dT_0}{dt} &= -\dot{Q}_{0\to1} \\ &= \frac{T_1(t) - T_0(t)}{R_{cng,in}} \end{aligned} \tag{3.58}$$

$$\begin{aligned} C_{node}\frac{dT_2}{dt} &= \dot{Q}_{1\to2} \\ &= \frac{T_1(t) - T_2(t)}{R_{cng,in}} \end{aligned} \tag{3.59}$$

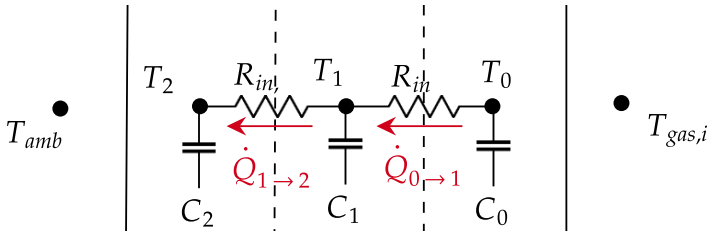

Figure 3.15: RC representation of the internal one-dimensional conductive heat-transfer paths within a wall discretized into three nodes.

3.7 Numerical solvers and implementation

This section describes the numerical strategies used to integrate the coupled system of heat transfer and gas transport equations developed in the previous sections. Based on the general governing equation (3.35), the energy balance for each discretized temperature node can be written as:

$$\frac{dT_i}{dt} = \frac{1}{C_i} \sum_{j \in \mathcal{N}(i)} \dot{Q}_{j \to i}(T_j, T_i, t), \tag{3.60}$$

where T_i is the temperature of node i, $\mathcal{N}(i)$ denotes the set of nodes thermally coupled to node i and $\dot{Q}_{j \to i}$ represents the heat-transfer contributions between these nodes and node i. These contributions include diffusion, convection, gas advection, and radiative exchanges, as described in the previous section.

Applying this formulation for all temperature nodes, and defining $\mathbf{T}(t) = [T_0, \ldots, T_N]^T$ as the nodal temperature vector and $\mathbf{C} = \mathrm{diag}(C_0, \ldots, C_N)$ as the diagonal matrix of nodal heat-capacities, the problem becomes as set of coupled ordinary differential equations (ODEs):

$$\frac{d\mathbf{T}(t)}{dt} = \mathbf{C}^{-1}\, \mathbf{Q}(t, \mathbf{T}(t)) = \mathbf{F}(t, \mathbf{T}(t)), \tag{3.61}$$

where $\mathbf{F}(t, \mathbf{T}(t))$ represents the thermal evolution operator resulting from heat exchanges between neighbouring nodes.

To solve this system numerically, the following time-integration schemes, mentioned in the review of literature, are considered: the Forward Euler method, the Backward Euler method, the Runge-Kutta (RK) scheme and the Backward Differentiation Formula (BDF) approach.

The Forward Euler and RK schemes are explicit methods, for which the state at the next time step is computed directly from known quantities at the current time step. As a result, they are simple to implement but require very small time steps to ensure numerical stability. In contrast, the Backward Euler and BDF schemes are implicit. They involve the solution of a (generally non linear) system of equations at each time step, since the state at the next time level appears implicitly in the formulation. Although computationally more expensive per time step, implicit methods offer superior stability properties and are therefore well suited for stiff systems.

The numerical implementation of these solvers, along with their stability properties, is discussed below. Based on this analysis, two integration schemes are selected for use in the simulations.

3.7.1 Forward Euler

The explicit Forward Euler method is one of the simplest time-integration schemes to solve a system of global ODEs. It is a first-order, fully explicit method in which the state at the next time step is computed directly from the current state and its time derivative. Applied to the thermal balance of node i, and based on equation (3.60), the update equation reads:

$$T_i(t + \Delta t) = T_i(t) + \frac{\Delta t}{C_i} \sum_{j \in \mathcal{N}(i)} \dot{Q}_{j \to i}(T_j, T_i, t) \tag{3.62}$$

where $\frac{1}{C_i} \sum_{j \in \mathcal{N}(i)} \dot{Q}_{j \to i}(T_j, T_i, t)$ corresponds to the first time derivative since it is equal to $\frac{dT_i}{dt}$ (see equation (3.60)).

In the *Python* implementation, equation (3.62) is applied sequentially at each time step to update the temperature of all discretized nodes of the masonry stove.

Being a first-order explicit scheme, the Forward Euler method is conditionally stable, requires sufficiently small time steps to ensure numerical stability. In thermal RC networks with small time constants, this leads to very restrictive time-step constraints. As a consequence, although the method is simple and computationally inexpensive per time step, the total computational time becomes large for long transient simulations. Moreover, its first-order accuracy limits the achievable precision.

For these reasons, the Forward Euler scheme was primarily used for initial testing and debugging, due to its straightforward implementation and its clear correspondence with the used RC network physics. Nevertheless, it was not retained for the final production simulations presented in this thesis.

3.7.2 Runge–Kutta (RK45)

The Runge-Kutta (RK) methods extend the Forward Euler scheme by evaluating the time derivative at several intermediate stages within a single time step, thereby achieving higher orders of accuracy. Starting from the global ODE for each thermal node i, defined in equation (3.60), a general explicit RK method with s stages can be written as (with t^n the current time and $t^{n+1} = t^n + \Delta t$):

$$T_i^{n+1} = T_i^n + \Delta t \sum_{k=1}^{s} b_k \, k_i^{(k)}, \tag{3.63}$$

$$\text{with} \quad k_i^{(k)} = f_i\left(\mathbf{T}^n + \Delta t \sum_{m=1}^{k-1} a_{km} \mathbf{k}^{(m)},\, t^n + c_k \Delta t \right), \qquad k = 1, \ldots, s. \tag{3.64}$$

where where $f_i(\mathbf{T}, t)$ denotes the right-hand side of the energy balance for node i, i.e. the sum of all heat-transfer contributions divided by the corresponding thermal capacitance C_i. The coefficients a_{km}, b_k, and c_k are coefficients defining the specific RK scheme. t^n and t^{n+1} define the current and next time step ($t^{n+1} = t^n + \Delta t$).

As an example, the classical fourth-order Runge–Kutta (RK4) method is recalled below. For each thermal node i, the intermediate stages are computed as:

$$k_1 = f_i(\mathbf{T}^n, t^n), \tag{3.65}$$

$$k_2 = f_i\left(\mathbf{T}^n + \frac{\Delta t}{2} k_1,\, t^n + \frac{\Delta t}{2}\right), \tag{3.66}$$

$$k_3 = f_i\left(\mathbf{T}^n + \frac{\Delta t}{2} k_2,\, t^n + \frac{\Delta t}{2}\right), \tag{3.67}$$

$$k_4 = f_i(\mathbf{T}^n + \Delta t\, k_3,\, t^n + \Delta t)\,, \tag{3.68}$$

and the temperature update is given by:

$$T_i^{n+1} = T_i^n + \frac{\Delta t}{6}\left(k_1 + 2k_2 + 2k_3 + k_4\right). \tag{3.69}$$

In the numerical implementation of the developed numerical model, an embedded adaptive Runge–Kutta method of order 4(–5), denoted RK45, is employed. This method is available through the `scipy.integrate.solve_ivp` function in *Python*. The RK45 scheme combines a fourth and a fifth order Runge–Kutta method to estimate the local truncation error and automatically adjust the time step. This adaptive time-stepping strategy allows the solver to maintain accuracy while minimizing computational effort, particularly during slowly varying thermal dynamics.

The algorithmic procedure used to integrate the coupled system of thermal equations with the RK45 method in the *Python* computer code can be summarized as follows:

1. Evaluate the temperature derivatives for all gas and wall nodes by computing the heat-transfer terms $\sum_{j\in\mathcal{N}(i)} \dot{Q}_{j\to i}(T_j, T_i, t)$ through the function `dTdt`, developed from the heat-transfer relations described in Section 3.6.4 and provided as input to the `solve_ivp` function.

2. Perform adaptive RK integration over the current time interval using the RK45 algorithm implemented in `solve_ivp`.

3. Update the temperatures $\mathbf{T}(t + \Delta t)$ from the solution returned by `solve_ivp`.

4. Proceed to the next time step until the final simulation time is reached.

This approach yields a fully coupled, explicit and adaptive solution of the transient thermal behaviour of the masonry stove. Numerical stability is discussed in Section 3.7.5.

3.7.3 Backward Euler

After the two explicit schemes, to address the stiffness of the thermal network, a first-order implicit Backward Euler (BE) scheme is implemented. Stiffness arises because gas nodes respond rapidly to combustion dynamics, while wall and radiative processes evolve more slowly. Explicit integration would therefore require prohibitively small time steps Δt for stability. The Backward Euler method allows stable integration with larger time steps, although it is only first-order accurate and requires iterative solution of a non-linear system at each step.

Starting from the global ODE system in equation (3.61), the Backward Euler time discretization over a time step from t^n to t^{n+1} is written as:

$$\frac{\mathbf{T}^{n+1} - \mathbf{T}^n}{\Delta t} = \mathbf{C}^{-1}\,\mathbf{F}(\mathbf{T}^{n+1}, t^{n+1}), \tag{3.70}$$

where the derivative function $\mathbf{F}$ is evaluated at the unknown future step $\mathbf{T}^{n+1}$. Because $\mathbf{F}(\mathbf{T}^{n+1}, t^{n+1})$ depends on the temperatures at the next time step, equation (3.70) generally requires an iterative solution. Temperature-dependent parameters, such as convective and radiative conductances, are updated using Picard iterations, starting from an initial guess $\mathbf{T}^n$, until convergence is reached. Linear heat transfer terms (conduction, convection) typically converge in a single iteration, while non-linear radiation requires multiple iterations.

To try to reduce the computational effort, the non-linear radiative contributions in $\mathbf{F}$ are linearized over each time step (see Appendix B.4). The Backward Euler update can then be simplified in a linear matrix form:

$$\underbrace{\left(\mathbf{I} + \Delta t\,\mathbf{C}^{-1}\mathbf{K}\right)\mathbf{T}^{n+1}}_{\mathbf{A}\,\mathbf{T}^{n+1}} = \underbrace{\mathbf{T}^n + \Delta t\,\mathbf{C}^{-1}\mathbf{f}}_{\mathbf{b}}, \tag{3.71}$$

where $\mathbf{K}$ is the global conductance matrix including conductive, convective, and linearized radiative couplings, and $\mathbf{f}$ collects source terms such as combustion contributions. The system is sparse and diagonally dominant, since each node only interacts with its neighbours. Equation (3.71) can now be efficiently solved in *Python* using `scipy.sparse.linalg.spsolve`.

To illustrate the possible form of this matricidal formulation for a node i of the discretized system, the generic nodal formulation can written as:

$$\underbrace{\left(\frac{C_i}{\Delta t} + \sum_j G_{ij}\right) T_i^{n+1} - \sum_j G_{ij} T_j^{n+1}}_{\left[\mathbf{A}\,\mathbf{T}^{n+1}\right]_i} = \underbrace{\frac{C_i}{\Delta t} T_i^n + b_{\text{ext}}}_{b_i}. \tag{3.72}$$

where G_{ij} are the conductances between node i and neighbours j, including linearized radiation, convection, and conduction. Nodes with prescribed temperatures (e.g., the first gas segment representing the combustion chamber) are accounted for via the term b_{ext} on the right-hand side, ensuring proper coupling with neighbouring nodes while maintaining the fixed boundary temperature.

The Backward Euler solver is implemented in *Python* following this algorithm:

1. Assemble the conductances $G_{i,j}$ at time t^n among which the linearized radiative coefficients.
2. Construct the implicit matrix $\mathbf{A} = \mathbf{I} + \Delta t\,\mathbf{C}^{-1}\mathbf{K}$ and the right-hand side $\mathbf{b} = \mathbf{T}^n + \Delta t\,\mathbf{C}^{-1}\mathbf{f}$.
3. Apply boundary and Dirichlet constraints, including the upstream temperature of the combustion chamber.

4. Solve the linear system $\mathbf{A}\,\mathbf{T}^{n+1} = \mathbf{b}$ using `spsolve`.
5. Update temperature-dependent parameters (convective and radiative coefficients) using Picard iterations until convergence.
6. Update the nodal temperature vector and proceed to the next time step.

In this work, the Backward Euler method was implemented as a standard first-order implicit approach to explore the behavior of the coupled thermal system. While it is usually unconditionally stable, the method required multiple iterations to converge due to the temperature-dependent radiative and convective terms, resulting in substantial computational time. Consequently, the Backward Euler approach proved inefficient for realistic simulations and was not used for the final results presented in the next sections. Instead, the higher-order implicit BDF method was studied.

3.7.4 Backward Differentiation Formula (BDF)

The Backward Differentiation Formula (BDF) approach extends the implicit Backward Euler scheme to higher-order multistep formulas and includes adaptive time-stepping with stiffness detection. It solves the same system of ODEs given in equation (3.61) by approximating the time derivative at t^{n+1} using a backward finite-difference formula involving the current solution and the previous k solution values:

$$\sum_{j=0}^{k} \alpha_j(\{\Delta t\})\,\mathbf{T}^{\,n+1-j} = \Delta t^{n+1}\,\mathbf{F}\big(t^{\,n+1},\,\mathbf{T}^{\,n+1}\big),$$

where:

- the coefficients α_j depend on the current and recent time steps $\{\Delta t\} = \{\Delta t^{n+1}, \Delta t^{n}, \ldots, \Delta t^{n+1-k}\}$,
- k denotes the order of the BDF method, i.e. the number of previous time steps used ($k = 1$ reduces to the Backward Euler method, $k = 2$ yields a second-order approximation, etc.),
- j indexes the individual solution vectors from $n+1$ down to $n+1-k$

For constant time step and fixed order, the α_j reduce to standard BDF constants. However, in practice, modern solvers implement variable-step, variable-order BDF schemes (orders 1–5), automatically adapting both the time step and the integration order based on error estimates. At each time step, the resulting non-linear implicit system is solved using Newton iterations. The equation above therefore describes the underlying numerical method, while the solver handles adaptivity and non-linear solution procedures internally.

The BDF method is particularly adapted for stiff systems, as in masonry stoves where high-temperature nodes in the combustion chamber exchange heat rapidly with slow-changing accumulator nodes. Implicit methods like BDF allow stable integration with large time steps without numerical instability.

In this work, the BDF approach is implemented using again the `solve_ivp` function from the *Python* `scipy.integrate` module, with the argument `method='BDF'`. This solver provides a modern implementation of a variable-order, variable-step BDF scheme.

At each internal time step, `solve_ivp` performs the following operations:

1. Call the user-defined function `dTdt` to evaluate the derivative function $\mathbf{F}(t, \mathbf{T})$, which computes all conductive, convective, radiative, and advective heat-transfer terms for each node, as described in Section 3.6.4.
2. Integrate the ODE system forward in time using the BDF scheme, with adaptive time-step control based on local truncation error, adaptive selection of the BDF order (from 1 to 5), and Newton iterations to solve the resulting non-linear implicit system.
3. Update the temperatures $\mathbf{T}$ from the solution returned by `solve_ivp` and proceed until the final simulation time is reached.

In the *Python* implementation, switching between explicit RK45 and BDF only requires changing the method argument passed to `solve_ivp`. All other elements of the code remain identical.

3.7.5 Stability criterion

The different time-integration schemes described above are subject to different stability properties. Before selecting an appropriate time step, it is therefore necessary to identify the stability limits imposed by the thermal RC network and by gas advection. These constraints determine the maximum admissible time step for explicit schemes and provide useful accuracy guidelines even for unconditionally stable implicit methods. The stability criteria presented in this section are derived from standard results in the numerical analysis literature, whose sources are mentioned in the review of literature on numerical solvers (Section 2.2.3).

The first stability restriction arises from the explicit treatment of the thermal RC network which includes wall conduction, gas-wall exchange, and radiative couplings. For a simple linear ODE:

$$\frac{dy}{dt} = \lambda y \tag{3.73}$$

the explicit Forward Euler scheme is stable if [71]:

$$\left| \frac{y^{n+1}}{y^n} \right| = |1 + \Delta t\, \lambda| \leq 1 \qquad \Leftrightarrow\ -2 < \Delta t\, \lambda < 0 \tag{3.74}$$

By analogy with equation (3.73), a linearized nodal thermal balance can be written as:

$$\frac{dT}{dt} = -\frac{1}{RC}\,(T - T_0) \tag{3.75}$$

with T_0 the temperature of a neighbouring node. Identifying $\lambda = -1/(RC)$ (the decay rate of the node temperature towards its neighbours) yields the explicit stability condition:

$$-2 < \Delta t \left(-\frac{1}{R\,C} \right) < 0 \qquad \Leftrightarrow\ \Delta t < 2\,\frac{C}{G}, \quad \text{with } G = \frac{1}{R} \tag{3.76}$$

In the general case, each node i exchanges heat with several neighbouring nodes j. The local explicit stability limit therefore becomes for one node:

$$\Delta t < 2\ \frac{C_i}{\sum_j G_{ij}} \tag{3.77}$$

where C_i is the nodal thermal capacitance and G_{ij} are the conductances connecting node i to its neighbours.

For explicit Runge–Kutta methods, the stability limit is extended. For a classical fourth-order RK scheme, the stability region leads to the approximate condition:

$$\Delta t < 2.785 \, \frac{C_i}{\sum_j G_{ij}} \tag{3.78}$$

This value is used here as a conservative guideline for estimating admissible time steps for the explicit $RK45$ solver. Although `solve_ivp` employs adaptive time stepping with embedded error control, RK45 remains an explicit Runge–Kutta method and is therefore ultimately subject to stability constraints.[4]

In practice, the admissible time step for explicit schemes is governed by the most restrictive ratio $C_i / \sum_j G_{ij}$ over all gas and wall nodes in the discretized network. Table 3.5 summarizes the corresponding characteristic expressions for the different node configurations present in the numerical model.

A second stability restriction comes from upwind discretization of gas advection between gas segments. Stability requires that the Courant–Friedrichs–Lewy (CFL) limit is satisfied for each gas segment i:

$$\mathrm{CFL}_i = \frac{u_i \Delta t}{\Delta x_i} \leq 1 \qquad \Leftrightarrow \Delta t \leq \frac{\Delta x_i}{u_i} \tag{3.79}$$

where u_i is the gas velocity and Δx_i the length of the gas control volume i in the flow direction. Expressed in mass form, using $m_{gas,i} = \rho_{gas} A \Delta x_i$ and $\dot{m}_{gas} = \rho_{gas} u_i A$, this condition becomes:

$$\Delta t \leq \frac{m_{gas,i}}{\rho_{gas} A} \frac{\rho_{gas} A}{\dot{m}_{gas}} \qquad \Leftrightarrow \Delta t \leq \frac{m_{gas,i}}{\dot{m}_{gas}} \tag{3.80}$$

This constraint guarantees that advection over one time step does not move more mass (and therefore not more advected energy) out of a control volume than the mass currently stored in it.

Implicit schemes such as Backward Euler and BDF are unconditionally stable with respect to the RC network, thereby removing the spectral stability constraint associated with conduction, convection, and radiation. However, the advective CFL condition remains a practical guideline for accuracy and monotonicity. Even for implicit schemes that are theoretically unconditionally stable, large violations of the CFL condition may lead to non-physical oscillations or loss of solution accuracy.

The final stability constraints applied for each solver are represented in Table 3.6. In practice, the global time step used in the masonry stove model is chosen based on the

[4] Adaptive error control does not guarantee stability for explicit methods, particularly for stiff thermal systems, and may select time steps that are accurate but unstable.

global constraint:

$$\Delta t \leq SF \times \min_i \left(\frac{z\, C_i}{\sum_j G_{ij}}, \frac{m_{gas,i}}{\dot{m}_{gas}} \right) \tag{3.81}$$

with $z = 2$ for Euler explicit forward scheme, $z = 2.785$ for Runge-Kutta scheme and the z term omitted for implicit solvers. A safety factor SF (=0.9) is applied to ensure robust numerical behaviour.

Node interaction	**Characteristic stability ratio expression**
Gas node in the middle of f refractory walls	$c_{p,gas} m_{gas} \left(\sum_f \frac{1}{R_{gas,rfr,f}} \right)^{-1}$
Gas node in the middle of f casing walls	$c_{p,gas} m_{gas} \left(\sum_f \frac{1}{R_{gas,cng,f}} \right)^{-1}$
Refractory wall node in contact with gas (including linearised radiation via $h_{\mathrm{rad},j}$)	$c_{p,rfr} m_{rfr} \left(\frac{1}{R_{gas,rfr}} + \frac{1}{R_{rfr,rfr}} + \sum_j h_{rad,j}\, A \right)^{-1}$
Casing wall node in contact with gas	$c_{p,cng} m_{cng} \left(\frac{1}{R_{gas,cng}} + \frac{1}{R_{cng,cng}} \right)^{-1}$
Internal refractory wall conduction (uniform mesh: $R_{left} = R_{right}$)	$c_{p,rfr} m_{rfr} \left(\frac{2}{R_{rfr,rfr}} \right)^{-1}$
Internal casing wall conduction	$c_{p,cng} m_{cng} \left(\frac{2}{R_{cng,cng}} \right)^{-1}$
Casing wall node in contact with ambient (convection in $R_{cng,air}$, linearised radiation in h_{rad})	$c_{p,cng} m_{cng} \left(\frac{1}{R_{cng,cng}} + \frac{1}{R_{cng,air}} + h_{rad}\, A_{cng,ext} \right)^{-1}$
Refractory wall node in contact with casing wall	$c_{p,rfr} m_{rfr} \left(\frac{1}{R_{rfr,cng}} + \frac{1}{R_{rfr,rfr}} \right)^{-1}$
Casing wall node in contact with refractory wall	$c_{p,cng} m_{cng} \left(\frac{1}{R_{rfr,cng}} + \frac{1}{R_{cng,cng}} \right)^{-1}$

$m_{\mathrm{gas}}, m_{\mathrm{rfr}}, m_{\mathrm{cng}}$ are the masses of the node control volumes (i.e. the local control volume associated with each node, not the total wall mass).

Table 3.5: Characteristic stability ratios for all node types in the masonry stove RC network, used to determine the explicit RC network stability criterion.

Solver	**RC network / thermal stability**	**Gas advection (CFL)**
Forward Euler (explicit)	$\Delta t < \frac{2\,C}{\sum G}$	$\Delta t \leq \frac{m_i}{\dot{m}_i}$
Runge–Kutta (explicit, RK45)	$\Delta t < \frac{2.785\,C}{\sum G}$	$\Delta t \leq \frac{m_i}{\dot{m}_i}$
Backward Euler (implicit)	Unconditionally stable	$\Delta t \leq \frac{m_i}{\dot{m}_i}$
BDF (implicit)	Unconditionally stable	$\Delta t \leq \frac{m_i}{\dot{m}_i}$

Table 3.6: Summary of stability criteria for the four solvers.

3.8 Simulation results

This section presents the first results obtained with the numerical model developed in the previous sections, applied to the studied *B14 V5 in kit Medi Batchblock* masonry stove. The initial model setup and input parameters are first described, including the spatial discretization of the flue gas path and the masonry walls. The numerical behaviour of the model is then analysed through a stability study, focusing on the choice of the maximum time step. The results are also used to investigate the influence of wall discretization on accuracy and computational cost, leading to a final optimal choice of number of wall nodes. Finally, based on the two previous results, simulations performed with Runge–Kutta and BDF solvers are compared. This comparison is used to present the main thermal results of the integrated stove model, including gas and wall temperature evolution, surface temperatures, and heat power and energy released to the ambient, and leads to the selection of the numerical solver retained for further analysis.

3.8.1 Model setup and input parameters

The masonry stove model to which the simulation model is applied is the *B14 V5 in kit Medi Batchblock*, developed by the French company *UZUME* that is the supplier for the *Renolow* project of *LowTech Liège* (Figure 3.16). Experimental data were also gathered on this stove.

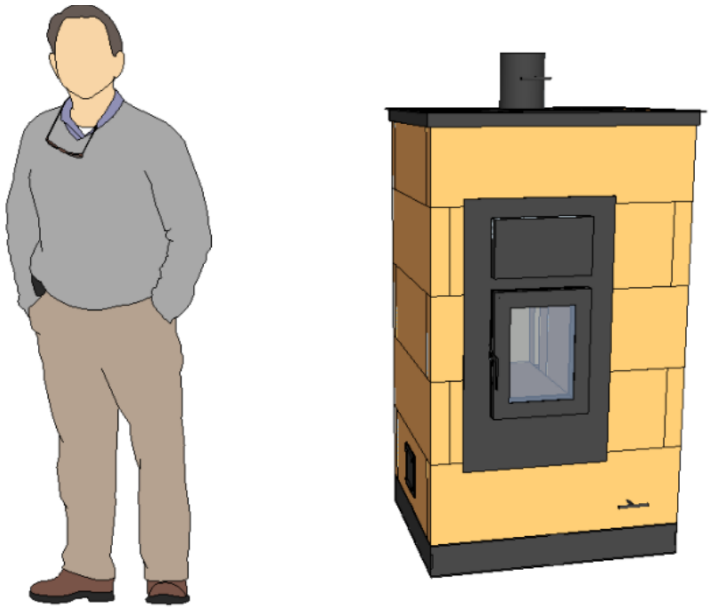

Figure 3.16: Sketch of the *B14 V5 in kit Medi Batchblock* masonry stove [72].

This type of stove has complex accumulator channels. The flue gas flow through these channels has been represented schematically on the left part of Figure 3.17. Based on this path, the accumulator was discretized into 18 gas segments ($M = 18$), following the discretization rules of Section 3.3. This discretization is shown on the right side of Figure 3.17 and in more details in Figure 3.18. In addition, following the rules, 5 gas segments were subdivided into two wall sub-elements to be able to keep heat transfer consistency with gas segments located on both sides of the corresponding walls. These sub-elements are enumerated and indicated by dotted lines in Figure 3.18, leading to a total of 23 wall

segments ($N = 23$).

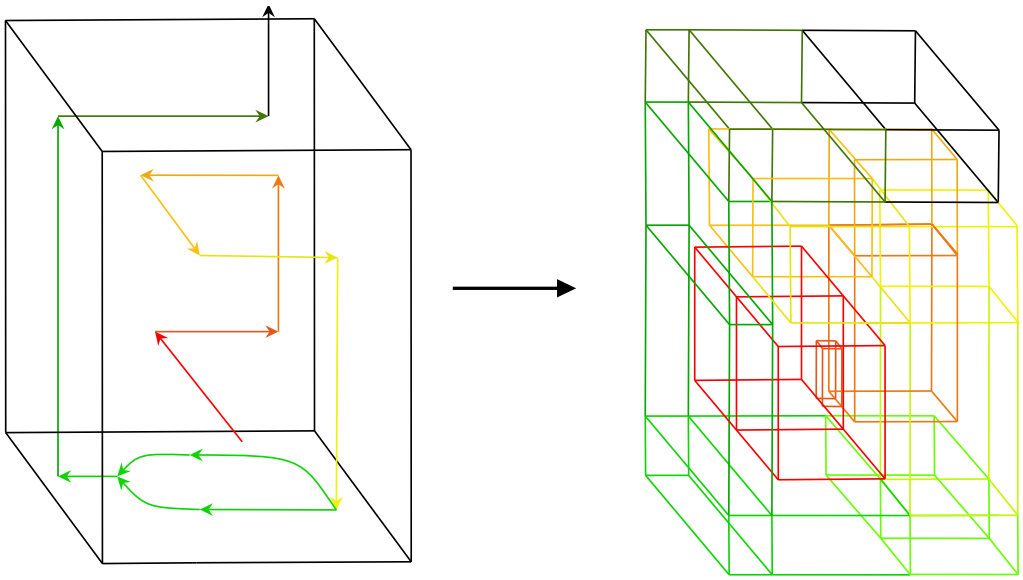

Figure 3.17: Flue gas path in the *B14 V4* masonry stove (left) and gas segment discretization of this stove (right).

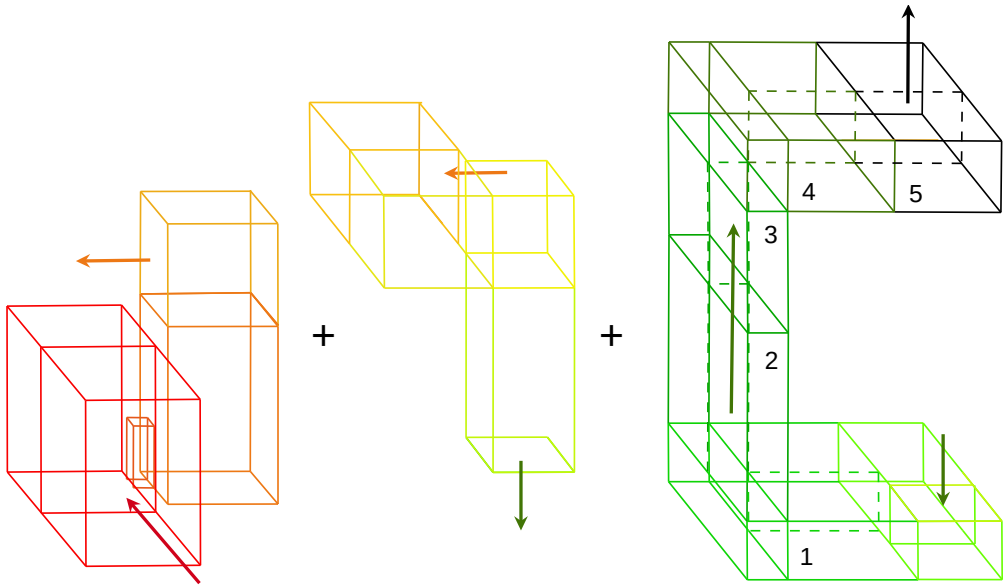

Figure 3.18: Discretization in gas segments and wall sub-elements of the *B14 V4* masonry stove.

The input parameters needed to run the model of a wanted masonry stove are described in Sections 3.4.2, 3.5.2 and 3.6.2. Their values for the studied *B14 V5* stove are reported in Tables C.1, C.2 and C.3 in Appendix C.1. Some input parameters are set to the default values proposed by the *Python* model developed, as the objective of this section is to analyse the model's initial behaviour rather than to perform a direct comparison with known experimental data. Similarly, the parameters defining the flue gas mass flow rate profile were not fixed yet (parameters defined in Section 3.6.3). They are initially set to

physical plausible values for preliminary simulations:

$$t_{ramp,up} = 600 \text{ [s]} \tag{3.82}$$

$$t_{ramp,down} = 200 \text{ [s]} \tag{3.83}$$

Their influence is investigated in Section 5.2.2 through a sensitivity analysis based on comparisons between model outputs and measured wall temperatures, which identifies a plausible and narrow range of values for these parameters.

With all required inputs defined, the simulation can be performed using the Runge–Kutta (RK) and BDF schemes selected earlier. Before comparing their results, however, an analysis of the time step stability is required.

3.8.2 Stability analysis and optimal time step

Based on the stability criteria derived in Section 3.7.5, this section investigates how these theoretical constraints are transposed into practical limits for the numerical simulations. In particular, it examines to what extent the stability limits can be relaxed without significantly affecting the accuracy of the predicted thermal behaviour.

Both RK and BDF schemes are implemented using the `scipy.integrate.solve_ivp` function, through the `'RK45'` and `'BDF'` options. These solvers rely on adaptive time stepping based on local error control. However, error control alone does not guarantee numerical stability, especially for stiff thermal systems. In practice, the solver may select time steps that satisfy accuracy tolerances but still lead to unstable behaviour. For this reason, a maximum allowable time step, Δt_{max}, must be provided to bound the adaptive stepping. This parameter directly affects both numerical accuracy and computational cost, and its appropriate value is determined in this section.

The thermal behaviour of a masonry stove can be divided into two distinct phases: the combustion (accumulation) phase and the post-combustion (release) phase. These phases show different dynamics and are therefore governed by different stability constraints. During combustion, high flue-gas mass flow rates, dominant advective heat transfer, and steep temperature gradients result in fast system dynamics. In this regime, numerical stability and accuracy are primarily controlled by the Courant-Friedrichs-Lewy (CFL) condition associated with gas advection.

After combustion, the dampers are closed and the flue gas mass flow rate progressively decreases to zero. Advection then vanishes, and the system dynamics slow down considerably. In this post-combustion phase, numerical stability is governed by the thermal RC network describing heat exchange between the gas and the masonry walls.

3.8.2.1 Combustion phase stability limits

Applying the global stability criterion (Equation (3.81)) to the discretised *B14 V5* model shows that, during combustion, the most restrictive stability condition is imposed by the advective CFL limit in the third gas segment:

$$\Delta t \leq 0.021 \text{ [s]}. \tag{3.84}$$

Using this value as $\Delta t_{\max}$ for the RK scheme provides the most accurate solution since it respects all stability criteria and is therefore used as a reference for assessing the impact

of larger time steps.

However, this restrictive limit is imposed by the third discretized gas segment, which corresponds to the venturi throat. While this specific segment plays an important physical role in accelerating the flue gases, its control volume and gas-wall exchange areas are significantly smaller than those of all other segments. As a result, it has a limited influence on the global thermal behaviour of the stove. Imposing the CFL limit associated with this segment would therefore impose a very small time step without significantly improving the accuracy of global thermal results.

A more representative stability limit, the next more restrictive limit, is instead imposed by the fifth gas segment, yielding:

$$\Delta t \leq 0.228 \text{ [s]}. \tag{3.85}$$

This limit is considered more relevant for identifying when numerical instability arises during combustion.

3.8.2.2 Post-combustion stability limits

In the post-combustion phase, the flue-gas mass flow rate reaches zero (at $t = t_{\text{comb}} + t_{\text{ramp,down}}$), advection vanishes and the CFL condition no longer applies. Therefore, stability is governed by the thermal RC network. For the explicit RK solver, stability remains conditional, and the most restrictive RC-based limit yields:

$$\Delta t \leq 0.766 \text{ [s]}, \tag{3.86}$$

which is imposed by the thermal coupling between the gas node of the third discretized gas segment and its adjacent refractory wall nodes. As previously discussed, this segment corresponds to the venturi throat and has an atypically small control volume. It is therefore not representative of the global thermal behaviour. The next RC-based stability limit imposed after this one is associated with the fourth gas segment. This limit is more representative of the discretized thermal behaviour and is:

$$\Delta t \leq 2.501 \text{ [s]}. \tag{3.87}$$

For the implicit BDF solver, the RC network is unconditionally stable. Consequently, RC-based stability limits do not constrain $\Delta t_{\max}$ in the post-combustion phase, although excessively large time steps may still degrade accuracy.

3.8.2.3 Tested time steps and reference cases

Based on previous considerations, a range of maximum time steps was tested for each solver. For the RK scheme solver, the reference solution corresponds to giving $\Delta t_{\max} = 0.02$ s to `solve_ivp`, while larger values up to 5 s were tested to explore the trade-off between computational efficiency and accuracy while staying reasonably close to the RC-based limit. For the BDF approach solver, a conservative reference value of $\Delta t_{\max} = 0.1$ s was selected, and larger values up to 70 s were investigated. This reference value was chosen because, although the BDF approach is unconditionally stable and can handle large time steps, excessively large time steps may still degrade accuracy during fast transients by exceeding physical transport times. The different simulations, each using a

specific maximum time step, were performed for a 5-hour stove operation.

From the different results obtained, numerical accuracy was quantified using the global absolute root-mean-square error ($RMSE_{global}$), computed by comparing temperature time histories from the reference and tested simulations over all nodes and over the full simulation duration (5 hours of stove operation). All temperature fields, spatial nodes, and time steps were aggregated into a single dataset. From this dataset, the global absolute RMSE is then computed as:

$$\mathrm{RMSE}_{\mathrm{global}} = \sqrt{\frac{1}{N}\sum_{k=1}^{N}(a_k - b_k)^2} \quad [^\circ\mathrm{C}] \tag{3.88}$$

where a_k denotes the reference temperature time series (simulation with the smallest $\Delta t_{\max}$) and b_k is the corresponding series from the simulation being compared.

Computational performance was evaluated through the CPU speed-up relative to the reference simulation.

3.8.2.4 BDF solver behaviour

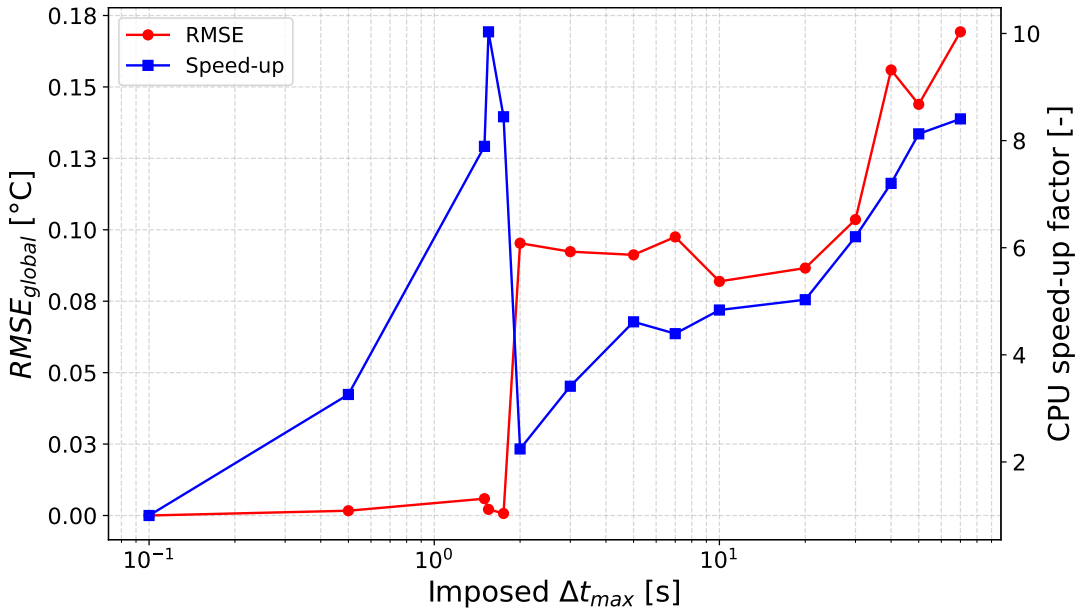

Figure 3.19: Effect of the maximum time step on solution accuracy (RMSE) and computational efficiency (CPU speed-up) for the BDF solver.

For the BDF solver, a maximum CPU speed-up is observed around $\Delta t_{\max} \approx 1.55$ s on Figure 3.19. At this value, the imposed maximum time step matches the time scale naturally selected by the adaptive BDF scheme in `solve_ivp`: the solver can take large time steps fixed at this value during the slow post-combustion phase without needing step size corrections, while still reducing the time step as required to accurately resolve the fast combustion transients. All this minimizes the number of time steps as well as the number of function evaluations inside `solve_ivp`, yielding optimal computational efficiency.

Figure 3.19 shows that smaller values of Δt_{max} unnecessarily constrain the adaptive solver, forcing smaller time steps than required and leading to longer computation times without a significant gain in accuracy. Moreover, slightly larger values, just above $\Delta t_{\max} = 1.55$ s, result in increased step rejections and additional function evaluations inside `solve_ivp`, as the proposed maximum time step no longer corresponds to the one naturally selected by the BDF scheme to solve the problem during the post-combustion phase. This leads to a reduction of the computational efficiency. Finally, for even larger values, the solver may take time steps that are too large to properly resolve the fast combustion transients, leading to the apparition of small instabilities and a noticeable increase in global RMSE. In that case, although computation time may decrease due to larger steps, this occurs at the expense of accuracy.

Based on this trade-off, $\Delta \mathbf{t_{max}} = \mathbf{1.55\ s}$ is selected for all subsequent BDF simulations. This choice exploits the slow post-combustion dynamics while ensuring accurate resolution of fast combustion transients. Using this value, the computation time was reduced from 1036 s (reference case) to 103 s.

3.8.2.5 RK solver behaviour

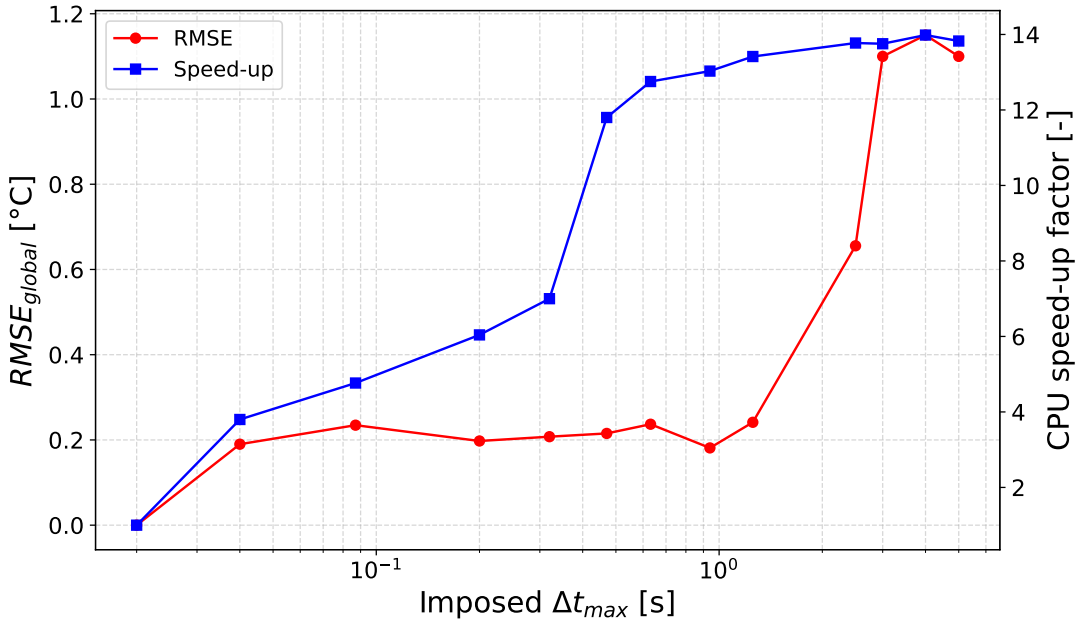

Figure 3.20: Effect of the maximum time step on solution accuracy ($RMSE_{global}$) and computational efficiency (CPU speed-up) for the RK solver.

For the explicit RK solver, Figure 3.20 shows that increasing Δt_{max} generally improves computational efficiency, as fewer function evaluations are required in `solve_ivp`, particularly during the slower post-combustion phase. However, larger maximum time steps often allow time steps beyond the stability constraints, which increases numerical errors.

Between $\Delta t_{\max} = 0.02$ s and 0.2 s, the global RMSE increases only slightly. In this range, the solver exceeds the CFL limit of the non-representative third gas segment, causing small instabilities locally while all other segments remain stable under the physically representative limit of 0.228 s (equation 3.85).

For higher maximum time steps, the solver inside `solve_ivp` automatically reduces step sizes as needed to stay stable during fast combustion transients, while taking larger steps during the slower post-combustion dynamics. This allows the RMSE to remain nearly constant, while CPU time decreases.

When Δt_{max} approaches the RC-based post-combustion stability limit of 2.5 s (equation (3.87)), the solver occasionally attempts steps exceeding this limit. This results in small oscillations, indicating loss of stability extending into the post-combustion phase, in addition to the minor instabilities already present during combustion. This additional instabilities lead to a rapid increase in the global RMSE.

As a result, $\Delta \mathbf{t_{max}}$**=1.25 s**, the point on Figure 3.20 just before the rapid increase in global RMSE, is selected as the optimal compromise for the RK solver. This value keeps the global RMSE well below 1 °C (acceptable error) while providing a CPU speed-up of approximately 13.4. Using this Δt_{max}, the computation time was reduced from 12 hours 34 min (reference case ($\Delta t_{max} = 0.02$ s)) to 55 min.

3.8.3 Effect of wall discretization

Once the time-integration parameters have been defined for both numerical schemes, the remaining modelling choice concerns the spatial discretization of the refractory and casing walls. This discretization is defined by the number of temperature nodes used across the wall thickness, denoted n_{nodes}. Increasing the number of nodes generally improves the representation of heat transfer within the walls by better capturing temperature variations. However, since the model includes several dozen discretized walls whose temperatures are updated at each time step, increasing n_{nodes} also significantly increases computational cost. The objective of this section is therefore to identify an appropriate compromise between numerical accuracy and computational efficiency.

To this end, simulations were performed using four different wall discretizations: n_{nodes} =2 (minimum possible number of wall nodes), 3, 4 and 5. The results obtained with five nodes were taken as the reference solution, as this configuration provides the finest spatial resolution among the tested cases. Values higher than five were not considered as the wall thicknesses stay relatively small and the aim of the present model is not to resolve local temperature gradients across the wall thickness, but rather to accurately predict global and surface thermal quantities.

The results obtained with two, three and four nodes were compared to the five-node reference in terms of both computational time and numerical error. The error was quantified using the absolute root-mean-square error (RMSE) in degrees Celsius (equation 3.88). In addition, a relative RMSE expressed as a percentage, $RMSE_{\%}$, was introduced to facilitate comparison between quantities with different temperature ranges. It is defined as:

$$\text{RMSE}_{\%} = 100\,\frac{\text{RMSE}}{\max\limits_{k}(a_k) - \min\limits_{k}(a_k)} \quad [\%] \tag{3.89}$$

where a_k denotes the temperature time series of the reference simulation obtained with $n_{\text{nodes}} = 5$. The temperatures in a_k are in K to avoid division by zero for low temperatures.

Both absolute and relative RMSE values were computed simultaneously for the following temperature quantities of the numerical model: mean refractory wall temperatures, mean casing wall temperatures, casing surface temperatures, and gas temperature nodes. Together, these quantities represent all temperature fields associated with the discretized spatial nodes of the model. By aggregating all temperature fields, spatial nodes, and time steps into a single dataset, the global error indicators $RMSE_{\text{global}}$ and $RMSE_{\%,\text{global}}$ are obtained and used for comparison.

Table 3.7 summarizes these global RMSEs values obtained for the different wall discretizations, along with the relative computational time gain compared to the five-node reference case.[5]

Number of wall nodes	**RMSE$_{\text{global}}$ [°C]**	**RMSE$_{\%,\text{global}}$ [%]**	**Time gain [%]**
2	2.11	0.17	54.3
3	0.80	0.06	38.7
4	0.27	0.02	10.2

Table 3.7: Simulation results comparison for 2, 3, 4 and 5 wall nodes.

The results clearly show that increasing the number of wall nodes beyond three leads to only marginal improvements in accuracy. Indeed, the global RMSE decreases from 0.80 °C (0.06%) with three nodes to 0.27 °C (0.02%) with four nodes, which is a minor gain in accuracy compared to the associated loss in computational efficiency of 28.5% (=38.7% - 10.2%). Conversely, reducing the wall discretization to two nodes also provides a reduction in computation time, but this gain is smaller than the improvement obtained when reducing from four to three nodes. Moreover, this time saving comes at the cost of a global RMSE exceeding 2 °C (2.11 °C). Such an error level becomes significant for subsequent analyses, particularly those related to thermal comfort. Finally, three nodes already allow a 20-hour stove operation simulation to be completed in a reasonable computation time of 243 s, so there is no strong incentive to reduce to two nodes, which would only reduce to 181 s while increasing inaccuracy.

Based on these results, $\mathbf{n_{nodes}}$=**3** is selected as the optimal wall discretization. This choice provides the best compromise between numerical accuracy and computational efficiency and is therefore retained for all subsequent simulations and as the default model configuration.

[5] All the results correspond to simulations of a 20 hour stove operation (2 hours of combustion followed by 18 hours of heat release) and were performed using the BDF solver.

3.8.4 Combustion submodel results

With the maximum time step to provide to the `solve_ivp` function and the number of wall nodes defined, the first results of the numerical model for the *B14 V5* masonry stove (using the inputs from Section 3.8.1) can now be obtained and analysed. In this section, the outputs of the combustion model are presented. Results for the global model, including heat storage and restitution, are discussed in the following section. The combustion model outputs include: the adiabatic gas temperature, the nominal mass flow rate, and the temperature profile of the flue gas. The adiabatic gas temperature and nominal mass flow rate results are summarized in Table 3.8 while Figure 3.21 illustrates the flue gas temperature profile obtained.

The obtained values in Table 3.8 are consistent with typical mass flow rates and wood combustion temperatures in masonry stoves. Furthermore, the temperature profile of the flue gas in the combustion chamber (first gas segment) follows the sequence described in Section 3.5.4, showing a plateau at the computed adiabatic gas temperature of 1223 K, preceded by a rapid increase and followed by a more gradual decrease. These results validate the general behaviour of the combustion model.

Parameter	**Value**	**Unit**
$\dot{m}_{gas,nom}$	0.0259	[kg/s]
$T_{gas,ad}$	1223.299	[K]

Table 3.8: Results of the adiabatic combustion chamber model for the *B14 V5* masonry stove simulation.

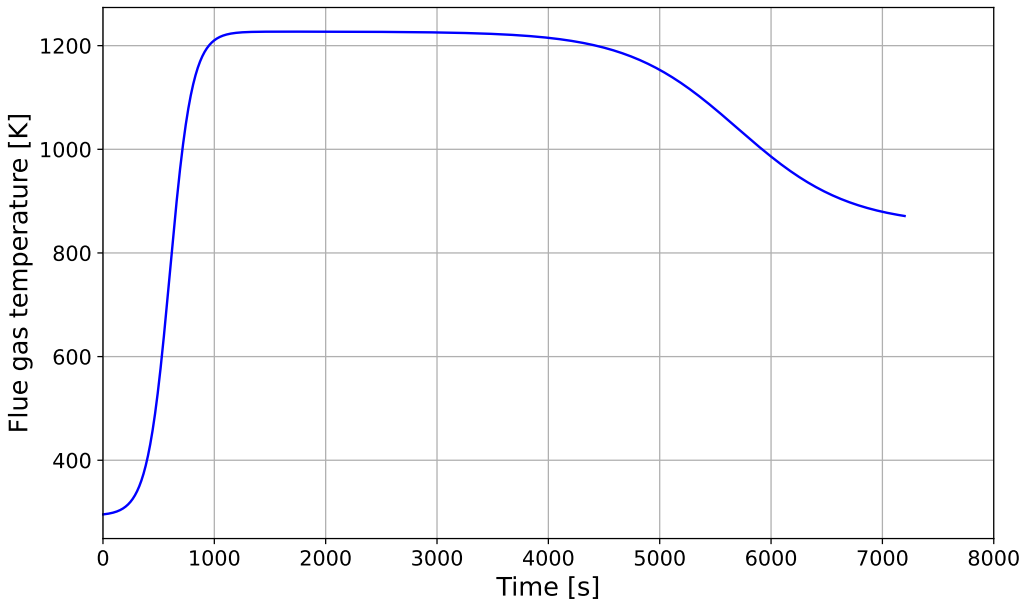

Figure 3.21: Flue gas temperature profile during combustion period for the *B14 V5* masonry stove simulation.

3.8.5 Integrated stove simulation results

This subsection presents the results obtained from the simulation of the masonry stove model described previously. The main goal is to verify that the global temperature trends produced by the numerical model are consistent with typical masonry stove behaviour and to observe potential differences between solvers used. This initial verification focuses on the overall thermal behaviour of the stove, rather than on accurately reproducing of the specific *B14 V5* stove which is performed through a more detailed comparison with experimental data in Section 5. Global trends of masonry stove thermal behaviour, that could be used as references, are documented in the literature, including data and temperature profiles provided by *UZUME* [35] and experimental measurements from Damien Lehmann, research engineer at AFPMA [73].

The following results are analysed looking at the gas temperature evolution in discretized gas segments, mean temperatures within the wall sub-elements, all surface temperatures in contact with the ambient, and the stove's power output. The imulations were performed using the two selected solvers, RK and BDF, with their respective optimal maximum time steps (Δt_{max}) and three wall nodes ($n_{nodes} = 3$). The stove operation was simulated over 20 hours, including 2 hours of combustion followed by 18 hours of heat release, using the input parameters relative to the **B14 V5** stove described in Section 3.8.1.

3.8.5.1 Gas temperature evolution

Firstly, the gas temperature evolution over time is analysed. For that, Figure 3.22 presents the evolution of gas temperature in the combustion chamber and in the first gas segment immediately downstream of this chamber. The results are shown for simulations performed with both RK and BDF scheme-based solvers.

In the top figure, it can be seen that the temperature in the combustion chamber rises sharply and is then followed by a plateau and a gradual decrease, which is consistent with literature. In the second gas segment (bottom figure), a slight deviation from the smooth temperature decrease is observed between approximately 6800 and 7400 seconds after ignition (see zoom). This corresponds to the transition from active combustion with high flue-gas flow to the closure of the dampers and the reduction of the flue gas mass flow. The transition can be understood in two phases:

- From 6800 to 7200 seconds, the combustion is ending and its power gradually decreases, causing the flue gas temperature in the first segment to decline. The channel walls, with their high thermal inertia, remain hot from the previously heated flue gas in the accumulator. As a result, the temperature difference between the walls and the flue gas is smaller, reducing the rate of heat transfer from the gas to the walls. This slows the cooling of the flue gas, producing a temporary "plateau" in the temperature curve.
- From 7200 to 7400 seconds, the dampers close, progressively reducing the mass flow to zero. With less flue gas flowing from the combustion chamber, the second segment no longer receives the heat it previously obtained, resulting in a steeper temperature drop. This behaviour propagates to downstream gas segments until the mass flow reaches zero.

After 7400 seconds, the flue gas mass flow rate is assumed to be zero, and each gas segment exchanges energy solely with its surrounding walls. In this regime, the gas volumes

contribute to the overall thermal inertia, causing the temperature decrease to slow down again. A similar pattern is observed in all downstream segments and also in the first segment that shows a reduced cooling rate at 7400 seconds.

Finally, the overall trends are similar for the two solvers. The RK and BDF solvers yield nearly identical results, which is expected since both are implemented within the same *Python* function and with adapted time steps. This close agreement is illustrated by the RK solution (blue curve), which lies almost entirely beneath the BDF solution (red curve) upon visual inspection.

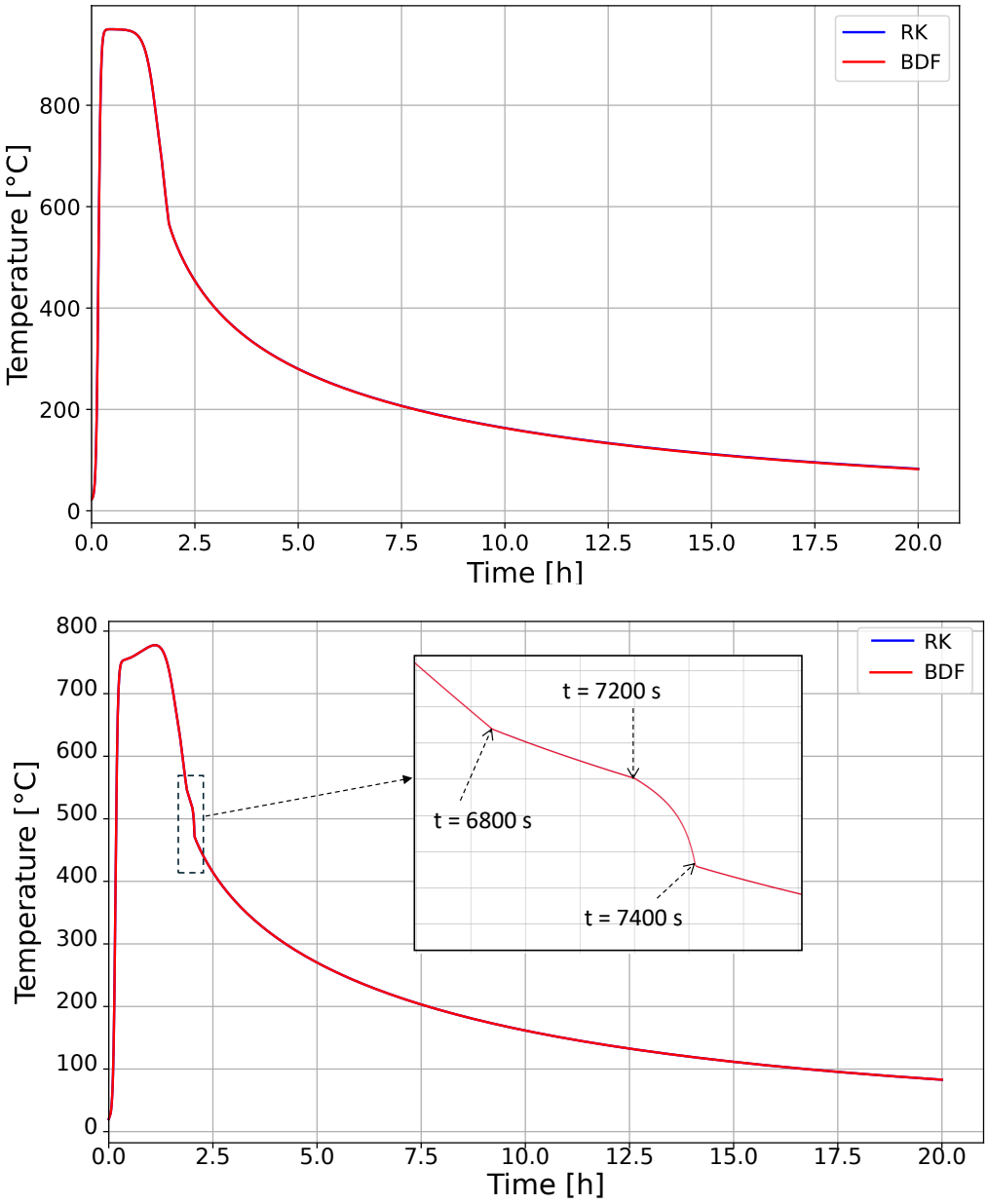

Figure 3.22: Evolution of flue gas temperature in the combustion chamber (top) and in gas segment 2 (bottom), computed using the RK and BDF schemes.

3.8.5.2 Wall temperature evolution

The second set of plots, shown in Figures 3.23 and 3.24, presents the mean temperature evolution of the refractory and casing walls located on the back side of discretized gas segment 2. As introduced earlier, this segment is immediately downstream of the combustion chamber (see second discretized volume in red in Figure 3.17). The mean temperature of a wall corresponds to the average over its internal nodes, representing the global thermal behaviour of the wall.

These figures highlight the usual thermal inertia of the stove. Both layers heat rapidly during combustion (2–2.5 hours) and cool much more slowly afterwards due to their thermal mass, maintaining mean temperatures around 50°C even after 20 hours. Since gas segment 2 is located just after the combustion zone, its walls are among the hottest in the stove; most other walls are at slightly lower mean temperatures after 20 hours. A further analysis of the figures also show that the refractory layer reaches its peak temperature first, around 2 hours, directly following the combustion phase. The casing layer reaches its maximum later, around 2.5 hours. This delay is consistent with masonry stove behaviour: the refractory layer, in direct contact with the hot flue gas, heats first and has a thermal inertia, which delays heat transfer towards the outer casing. Overall, these results are in good agreement with typical masonry stove behaviour documented in the literature, confirming that the numerical model captures the expected thermal behaviour of a masonry stove.

Finally, the temperature profiles obtained with the RK and BDF solvers are nearly identical, as observed previously in the gas temperature evolution. The RK curve closely follows the BDF curve, remaining hidden below it on the graphs.

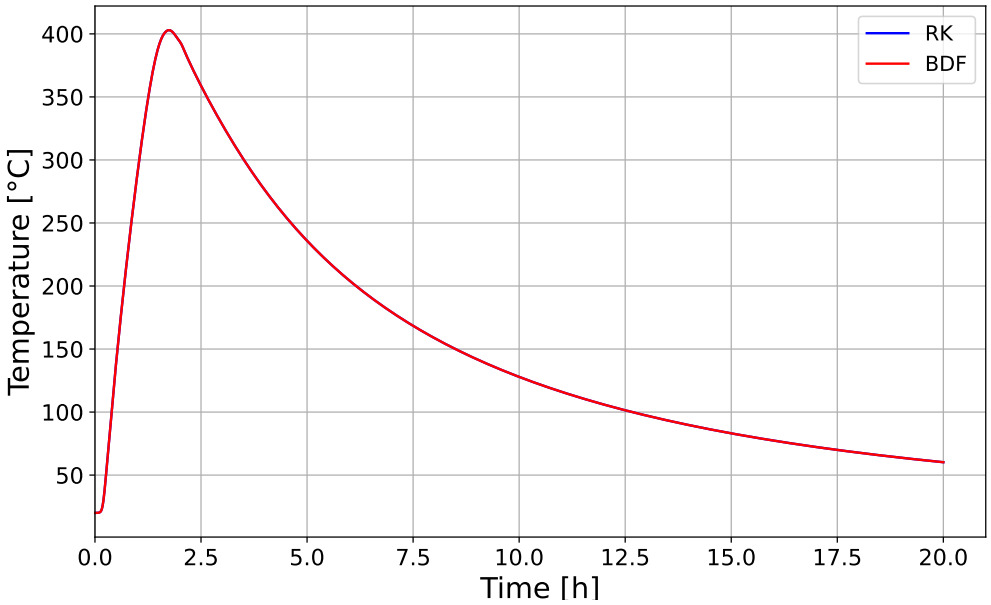

Figure 3.23: Mean temperature evolution of refractory wall of gas segment 2, computed using the RK and BDF schemes.

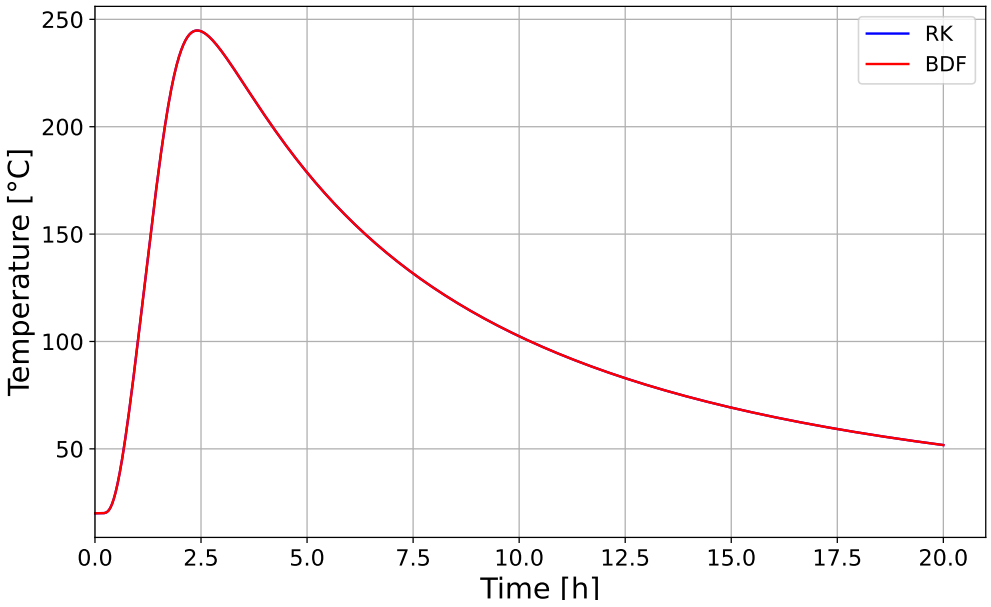

Figure 3.24: Mean temperature evolution of casing wall of gas segment 2, computed using the RK and BDF schemes.

3.8.5.3 Surface temperature evolution

The third set of plots, shown in Figure 3.25, presents the temperature evolution of the outer surfaces of the casing walls in contact with the ambient environment. The results are shown for the back wall of the discretized gas segment number 2 and for the left wall of the discretized gas segment number 16. In the *B14 V5* stove, whose configuration is taken as input, the left casing wall of segment 16 is located on the external left side of the stove. On this side, the casing walls are directly in contact on one side with the ambient and on the other with the flue gas without intermediate refractory layer, whereas the back wall of segment 2 consists of both a refractory layer and a casing layer and has its casing surface located on the external back side of the stove.

A comparison of the two temperature profiles shows that the temperature peak of segment 16 is narrower. This behavior is explained by the lower thermal inertia of this wall, which is composed of a single casing layer. In contrast, the back wall of segment 2, which includes both refractory and casing layers, shows a broader temperature peak and a delayed cooling phase.

Moreover, the surface temperatures of the segment 16 are lower than those of segment 2. This is expected since segment 2 is located immediately after the combustion chamber and is therefore exposed to hotter flue gases. On the other hand, the flue gas reaches segment 16 only after passing through several upstream segments of the accumulator, having already transferred a significant portion of its thermal energy to the surrounding walls. Once again, these results are in good agreement with typical masonry stove behaviour, and the BDF and RK time-integration schemes produce nearly identical results upon visual inspection.

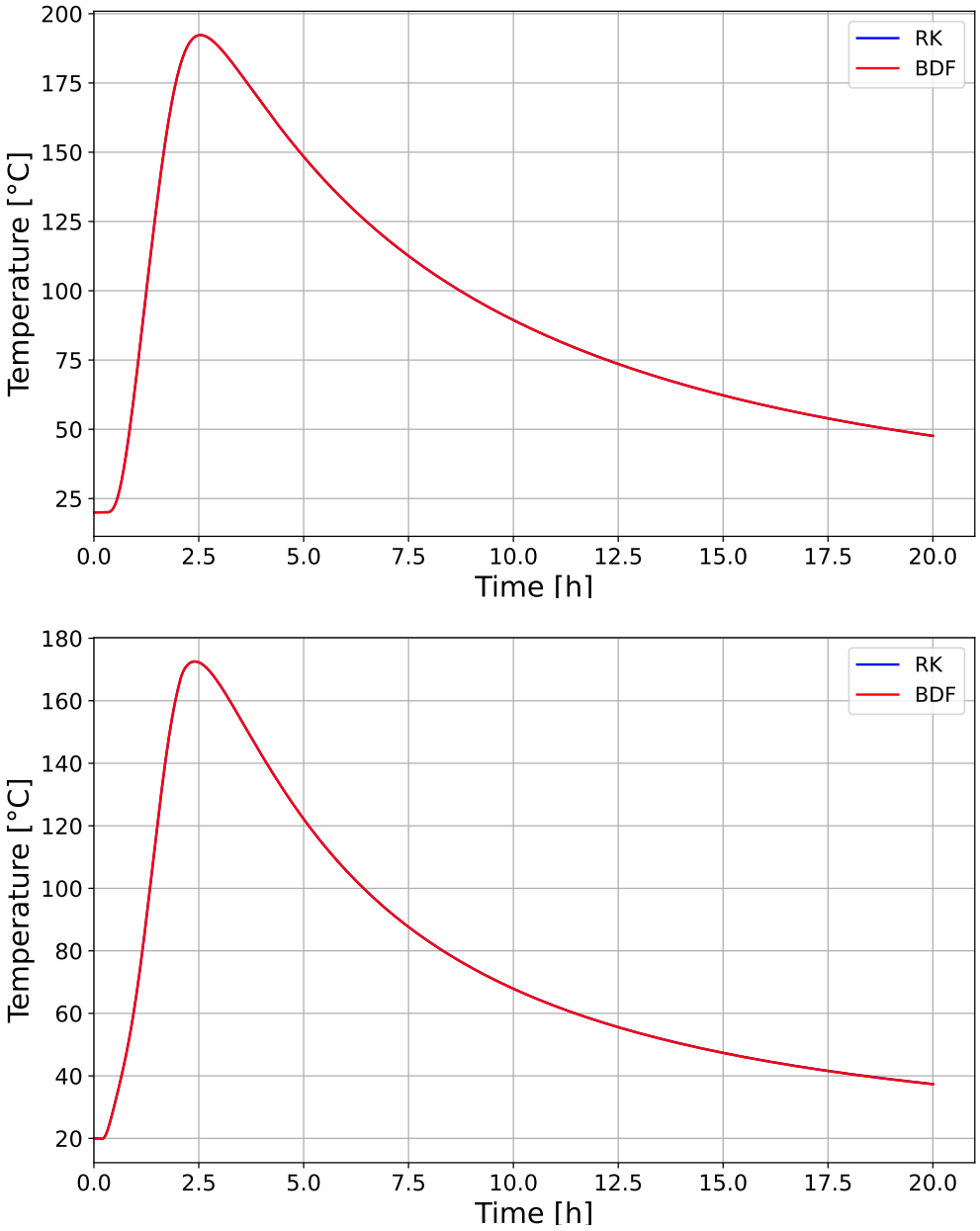

Figure 3.25: Surface temperature evolution of casing walls: back wall of gas segment 2 (top) and left wall of gas segment 16 (bottom), computed using the RK and BDF schemes.

3.8.5.4 Power and energy released

Finally, Figure 3.26 shows the instantaneous (time-resolved) power emitted to the ambient through convection and radiation, together with the cumulative fraction of the wood energy that has been released to the ambient room over time. The cumulative proportion of energy released at time t_1 is calculated as:

$$\%_{restored}(t_1) = \frac{E_{restored}(t_1)}{E_{wood}} \tag{3.90}$$

where:

- $E_{wood} = m_{wood} LHV_{wood}$ is the total energy contained in the wood that is burned,

- $E_{restored}(t_1)$ is the cumulative energy restored to the ambient up to time t_1. It is obtained by time integration of the heat power transferred to the ambient, $\dot{Q}_a$, using a trapezoidal rule over the time step Δt of the stored solution output:

$$E_{restored}(t_1) = \sum_{k=1}^{N_1} \frac{\dot{Q}_a(t_k) + \dot{Q}_a(t_{k-1})}{2} (t_k - t_{k-1}) \tag{3.91}$$

  where t_k denotes the discrete time instants returned by the numerical solver, and N_1 is the index such that $t_{N_1} = t_1$.

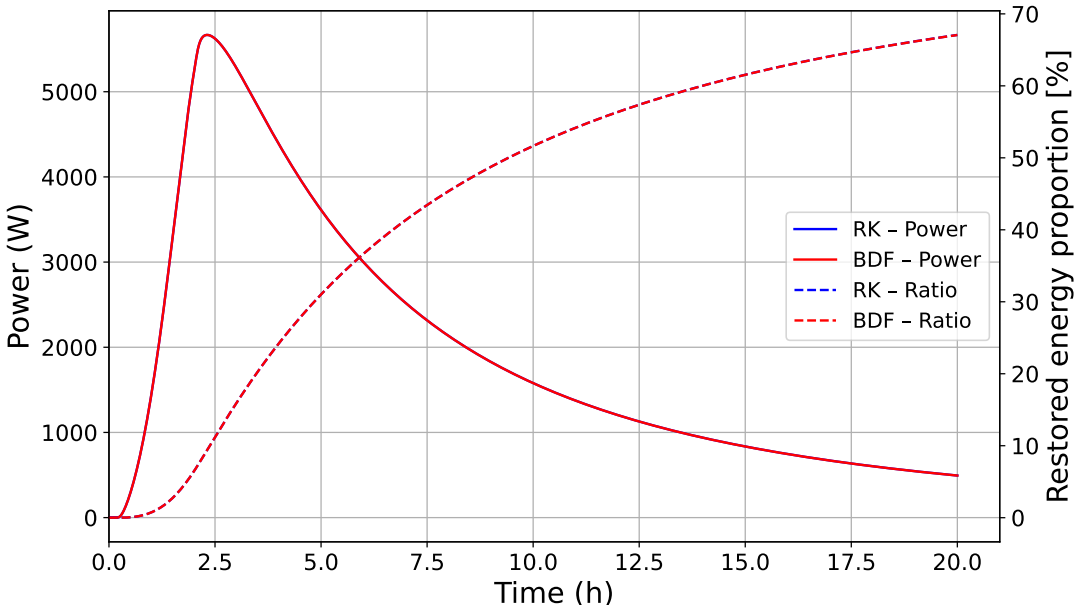

Figure 3.26: Instantaneous heat power emitted by the stove to the ambient through convection and radiation (left axis), and cumulative fraction of wood's chemical energy released to the ambient (right axis), both plotted as a function of time.

The observed curves reflect the thermal inertia of the stove, with a gradual decrease in emitted power and continued heat release long after combustion ends. After 20 hours of operation, approximately 67% of the wood's energy has been released to the ambient, and the average emitted power is about 1970 W. This value is in good agreement with the nominal power of 2000 W reported in the stove *B14 V5* data sheet (Appendix C.3). The shape of the power and energy curves shown in Figure 3.26 is also consistent with trends reported in the masonry stove literature [74]. It should be also noted that the 67% value is not the final stove efficiency, since the walls are still above room temperature after 20 hours. Over a longer time period, the efficiency would continue to increase as the stored heat is progressively released until reaching ambient temperature. For example, after 24 hours, the released energy fraction reaches approximately 70%. Overall, these results confirm that the model is able to realistically represent both the power output and the energy release dynamics of a masonry stove.

As observed for the other time evolutions, the BDF and RK time-integration schemes yield nearly identical results when compared visually.

3.9 Final numerical solver selection

After having excluded the Forward and Backward Euler solvers (see Section 3.7), the final choice lies between the Runge–Kutta (RK) and Backward Differentiation Formula (BDF) approaches. The results presented in the previous section clearly show that both RK and BDF lead to very similar temperature and power predictions. This observation is confirmed by computing the global absolute (in °C) and relative (in %) root-mean-square errors (RMSE) between the simulation results obtained using the RK and BDF time-integrations schemes. The global RMSE values are calculated over all the temperature fields defined by the discretized spatial nodes using equations (3.88) and (5.1):

$$\mathrm{RMSE}_{\mathrm{global}} = 0.14 \quad [°\mathrm{C}]$$
$$\mathrm{RMSE}_{\%,global} = 0.01 \ [\%]$$

These differences are extremely small and are mainly attributed to the gas temperature evolution in segment 3 when using the RK solver. All other temperature nodes remain nearly identical for both solvers. As discussed in Section 3.8.2, the imposed maximum time step of 1.25 s for the RK solver does not fully satisfy the stability criterion during the combustion phase for this specific segment (the venturi throat), leading to oscillations in its gas temperature evolution (see Fig. 3.27). These oscillations are rapidly attenuated in the downstream gas segments, which remain stable. In contrast, the BDF solver, being implicit, remains unconditionally stable even for this discretized segment.

Furthermore, the full 20-hour stove operation simulation presented in Section 3.8.5 required 3840 s (≈ 1 h 04 min) with the RK solver and 1279 s (≈ 21 min) with the BDF solver. The BDF approach therefore offers a significant reduction in computational cost. Consequently, the BDF solver was selected for further comparison with experimental data and for the final parametric study, aiming to represent as accurately as possible the French-type *B14 V5* masonry stove. This solver provides comparable accuracy without numerical instabilities while achieving significantly faster computation times.

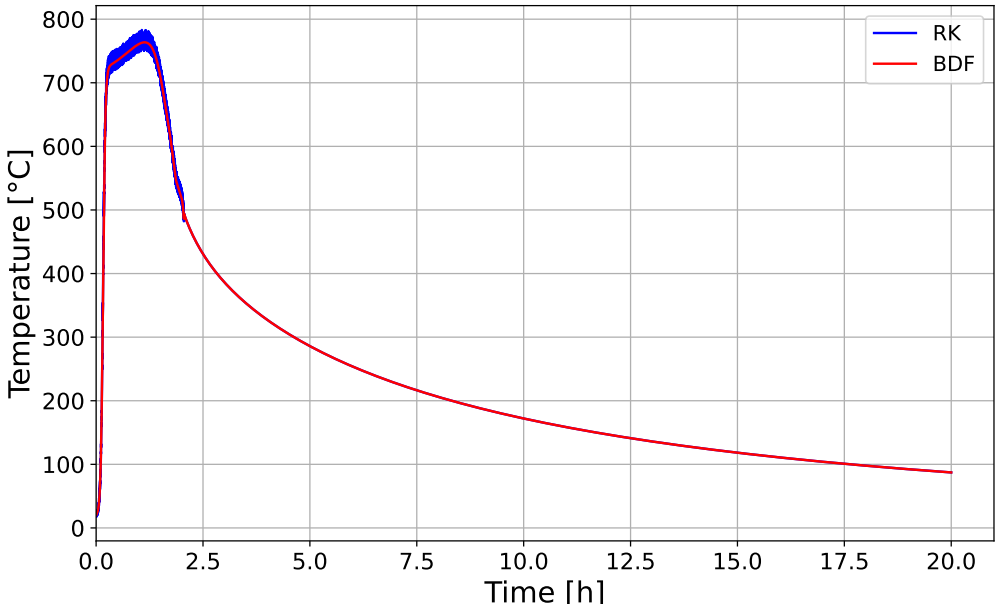

Figure 3.27: Evolution of gas temperature in the third discretized gas segment for the RK and BDF schemes.

Chapter 4

Experimental data measurement

This chapter presents the experimental investigation conducted on the studied *B14 V5 in kit Medi Batchblock* masonry stove. It first describes the experimental setup, including the context, measuring equipment and measurement procedure. The experimental results obtained during the measurement campaigns are then presented and analysed, providing a first analysis of the measurements and a reference dataset for later numerical model comparison.

4.1 Experimental setup

The experimental campaigns were carried out on the masonry stove manufactured by *UZUME*, a small French company specialized in masonry stoves and working in open-source. This company is also the stove supplier for the *Renolow* project. The tested unit was the *B14 V5* kit model (see Figure 4.1). The corresponding technical data sheet, provided by the manufacturer, is presented in Appendix C.3 and serves as a reference for preliminary verification of the experimental results.

Figure 4.1: Masonry stove used for the experimental measurements.

The stove was installed in a residential house belonging to a member of the *Renolow* project team, located in Stoumont, Belgium. Two experimental measurement campaigns were conducted. The first one took place on 27 May 2025 (starting at 08:35), corresponding to a summer and non-optimal operating condition of the stove. Indeed, under normal use, the stove is not operated during this period, as it is designed for colder months (October to April), when sufficient natural draft is ensured by the temperature difference between indoor and cold outdoor air. Therefore, to help flow circulation during the ignition, a compressor was used to supply air at the stove air inlets for the first 5 minutes during the summer campaign. This allowed the accumulator to have time to heat up to ensure a sufficient temperature gradient to initiate natural draft. This measuring campaign is named the **Summer test**. The second one was carried out on 27 November 2025, starting at 09:30, corresponding to winter conditions and therefore to an optimal operating behaviour of the masonry stove. This campaign is named the **Winter test**.

4.2 Measuring instruments

Table 4.1 shows the measuring instruments used for both experiments. Additional instruments were deployed during the winter campaign to record a denser temperature map. The instruments are briefly described below:

- ***Parkside* digital laser infrared (IR) thermometer** (Figure 4.2a): used for spot surface temperature measurements.
- ***FLIR C5* infrared (IR) camera** (Figure 4.2b): used for thermal imaging and temperature mapping of the stove surfaces at selected times.
- ***FLUKE* digital thermometer** (Figure 4.2c): used with connected probes for contact temperature measurements.
- ***TME* and *FLUKE* type-k probes**: connected to a *FLUKE* digital thermometer for continuous wall surface temperature monitoring.
- **Digital scale**: used for weighing fuel batches loaded.
- **Tape measure**: used for geometric measurements.
- ***Laserliner* wood moisture meter**: used for determining wood moisture content.

(a) Parkside infrared thermometer [75].

(b) FLIR C5 infrared camera [76].

(c) FLUKE digital thermometer with Type-K thermocouple probe [77].

Figure 4.2: Measuring instruments for experimental measurements.

	Instrument	
Measured data	**Summer test**	**Winter test**
Wood mass	Digital scale	
Stove dimensions	Tape measure	
IR pictures		*FLIR* C5
Wood moisture content	*Laserliner* wood moisture meter	
Casing wall surface temperatures	*Parkside* laser IR thermometer	
		FLUKE thermometer + *TME* contact probe
		FLUKE thermometer + *FLUKE* thermocouple probe

Table 4.1: Summary of instruments used in the summer and winter test campaigns.

Additional auxiliary equipment was also used. A compressor was employed during the summer test to assist ignition, as previously mentioned. Aluminium tape was used to fix the probes onto the stove surfaces (see Figures 4.3a and 4.3b). Aluminium tape was selected due to its high thermal conductivity, allowing it to rapidly reach the surface temperature without introducing significant thermal insulation effects.

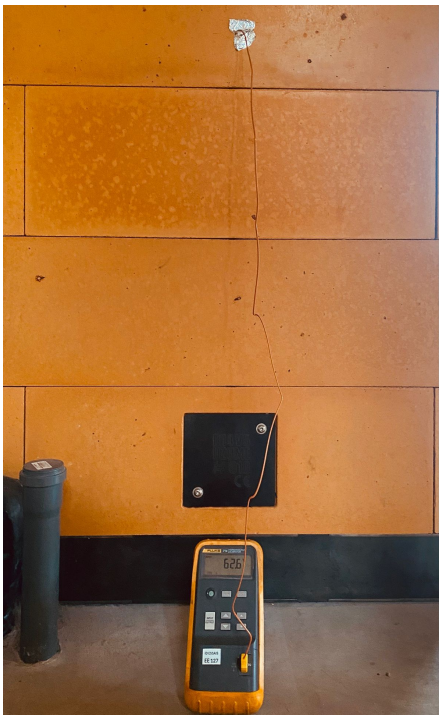

(a) Type-K thermocouple probe installation.

(b) Type-K contact probe installation.

Figure 4.3: Probe installation with aluminium tape on stove surfaces.

4.3 Pre-test data collection

Before ignition in both the summer and winter tests, a set of preliminary parameters was measured. These data, summarized in Table 4.2, include the stove's geometric dimensions, the mass and moisture content of the wood batch, and initial temperature conditions for both the internal air inside the stove's channels and the stove walls.

	Value	
Measured data	**Summer test**	**Winter test**
Masonry stove dimensions	See Table C.4 in Appendix C.2	
m_{fuel} burned	14.5 [kg]	15 [kg]
Wood moisture content (wt)	18 [%]	18 [%]
$T_{init,walls}$	293.15 [K]	311.65 [K] [6]
$T_{init,gas}$	293.15 [K]	298.15 [K] [6]
Temperature of air supplied $T_{air,su}$	288.65 [K][7]	279.15 [K] [7]

Table 4.2: Pre-test experimental data measured prior to the combustion for summer and winter test campaigns.

4.4 Measurement procedure during stove operation

After the pre-test data collection, temperature measurements were carried out over a total duration of six hours. Due to limited accessibility inside the stove and at the chimney, as well as the limited number of available instruments, only surface temperatures on the four vertical sides of the stove could be measured at selected points. These measurements were performed at fixed locations, with a sampling frequency adapted to the expected thermal dynamics:

- First 2 hours: measurements at least every 2 minutes, in order to capture the rapid casing walls temperature increase associated with combustion and flue gas flow.
- Between 2 and 4 hours: measurements at least every 5-7 minutes, as the combustion progressively ends and temperature gradients become smaller.
- Between 4 and 6 hours: measurements at least every 10 minutes, to capture the slow heat release phase, during which temperature changes are small and gradual due to the stove's high thermal inertia.

After two hours, combustion has finished, and both the air inlet and chimney dampers were closed in both experiments.

Surface temperatures were measured at fixed points on each of the front (door side), right, back and left faces of the stove. The positions of these measurement points taken during the summer and winter experiments are shown in Figures 4.4a to 4.4c. These figures show the positions of the measurements taken for the summer and winter experiments with the different devices. They also present the discretisation of the stove walls used in the

[6] In the winter test, the stove walls and the initial air inside the stove's channel were initially warmer due to residual heat from a combustion performed by the stove's owner the previous day.

[7] Air supply temperatures correspond to the average outdoor temperatures in Liège for 27 May and 27 November, respectively [78, 79].

numerical model, indicated by the red separations, so that the experimental data can later be compared with the corresponding discretized segment temperature. The measurement points differ between the two campaigns, as additional measuring devices were available during the winter campaign, allowing for a larger number of locations to be monitored.

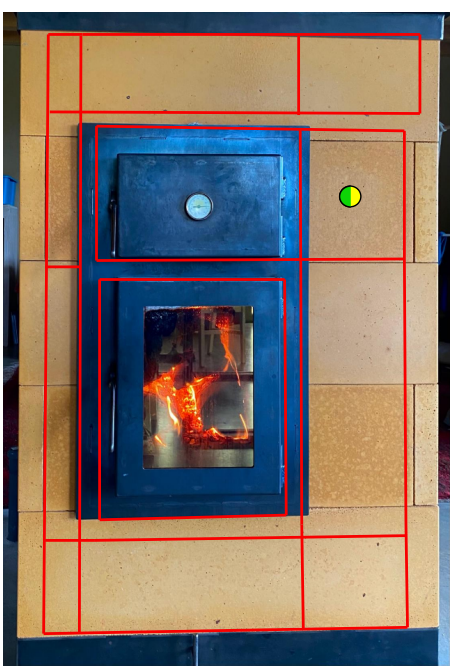

(a) Front face

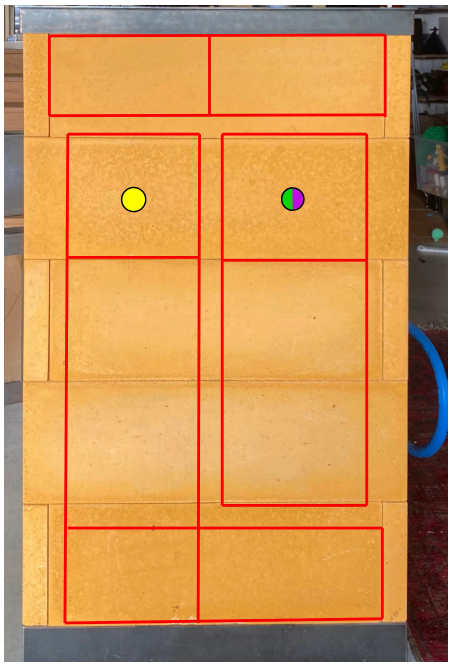

(b) Right face

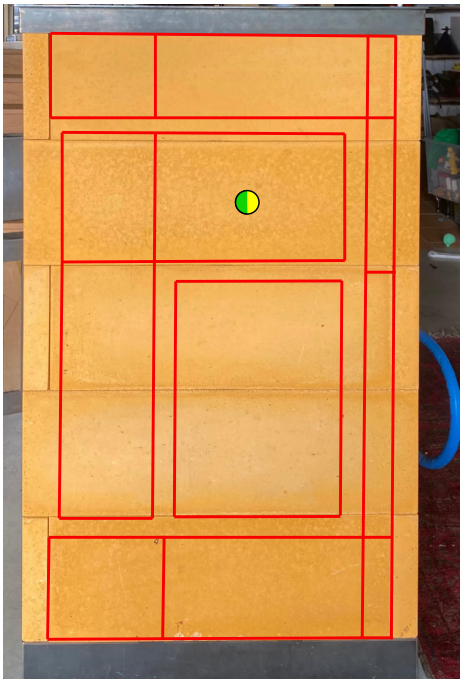

(c) Back face

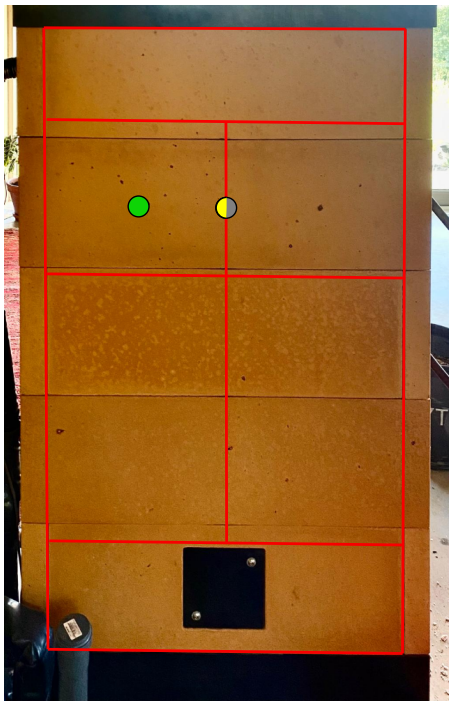

(d) Left face

Figure 4.4: Measurement points for experimental data gathering during summer and winter test campaigns.
Green: points measured during summer test with laser IR thermometer; yellow: points measured during winter test with laser IR thermometer; purple: point measured during winter test with contact probe; grey: point measured during winter test with thermocouple probe.

4.5 Experimental results

Based on the measurement procedure described above, experimental data were obtained by recording at each measurement taken over a 6 hour period, the elapsed time since ignition and the corresponding surface temperature. The resulting temperature curves for the summer and winter test campaigns are shown in Figures 4.5a to 4.5d. These plots show the experimental data obtained using the different instruments and recorded at the measurement points described in Section 4.4.

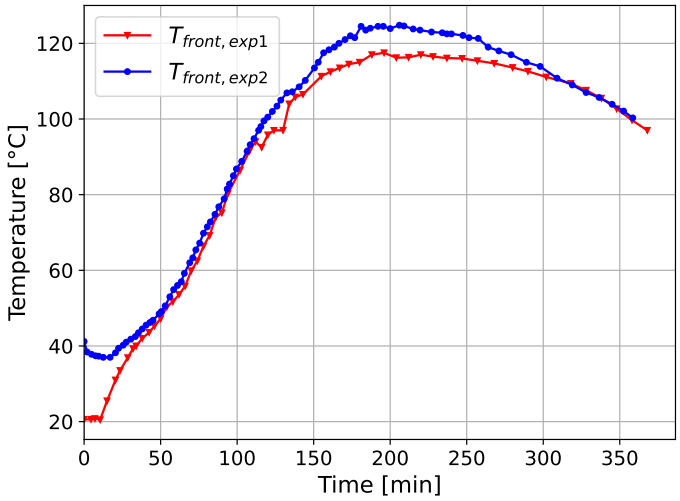

(a) Front side surface temperature evolution.

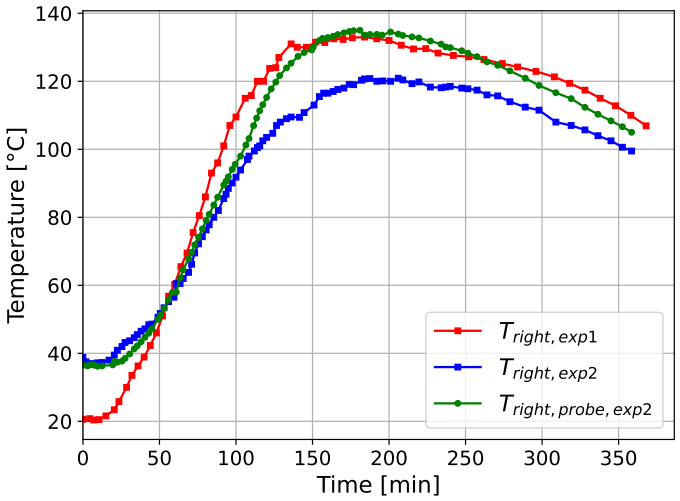

(b) Right side surface temperature evolution.

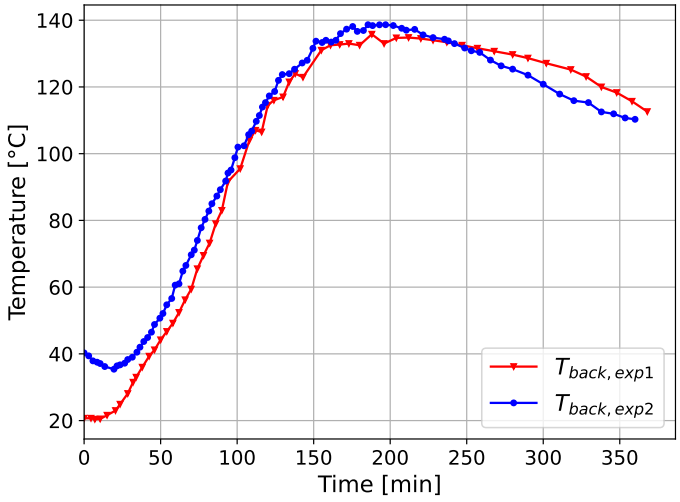

(c) Back side surface temperature evolution.

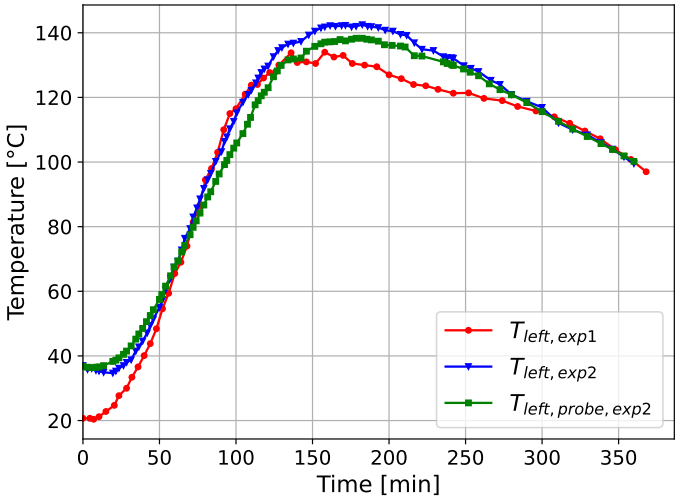

(d) Left side surface temperature evolution.

Figure 4.5: Surface temperature evolution on the four vertical sides of the masonry stove during the summer (=exp1) and winter (=exp2) test campaigns.

Infrared thermal images were also taken during the winter experiment. Figure 4.6 shows the thermal images captured at 1 hour 42 minutes after ignition. At this time, the motion of the flue gases within the stove's internal channels is clearly visible, particularly through

its direct influence on the wall surface temperatures. High-temperature L-shaped regions, highlighted in red, can be observed on the right and back faces, following the path of the accumulator channels.

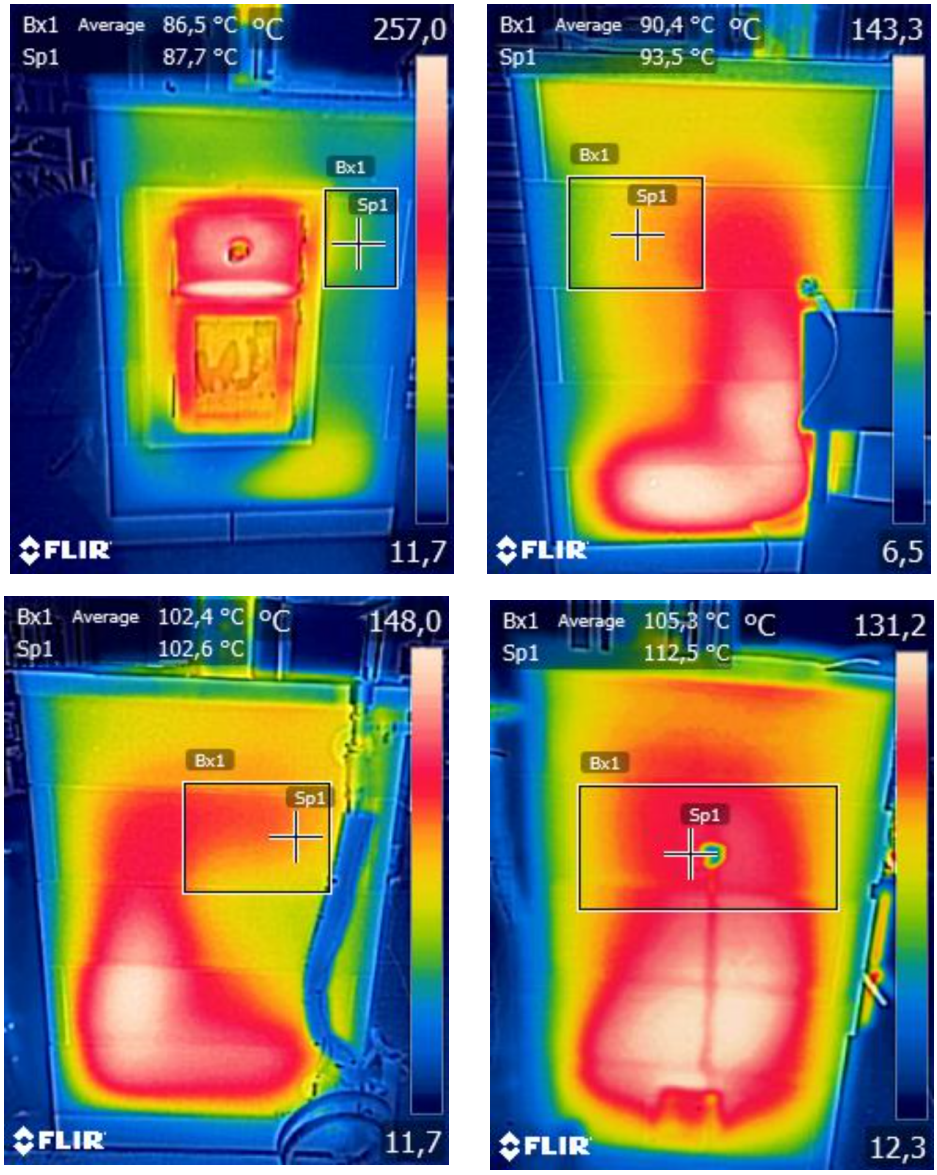

Figure 4.6: Thermal images of the stove four sides at 1 h 42 min after ignition (in the order: front, right, back and left).

Additional thermal images, recorded at 3 h 10 min and 6 h 02 min after ignition, are provided in Appendix D.1. Compared to the images at 1 h 42 min, when L-shaped high-temperature regions were clearly visible, these later images show that heat has spread more uniformly across the stove external surface walls. The previously observed L-shaped regions are replaced by broader red areas, indicating more uniform surface heating.

Each of the captured thermal image provides two temperature measures: a point temperature (*Sp1*), recorded at the center of the crosses on the figures, and an area-averaged temperature (*Bx1*), calculated over the rectangular regions shown on the figures. The

point locations were selected to match the positions of the laser infrared thermometer measurements, while the averaging areas correspond to the surface areas of the discretized wall elements used in the numerical model (see red delimitations in Figure 4.4). These specific positions were selected for easier further analysis.

The numerical model provides, for each discretized wall element of the stove's external surface, the time evolution of the temperature representing the spatially averaged value over that element. In contrast, the experimental measurements were recorded at discrete points on the stove surfaces using contact probes and an infrared thermometer. Consequently, in the next chapter, the experimental point measurements are compared to the model-predicted area-averaged temperatures. To ensure the validity of this comparison, the area-averaged temperatures obtained from the infrared thermal images were mapped to the corresponding discretized wall elements on the stove's surfaces. This mapping allows us to verify whether the point measurements, taken near the center of each discretized wall element, are representative of the average temperature over that element. Such validation, carried out below, is essential to interpret any differences between experimental and numerical results correctly.

Table 4.3 summarizes, for the three thermal image times and the four stove surfaces, the area-averaged temperature (*Bx1*), the point temperature from the thermal image (*Sp1*), and the temperature measured at the same location using the laser infrared thermometer.

Face	**Device**	**1h42min**	**3h10min**	**6h02min**
Front side temperatures [°C]	**Bx1**	86.5	123.1	96.8
	Sp1	87.7	124.1	100
	IR thermom.	87.9	124.2	100.3
Right side temperatures [°C]	**Bx1**	90.4	115.8	98.7
	Sp1	93.5	119.4	99.4
	IR thermom.	93	120	99.5
Back side temperatures [°C]	**Bx1**	102.4	131.7	99.9
	Sp1	102.6	130	97.9
	IR thermom.	102.1	129.3	95.5
Left side temperatures [°C]	**Bx1**	105.3	127	87.9
	Sp1	112.5	137.4	99.1
	IR thermom.	115.2	139	100

Table 4.3: Comparison of surface temperatures on the four stove faces at three different times during the winter test, measured with the infrared camera (mean area temperature *Bx1* and point temperature value *Sp1*) and the laser infrared thermometer.

This Table shows that, for all faces, the temperatures measured at the same point using the infrared thermometer and the infrared camera (*Sp1*) show very good agreement, val-

idating the reliability of the point temperature measurements. In addition, for the front, right and back faces, the point temperatures are close to the corresponding area-averaged temperatures (*Bx1*), confirming that these point measurements will be representative of the temperatures over the discretized wall elements in the numerical model. Consequently, if the numerical model accurately represents the masonry stove, its predicted surface temperatures should closely match the experimental point measurements.

On the left face, however, the area-averaged temperature is approximately 10 °C lower than the point measurements. This suggests the presence of a non-uniform temperature distribution across this area, likely due to its larger size compared to the area of the other discretized segments on which temperatures were measured. Consequently, the numerical model for this side is expected to predict a surface temperature closer to the area-averaged value (*Bx1*) rather than the point measurements, meaning the model's predicted surface temperature should be lower than the experimental point measurements by roughly 10 °C, at least from 1 h 40 min after ignition until the end of measurements at 6 h 02 min.

Chapter 5

Numerical model vs experimental data

This chapter combines the modelling framework developed in Chapter 3 with the experimental measurements presented in Chapter 4, in order to assess the predictive capability of the numerical model. First, the model configuration adopted for the experimental comparisons is presented. Then, a parametric study is carried out to address uncertainties in the representation of the combustion process through the flue gas temperature profile and to evaluate the sensitivity of the model to the characteristic times governing the mass flow rate evolution. Finally, the numerical predictions obtained with the selected model configuration are compared with the experimental temperature measurements.

5.1 Model configuration for comparison with experiments

The numerical model used for comparison with experimental data relies on the same masonry stove geometry, wall discretization, material properties and numerical settings as those presented in Section 3.8. These parameters are intrinsic to the **B14 V5** masonry stove used in the experiments, and are kept identical for all simulations in this chapter.

In contrast, operating conditions related to combustion and to the stove's initial thermal state vary between campaigns, and are defined based on experimental measurements. Table 5.1 summarizes these input parameters that differ between the summer and winter test campaigns. All other input parameters defined in previous sections are identical to those used developed for the *B14 V5* masonry stove in Section 3.8, which are listed in Appendix C.1 and C.2. In this table, the duration of the heat restitution phase is fixed to four hours, in order to match the 6 hour (2 hours combustion and 4 hours restitution) experimental measurement window and ensure consistent comparison of the thermal response of the masonry stove.

Input parameter	**Summer test**	**Winter test**
$T_{init,walls}$	293.15 [K]	311.65 [K]
T_{out}	288.15 [K] [9]	279.15 [K] [9]
$t_{release}$	4 [h]	4 [h]
m_{fuel}	14.5 [kg]	15 [kg]
$T_{init,gas}$	293.15 [K]	298.15 [K]
$T_{a,su}$	288.15 [K] [10]	279.15 [K] [10]

Table 5.1: Input parameters modified for experimental data comparison.

[9] Outside temperatures correspond to the average outdoor temperatures in Liège for the day of the experiment (27 May and 27 November 2025), respectively [78, 79].

[10] The air supplied to the masonry stoves is taken from the outside and is therefore set equal to the outside temperature T_{out}.

The distinction between fixed model parameters and experiment-dependent inputs allows to ensure that the simulated operating conditions remain consistent with the experimental test campaigns. The numerical model configuration defined in this section is used for all simulations presented in the next sections, unless stated otherwise.

5.2 Parametric study and model calibration

This section uses the obtained experimental results to analyse two remaining uncertainties in the numerical model. The first is the thermal power released by combustion, represented by the flue gas profile, which was set in Section 3.5.4 based on literature. The second concerns the temporal characteristics of the flue gas mass flow rate, namely the ramp-up and ramp-down durations, introduced in Section 3.6.3 which have not yet been defined.

5.2.1 Calibration of combustion intensity factor

In the numerical model developed, combustion is not resolved kinetically or spatially. Its influence is introduced exclusively through the flue gas temperature in the combustion chamber. Due to the absence of experimental measurements inside the combustion chamber and flue gas channels, the temporal evolution of the flue gas temperature is prescribed using fixed parameters derived from literature on wood combustion (see section 3.5.4). These parameters cannot be calibrated directly for the studied stove, as no in-situ combustion or flue gas temperature measurements were possible.

Although the prescribed flue gas temperature profile is based on representative literature data, real combustion conditions vary from one combustion to another and may depend on stove-specific characteristics such as combustion chamber geometry, air leakage, bypass flows, excess air, and flame structure in the combustion chamber. These factors influence the actual heat released to the flue gases, and therefore the effective thermal power available in the flue gases for heat transfer may differ from the nominal value predicted by the previously developed combustion sub-model.

To account for these possible uncertainties, a scalar combustion intensity factor, denoted λ_c, is introduced. This factor acts as a global scaling coefficient applied to the flue gas temperature profile obtained from the combustion sub-model. In practice, λ_c modifies the energy content of the combustion gases. This changes the effective thermal power transferred to the masonry without modifying the temporal shape of the temperature profile, the heat-transfer correlations, or the flow modelling. As a result, differences in the combustion due to stove combustion chamber design or real conditions are implicitly accounted for.

For a given value of λ_c, the scaled flue gas temperature profile is used as input to the thermal model, and the resulting wall temperature predictions are compared with experimental measurements. Each experimental measurement point is matched the corresponding discretized wall element temperature in the middle of which the point measurement was taken (see Figure 4.4 for the correspondence between measurement locations and model discretized elements).

To quantify the overall discrepancy between the model predictions and the experimental

measurements for a given campaign and a given value of λ_c, the global relative root-mean-square error, $\mathrm{RMSE}_{\%,global}$, is computed. This metric considers all measurement points simultaneously (IR thermometer and probe measurements shown in Figure 4.4) and normalizes the absolute error by the total experimental temperature range, providing a dimensionless percentage error that is easy to compare across different campaigns. Mathematically, the global relative RMSE is defined:

$$\mathrm{RMSE}_{\%,global} = 100, \frac{\mathrm{RMSE}}{\max_k(a_k) - \min_k(a_k)} \quad [\%], \tag{5.1}$$

where a_k denotes the experimental temperature values for all points considered in the campaign, and RMSE is the absolute RMSE over the complete set of measurements, computed using equation 3.88. The experimental data is used for normalization since, as it defines the physical reference scale, while the numerical model represents an approximation of the real system.

Using this formulation, $RMSE_{\%,global}$ represents the overall difference between the model-predicted surface temperatures and the experimental measurements for a given simulation. By computing this metric for each value of λ_c, which is performed in Figure 5.1, it is possible to systematically evaluate the effect of the combustion scaling factor on model accuracy.

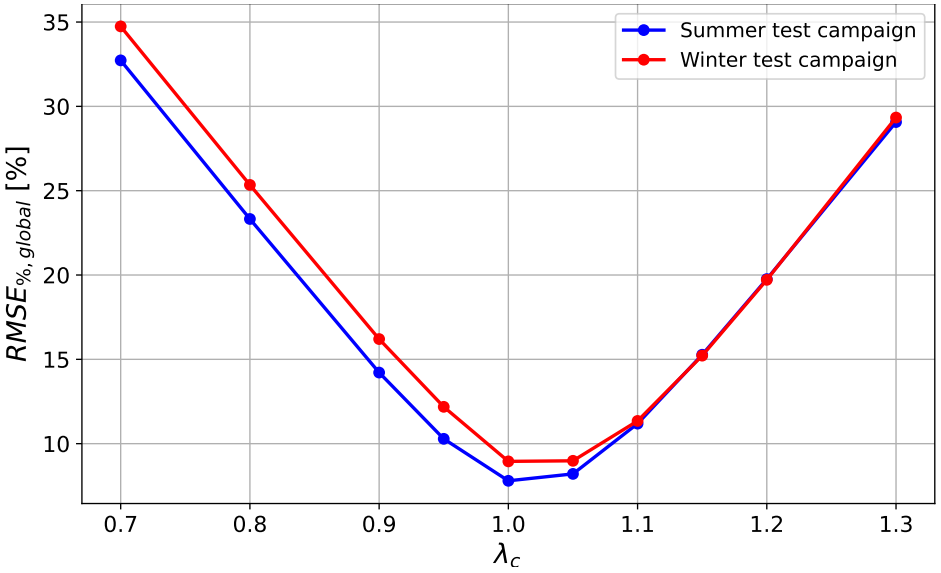

Figure 5.1: Evolution of the global relative RMSE, computed between experimental temperatures and corresponding model predictions, as a function of the combustion intensity factor, λ_c, for summer and winter test campaigns.

Both curves exhibit a clear minimum of the global error for $\lambda_c = 1$, corresponding to a global relative RMSE below 10% for both experimental campaigns ($RMSE_{\%,global}$ of 8.95% for winter campaign and of 7.80% for summer campaign). This optimal value of 1 indicates that the nominal combustion model, developed in section 3.5.4, provides an accurate estimation of the global heat release without requiring empirical correction. While based on literature, this model successfully captures the combustion behaviour at the scale relevant for thermal storage and wall temperature evolution in the studied masonry stove.

5.2.2 Sensitivity analysis of mass-flow ramp parameters

The temporal characteristics of the flue gas mass flow rate, namely the ramp-up and ramp-down durations do not represent intrinsic combustion properties, but rather act as effective transport smoothers for the flue gas mass flow rate. They account for several physical phenomena that are not explicitly resolved in the model, such as the progressive establishment of chimney draft, flow inertia, and hydraulic effects along the flue gas path.

Although stove installations are generally designed to provide an optimal draft, the actual transient behavior of the flue gas flow rate can vary from one installation to another and from one firing to the next. As a result, these ramp durations are not directly measurable and cannot be considered as fixed physical parameters. Their role is instead to control the timing at which the mass flow rate reaches its nominal value. In this way, they influence the transient heat flux exchanged between the combustion gases and the stove walls.

Because the ramp-up and ramp-down durations are not directly measurable or intrinsic material properties, their influence on the model cannot be determined by direct parameter identification. Instead, the sensitivity of the model to these parameters is investigated using the available external wall temperature measurements. For each combination of ramp parameters, the model-predicted wall temperatures are compared with the experimental data using the global relative RMSE defined in equation 5.1. The evolution of this RMSE with varying ramp-up and ramp-down durations reveals how changes in the mass flow rate timing affect the model's predictions. It quantifies the model's ability to reproduce the observed wall surface temperatures depending on the value of the ramp parameters.

For each sensitivity analysis, one parameter, either the ramp-up duration $t_{\text{ramp,up}}$ or the ramp-down duration $t_{\text{ramp,down}}$, is varied while the other is kept constant. The ranges tested are not intended to identify unique parameter values for a given firing, but to quantify the impact of plausible variations in the flue gas mass flow rate on the predicted wall temperatures.

Figures 5.2 present the evolution of the global relative RMSE as a function of the ramp-up duration. For these tests, $t_{\text{ramp,down}}$ was fixed at 600 s, while $t_{\text{ramp,up}}$ was varied between 200 s and 700 s. This acceptable range was selected based on physical considerations related to draft establishment.

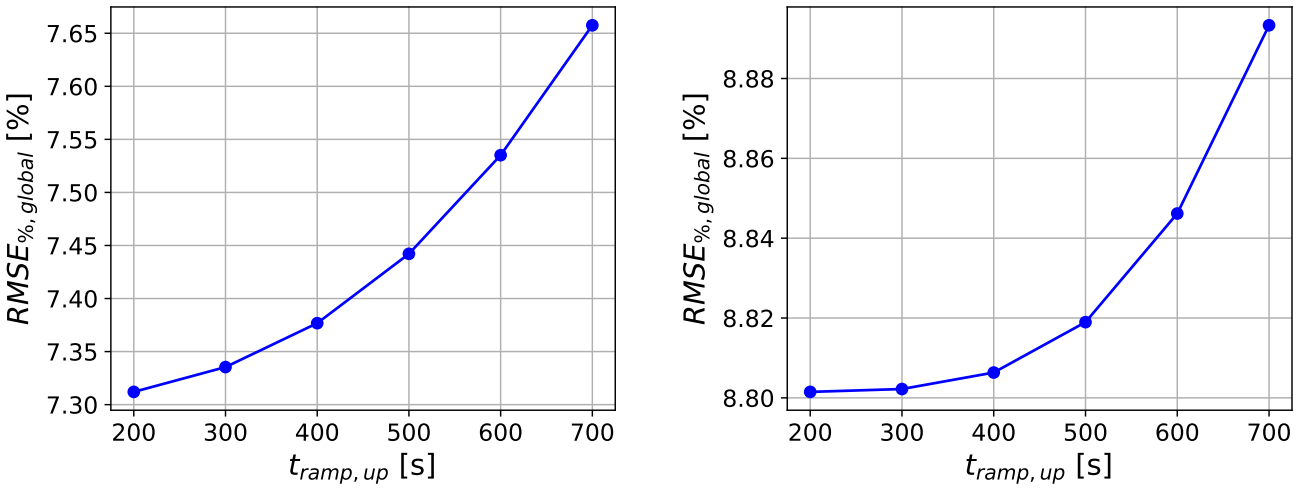

Figure 5.2: Global relative RMSE as a function of ramp up parameter, $t_{ramp,up}$, for both summer (left) and winter (right) test campaigns.

The results show that the lowest global error between the experimental measurements and the numerical model results is obtained for the smallest ramp-up duration given as input in the model. This small duration corresponds to a rapid establishment of the draft. It is also the $t_{ramp,up}$ value that best reproduces the real wall surface temperature evolution. The minimum global relative RMSE values are 7.31% for the summer test campaign and 8.80% for the winter test campaign. It is also observed that wall temperatures are only weakly sensitive to this parameter, with the error varying over a narrow range (7.31–7.66% and 8.80–8.89%). Based on these observations, a ramp-up duration of $t_{\text{ramp,up}} = 200$ s was selected for the next analyses, while knowing that this value represents an effective modelling choice rather than a physically unique parameter.

Figures 5.3 show the variation of the global relative RMSE with respect to the ramp-down duration. In this case, $t_{\text{ramp,up}}$ was fixed at 200 s, and $t_{\text{ramp,down}}$ was varied between 400 s and 800 s. This range reflects the slower decay of the flue gas flow rate after damper closure, which is influenced by residual buoyancy forces and the inertia of hot gases within the chimney.

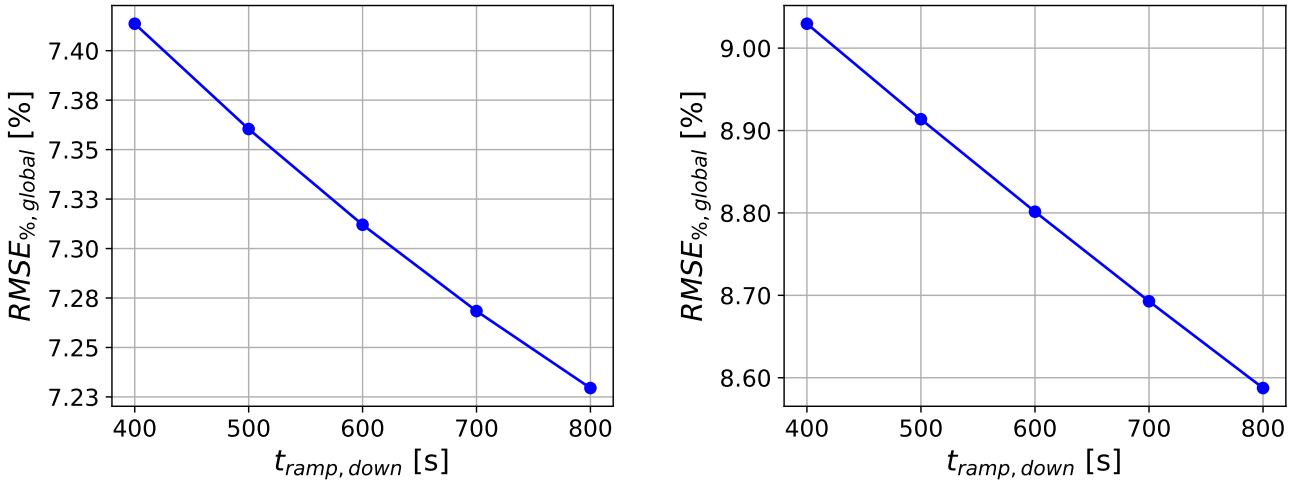

Figure 5.3: Global relative RMSE as a function of ramp-down duration, $t_{ramp,down}$, for summer (left) and winter (right) test campaigns.

For both experimental campaigns, the lowest error is obtained for the largest ramp-down duration tested, leading to the selection of $t_{\text{ramp,down}} = 800$ s for the final model configuration. As for the ramp-up duration, the influence of this parameter on the predicted wall temperatures remains limited: the relative RMSE varies only from 7.41% to 7.23% for the summer campaign and from 9.03% to 8.58% for the winter campaign.

This limited sensitivity indicates that the model predictions are robust with respect to reasonable variations of these transport-smoothing parameters, and that the associated uncertainty in these parameters has a limited effect on the predicted wall temperatures. To further verify that this conclusion also holds when both parameters are varied simultaneously, a combined sensitivity analysis was performed. This analysis confirmed the absence of any significant interaction or compensation effects between the ramp-up and ramp-down durations. The corresponding two-dimensional sensitivity maps are provided in Appendix E.1.

5.3 Final comparison with experimental data

This final section presents a quantitative comparison between the experimental point temperature measurements collected on the four vertical external walls of the stove and the simulated temperatures of the corresponding discretised nodes in the model. Each node represents the temperature averaged over its corresponding discretised area. The evaluation focuses on surface temperature accuracy using global and local error metrics to characterize the model's performance. As mentioned in Section 5.1, the numerical model is simulated over a 6 hour masonry stove operation to correspond to the experimental measurements. The purpose of the comparison is to assess whether the model reproduces the main features and magnitudes of the wall temperature evolution within experimental and modelling uncertainties.

Two error metrics are considered: the absolute root mean square error (RMSE) and the mean absolute error (MAE). The RMSE is described in equation (3.88) while the MAE is computed:

$$MAE = \frac{1}{N} \sum_{k=1}^{N} \| (a_k - b_k) \| \qquad [°C] \tag{5.2}$$

where a_k and b_k represent the experimental and simulated surface temperatures and N the number of data points. The RMSE penalizes larger deviations, while MAE provides a linear measure of typical absolute error. The relative RMSE expresses the deviation in percentage form, allowing comparison between different temperature levels.

Table 5.2 presents the error metrics for the summer campaign. Values are computed between the simulated and experimental data and are provided for each experimental measurement point on the four vertical external faces of the stove. Global metrics (in the "All faces" row) are computed by concatenating all experimental temperature measurements and their corresponding numerical predictions into a single dataset and computing the RMSE and MAE over the full set. Results for the winter campaign, including the distinction between thermometer infrared and probe measurements on the right and left faces, are provided in Appendix E.2 (Table E.1).

Considering first the full time (over the full operating period of 6 hours) results for both campaigns and faces separately in Tables 5.2 and E.1, RMSEs range approximately between 2 and 15 °C across all faces. When looking at the global value over all faces, the RMSE remains between 7.5 and 8.5 °C for both experiments (8.34 °C and 7.85 °C), corresponding to a mean absolute error of approximately 6.5 °C (and relative RMSEs of 7-8%). In addition, the similarity between the RMSE and MAE values indicates that the errors are relatively uniform over time, with no strong outliers or extreme peak deviations. This suggests that the discrepancies are systematic rather than dominated by isolated events. The results also show that, for nearly all faces and both campaigns, the model reproduces the combustion phase (0–120 min) more accurately than the restitution phase (120 min–end). During the restitution period, RMSE and MAE values are consistently increased copared to the combustion period ones, indicating reduced model accuracy once the system transitions to a heat release regime dominated by thermal diffusion within the structure.

		RMSE [°C]	MAE [°C]
Front side face	**0-120 min**	9.03	7.49
	120 min-end	6.52	5.92
	Full time	7.89	6.70
Right side face	**0-120 min**	4.41	3.63
	120 min-end	10.65	9.49
	Full time	8.11	7.20
Back side face	**0-120 min**	3.93	2.89
	120 min-end	4.73	4.14
	Full time	4.34	3.51
Left side face	**0-120 min**	8.37	6.36
	120 min-end	13.69	12.61
	Full time	11.38	9.55
All faces	**0-120 min**	6.83	5.09
	120 min-end	9.22	8.09
	Full time	8.34	6.60

Table 5.2: Error metrics for the summer test campaign.

To complement the quantitative error analysis, Figure 5.4 illustrates the temporal evolution of simulated and experimentally measured surface temperatures for the measured regions of the back and left stove faces during the winter and summer campaigns. These figures provide qualitative understanding into the time-dependent behaviour.

The largest deviations are observed for the left wall. As discussed in Section 4.5 (Table 4.3) and confirmed by IR thermal imaging, it was inferred that the experimental point measurements on the left wall would overestimate the area-averaged surface temperature of the numerical model by approximately 10 °C after the combustion period. This difference occurs because the numerical model outputs a discretised node temperature that represents the averaged temperature over a large discretised surface area for this location on the stove's external surface, whereas the experimental measurements correspond to localized points. During the restitution phase which is after combustion, the heat has had the time to diffuse into all directions within the masonry walls, leading to a more homogeneous surface temperature than that captured by point measurements. As a result, for the left wall, the simulated temperature remains systematically lower during the restitution phase despite satisfactory agreement during combustion. This behavior explains the higher error metrics observed for the left wall in both experimental campaigns.

By contrast, the back wall exhibits very good agreement throughout both experiments, with both the quantitative metrics, shown in Tables 5.2 and E.1, and the temporal evolu-

tion shown in Figure 5.4 confirming the model's ability to reproduce its thermal behaviour accurately. This is also the case for point measurements of the front and right faces, whose temperature evolutions are shown in Figure E.2 of Appendix E.2.

Nevertheless, a second and last notable deviation appears on the right side face during the winter campaign at the location of the probe measurement (see Table E.1 and Figure E.2). This discrepancy can likely be attributed to the probe placement during the experiment, which was slightly offset vertically and laterally from the center of the discretised surface area represented by the corresponding node in the numerical model. Since each node in the model represents the average temperature over its discretised area, a point measurement that does not coincide with this area's center may not accurately capture the mean temperature predicted by the simulation.

The higher errors on the left wall and the right probe during the winter campaign are partly due to experimental biases (temperature overestimation and bad probe position) that provide measurements non representative of the model outputs. Performing an analysis by excluding these measurements (so taking only IR thermometer measurement points of the front, right and back faces), the global RMSEs decreases to 6.95 °C (MAE 5.59 °C) for the summer test campaign and 3.90 °C (MAE 3.15 °C) for winter test campaign. This shows that, when the experimental data truly reflect the same physical quantity that the model predicts, the model's intrinsic accuracy is higher than suggested by the full dataset.

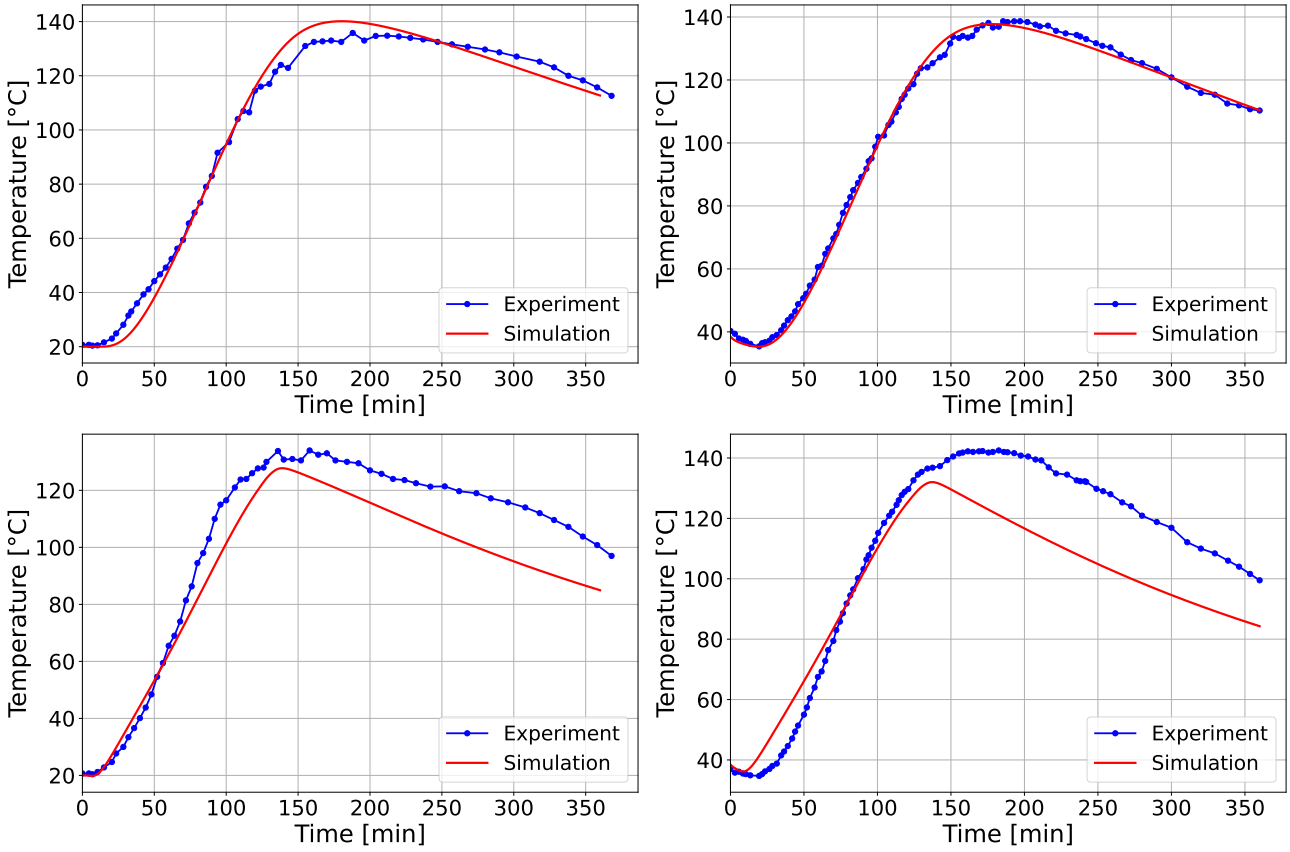

Figure 5.4: Comparison between experimental and simulated surface temperatures on the back (top) and left (bottom) side faces for winter (left) and summer (right) test campaigns.

Overall, the global RMSEs in the "All faces" row remain of similar magnitude for both test campaigns, indicating consistent model behaviour and robustness under different initial and boundary conditions. Their order of magnitude of approximately 7.5-8.5 °C may appear significant. However, these results should be interpreted in the context of experimental uncertainties, including instrument tolerances (e.g., 2–3.5 °C for the IR laser Parkside thermometer), approximations in taking measurements and variability even between multiple measurement devices measuring same points. For example, during the winter experiment at 1 h 42 min after ignition on the same point of the left wall, temperatures of 112.5 °C, 115.2 °C, and 109.9 °C were recorded using an IR camera, an IR laser thermometer, and a thermocouple probe, respectively.

In addition, considering that the measured surface temperatures range from 20°C to around 130°C, the relative RMSE corresponding to the 7.5°C-8.5°C error is approximately only of 9% (average temperature of the measurements over the 6 hour operation of around 90 °C for both test campaigns: relative $RMSE = (8/90) \times 100$). In this context, it can be inferred that, for a first-generation numerical model, the predicted wall surface temperatures reproduce the magnitude of the measurements with reasonable accuracy. Moreover, the closely match between experimental and simulated temperature trends in Figures 5.4 and E.2 indicates that the model provides a good representation of the global stove's thermal behaviour and inertia, as already shown in Section 3.8.5.

Beyond experimental uncertainty, some discrepancies can also be attributed to simplifying assumptions in the numerical model. The model assumes unidirectional (one-dimensional) heat transfer within the walls, which is reasonable during the combustion phase (0–120 min) when temperature gradients are high and heat flow is predominantly outward. However, this approximation becomes less valid during the restitution phase (120 min-end), when heat has diffused not only through the wall thickness but also along its surface, contributing to surface temperature homogenization. This simplification could be the cause of the larger deviations observed during the restitution phase. Another simplification concerns radiative conditions, where the room is idealized as having uniform walls with emissivity $\epsilon = 1$. In reality, the presence of windows and heterogeneous surfaces alters the idealized radiative heat transfer, further contributing to differences between experimental and simulated temperatures.

Several future improvements could be considered to get rid of these limitations and enhance the accuracy. These include improving the physical representation of the system by implementing multidimensional wall heat transfer (relaxing unidirectional assumption), as well as improved experimental measurements with better spatial coverage and sensor placement. Incorporating internal temperature and mass flow rate measurements within the stove would also enhance model accuracy by better representing the current uncertainty in the combustion and mass flow rate phenomena.

Chapter 6
Conclusion and perspectives

6.1 Conclusion

To respond to the challenges related to climate change and resource depletion, the European Union has defined ambitious targets for 2030 and 2050. In this context, several initiatives have been developed in Belgium, and more specifically in Wallonia, to support this transition. Among them, the RENOBATEX funding mechanism, implemented under the Wallonia Recovery Plan, aims to support housing renovation projects that promote energy efficiency and sobriety. One of the projects financed through this programme is carried by the ecological low-tech community, and more specifically by the non-profit organisation *LowTech Liège*, through the *Renolow* project. This initiative promotes renovation strategies based on low-tech principles, with a strong focus on household heating solutions by installing French-type masonry stoves manufactured by the French company *UZUME*.

Due to the lack of detailed and accessible models for this type of masonry stove, this thesis aimed to contribute to this effort by developing a detailed transient numerical model of a French-type masonry stove. The proposed model predicts the temporal evolution of temperatures throughout nearly all parts of the stove. These outputs could then be used by *LowTech Liège* for further quantifying thermal comfort and/or energy benefits provided by the stove, helping them to promote the adoption of such systems by end users.

The work first presented a state of the art on masonry stoves and thermal modelling approaches, in order to describe the main physical phenomena involved and the numerical methods commonly used to represent them. The second part detailed the physical and numerical modelling of a French-type masonry stove, separating the combustion process from the heat transfer dynamics and adopting a discretised representation of the masonry structure.

Combustion was modelled using an adiabatic combustion chamber model and a sigmoid-based flue gas temperature profile. This modelling predicts the flue gas temperature evolution in the combustion chamber, representing the heat released by the combustion. It also computes the associated nominal flow rate in the accumulator channels. On the other hand, the heat exchange processes were represented through an RC network leading to a system of coupled ODEs. To solve this resulting system, the influence of solver choice was analysed through stability and efficiency considerations, highlighting the efficiency of the implicit Backward Differentiation Formula (BDF) implemented via the `solve_ivp` function in *Python*. The final resulting numerical model predicted the temporal evolution of temperatures throughout the discretised parts of the masonry stove, as well as the

instantaneous thermal power released to the ambient.

In order to assess the validity and accuracy of the proposed modelling approach, experimental data were gathered. Experimental measurements were carried out on a *B14 V5 UZUME* French-type masonry stove, and two experimental campaigns were considered under both summer and winter operating conditions. The measurements were performed over a period of six hours in situ in a private house. Due to the limited accessibility inside the stove, measurements were limited to point measurements of external surface temperatures on the four side walls of the stove.

Each experimental point measurement was compared with the simulated temperature of the corresponding discretised node in the model. The comparison showed that the model is able to reproduce the main thermal behaviour of the stove, with simulated temperature profiles closely matching the experimental trends over the measurement period. The absolute RMSE, obtained between simulated and experimental external wall surface temperatures, was around 8 °C for both experimental campaigns, corresponding to a mean absolute error of approximately 6.5 °C. This level of accuracy is considered satisfactory for a first-generation model, given the measurement uncertainties, the external surface temperatures ranging from 20 °C to large temperatures of about 130 °C, and the modelling assumptions. The results also confirmed that the model accurately captured the combustion phase dynamics of the stove, while some higher deviations appeared for the heat restitution phase. In addition, the model-predicted trends of gas and wall temperatures were consistent with those reported in the literature, further supporting the physical relevance of the proposed model.

Beyond this direct validation, the proposed model was calibrated using available experimental data to account for uncertainties in the combustion modelling. After calibration, the model provides the best achievable representation, within the model, of the energy transferred from the combustion to the masonry walls, reproducing the evolution of the external wall surface temperatures in good agreement with experimental data. Sensitivity analyses, based on the same experimental data, confirmed that the model is robust with respect to variations in flow-related parameters.

Overall, this thesis provides a computationally efficient numerical model of a French-type masonry stove. As verified by comparing to literature and experimental data, the model reliably reproduces the transient thermal behaviour of the stove, capturing the overall shape and trends of temperature profiles throughout it. It also predicts external wall surface temperatures with reasonable quantitative accuracy by comparison with experimental data. It forms a solid foundation for further research and represents a contribution to the diffusion and analysis of low-tech heating solutions in the context of the energy transition.

6.2 Limitations

Although the model provides a solid foundation, some limitations remain, which also suggest directions for further improvement. These are mainly related to the limited availability of experimental data, particularly internal temperatures and flue gas flow measurements, which could not be gathered on the experimental masonry stove used.

This constraint limited the calibration of combustion and flow dynamics to surface temperatures only, reducing its accuracy.

In addition, measurement uncertainties and not accurate sensor positioning may have contributed to local deviations between measured and simulated surface temperatures.

Finally, the unidimensional heat transfer assumption used to model heat conduction within the walls partly explains the reduced accuracy observed during the restitution period. During the combustion phase, heat is mainly unidirectional from the flue gas to the ambient and is well captured by the model, while during the restitution phase, heat spreads in multiple directions within the walls, which is not represented by the one-dimensional model of the walls.

6.3 Future work

While these limitations constrain the current model, they also point to opportunities for future improvements. Future work could focus on improving the physical representation of the model through different improvements. Firstly, introducing multidimensional wall conduction would allow a more accurate simulation of heat diffusion in all directions within the walls and give more accurate temperature evolutions.

In addition, a detailed representation of the hydraulic circuit of the accumulator could also be developed to better capture natural draft-driven flue gas flow to represent this phenomena more accurately.

Furthermore, additional experimental validation in a dedicated laboratory environment would enable more accurate calibration of combustion and mass flow rate dynamics, thanks to fully controlled and reproducible conditions, as well as access to measurements that are difficult to implement in situ. Nevertheless, some measurements could potentially be improved even in situ, for example by adding more wall surface temperature sensors to increase spatial coverage, or by implementing additional flue gas temperature measurements within the stove channels.

Finally, in parallel, further optimisation of the *Python* implementation could reduce computation time and facilitate broader use of the model.

Appendix A
Combustion

A.1 Stoichiometric fuel-to-air-ratio computation

The fuel–to-air ratio is written as:

$$f = \frac{f_{st}}{1 + ex} \tag{A.1}$$

where f_{st} is the stoichiometric fuel–air ratio (corresponding to an excess of air of zero, $ex = 0$).

The complete and stoichiometric ($ex = 0$) combustion reaction of the generic fuel $C_xH_yO_z$ is:

$$\begin{aligned} C_xH_yO_z + \left(x + \frac{y}{4} - \frac{z}{2}\right)(O_2 + 3.76N_2) \\ \rightarrow xCO_2 + \frac{y}{2}H_2O + 3.76\left(x + \frac{y}{4} - \frac{z}{2}\right)N_2. \end{aligned}$$

From this reaction, the fuel and air masses can be obtained using molar masses, M:

$$\begin{aligned} m_{fuel} &= 1 \times M_{fuel} = (M_C \times x + M_H \times y + M_O \times z) \\ &= 12.01x + 1.008y + 16z \quad \text{[g]} \end{aligned} \tag{A.2}$$

$$\begin{aligned} m_a &= n_a M_a = n_a(0.79M_{N_2} + 0.21M_{O_2}) = n_a(0.79 \times 28.013 + 0.21 \times 31.998) \\ &= n_a(28.85) \quad \text{[g]} \end{aligned} \tag{A.3}$$

with n_a the number of moles of air per mole of fuel:

$$n_a = \left(x + \frac{y}{4} - \frac{z}{2}\right)(1 + 3.76) = \left(x + \frac{y}{4} - \frac{z}{2}\right) 4.76 \tag{A.4}$$

This leads to the stoichiometric fraction of fuel mass on air mass:

$$f_{st} = \frac{12.01x + 1.008y + 16z}{28.85\left(x + \frac{y}{4} - \frac{z}{2}\right)4.76}. \tag{A.5}$$

Appendix B

Heat transfer modelling

B.1 Correlations for Nusselt number

This appendix presents the correlations used in the numerical model to evaluate the convective heat-transfer coefficient, $h_{\text{conv,gas}}$, between the flue gas and a wall surrounding it. The coefficient is obtained from the Nusselt number, which depends primarily on the Reynolds number Re and, in some cases, on the Prandtl number Pr. The correlations adopted are primarly taken from Incropera et al. heat and mass transfer textbook [36].

Based on Re, the flow regime is classified according to standard criteria:

- Laminar flow: $Re < 2300$,
- Transitional flow: $2300 \leq Re < 5000$,
- Turbulent flow: $Re \geq 5000$.

At each time step, this Reynolds number is evaluated for each gas segment to determine the flow regime, and the corresponding correlations are then used to compute the Nusselt number Nu_D depending on it. The correlations used are correlations for thermally developing internal flow in the entry region since in it is such flows that are developing in the masonry stove's channels. The correlations used are:

- **Laminar flow with $Pr \leq 1$ and constant wall temperature**

  The correlation proposed by Baehr and Stephan is adopted:

$$Nu_D = \frac{\dfrac{Nu_{\text{fd,lam}}}{\tanh\left(2.264\, Gz_D^{-1/3} + 1.7\, Gz_D^{-2/3}\right)} + 0.0499\, Gz_D\, \tanh\left(1/Gz_D\right)}{\tanh\left(2.432\, Pr^{1/6}\, Gz_D^{-1/6}\right)}, \tag{B.1}$$

  where the Graetz number is defined as:

$$Gz_D = \frac{Re\, Pr\, D_h}{L}. \tag{B.2}$$

  The fully developed laminar Nusselt number $Nu_{\text{fd,lam}}$ depends on the cross-sectional aspect ratio and is obtained for each gas segment depending on its aspect ratio by interpolation from Table B.1 in Appendix B.2.

- **Laminar flow with $Pr > 1$**

For this case, the Kays and Hausen correlation is used:

$$Nu_D = Nu_{\text{fd,lam}} + \frac{0.0668\, Gz_D}{1 + 0.04\, Gz_D^{2/3}}. \tag{B.3}$$

- **Turbulent flow**

  The Nusselt number is based on the fully developed turbulent value $Nu_{\text{fd,turb}}$, corrected to account for thermal entry effects:

$$Nu_D = Nu_{\text{fd,turb}} \left(1 + \frac{C}{(L/D_h)^m}\right). \tag{B.4}$$

  The fully developed turbulent Nusselt number is computed using the Gnielinski correlation, valid for $0.5 \leq Pr \leq 2000$:

$$Nu_{\text{fd,turb}} = \frac{\frac{f}{8}(Re - 1000)Pr}{1 + 12.7\sqrt{f/8}(Pr^{2/3} - 1)}, \tag{B.5}$$

  where the Moody friction factor f is given by:

$$f = (0.79 \ln(Re) - 1.64)^{-2}. \tag{B.6}$$

  For straight rectangular ducts, the correction parameters are taken as $C = 0.9756$ and $m = 0.760$ [68].

- **Transitional flow**

  In the transitional regime, a linear blending between laminar and turbulent correlations is applied:

$$Nu_D = f_t\, Nu_{D,\text{turb}} + (1 - f_t)\, Nu_{D,\text{lam}}, \tag{B.7}$$

  with the blending factor:

$$f_t = \frac{Re - 2300}{2700}. \tag{B.8}$$

B.2 Nusselt numbers for laminar flow in rectangular ducts

Aspect ratio	Nusselt number
1.00	2.98
1.43	3.08
2.00	3.39
3.00	3.96
4.00	4.44
8.00	5.60
10^6	7.54

Table B.1: Nusselt numbers for fully developed laminar flow in tubes of rectangular cross sections and of dimensions $L \times l$: aspect ratio=L/l.

B.3 Wall surface resistance effect

As mentioned in Sections 3.6.6.3 and 3.6.6.4, some of the heat exchanges that should physically occur at the wall surfaces are applied directly to the first temperature node inside the wall which corresponds to the central node of the first lumped wall element. In practice, this means that the small conduction resistance between the surface and the centre of the first wall cell:

$$R_{surf} = \frac{\Delta x/2}{k\,A},$$

is ignored. This choice was mainly made to avoid carrying an additional surface node for every wall, which would complicate the system and increase the number of ODEs quite noticeably.

The first place where this occurs is for the radiative exchange between ambient and the stove's walls. Because the Stefan–Boltzmann law involves T^4, the surface resistance cannot be merged into a simple linear heat-transfer coefficient. The only way to model it exactly is to introduce an explicit surface temperature node and write a separate balance for it. That is why, to avoid this additional nodes and the associated computation cost, radiative fluxes are applied directly to the first centred node in the model used. Since radiative fluxes also appear between the facing walls inside a channel, it is the second place where the surface resistance is neglected.

To check whether this approximation is acceptable, a second version of the model was written in *Python*, this time including explicit surface nodes to be able to represent the exact physics. This version without approximation was used as the reference. It provides to each wall two additional temperature nodes, one on each side. These surface

temperatures evolve according to:

$$\frac{dT_{surf,int}}{dt} = \frac{\dot{Q}_{in} + \dot{Q}_{cond,int}}{C_{wall,surf}} \tag{B.9}$$

$$\frac{dT_{surf,ext}}{dt} = \frac{\dot{Q}_{out} + \dot{Q}_{cond,ext}}{C_{wall,surf}} \tag{B.10}$$

where:

- $\dot{Q}_{in}$ and $\dot{Q}_{out}$ are the heat exchanges entering the wall from the internal surface and leaving it from the external surface,
- $\dot{Q}_{cond,int}$ and $\dot{Q}_{cond,ext}$ the conduction heat transfer between the surface node and the first centered node in the wall:

$$\dot{Q}_{cond,int} = \frac{T_{wall,1} - T_{surf,int}}{R_{surf,wall}} \tag{B.11}$$

$$\dot{Q}_{cond,ext} = \frac{T_{wall,n_{nodes}} - T_{surf,ext}}{R_{surf,wall}} \tag{B.12}$$

  with $T_{wall,1}$ and $T_{wall,n_{nodes}}$ the first and last entered wall nodes,

- $C_{wall,surf}$ is the thermal heat capacity of each surface node. It is chosen as a fraction of the capacity of an internal wall cell (here 10%): $C_{wall,surf} = 0.1\, C_{inter,node}$

Once these surface temperatures are updated, the effect on the internal nodes follows simply by applying the opposite conductive fluxes:

$$\frac{dT_{wall,1}}{dt} = \frac{-\dot{Q}_{cond,int}}{C_{inter,node}} \tag{B.13}$$

$$\frac{dT_{wall,n_{nodes}}}{dt} = \frac{-\dot{Q}_{cond,ext}}{C_{inter,node}} \tag{B.14}$$

To validate the assumption of neglecting the surface resistance, this extended version and the simplified version, described in the report in section 3.6.6, were run under identical conditions (10-hour cycle: 2 hours combustion, 8 hours release), using the same BDF solver and the same physical inputs. Their results were compared using both the $RMSE$ and the relative $RMSE$:

$$\mathrm{RMSE} = \sqrt{\frac{1}{N}\sum_{k=1}^{N}(a_k - b_k)^2} \quad [^\circ\mathrm{C}] \tag{B.15}$$

$$\mathrm{RMSE}_{\%} = 100\,\frac{\mathrm{RMSE}}{\max\limits_{k}(a_k) - \min\limits_{k}(a_k)} \quad [\%] \tag{B.16}$$

where a_k denotes the time series of a given temperature type (e.g. all refractory nodes) for the simplified model and b_k the corresponding series for the reference model including surface nodes. The statistics are computed over the full simulation time and over all nodes of a given type.

Table B.2 reports the resulting errors for refractory wall nodes, casing wall nodes, casing external surface nodes, and gas segment nodes. The relative errors remain below about 1.1 % and below 0.43 % for external surface temperatures, which are the most relevant quantities for further comfort analysis. Relative errors for refractory walls and gas segments remain around 1% even with absolute RMSE of around 10 °C since the flue gas can go until temperatures of 1000°C and the refractory walls are the walls directly in contact with these gases therefore reaching also very high values. Furthermore, the computation time was 18 min 55 s for the resolution for the simplified model whereas it increased by about 56% (to approximately 29 min 30 s) when including the additional surface nodes. In other words, although including surface nodes gives a slightly more detailed representation, the influence on the overall thermal evolution is minor while the computational time doubles. Neglecting the surface resistance in the main model is therefore justified.

Type of temperature node	**RMSE [°C]**	**Relative RMSE [%]**
Refractory wall nodes	9.14	1.03
Casing wall nodes	2.99	0.54
Surface casing wall nodes in contact with ambient [11]	2.08	0.43
Gas segment nodes	12.6	1.11

Table B.2: *RMSE* between the simplified model (neglecting surface resistances in some radiative exchanges) and the reference model including explicit surface nodes, over a 10 h cycle.

B.4 Linearisation of radiative heat transfers

In order to apply the Backward Euler scheme in matrix form, all heat-transfer terms must be expressed as functions that are linear in the temperatures over a given time step. This makes it possible to decompose the non-linear flux vector $\mathbf{F}(\mathbf{T}, t)$ into a global conductance matrix $\mathbf{K}$ and a source vector $\mathbf{f}$. Most contributions (conduction, convection and gas–wall exchange) are already linear or only weakly non-linear in temperature and can be inserted directly into the global conductance matrix. However, radiative heat transfer is strongly non-linear due to the T^4 dependence of Stefan-Boltzmann's law. Therefore, the radiative exchange between walls and ambient air, as well as radiation between facing walls inside a channel, must be linearised to obtain a linear expression in temperature of the form:

$$\dot{Q}_{\text{rad}} = \varepsilon\sigma A \left(T_j^4 - T_i^4\right) \;\approx\; G_{\text{rad}} \left(T_j - T_i\right), \tag{B.17}$$

where G_{rad} [W/K] is the conductance.

For the radiation of both next heat transfers, the linearization is performed using a first-order Taylor expansion around an intermediate temperature. It consists of computing the first derivative of the linearized temperature ($= 4\epsilon\sigma T^3$) and then evaluate it at an intermediate temperature giving a good approximation of the slope between the two

[11] For the simplified model, the surface temperature is obtained by linear extrapolation from the two outermost casing nodes, see Eq. (3.52).

temperatures. This intermediate temperature is, based on notations in equation (B.17):

$$\overline{T} = \frac{T_j + T_i}{2} \tag{B.18}$$

This would finally give the conductance:

$$G_{rad} = 4\epsilon\sigma A\overline{T}^3 \tag{B.19}$$

Wall-ambient radiation

Applying this for the radiation between a wall surface and the ambient air in the numerical model, the radiation heat power based on the temperature of the wall at next time step, T^{n+1}, leads to:

$$\dot{Q}_{rad} = \epsilon\sigma A\left((T^{n+1}_{wall})^4 - T^4_{amb}\right) \tag{B.20}$$

$$\approx G_{rad}(T^{n+1}_{wall} - T_{amb}) \tag{B.21}$$

with:

- $G_{rad} = 4\epsilon\sigma A\overline{T}^3$
- $\overline{T} = \frac{T^n_{wall}+T_{amb}}{2}$ and T^n_{wall} the temperature evaluated at the current time.

Radiation between internal wall surfaces

In the model, the radiative exchange between two walls j and k inside the same gas segment is computed from the standard radiosity relation:

$$\dot{Q}_{jk} = \frac{\sigma\left(T_j^4 - T_k^4\right)}{\dfrac{1-\epsilon_k}{\epsilon_k A_k} + \dfrac{1}{F_{jk}A_j} + \dfrac{1-\epsilon_j}{\epsilon_j A_j}}, \tag{B.22}$$

where $\dot{Q}_{jk}$ is the net radiative heat flow rate from surface j to surface k, ε_j and ε_k are the surface emissivities, and F_{jk} is the view factor.

Applying the same linearisation as before, this gives:

$$G_{rad} = \frac{4\epsilon\sigma\overline{T}^3}{\dfrac{1-\epsilon_k}{\epsilon_k A_k} + \dfrac{1}{F_{jk}A_j} + \dfrac{1-\epsilon_j}{\epsilon_j A_j}} \tag{B.23}$$

with $\overline{T} = \frac{T^n_j+T_k}{2}$ and T^n_j and T^n_k are the temperatures at the current time.

This linearisation yields a symmetric radiative coupling between wall surfaces that can be directly included in the conductance matrix $\mathbf{K}$ of the implicit solver. As a result, all radiative contributions enter the global system in the same way as conductive and convective terms, enabling a consistent fully implicit Backward Euler integration of the coupled thermal network.

Appendix C

B14 V5 masonry stove data

C.1 Inputs for *B14 V5* masonry stove simulation

Input	**Value**	**Source/Justification**
Dimensions ($L \times H \times w$) of the discretized gas and wall segments	See Appendix C.2	Measured on the stove on which experimental data were taken
Matrix of wall compositions for each segment	See Appendix C.2	Built based on the stove configuration on which experimental data were taken
Array of shared walls	See Appendix C.2	Built based on the stove configuration on which experimental data were taken
Array of flue gas direction in gas segments	See Appendix C.2	Built based on the stove configuration on which experimental data were taken
Array of divided gas segments	See Appendix C.2	Built based on the stove configuration on which experimental data were taken
e_{rfr} e_{cng}	0.05 [m] 0.0425 [m]	Measured on the stove on which experimental data were taken
ρ_{rfr} k_{rfr} $c_{p,rfr}$	2200 [kg/m^3] 1.35 [W/mK] 980 [J/kgK]	Values obtained from Damien Lehmann, laboratory technician of the AFPMA[12]
ρ_{cng} k_{cng} $c_{p,cng}$	2000 [kg/m^3] 1.3 [W/mK] 960 [J/kgK]	Values for CEB casing and also confirmed by several scientific sources: [80, 81, 82]
$T_{init,walls}$	293.15 [K]	Default valueimposed by the numerical model
n_{nodes}	3	Default value imposed by the numerical model (see section 3.8.3)

Table C.1: Input values for the setup part of the model for the simulation of the *B14 V5 in-kit Medi Batchblock* (corresponding to the generic inputs listed in section 3.4.2).

[12]Damien Lehmann gave access to technical sheets of refractory bricks commonly used for masonry stoves. Notably, technical sheets from the company PRSE, a French company specialized in refractory bricks.

Input	**Value**	**Source/Justification**
ex	1.1 [-]	Optimal value of excess of air for wood combustion [55]
wt	0.18 [-]	Wood moisture content measured on the burned wood.
LHV_{fuel}	15×10^6 [J/kg]	It is a good approximation for dry hardwoods (such as ash or oak) in logs with 20% moisture content (seasoned hardwood) [83, 84, 85].
m_{fuel}	14 [kg]	Corresponds to the mass of wood recommended by *UZUME* for 1 combustion in the day (see data sheet of Appendix C.3)
$c_{p,fuel}$	1.7×10^3 [J/kgK]	Representative specific value of wood based on scientific literature: [87, 88, 89]
t_{comb}	7200 [s]	Time given by *UZUME* for combustion of 14 kg of wood on the *Medi Batchblock* data sheet [86]
$T_{gas,init}$	293.15 [K]	Default value imposed by the numerical model
T_{ref}	293.15 [K]	Default valueimposed by the numerical model
$T_{a,su}$	283.15 [K]	Equal to outside temperature (see Table C.3)
$T_{fuel,su}$	293.15 [K]	Default value imposed by the numerical model

Table C.2: Input values for the combustion simulation in the *B14 V5 in kit Medi Batchblock* masonry stove (corresponding to the generic inputs listed in Table 3.2).

Parameter	**Value**	**Source/justification**
ϵ_{walls}	0.9 [-]	Value obtained from Damien Lehmann, laboratory technician of the AFPMA[12]
ϵ_{gas}	0.2 [-]	Default value imposed by the numerical model (see section 3.6.2)
T_{out}	283.15 [K]	Default value imposed by the numerical model (see section 3.6.2)
$t_{release}$	18 [h]	User choice

Table C.3: Input values for thermal storage and heat-release simulations of the *B14 V5 in-kit Medi Batchblock* masonry stove (corresponding to the generic inputs listed in Table 3.4).

C.2 Detailed geometry inputs

This appendix provides the geometric and discretized segment configuration inputs that must be given to the numerical model to model the experimental *B14 V5 in kit Medi Batchblock* masonry stove. It gives all the necessary inputs that were defined in section 3.4.2:

- Arrays with dimensions in [m] of each discretized gas segment ($M = 18$ segments) and wall sub-elements ($N = 23$ segments because 5 gas segments divided in 2 wall sub-elements (see array C.10)). These dimensions have been obtained by discretizing the flue gas path based on measurements taken on the experimental masonry stove (see Table C.4):

$$\begin{aligned} L_{gas} = [&0.280 \quad 0.280 \quad 0.040 \quad 0.260 \quad 0.260 \quad 0.280 \quad 0.280 \quad 0.250 \\ &0.250 \quad 0.325 \quad 0.335 \quad 0.660 \quad 0.660 \quad 0.660 \quad 0.660 \quad 0.660 \\ &0.660 \quad 0.660] \end{aligned} \tag{C.1}$$

$$\begin{aligned} H_{gas} = [&0.400 \quad 0.400 \quad 0.300 \quad 0.450 \quad 0.230 \quad 0.230 \quad 0.230 \quad 0.230 \\ &0.500 \quad 0.240 \quad 0.240 \quad 0.240 \quad 0.265 \quad 0.450 \quad 0.280 \quad 0.195 \\ &0.170 \quad 0.170] \end{aligned} \tag{C.2}$$

$$\begin{aligned} w_{gas} = [&0.280 \quad 0.280 \quad 0.040 \quad 0.200 \quad 0.200 \quad 0.330 \quad 0.330 \quad 0.200 \\ &0.200 \quad 0.275 \quad 0.275 \quad 0.355 \quad 0.130 \quad 0.130 \quad 0.130 \quad 0.130 \\ &0.380 \quad 0.250] \end{aligned} \tag{C.3}$$

$$\begin{aligned} L_{walls} = [&0.280 \quad 0.280 \quad 0.040 \quad 0.260 \quad 0.260 \quad 0.280 \quad 0.280 \quad 0.250 \\ &0.250 \quad 0.325 \quad 0.335 \quad 0.330 \quad 0.330 \quad 0.660 \quad 0.330 \quad 0.330 \\ &0.330 \quad 0.330 \quad 0.660 \quad 0.330 \quad 0.330 \quad 0.335 \quad 0.325] \end{aligned} \tag{C.4}$$

$$\begin{aligned} H_{walls} = [&0.400 \quad 0.400 \quad 0.300 \quad 0.450 \quad 0.230 \quad 0.230 \quad 0.230 \quad 0.230 \\ &0.500 \quad 0.240 \quad 0.240 \quad 0.240 \quad 0.240 \quad 0.265 \quad 0.450 \quad 0.450 \\ &0.280 \quad 0.280 \quad 0.195 \quad 0.170 \quad 0.170 \quad 0.170 \quad 0.170] \end{aligned} \tag{C.5}$$

$$\begin{aligned} w_{walls} = [&0.280 \quad 0.280 \quad 0.040 \quad 0.200 \quad 0.200 \quad 0.330 \quad 0.330 \quad 0.200 \\ &0.200 \quad 0.275 \quad 0.275 \quad 0.355 \quad 0.355 \quad 0.130 \quad 0.130 \quad 0.130 \\ &0.130 \quad 0.130 \quad 0.130 \quad 0.380 \quad 0.380 \quad 0.250 \quad 0.250] \end{aligned} \tag{C.6}$$

- Boolean matrices representing the presence or not of a refractory or casing layer on each side of each discretized wall sub-element (based on the notation explained for matrix 3.1):

$$\text{rfr}_{\text{walls}} = \begin{bmatrix} 1 & 1 & 1 & 1 & 0 & 1 \\ 1 & 1 & 1 & 1 & 1 & 0 \\ 0 & 1 & 0 & 1 & 1 & 1 \\ 1 & 0 & 1 & 1 & 1 & 1 \\ 0 & 1 & 1 & 0 & 1 & 1 \\ 1 & 1 & 0 & 1 & 1 & 0 \\ 1 & 1 & 0 & 1 & 0 & 1 \\ 0 & 1 & 1 & 0 & 1 & 1 \\ 1 & 0 & 1 & 0 & 1 & 1 \\ 0 & 1 & 0 & 1 & 0 & 0 \\ 0 & 1 & 0 & 1 & 0 & 0 \\ 0 & 1 & 0 & 1 & 0 & 0 \\ 0 & 1 & 0 & 1 & 0 & 0 \\ 0 & 0 & 0 & 1 & 0 & 0 \\ 0 & 0 & 1 & 0 & 0 & 0 \\ 0 & 0 & 1 & 0 & 0 & 0 \\ 0 & 0 & 1 & 0 & 0 & 0 \\ 0 & 0 & 1 & 0 & 0 & 0 \\ 0 & 0 & 0 & 0 & 0 & 0 \\ 0 & 0 & 0 & 1 & 0 & 0 \\ 0 & 0 & 0 & 1 & 0 & 0 \\ 0 & 0 & 0 & 1 & 0 & 0 \\ 0 & 0 & 0 & 1 & 0 & 0 \end{bmatrix} \qquad \text{cng}_{\text{walls}} = \begin{bmatrix} 0 & 0 & 0 & 0 & 0 & 1 \\ 0 & 0 & 0 & 0 & 1 & 0 \\ 0 & 0 & 0 & 0 & 0 & 0 \\ 0 & 0 & 1 & 0 & 1 & 0 \\ 0 & 0 & 1 & 0 & 1 & 0 \\ 0 & 0 & 0 & 0 & 1 & 0 \\ 0 & 0 & 0 & 0 & 0 & 1 \\ 0 & 0 & 1 & 0 & 0 & 1 \\ 0 & 0 & 1 & 0 & 0 & 1 \\ 0 & 0 & 1 & 0 & 0 & 1 \\ 0 & 0 & 1 & 0 & 1 & 0 \\ 0 & 0 & 0 & 0 & 1 & 0 \\ 0 & 0 & 0 & 0 & 0 & 1 \\ 1 & 0 & 0 & 0 & 1 & 1 \\ 1 & 0 & 0 & 0 & 1 & 0 \\ 1 & 0 & 0 & 0 & 0 & 1 \\ 1 & 0 & 0 & 0 & 1 & 0 \\ 1 & 0 & 0 & 0 & 0 & 1 \\ 1 & 1 & 0 & 0 & 1 & 1 \\ 0 & 1 & 0 & 0 & 1 & 0 \\ 0 & 1 & 0 & 0 & 0 & 1 \\ 0 & 1 & 1 & 0 & 0 & 1 \\ 0 & 1 & 1 & 0 & 1 & 0 \end{bmatrix} \tag{C.7}$$

- Array of shared walls (based on the notation explained for matrix 3.2):

$$\text{shared}_{\text{rfr}} = \begin{bmatrix} (0, \text{'LEFT'}) & (15, \text{'RIGHT'}) \\ (0, \text{'RIGHT'}) & (8, \text{'LEFT'}) \\ (0, \text{'TOP'}) & (6, \text{'BOTTOM'}) \\ (0, \text{'BOTTOM'}) & (12, \text{'TOP'}) \\ (1, \text{'LEFT'}) & (14, \text{'RIGHT'}) \\ (1, \text{'RIGHT'}) & (3, \text{'LEFT'}) \\ (1, \text{'RIGHT'}) & (2, \text{'TOP'}) \\ (1, \text{'RIGHT'}) & (2, \text{'FRONT'}) \\ (1, \text{'RIGHT'}) & (2, \text{'BACK'}) \\ (1, \text{'TOP'}) & (5, \text{'BOTTOM'}) \\ (1, \text{'BOTTOM'}) & (11, \text{'TOP'}) \\ (3, \text{'FRONT'}) & (8, \text{'BACK'}) \\ (3, \text{'BOTTOM'}) & (10, \text{'TOP'}) \\ (4, \text{'FRONT'}) & (7, \text{'BACK'}) \\ (4, \text{'TOP'}) & (22, \text{'BOTTOM'}) \\ (5, \text{'LEFT'}) & (16, \text{'RIGHT'}) \\ (5, \text{'TOP'}) & (19, \text{'BOTTOM'}) \\ (6, \text{'LEFT'}) & (17, \text{'RIGHT'}) \\ (6, \text{'TOP'}) & (20, \text{'BOTTOM'}) \\ (7, \text{'TOP'}) & (21, \text{'BOTTOM'}) \end{bmatrix} \qquad \text{shared}_{\text{cng}} = [\,] \tag{C.8}$$

- Array of the directions of the flue gas in the 18 discretized gas segments:

$$H_{gas} = [front \quad front \quad right \quad up \quad up \quad back \quad back \quad down \quad down \\ left \quad left \quad left \quad top \quad top \quad top \quad top \quad right \quad right] \tag{C.9}$$

- Array of discretized gas segments divided into two wall sub-elements:

$$\mathrm{div}_{gas,seg} = \begin{bmatrix} 11 : [11, 12] \\ 13 : [14, 15] \\ 14 : [16, 17] \\ 16 : [19, 20] \\ 17 : [21, 22] \end{bmatrix} \tag{C.10}$$

Part of stove measured	**Dimensions (L x w x H) [cm]**
External dimensions	84.5 x 75 x 133.5
Combustion chamber	56 x 28 x 40
Venturi section	5 x 5 x 30
Upward tube	26 x 20 x 68
Oven dimensions (above combustion chamber)	56 x 33 x 23
Downward tube	25 x 20 x 73
Ground segment (under the combustion chamber)	66 x 63 x 24
Lateral segment (left of combustion chamber)	66 x 13 x 119
Top segment (above oven)	66 x 63 x 17

Table C.4: Dimensions of the *B14 V5 Medi Batchblock* masonry stove (used for the simulation).

C.3 *B14 V5* masonry stove datasheet

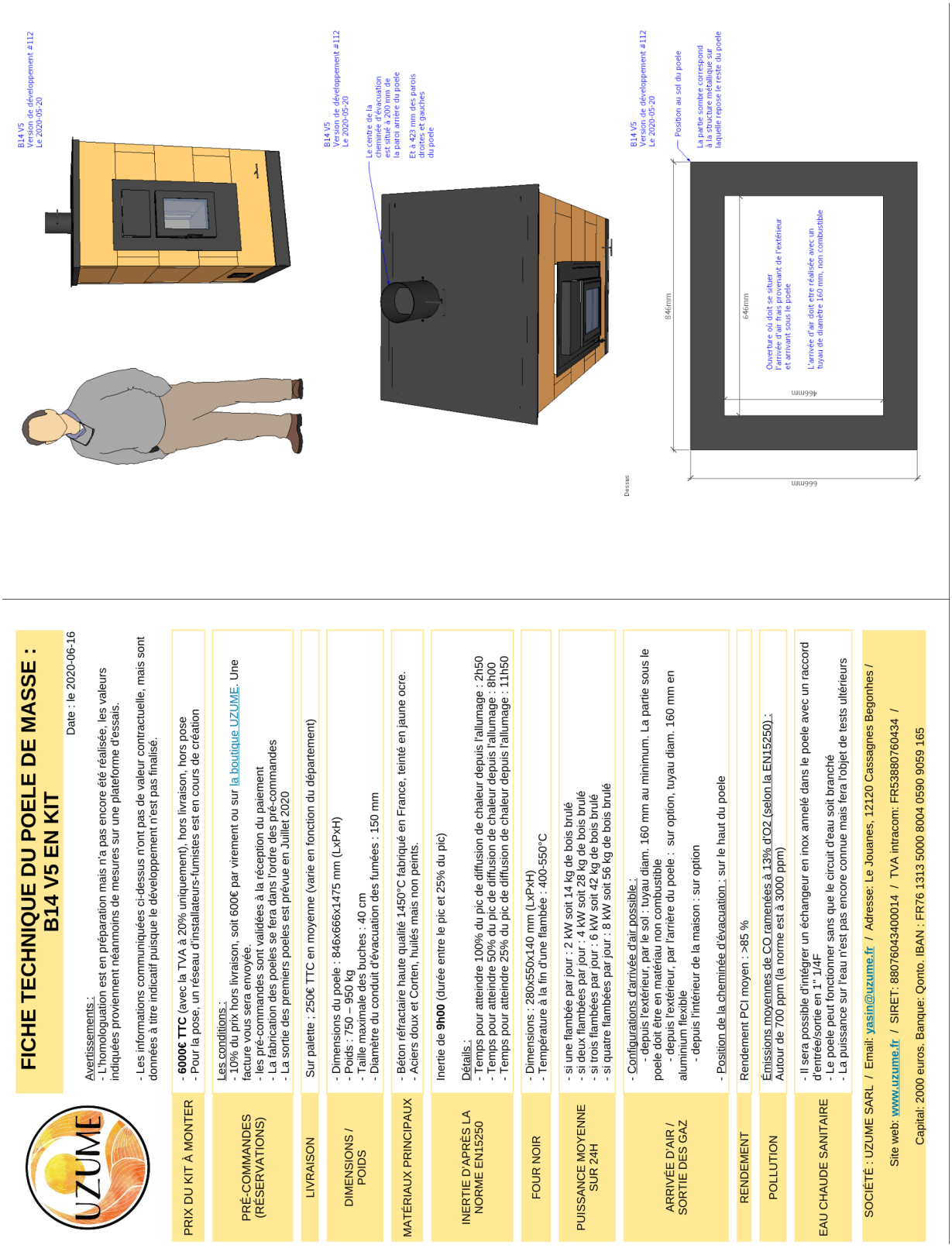

Figure C.1: Technical data sheet of *B14 V5* masonry stove.

Appendix D

Experimental results

D.1 Infrared thermal images

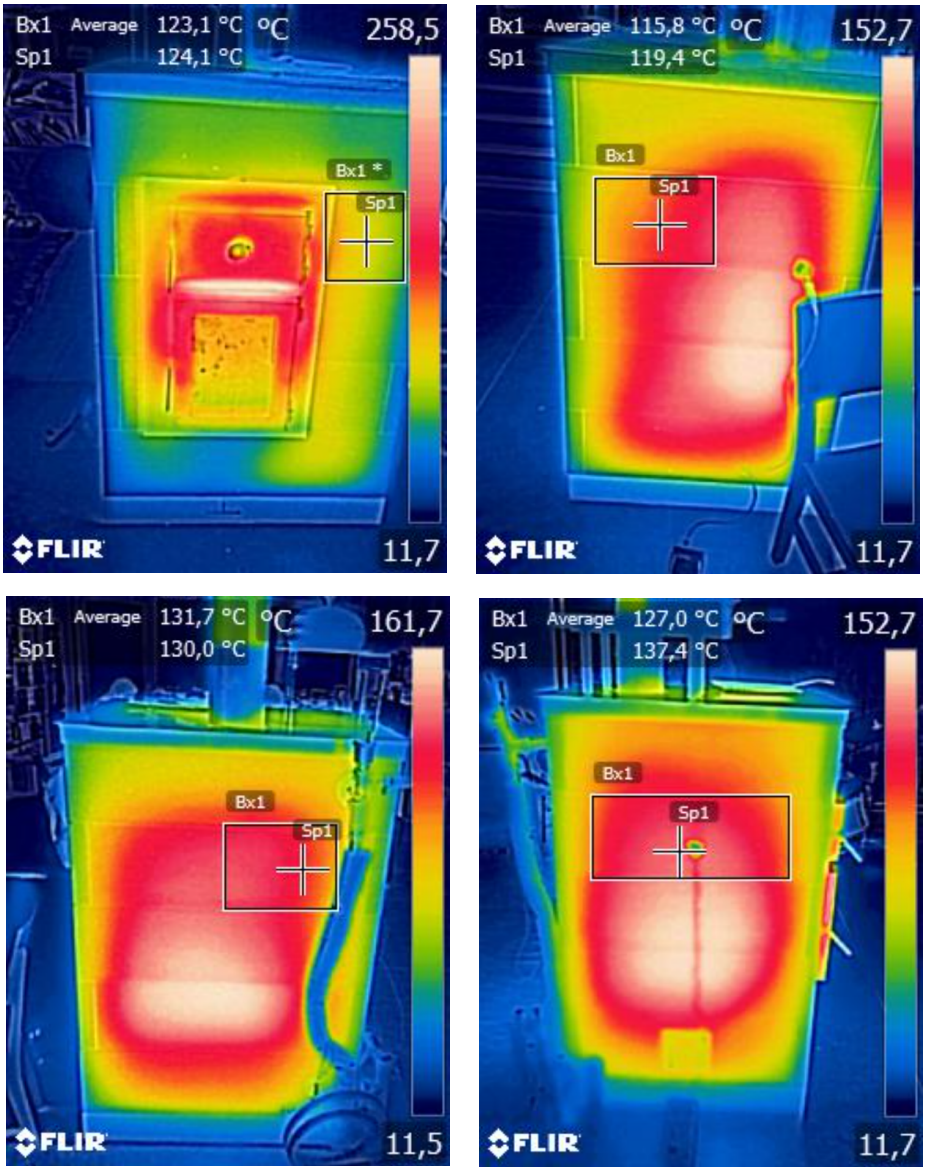

Figure D.1: Thermal images of the stove four sides at 3 h 10 min after ignition (in the order: front, right, back and left).

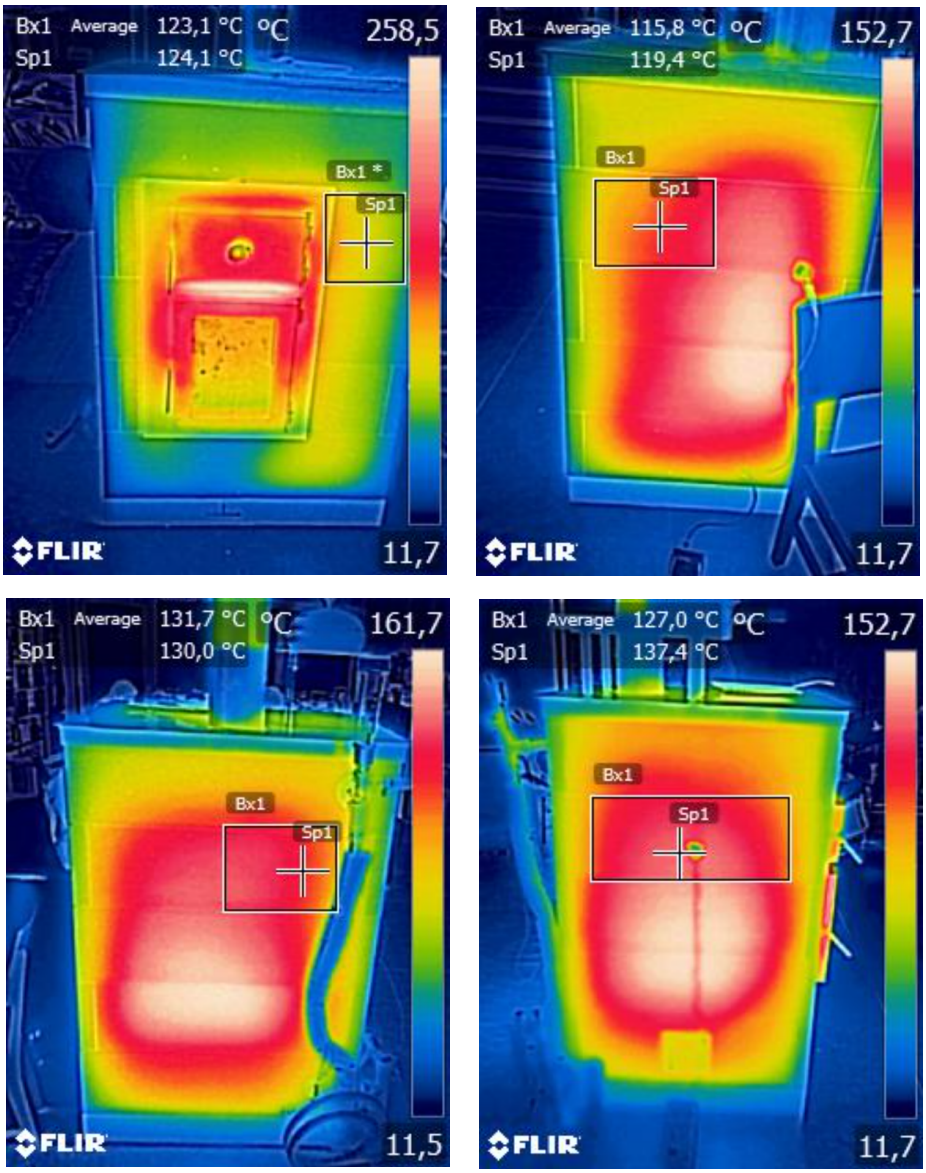

Figure D.2: Thermal images of the stove four sides at 6 h 02 min after ignition (in the order: front, right, back and left).

Appendix E

Comparison of experimental and numerical results

E.1 Combined sensitivity analysis of mass-flow ramp parameters

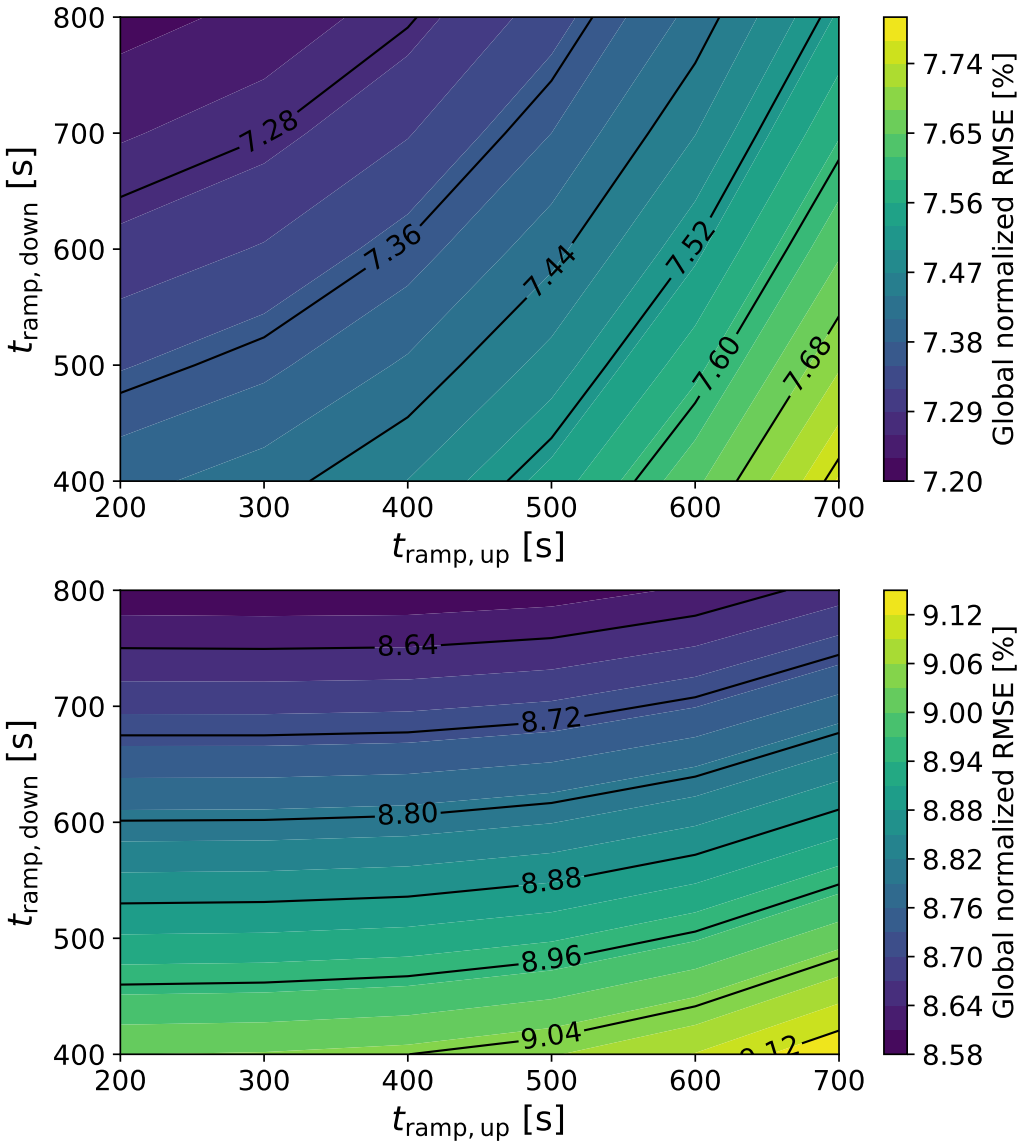

Figure E.1: Two-dimensional sensitivity maps of the global relative RMSE between experimental wall temperatures and corresponding model predictions as a function of the ramp-up and ramp-down durations, for summer (top) and winter (bottom) experimental campaigns.

E.2 Supplementary error analysis between experimental and simulation data

		RMSE [°C]	MAE [°C]
Front side face	**0-120 min**	2.93	2.45
	120 min-end	5.64	5.08
	Full time	4.46	3.72
Right side face (IR thermom.)	**0-120 min**	4.34	3.85
	120 min-end	5.03	4.26
	Full time	4.72	4.09
Right side face (probe)	**0-120 min**	9.89	7.61
	120 min-end	9.28	7.54
	Full time	9.51	7.49
Back side face	**0-120 min**	1.77	1.61
	120 min-end	1.99	1.70
	Full time	1.87	1.64
Left side face (IR thermom.)	**0-120 min**	6.75	5.50
	120 min-end	19.69	18.44
	Full time	14.66	11.93
Left side face (probe)	**0-120 min**	5.59	5.02
	120 min-end	17.26	15.39
	Full time	12.75	10.16
All faces (mean)	**0-120 min**	4.78	4.04
	120 min-end	9.86	8.84
	Full time	7.85	6.41

Table E.1: Error metrics for the winter test campaign.

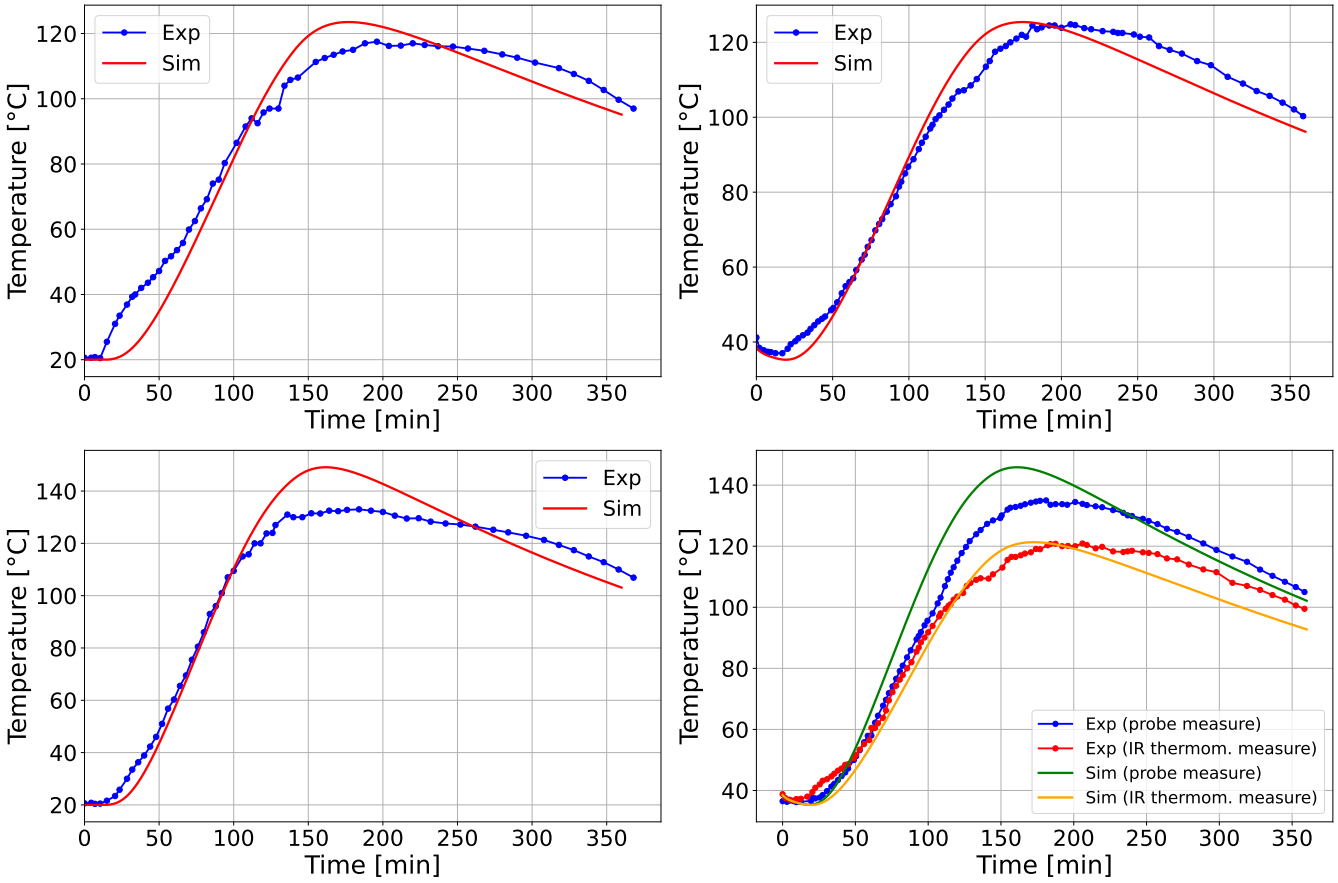

Figure E.2: Comparison between experimental and simulated surface temperatures on the front (top figures) and right (bottom figures) side faces for summer (left figures) and winter (right figures with the two measurement points measured with probe and IR thermometer for the right face) campaigns (Exp = experiment; Sim = simulation).

Appendix F

Review of literature of thermal comfort

F.1 General review of literature

This Appendix proposes a complete overview on the state-of-the-art of thermal comfort. It is based on information from norms from ASHRAE [90] and ISO (ISO 7730 [91], ISO 7726 [93], ISO 8996 [94] and ISO 10551 [95]), from reviews of literatures already performed in thesis [96, 97, 98, 101] and from scientific papers [99, 100, 102, 103, 104].

1 Introduction

The term comfort is intrinsically linked to the sensation of well-being experienced under specific conditions in an environment. In buildings, this notion is linked to the concept of Indoor Environmental Quality (IEQ), which includes air quality, lighting, and thermal and acoustic conditions. This thesis focuses specifically on the thermal dimension of comfort. The major role of a building is to ensure a pleasant indoor climate that is not overly dependent on outdoor conditions. Apart from aesthetics, a building will be judged primarily on the thermal comfort it provides to its occupants.

Thermal comfort is most often defined with the satisfaction of the occupant of the environment as point of reference. This is reflected in the definition provided by ASHRAE (American Society of Heating, Refrigerating and Air-Conditioning Engineers), which is also adopted in the ISO 7730 standard (International Organization for Standardization): *«the condition of mind which expresses satisfaction with the surrounding thermal environment and is assessed by subjective evaluation.»*.

The definition implies the existence of interaction mechanisms between an environment characterized by physical quantities (air temperature, average radiant temperature, relative humidity and air velocity) and the occupant characterized by a set of physiological mechanisms (e.g. homeothermy, regulation of thermal and mass exchanges) and psychological aspects (e.g. comfort perception and adaptation). These diverse factors must all be taken into account when studying thermal comfort and are reviewed in this review of literature section.

To quantify these mechanisms, thermal comfort is typically assessed through different approaches. The most simple is to use simple environmental indices as values representing the comfort. Two other types of models are also used to quantify it. The first, named the static or analytic approach, is based on the calculation of the thermal balance of the human body. This type of model, based on physical and physiological principles, assumes that thermal sensation results directly from the heat exchange between the body and its environment. Due

to their relative simplicity and ease of calculation, these models are widely used. However, they offer a somewhat reductive view of thermal comfort in some cases. To address these limitations, a second methodology, known as the adaptive approach, has been developed. In addition to the physical and physiological dimensions of thermal comfort, it incorporates psychological factors such as individual perception, prior thermal experiences, and mood. These elements influence how occupants experience and adapt to their surroundings to maintain comfort. Therefore, the adaptive approach provides a more comprehensive understanding of thermal comfort and is essential to the study at hand.

2 Physiological basis

Human are classified as homeothermic organisms: their internal body temperature is constant (around 37°C) regardless of their environment. The human body is continuously looking for a state of thermal equilibrium with its surroundings. To maintain this balance, the heat produced internally by the body and conducted to its skin surface must be compensated by losses to the environment. These losses occur through different modes of heat transfer (conduction, convection and radiation) and mass transfer (evaporation and respiration).

The physiological basis of thermal comfort is closely tied to this homoeothermic nature of humans and the body's thermoregulatory system of which it is endowed. This system is the temperature controller of the body. It functions in a non-linear and feedback-driven manner (Figure F.1). It relies on inputs from: internal thermoreceptors, primarily warm-sensitive receptors located in the hypothalamus and using the temperature of arterial blood as measure, and skin thermoreceptors, which are often more sensitive to cold stimuli. These thermoreceptors detect interactions with the environment and internal metabolic heat production that is heat generated through cellular activity such as muscle contractions or organ function (e.g., brain and digestive organs). Based on this sensory input, the thermoregulatory system initiates either autonomic and/or behavioural responses to maintain thermal balance.

Autonomic thermoregulation, controlled by the hypothalamus, ensures the dynamic regulation of human body temperature without conscious effort. It aims to maintain a core temperature near 37°C and a mean skin temperature around 34°C under normal conditions. To achieve this, autonomic thermoregulation activates three mechanisms that can be distinguished: sweating, chills and vasomotion (vasodilation or vasoconstriction). In response to cold, the body initiates vasoconstriction. It reduces blood flow towards the skin, thereby lowering skin temperature and heat exchanges with the external environment. If this is insufficient, shivering begins to increase the production of heat by the organism through involuntary muscular contractions. In contrast, when facing heat, the goal is to increase heat dissipation. Firstly, vasodilatation, increasing skin blood flow and skin temperature, is engaged. If needed, sweating is triggered via the sweat glands which secrete fluid that cools the body by evaporation.

Behavioural thermoregulation complements the autonomic system, often involving conscious or semi-conscious actions. The information from the different receptors integrated at the cortical level allow the body to consciously react and direct his behaviours to effectively fight against cold or heat: it can reduce or increase the surfaces exposed to the external environment by changing his posture or clothing, or changing physical activity to regulate metabolic heat production (voluntary movements). Through such actions, the individual can

anticipate or respond to thermal discomfort more effectively.

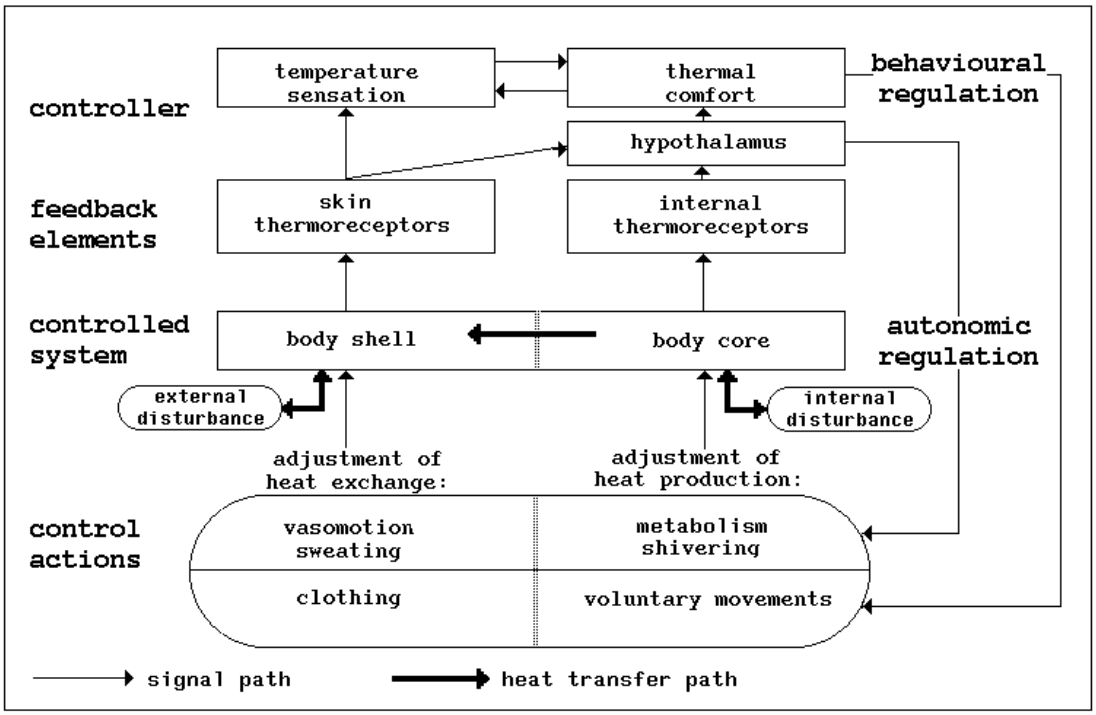

Figure F.1: Diagram of autonomic and behavioural human temperature regulation

3 Physical basis

The physical basis of thermal comfort treats the human body as a thermal system having interactions with the environment through heat exchanges. As discussed in the physiological basis of thermal comfort, humans are homeothermic beings, and thermoregulation plays a crucial role to regulate the thermal exchanges. The heat produced by the metabolic processes of the body is dissipated to the environment through skin surface and via the respiratory tract as sensible or latent heat. Sensible heat exchanges occur via three physical mechanisms: conduction, convection, and radiation (whose governing equations, already introduced in Section 2.2.1, are now applied to this specific context), while latent heat transfer occurs primarily through evaporation of moisture from the skin and respiratory tract. This section details these mechanisms whose computations are, for the majority, dependent on the physical characteristics of the environment: air temperature, average radiant temperature, relative humidity and air velocity.

3.1 *Sensible heat*

Sensible heat transfer occurs from the skin surface to the surrounding environment and is modulated by clothing. The three main mechanisms of sensible heat transfer are convection, radiation, and, to a lesser extent, conduction.

Conduction is only significant at points where the body is in direct contact with surfaces at different temperatures. For example, in a standing person, it concerns only the feet that are

in contact with the floor, resulting in a minimal exchange area and negligible heat transfer. Consequently, this mode is often considered negligible in thermal comfort assessment. In situations involving larger contact areas (e.g., when sitting on furniture), the thermal properties of these objects are modelled using an additional insulation value to the one of clothes.

Convective heat transfer corresponds to the exchange between the skin surface and the environment, directly or through clothes. It is driven by a gradient of temperature between the skin (or the clothes) and the air and is strongly influenced by air movement. The ASHRAE describe this heat flux as [90]:

$$C = h_c f_{cl}(T_{cl} - T_a) \tag{F.1}$$

where:

h_c: convective heat transfer coefficient [W/m^{2}K]
f_{cl}: clothing area factor [-]
T_{cl}: clothing surface temperature [K]
T_a: the air temperature [K]

The clothing area factor is the ratio of clothed body surface to the total body surface, expressed as A_{cl}/A_D. The clothed body surface, A_{cl}, could be obtain by measuring it experimentally while the body surface area, A_D, depends on morphology and is calculated using the Dubois formula:

$$A_D = 0.20 m^{0.425} l^{0.725} \tag{F.2}$$

where m is body mass [kg] and l is height [m]. However, in most of the cases, for simplicity, the values of f_{cl} are taken directly from tables for example available in the *ASHRAE Handbook* [90]. The convective heat transfer coefficient, h_c, depends on varies with air velocity, activity and posture (e.g., seated, walking). ASHRAE provides empirical relations for different conditions (see Table F.1). The clothing temperature, T_{cl}, is a function of the clothing insulation, I_{cl}. This insulation reduces the effective heat transfer by introducing thermal resistance. Standard values of clothing insulation are provided in Table F.2.

Equation	**Limits**	**Condition**
$h_c = 8.3V^{0.6}$	$0.2 < V < 4.0$	Seated with moving air
$h_c = 3.1$	$0 < V < 0.2$	
$h_c = 2.7 + 8.7V^{0.67}$	$0.15 < V < 1.5$	Reclining with moving air
$h_c = 5.1$	$0 < V < 0.15$	
$h_c = 8.6V^{0.53}$	$0.5 < V < 2.0$	Walking in still air
$h_c = 5.7(M - 0.8)^{0.39}$	$1.1 < M < 3.0$	Active in still air
$h_c = 6.5V^{0.39}$	$0.5 < V < 2.0$	Walking on treadmill in still air
$h_c = 14.8V^{0.69}$	$0.15 < V < 1.5$	Standing person in moving air
$h_c = 4.0$	$0 < V < 0.15$	

Note: h_c in W/(m^2·K), V in m/s, and M in mets, where 1 met = 58.2 W/m^2.

Table F.1: Equations for Convection Heat Transfer Coefficient in thermal comfort [90].

Radiation occurs between the human body and surrounding surfaces (walls, objects, etc.). It is driven by surface temperatures and the relative orientation of the body to these surfaces, described using view factors, F. To simplify the complexity of radiative exchanges, ASHRAE proposed a simplified formulation based on the mean radiant temperature, T_{mr}, a weighted

average of the surface temperatures of the surrounding elements based on their emissivity and relative. This formulation is valid provided that the thermal environment is homogeneous. It is calculated:

$$R = h_r f_{cl}(T_{cl} - T_{mr}) \tag{F.3}$$

Where the linear radiative heat transfer coefficient is given by:

$$h_r = 4\sigma\epsilon f_{eff}\left(273.15 + \frac{T_{mr} + T_{cl}}{2}\right)^3 \tag{F.4}$$

with

- f_{eff} : effective radiation area factor [-], the ratio of the effective radiation area of the body, A_r, and the area of the body A_D ($=A_r/A_D$); typically 0.70 (seated) or 0.73 (standing)
- σ : Stefan-Boltzmann constant [W/(m^2 K^4)]
- ϵ : surface emissivity [-]

In most of the cases, for indoor environments, h_r is nearly constant and equal to 4.7 W/m^{2}K. It has to be eventually adjusted by emissivity if emissivity is significantly below unity : $h_r = 4.7\epsilon$.
The mean radiant temperature, T_{mr}, can be determined by two different ways:

1. Using a blackbody globe thermometer (ISO 7726 norm [93]):

$$T_{mr} = \left[(T_g)^4 + \frac{0.25 \times 10^8}{\epsilon_g}\left(\frac{T_g - T_a}{D}\right)^{\frac{1}{4}}(T_g - T_a)\right]^{\frac{1}{4}} \tag{F.5}$$

   with T_g the temperature of the globe [K] and ϵ_g the emissivity of the black globe [-].

2. Using surface temperatures and view factors (ISO 7726 / ASHRAE [93][90]):

$$T_{mr}^4 = T_1^4 F_{p-1} + T_2^4 F_{p-2} + ... + T_N^4 F_{p-N} \tag{F.6}$$

$$\Leftrightarrow T_{mr} = \sqrt[4]{\sum_i^N T_i^4 F_{p-i}} \tag{F.7}$$

   with T_N the surface temperature of surface N and F_{p-N} the view factor between a person and surface N.

In practice, to simplify the expression of sensible heat through the skin, a simplified model proposed by ASHRAE is used combining equations F.3 and F.1. It combines the convective and radiative fluxes through the integration of the operating temperature, T_o and an effective heat transfer coefficient, $h = h_c + h_r$:

$$C + R = f_{cl} h (T_{cl} - T_o) \tag{F.8}$$

$$T_o = \frac{h_r T_{mr} + h_c T_a}{h_r + h_c} \tag{F.9}$$

3.2 *Latent heat*

Latent heat is transferred through evaporation, mode of heat exchange due to the change of state of water, either at the skin or via the respiratory tract.

At the **skin surface**, latent heat loss occurs through sweating, controlled by thermoregulation. The evaporative exchanges are induced by the difference in vapor pressure between skin and ambient air and by the moisture of the skin:

$$E_{sk} = \frac{\omega(p_{sk,s} - p_a)}{R_{e,cl} + (1/(f_{cl}h_e))} \tag{F.10}$$

where

ω	:	skin wettedness (0 to 1) [-]
$p_{sk,s}$	:	water vapor pressure at skin [kPa] (typically saturated at T_{sk})
p_a	:	water vapor pressure in ambient air [kPa]
$R_{e,cl}$	:	evaporative heat transfer resistance of clothing layer [m^2·kPa/W]
h_e	:	evaporative heat transfer coefficient [W/(m^2·kPa)]

The evaporative heat transfer coefficient, h_e, can be computed based on the convective one, h_c, using the Lewis ratio, $LR = h_e/h_c$, that is typically around 16.5 K/kPa.
The evaporative heat transfer resistance of clothing layer, $R_{e,cl}$, can be derived from the clothing insulation, I_{cl}, for which different values are known (Table F.2):

$$R_{cl} = 0.155 I_{cl} \tag{F.11}$$

The skin wettedness represents the equivalent fraction of wet skin to obtain the observed evaporation (for $omega = 1$ the skin is completely wet). This value is never null, there is always a diffusion of water through the skin cells. This is insensitive perspiration, it is worth 6% of the maximum evaporation. ω is expressed as: $\omega = E_{sk}/E_{max}$ with E_{max} obtained by changing ω by 1 in equation F.10. This expression cannot be used since knowing ω requires the value of the unknown, E_{sk}. An alternative formulation is used based on the evaporative heat loss by regulatory sweating, E_{rsw}:

$$E_{rsw} = \dot{m}_{rsw} h_{fg} \tag{F.12}$$

with h_{fg} the heat of vaporization of water ($= 2.43 \times 10^6$ J/kg) and $\dot{m}_{rsw}$ the rate at which regulatory sweat is generated in kg/(sm^2). The skin wettedness can than be obtained from the regulatory sweating wettedness (ASHRAE formulas):

$$\omega_{rsw} = E_{rsw}/E_{max} \tag{F.13}$$

$$\omega = \omega_{rsw} + 0.06(1 - \omega_{rsw}) \tag{F.14}$$

Respiration contributes to both sensible and latent heat loss. At the outlet of the lungs, the expired air is at a temperature close to the internal temperature of the body and almost saturated. These conditions provide a transfer of heat and mass while breathing. ASHRAE provides simplified expressions for these in standard conditions (20°C and RH of 50%):

$$C_{res} = 0.0014M(34 - T_a) \tag{F.15}$$

$$E_{res} = 0.0173M(5.87 - p_a) \tag{F.16}$$

4 Thermal balance

To describe the full thermal balance of the human body, two final components must be taken into account: metabolic heat production and heat storage in the body.

The **metabolic rate** of work produced by the body is noted M. The human body constantly produces energy from its metabolic activity which is the reflection of its cellular life. Metabolism is measured through indirect calorimetry by measuring inhaled flow rate of oxygen and carbon dioxide production. ASHRAE gives a formula to compute this metabolic rate based on these parameters:

$$M = \frac{21(0.23RQ + 0.77)\dot{V}_{O_2}}{A_D} \tag{F.17}$$

where

RQ : respiratory quotient; the molar ratio of $\dot{V}_{CO_2}$ exhaled to $\dot{V}_{O_2}$ inhaled [-]
$\dot{V}_{O_2}$: volumetric rate of oxygen consumption at conditions STPD (0°C and 101.325kPa)

The unit used to define the metabolic rate is the *met*. It is defined based on the metabolic rate of a sedentary person (seated and at rest): 1 met = 58.1 W/m^2. When direct data of O_2 and CO_2 are unavailable, reference tables from ASHRAE [90] or ISO 8996 [94] may be used. Table F.9 in Appendix F.2 shows some examples of these values. Only one part of the metabolic rate is converted into heat, the rest is converted into mechanical work for the muscles, W. The quantity used for muscles is defined by the mechanical efficiency, η : $\eta = W/M$. It is usually low (0–0.1, up to 0.24 in optimal conditions).

Heat storage occurs for the part of metabolic heat that is not used for mechanical work and not dissipated to the environment. The body can be considered as two thermal compartments able to store heat: the skin and the core. Each of them has is own quantity of heat stored represented:

$$S_{cr} = \frac{(1 - \alpha_{sk})mc_{p,b}}{A_D}\frac{dT_{cr}}{dt} \tag{F.18}$$

$$S_{sk} = \frac{\alpha_{sk}mc_{p,b}}{A_D}\frac{dT_{sk}}{dt} \tag{F.19}$$

where

α_{sk} : fraction of body mass concentrated in skin compartment [-]
m : body mass [kg]
$c_{p,b}$: specific heat capacity of body (=3490 [J/kgK])
A_D : Dubois surface area [m^2]
T_{cr} : temperature of core compartment [K]
T_{sk} : temperature of skin compartment [K]
t : time [s]

Combining all the exchanges of heat and matter through convection (C and C_{res}), radiation R and evaporation (E_{sk} and E_{res}), the productions of heat and power (M and W) and the storage of heat in the body (S_{sk} and S_{cr}) described before and visible on Figure F.2, the **final thermal balance** of the body can be computed. The net heat production in the human

body (M-W) is either stored (S), causing the body's temperature to rise, or dissipated to the environment through skin surface (q_{sk}) and respiratory tract (q_{res}):

$$M - W = q_{sk} + q_{res} + S \tag{F.20}$$

$$= (C + R + E_{sk}) + (C_{res} + E_{res}) + (S_{sk} + S_{cr}) \tag{F.21}$$

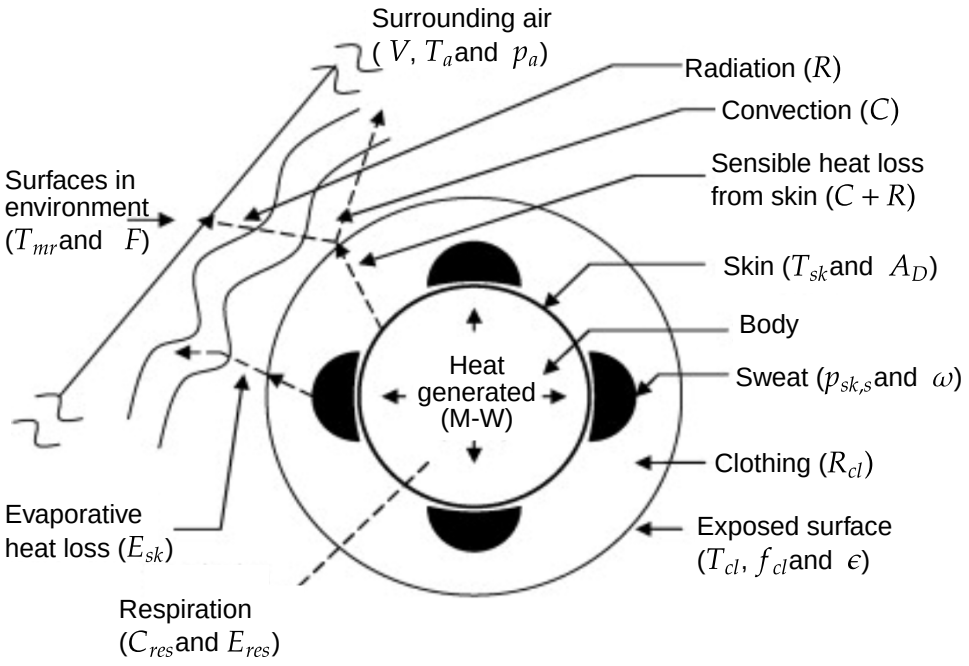

Figure F.2: Thermal interaction between a human body and its environment [90].

The final point whose impact on the thermal balance is crucial is clothing. Clothes strongly influence the heat exchanges between the human body and its environment. It acts as a barrier to heat and mass transfer, primarily through its insulating properties. Quantifying the thermal insulation of clothing is typically done in controlled laboratory conditions using thermal manikins and still air. Because direct measurement is impractical in most field or comfort studies, standard reference values are used. These values, derived from standardized experiments, are compiled into insulation tables (e.g., Table F.2). It is important to note that such values may not fully capture real-world scenarios, particularly for dynamic activities where garment fit, motion, and wind can affect insulation significantly. In thermal models, clothing is often idealized as a homogeneous layer where heat transfer occurs primarily by conduction between the skin and the outer surface of the fabric. This simplification allows for representing clothing by its intrinsic thermal insulation, I_{cl} [m^2·K/W], defined as the resistance to heat flow from the skin to the outer surface of the garment. The total insulation of a clothing ensemble can be approximated using a summation formula proposed by ASHRAE (source formula from McCullough and Jones, 1984):

$$I_{cl} = 0.835 \sum_i I_{clu,i} + 0.161 \tag{F.22}$$

where $I_{clu,i}$ represents the effective insulation of clothing i and I_{cl} the total ensemble insulation. Thermal insulation is expressed in units of *clo*, where 1 clo = 0.155 m^2·K/W.

Garment Description	$I_{cl,i}$	**Garment Description**	$I_{cl,i}$	**Garment Description**	$I_{cl,i}$
Underwear		Long-sleeved, flannel shirt	0.34	Long-sleeved (thin)	0.25
Men's briefs	0.04	Short-sleeved, knit sport shirt	0.17	Long-sleeved (thick)	0.36
Panties	0.03	Long-sleeved sweat shirt	0.34	**Dresses and skirts**	
Bra	0.01	**Trousers and Coveralls**		Skirt (thin)	0.14
T-shirt	0.08	Short shorts	0.06	Skirt (thick)	0.23
Full slip	0.16	Walking shorts	0.08	Long-sleeved shirtdress (thin)	0.33
Half slip	0.14	Straight trousers (thin)	0.15	Long-sleeved shirtdress (thick)	0.47
Long underwear top	0.20	Straight trousers (thick)	0.24	Short-sleeved shirtdress (thin)	0.29
Long underwear bottoms	0.15	Sweatpants	0.28	Sleevless, scoop neck (thin)	0.23
Footwear		Overalls	0.30	Sleeveless, scoop neck (thick)	0.27
Ankle-length athletic socks	0.02	Coveralls	0.49	**Sleepwear and Robes**	
Calf-length socks	0.03	**Suit Jackets and Vests**		Sleeveless, short gown (thin)	0.18
Knee socks (thick)	0.06	Single-breasted (thin)	0.36	Sleeveless, long gown (thin)	0.20
Panty hose	0.02	Single-breasted (thick)	0.44	Short-sleeved hospital gown	0.31
Sandals/thongs	0.02	Double-breasted (thin)	0.42	Long-sleeved, long gown (thick)	0.46
Slippers (quilted, pile-lined)	0.03	Double-breasted (thick)	0.48	Long-sleeved pajamas (thick)	0.57
Boots	0.10	Sleeveless vest (thin)	0.10	Short-sleeved pajamas (thin)	0.42
Shirts and Blouses		Sleeveless vest (thick)	0.17	Long-sleeved, long wrap robe	0.69
Sleeveless, scoop-neck blouse	0.12	**Sweaters**		Long-sleeved, short wrap robe	0.48
Short-sleeved, dress shirt	0.19	Sleeveless vest (thin)	0.13	Short-sleeved, short robe	0.34
Long-sleeved, dress shirt	0.25	Sleeveless vest (thick)	0.22		

Note: 1 clo = 0.155 m^2·K/W. Thin garments = summerweight, thick garments = winterweight [90].

Table F.2: Garment Insulation Values.

5 Psychological basis

The psychological basis of thermal comfort refers to sensation, the subjective experience individuals have of their thermal environment, as well as their behavioural responses within it. It is strongly associated to the physiological and physical basis mentioned earlier.

The behavioural responses correspond to the adaptation of individuals to their thermal environment. The relationship between the subject and his surroundings (the way he perceives them), their mood, their thermal experiences are psychological factors that affect thermal perception and prompt behavioural responses aiming at restoring comfort.

Thermal sensation is a perceptual experience that includes both qualitative aspects (e.g., feeling hot or cold, identifying the location of discomfort) and quantitative aspects (e.g.,

intensity of the sensation). This sensation arises from signals sent by thermoreceptors to the hypothalamus, which integrates this sensory input to evaluate the individual's overall thermal state. Several scales have been developed to measure thermal sensation, the most commonly used being the Bedford and ASHRAE scales. The ASHRAE scale is preferred in many studies because the Bedford scale conflates thermal sensation with thermal pleasure. The ASHRAE scale assigns numeric values ranging from -3 (cold) to +3 (hot), with 0 representing a neutral thermal sensation (see Figure F.3). The scales to quantify thermal neutrality are critical, as thermal neutrality should not be confused with thermal balance: while the human body can achieve thermal balance under a wide range of environmental conditions through thermoregulatory mechanisms, thermal neutrality occurs within a narrower range in which such mechanisms are minimally engaged.

Bedford comfort scale		**ASHRAE comfort scale**	
7	Much too warm	+3	Hot
6	Too warm	+2	Warm
5	Comfortably warm	+1	Slightly warm
4	Comfortable	0	Neutral
3	Comfortably cool	-1	Slightly cool
2	Too cool	-2	Cool
1	Much too cool	-3	Cold

Table F.3: Thermal sensation scale according to Bedford (left) and ASHRAE (right).

It is also essential to distinguish between three elements: the individual's internal thermal state, their perception of the thermal environment, and their overall feeling of thermal comfort, which results from the interaction of the first two. Assessing thermal comfort usually involves collecting subjective data from occupants about their thermal sensations, which serve as indicators of their internal thermal state. ISO Standard 10551 provides a structured methodology for this type of assessment, incorporating five key dimensions: three that concern the individual's thermal state (perception, emotional judgment, and preference), and two that relate to their evaluation of the environment (acceptability and tolerance).

6 Quantification of thermal comfort

The physical, physiological and psychological interactions between humans and their environment just developed earlier are known. The main problematic is to be able to use them to evaluate and quantify thermal comfort. In order to obtain a standardized quantification that could be used in norms, different models have been developed.

6.1 Simple environmental indices

These first indices give rapid but often inaccurate results. They only take into account environmental parameters as air temperature and humidity. They are useful in case of a first approach but does not take into account all the interactions and affecting parameters.

The operative temperature is an index of comfort integrating both convective (convective heat transfer coefficient, h_c, and air temperature, T_a) and radiative heat exchanges (radiative heat transfer coefficient, h_r, and mean radiant temperature, T_{mr}) as can be seen in equation F.9. It is defined as the temperature of an isothermal enclosure in which an occupant would exchange the same amount of heat by radiation and convection as in the actual environment they are in. Plotting the evolution of this index with air temperature for different mean radiant temperatures shows that even if the air temperature is low, if a radiative source is present (higher T_{rm}), the thermal comfort can be acceptable (see Figure F.3).

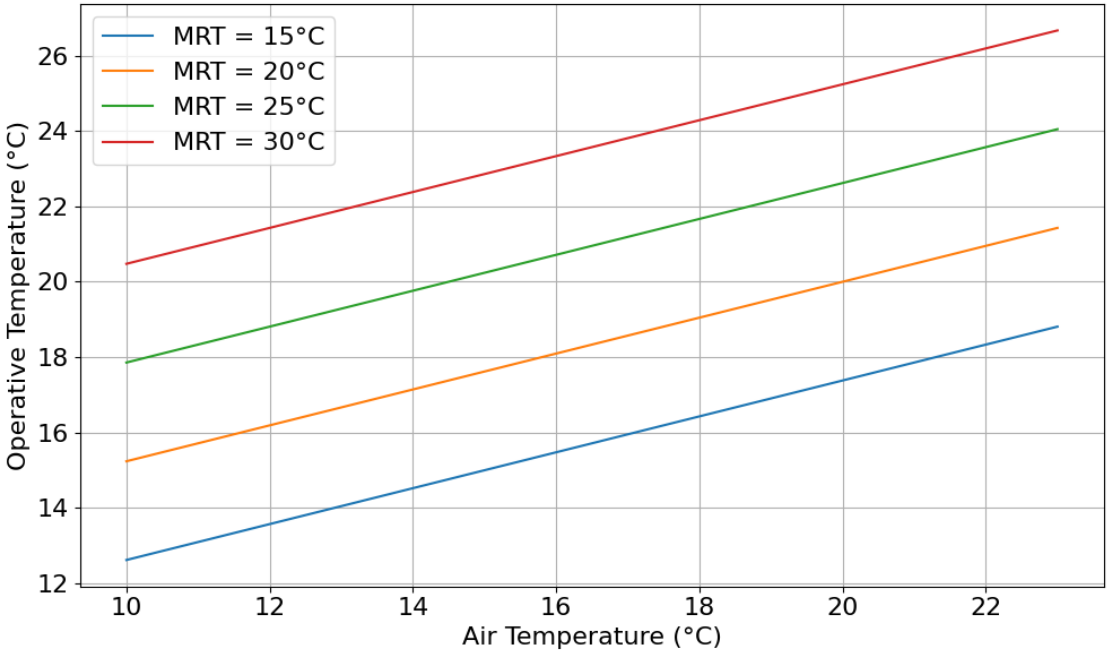

Figure F.3: Evolution of operative temperature with air temperature for different mean radiant temperatures ($h_c = 5W/m^2K$ and $h_r = 5.5W/m^2K$ in equation F.9).

The effective temperature, ET, combines humidity and temperature in a single index:

$$ET = f(T_a, RH). \tag{F.23}$$

It is defined as the temperature of a saturated enclosure which, in the absence of radiation, would exchange the same amount of heat and produce the same effect on the occupant as the real enclosure. This is the basic definition, but it has later been corrected taken also into account the body response defining the corrected effective temperature, ET^* as the equivalent dry-bulb temperature of an isothermal enclosure at 50% relative humidity, in which a subject would exchange the same amount of heat and have the same skin wettedness as in the real environment where they are located. The exact formula of ET^* that depends on air temperature (T_a), mean radiant temperature (T_{mr}), and partial water vapor pressure in the air (p_a), and takes into account the water vapor permeability of clothing, as well as the subject's metabolic activity is often complex and solved through numerical models. Among one of the possible formula, Steadman proposes an empirical simplified one that could be used in some cases (temperatures in °C and pressure in Pa):

$$ET^* \approx 0.64T_a + 0.36T_r + \frac{0.27p_a}{1000} \tag{F.24}$$

6.2 Static/analytical models

The static approach of thermal comfort is based on the human heat balance, essentially through physical and physiological models, to assess indoor thermal comfort or predict the thermal sensation. The take not only environmental parameters into account but also the interactions with the human body. Nevertheless, the occupant of the room is considered as a passive and static receptor of the climatic changes to which it is subjected. These models take into account only the heat exchanges between man and his immediate environment. To determine physiological quantities of individuals (skin temperature, internal temperature and skin wettedness) and heat exchanges between people and the environment (radiation, convection, conduction and evaporation), that are useful to quantify the thermal comfort, different models have been developed whose a part has already been developed in the previous paragraph. The different analytical models developed differ in the physiological modeling of thermoregulation. The simplest models consider the human body as an unique bloc and is applicable in stationary conditions. This kind of model has been proposed by Fanger through its Predicted Mean Vote (PMV) model, the most widely used in the literature. More complex models divide the body into several segments and allow simulation of the dynamics of physiological responses. In this sense, the Standard Effective Temperature (SET) model proposed by Gagge divides the body in two main segments making it applicable in unsteady conditions.

Fanger model (PMV and PPD)

This model has been developed based on extensive American and European laboratory experiments conducted in a well-controlled, homogenous and stationary environment. These experiments have determined the necessary physiological conditions (skin temperature and sweating) for thermal comfort. By writing the heat balance, Fanger expressed in an analytical way the thermal sensation using the Predicted Mean Vote index, PMV, as a function of the difference between the heat flux transferred from the body to the environment and the one corresponding to comfort conditions. The PMV predicts the average thermal sensation of a large group of people to their thermal environment. This index being the most mentioned in literature, it is used by various norms (ASHRAE 55, ISO 7730, EN 15251, ...) to quantify thermal comfort.

To compute this index, Fanger said that thermal comfort can be assessed on the basis of six main parameters, four of which are related to the environment and the other two to people. These environmental parameters are air temperature, mean radiant temperature, relative humidity and air velocity. The people-related parameters are metabolism and clothing. The PMV model incorporates the role of human physiology in maintaining thermal comfort through processes such as sweating, blood flow regulation, muscle shivering, etc., based on the assumption that thermal neutrality is the condition for optimal thermal comfort. Based on this, the formula given by Fanger is:

$$
\begin{aligned}
PMV = &\left[0.303 \cdot e^{-0.036M} + 0.028\right] \cdot (M - W) \\
&- 3.05 \times 10^{-3} \cdot [5733 - 6.99 \cdot (M - W) - p_a] \\
&- 0.42 \cdot [(M - W) - 58.15] \\
&- 1.7 \times 10^{-5} \cdot M \cdot (5867 - p_a) \\
&- 0.0014 \cdot M \cdot (34 - T_a) \\
&- 3.96 \times 10^{-8} \cdot f_{cl} \cdot \left[(T_{cl} + 273)^4 - (T_{mr} + 273)^4\right] \\
&- f_{cl} \cdot h_c \cdot (T_{cl} - T_a)
\end{aligned} \tag{F.25}
$$

where:

- The clothing area factor, f_{cl} can be computed from Tables or using the following relations given by Fanger:

$$
f_{cl} = \begin{cases} 1 + 1.290 \cdot I_{cl} & \text{si } I_{cl} \leq 0.078 \text{ m}^2\,\text{K/W} \\ 1.05 + 0.645 \cdot I_{cl} & \text{si } I_{cl} > 0.078 \text{ m}^2\,\text{K/W} \end{cases}
$$

- The convective heat transfer coefficient, h_c, can be obtained from Tables (see Table F.1) or using the relationships given by Fanger:

$$
h_c = \begin{cases} 2.38 \cdot |T_{cl} - T_a|^{0.25} & \text{if } 2.38 \cdot |T_{cl} - T_a|^{0.25} > 12.1 \cdot \sqrt{v_{ar}} \\ 12.1 \cdot \sqrt{v_{ar}} & \text{otherwise} \end{cases}
$$

- The clothing temperature, T_{cl}, is found by iteration using the formula:

$$
\begin{aligned}
T_{cl} =& 35.7 - 0.028 \cdot (M - W) \qquad \text{(F.26)} \\
&- I_{cl} \cdot \left\{3.96 \times 10^{-8} \cdot f_{cl} \cdot \left[(T_{cl} + 273)^4 - (T_{mr} + 273)^4\right] + f_{cl} \cdot h_c \cdot (T_{cl} - T_a)\right\} \qquad \text{(F.27)}
\end{aligned}
$$

From this PMV index computation and investigations involving several hundred individuals, Fanger proposed a discrete scale going from -3 (very cold environment) to +3 (very hot environment) with 0 when the body is at neutrality. If the sensation is close to neutrality (between -1 and 1) and there is no other source of discomfort, then the situation is considered comfortable according to Fanger.

Nevertheless, a person can feel out of the neutrality and yet not to be in discomfort. Thermal sensation being not enough to express comfort, Fanger proposed the Predicted Percentage Dissatisfied index, PPD, to complete his model. It allows to foresee the percentage of unsatisfied people to a thermal sensation:

$$
PPD = 100 - 95exp[-(0.0335PMV^4 + 0.2179PMV^2)] \tag{F.28}
$$

The PPD is not zero even for for a vote equal to zero (neutral sensation). At such a PMV, the relationship provides that still 5% of the population are dissatisfied. Then this percentage increases so symmetrical on both sides of the zero vote towards hot and cold sensations (see Figure F.4).

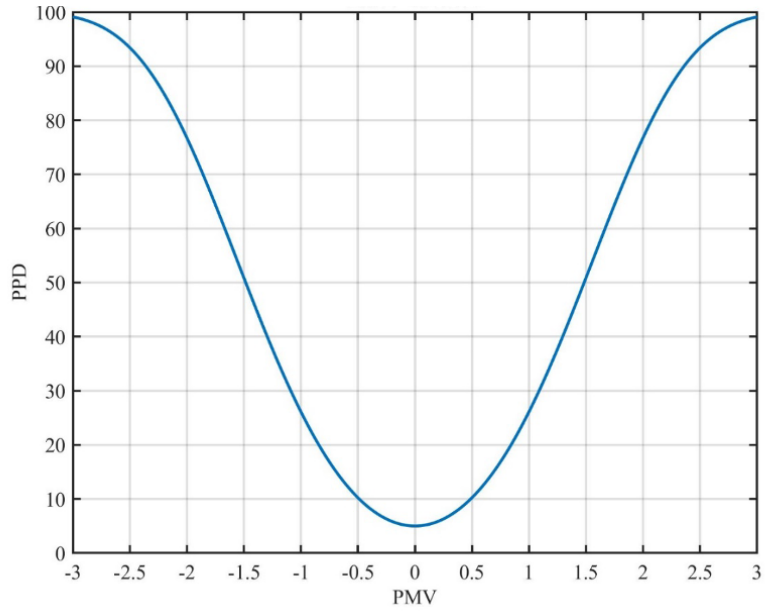

Figure F.4: Evolution of the PPD with variation of the PMV.

One critical point of PMV is that it was first developed in an experimental chamber and later validated in a fully air-conditioned building. This makes its generalization to all types of buildings less straightforward, particularly for naturally ventilated buildings. Natural ventilation is a critical issue in applying the PMV index for thermal comfort assessment, for two specific reasons: the degree of control and flexibility it offers to occupants, and the fluctuation of indoor climatic conditions. The occupants of buildings naturally ventilated have a tendency to accept more flexible climatic conditions. Therefore, to try to expand the PMV to free-running buildings, different corrected indexes were developed among which:

- The implementation of an expectation factor, e, by Fanger and Toftum. This factor was proposed in order to correct the observed discrepancies between the calculated PMV and the actual feeling of the occupants of naturally ventilated buildings and has been determined based on the analysis of a database of 3200 field surveys results from cities with different climates. e takes a value between 0.5 and 1 and the extended PMV is computed:

$$PMVe = e \times PMV \tag{F.29}$$

- Humphreys and Nicol have proposed a variable of incoherence based on statistics of the impact of the different input data of the model (metabolism, air speed, air and radiant temperature), the type of building (natural or forced ventilation) and the external temperature. This variable of incoherence has to be used to correct the PMV that is used on the ASHRAE scale:

$$D_{PMV-ASHRAE} = -4.03 + 0.0949T_o + 0.0058RH + 1.201(M \cdot I_{cl}) + 0.0008T_{ext}^2 \tag{F.30}$$

$$PMV_{new} = 0.8 \cdot (PMV - D_{PMV-ASHRAE}) \tag{F.31}$$

- Finally, Running Yao proposed an adaptive PMV starting from the $PMVe$. He proposed a correction factor, a, to adapt the PMV model based on occupant adaptation

(physiological and behavioral) in warm and cold climates. The correction factor has been fixed by Yao at 0.293 and -0.125 in hot and cold climates:

$$aPMV = \frac{PMV}{1 + a \cdot PMV} \tag{F.32}$$

Despite the different improvements in PMV, there are still discrepancies between the prediction results obtained and the actual thermal sensation of the occupants. Some studies, performed by Humpreys and Nicol, marked a systematic difference between PMV result and the actual average vote, both for naturally ventilated and air-conditioned spaces in some specific cases. Furthermore, other studies performed by Z. Zhao stated that in very warm or cold climates, the PMV overestimates the comfort level when the actual thermal sensation of the occupant is higher than a slight coolness (-1), while it underestimates the comfort level when the actual thermal sensation of the occupant is slightly warm or even warmer. This lead to the need of more adaptive models developed in the next section.

Gagge model

This model is a two-node model developed by Gagge, this make it a more complex model than the PMV one. But, it can be used to predict physiological responses or responses to transient situations. The two nodes are the internal core body, where all the metabolic heat is produced, and the skin that is considered isotherm. The model considers the exchanges between these two nodes and the environment. Skin temperature, skin wettedness, and skin heat flux are used in the calculation of the ET^* index (new effective temperature). The ET^* index depends on the subject's clothing and activity level. To standardize the calculation, a new index called SET (Standard Effective Temperature) was defined. SET represents the dry-bulb temperature of an isothermal environment at 50% relative humidity and an air velocity below 0.1 m/s, in which a person with a clothing insulation of 0.6 clo and a metabolic rate of 1.0 Met would experience the same thermal stress (in terms of skin temperature and skin wettedness) as in the actual environment. Thermal sensations can be inferred from the different SET values.

This model is more complex and less used than the Fanger model. Since it is representative in unsteady and heterogeneous environments, it could be used for assessing thermal comfort in vehicles for example. But, the Fanger model is much more used in standards to qualify thermal comfort in habitats where conditions are more stable.

6.3 Adaptive models

The adaptive theory of thermal comfort builds upon the static approach, as it was developed to address its limitations and uncertainties, particularly those of the PMV model, which was initially selected as the standard tool for assessing thermal comfort. When researchers applied the analytical models to large real-world datasets, they observed that the predicted comfort levels often did not align with occupants' actual perceptions. This discrepancy was especially pronounced in naturally ventilated buildings, where indoor conditions fluctuate more and follow outdoor climatic variations. In contrast, air-conditioned spaces often replicate the static conditions of climate chambers used during the development of analytical tools.

To explain these differences, some researchers introduced the concept of adaptation, arguing that factors beyond physical and physiological mechanisms influence thermal comfort perception. The central principle of the adaptive approach is that "if a change occurs that causes

discomfort, people react in ways that restore comfort." Given its inherently subjective nature, thermal comfort is affected by personal and contextual factors such as age, gender, ethnicity, and geographic/climatic origin. According to various definitions of adaptive actions, three main categories are typically distinguished:

- Physiological adaptation (e.g., acclimatization)
- Psychological adaptation (e.g., expectations and past experiences)
- Behavioral adaptation (e.g., adjusting clothing, opening windows, or using fans)

In general, the adaptive approach is grounded in empirical data collected across various building types, climates, and regions. These studies involve simultaneous measurements of physical environmental parameters,particularly outdoor temperature and its variation, which is commonly used as a model input, and the subjective responses of building occupants. Occupants typically report their thermal sensation using the ASHRAE scale (Table F.3) at the time of measurement. This large dataset is then analysed statistically to identify the temperature that occupants perceive as neutral or comfortable. These findings help define comfort conditions in similar building types under comparable climatic circumstances. Several adaptive comfort models and equations have been developed from such empirical analyses to be able to compute the comfort temperature depending on the external temperature. These comfort temperature obtained correspond to the operative temperature necessary to have in the buildings to have thermal comfort. Several relationships have been developed over the years:

- **Humphrey's adaptive model (1976)**:
  Humphreys investigated the correlation between thermal comfort temperature and monthly mean outdoor temperature, $T_{av,mth}$, through different surveys and obtained Figure F.5. From this Figure, he emphasized the distinction between naturally ventilated and air-conditioned buildings. In naturally ventilated buildings, the relation is linear with the monthly mean outdoor temperature while in air-conditioned buildings, the correlation is more complex and can be modelled with an exponential regression. Based on these results, he proposed a relationship depending on the monthly mean outdoor temperature for the 2 types of buildings:

$$T_{comf} = 11.9 + 0.534 \times T_{av,mth} \tag{F.33}$$

$$T_{comf} = 23.9 + 0.295 \times (T_{av,mth} - 22) \times \exp\left(-\frac{(T_{av,mth} - 22)}{24\sqrt{2}}\right) \tag{F.34}$$

  where the monthly mean outdoor temperature can be computed:

$$T_{av,mth} = \frac{1}{N}\sum_{i=1}^{N} T_{ext,i} \tag{F.35}$$

  with N the number of days in the month and $T_{ext,i}$ the mean outdoor temperature of day i.

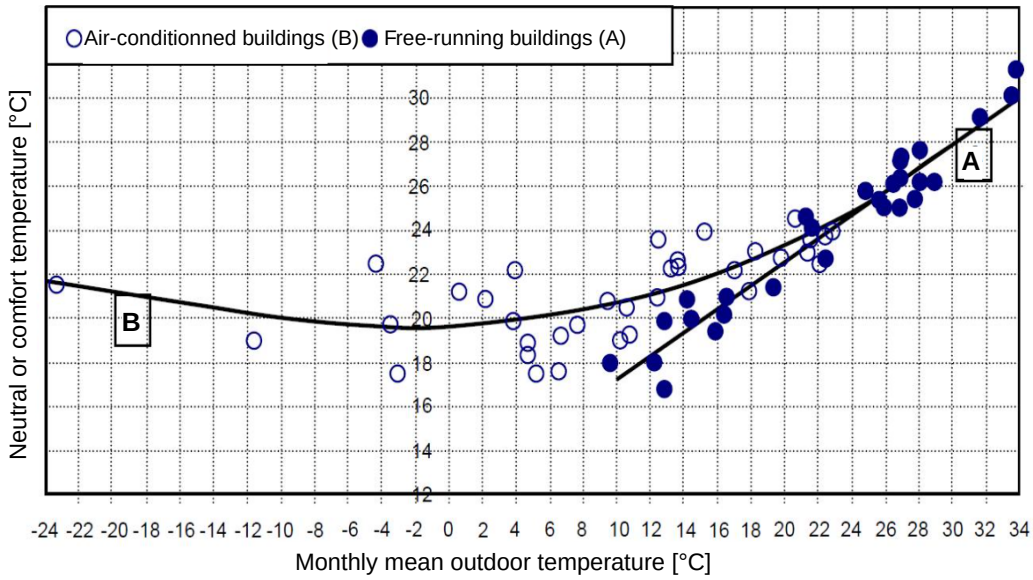

Figure F.5: Correlation between comfort temperature and monthly mean outdoor temperature for two types of buildings: free-running and air-conditioned buildings.

- **Auliciems' Multiple Regression (1983):**
  Using a similar dataset to Humphreys (including newer studies), Auliciems proposed a multiple regression linking comfort temperature to both indoor temperature at the moment of comfort vote, T_i, and monthly mean outdoor temperature, $T_{av,mth}$, for all types of buildings:
  $$T_{comf} = 0.48 \times T_i + 0.14 \times T_{av,mth} + 9.22 \tag{F.36}$$

- **ASHRAE RP-884 Project (by De Dear in 1995)**:
  This project compiled over 21,000 comfort observations from 160 buildings worldwide. The statistical analysis of the database made it possible to determine linear regressions for comfort temperature as a function of outdoor temperature. Figure F.6 shows the regressions obtained for air-conditioned buildings and naturally ventilated buildings, respectively. Each figure includes two regressions: one corresponds to comfort votes observed in situ (the adaptive model), and the other to the votes predicted by Fanger's static model (PMV). De Dear used this linear regression of comfort votes to develop a standard for adaptive comfort as an alternative to the static method in ASHRAE Standard 55. The developed method allows the calculation of the comfort temperature, T_{comf}, in naturally ventilated buildings based on the monthly average of the outdoor temperature, $T_{av,mth}$:
  $$T_{\text{conf}} = 0.31 \times T_{av,mth} + 17.8 \tag{F.37}$$
  De Dear introduced comfort acceptability bands: ± 2.5°C around T_{comf} for 90% acceptability and ± 3.5°C for 80% acceptability. ASHRAE Standard 55 recommends this adaptive model only for naturally ventilated buildings with specific conditions: operable windows, free clothing adjustment, light metabolic activity (e.g., office work) and outdoor temperatures between 10°C and 33°C.

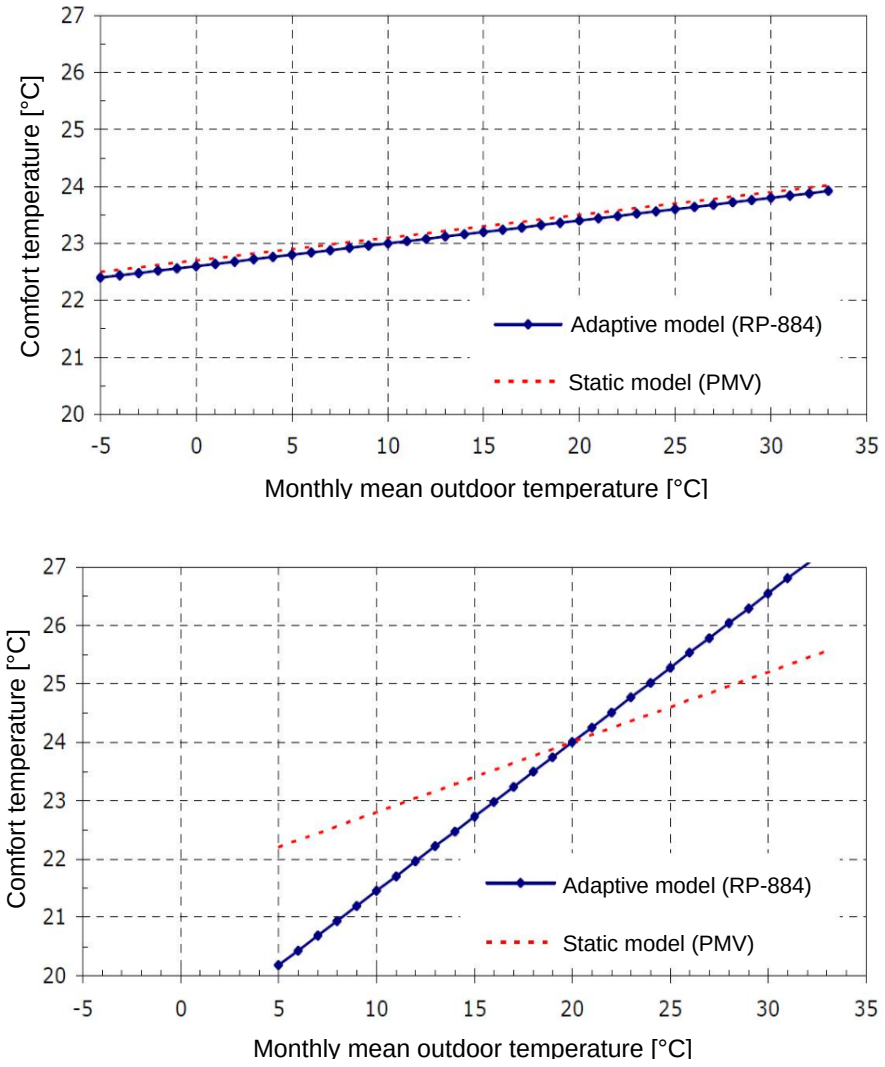

Figure F.6: Evolution of the comfort temperature with monthly mean outdoor temperature from a static model (PMV) and an adaptive model (developed by the RP-884 project) for air-conditioned buildings (top) and naturally ventilated buildings (bottom) [96].

- **SCATs project (1997-2000):**
  SCATs, Smart controls and Thermal Comfort, is an European project that investigated adaptive comfort across five European countries: United Kingdom, France, Sweden, Greece, and Portugal. The aim of the project was to implement a method for reducing energy consumption in air-conditioned buildings and to promote the use of naturally ventilated buildings (which consume significantly less energy) by developing a control system based on the adaptive approach to thermal comfort. Based on field studies, specific adaptive comfort algorithms were derived for each country.

  All the previous relationships used a monthly mean average outdoor temperature to predict the comfort temperature. However, most occupant responses to thermal conditions require a certain amount of time to take effect. This delay can range from a few hours to several days or even weeks, depending on the nature of the action. For instance, opening a window has an almost immediate impact, whereas adjusting clothing habits to seasonal changes occurs more gradually. Therefore, using a simple monthly average of

the outdoor temperature is insufficient for accurately estimating comfort temperature. Instead, a different indicator is needed, one that accounts for the sequential variations in outdoor climate conditions over time. That is why, the SCATs project decided to use the exponentially weighted running mean temperature, T_{rm}, that was developed earlier by Nicols and Humphreys to be more accurate:

$$T_{\mathrm{rm}} = (1-\alpha)\left[T_{\mathrm{od},1} + \alpha T_{\mathrm{od},2} + \alpha^2 T_{\mathrm{od},3} + \ldots\right] \tag{F.38}$$

where α is a constant between 0 and 1 and $T_{od,i}$ are daily average outdoor temperatures preceding the survey. AS an example, the ASHRAE 55 standard recommends $\alpha = 0.9$ for tropical and humid regions. The same standard recommends the use of daily average outdoor temperatures for 7 to 30 consecutive days prior to the survey date for the calculation of the exponentially weighted moving average temperature

Table F.4 presents the algorithms developed for each participating country. These algorithms calculate the comfort temperature (T_{comf}) based on the exponentially weighted running mean of the outdoor temperature using a time constant of $\alpha = 0.80$, T_{rm80}. While the SCATs project produced country-specific algorithms, it did not result in a harmonized European standard. This standardization were only later integrated into the EN 15251 standard.

Country	**Adaptive algorithm for calculating comfort temperature**	
	$T_{\mathrm{rm80}} = 10\,^{\circ}\mathrm{C}$	$T_{\mathrm{rm80}} > 10\,^{\circ}\mathrm{C}$
France	$0.049T_{\mathrm{rm80}} + 22.58$	$0.206T_{\mathrm{rm80}} + 21.42$
Greece	n.a.	$0.205T_{\mathrm{rm80}} + 21.69$
Portugal	$0.381T_{\mathrm{rm80}} + 18.12$	$0.381T_{\mathrm{rm80}} + 18.12$
Sweden	$0.051T_{\mathrm{rm80}} + 22.83$	$0.051T_{\mathrm{rm80}} + 22.83$
United Kingdom	$0.104T_{\mathrm{rm80}} + 22.58$	$0.168T_{\mathrm{rm80}} + 21.63$
All	$\mathbf{22.88}\,^{\circ}\mathrm{C}$	$\mathbf{0.302T_{\mathrm{rm80}} + 19.39}$

Table F.4: Adaptive algorithms for calculating comfort temperature developed during SCATs project.

- **In general (in current norms):**
  Adaptive models generally express comfort temperature (which corresponds to the operative temperature of the room) as a linear function of the running mean outdoor temperature:

$$T_{comf} = AT_{rm} + B \tag{F.39}$$

  with A and B values that can vary depending on the cases. For example, the norm EN 15251 proposes A = 0.33 and B = 18.8 with the T_{rm} computed with $\alpha = 0.8$.

7 Thermal comfort in the norms

At the European level, the European Committee for Standardization (CEN) recognises 18 standards related to thermal comfort, most of which align with ISO norms. These standards are classified into several categories based on the type of environment they address:

moderate (EN ISO 7730 and EN ISO 13732-2), hot (ISO 7243, ISO 7933 and EN ISO 13732-1) or cold (ISO 11079 and EN ISO 13732-1). In addition, the EN 15251 standard, now replaced by EN 16798 since 2019, includes thermal comfort (both static and adaptive theories) within the broader evaluation of indoor environmental quality (IEQ), alongside indoor air quality, visual comfort, and acoustic comfort. At the American level, thermal comfort in moderate environments is defined by ASHRAE Standard 55.

In this thesis, the focus is on the evaluation of thermal comfort in moderate environments, as this is most relevant for indoor conditions influenced by a masonry stove in Belgium. For such environments, two main European standards are considered in detail:

- EN 7730: thermal comfort assessment in mechanically ventilated buildings, based on the PMV/PPD method.
- EN 16798 (2019): updated version of EN 15251, expanding the scope to include both mechanically and naturally ventilated buildings and introducing an adaptive comfort model for the latter.

Both EN ISO 7730 and EN 16798 define comfort categories, expressed in terms of occupant expectations. Categories A, B, and C in EN ISO 7730 correspond to categories I, II, and III in EN 16798. EN 16798 adds a fourth category (IV) for conditions considered unacceptable or only acceptable for a limited part of the year (Table F.5).

EN 16798-1 Category	**ISO 7730 Category**	**Explanation**
I	A	High level of expectation and is recommended for spaces occupied by very sensitive and fragile persons with special requirements like handicapped, sick, very young children and elderly persons
II	B	Normal level of expectation and should be used for new buildings and renovations
III	C	An acceptable, moderate level of expectation and may be used for existing buildings
IV	Not considered	Values outside the criteria for the above categories. This category should only be accepted for a limited part of the year

Table F.5: Thermal comfort categories used in norms ISO 7730 and EN 16798 [91, 92].

7.1 EN ISO 7730

EN ISO 7730 provides an analytical method for evaluating moderate thermal environments, based on Fanger's model using PMV and PPD indices. It specifies validity ranges for the six parameters used to determine the PMV:

- Metabolic rate, M: 46 W/m^2 to 232 W/m^2 (0.8 met to 4 met);
- Clothing thermal insulation, I_{cl}: 0 m^2·K/W — 0.310 m^2·K/W (0 clo — 2 clo);
- Air temperature, T_a: 10°C to 30°C;
- Mean radiant temperature, T_{mr}: 10°C to 40°C;

- Relative air velocity, v_{ar}: 0 m/s to 1 m/s;
- Partial water vapour pressure, p_a: 0 Pa to 2700 Pa;

Based on PMV and PPD, three comfort categories are defined (Table F.6). The standard also provides seasonal operative temperature ranges for various mechanically ventilated building types. It briefly discusses adaptive effects in naturally ventilated buildings but does not propose a dedicated model.

Category	**PPD (%)**	**PMV**
A	< 6	$-0.2 < \text{PMV} < +0.2$
B	< 10	$-0.5 < \text{PMV} < +0.5$
C	< 15	$-0.7 < \text{PMV} < +0.7$

Table F.6: Comfort categories according to EN ISO 7730, based on PMV and PPD [91].

7.2 EN 16798

For mechanically conditioned buildings, EN 16798 adopts the PMV/PPD method but extends the classification to include a fourth category (Table F.7).

Category	**PPD (%)**	**PMV**
I	< 6	$-0.2 < \text{PMV} < +0.2$
II	< 10	$-0.5 < \text{PMV} < +0.5$
III	< 15	$-0.7 < \text{PMV} < +0.7$
IV	< 25	$-1.0 < \text{PMV} < +1.0$

Table F.7: Comfort categories for mechanically ventilated buildings according to EN 16798 norm, based on PMV and PPD indices [92].

For naturally ventilated buildings, EN 16798 introduces an adaptive comfort model based on the outdoor running mean temperature T_{rm} with a weighting factor $\alpha = 0.8$ (see Equation F.38). The model provides upper and lower comfort temperature (corresponding to operative temperatures) limits for each category (Table F.8). Furthermore, like the ISO 7730 standard, this standard also provides seasonal operative temperature ranges but this time also for non-ventilated buildings.

Category	**Upper and Lower limits**
I	Upper limit: $T_{comf} = 0.33T_{rm} + 18.8 + 2$ Lower limit: $T_{comf} = 0.33T_{rm} + 18.8 - 3$
II	Upper limit: $T_{comf} = 0.33T_{rm} + 18.8 + 3$ Lower limit: $T_{comf} = 0.33T_{rm} + 18.8 - 4$
III	Upper limit: $T_{comf} = 0.33T_{rm} + 18.8 + 4$ Lower limit: $T_{comf} = 0.33T_{rm} + 18.8 - 5$

Table F.8: Adaptive model comfort categories for naturally ventilated buildings according to EN 16798 [92].

F.2 Typical metabolic heat generations

Activity	W/m^2	met
Resting		
Sleeping	40	0.7
Reclining	45	0.8
Seated, quiet	60	1.0
Standing, relaxed	70	1.2
Walking (on level surface)		
3.2 km/h (0.9 m/s)	115	2.0
4.3 km/h (1.2 m/s)	150	2.6
6.4 km/h (1.8 m/s)	220	3.8
Office Activities		
Reading, seated	55	1.0
Writing	60	1.0
Typing	65	1.1
Filing, seated	65	1.2
Filing, standing	80	1.4
Walking about	100	1.7
Lifting/packing	120	2.0
Driving/Flying		
Car	60 to 115	1.0 to 2.0
Aircraft, routine	70	1.2
Aircraft, instrument landing	105	1.8
Aircraft, combat	140	2.4
Heavy vehicle	185	3.2
Miscellaneous Occupational Activities		
Cooking	95 to 115	1.6 to 2.0
Housecleaning	115 to 200	2.0 to 3.4
Seated, heavy limb movement	130	2.2
Machine work		
sawing (table saw)	105	1.8
light (electrical industry)	115 to 140	2.0 to 2.4
heavy	235	4.0
Handling 50 kg bags	235	4.0
Pick and shovel work	235 to 280	4.0 to 4.8
Miscellaneous Leisure Activities		
Dancing, social	140 to 255	2.4 to 4.4
Calisthenics/exercise	175 to 235	3.0 to 4.0
Tennis, singles	210 to 270	3.6 to 4.0
Basketball	290 to 440	5.0 to 7.6
Wrestling, competitive	410 to 505	7.0 to 8.7

Table F.9: Typical Metabolic Heat Generation for Various Activities.

Bibliography

[1] IPCC. *Climate Change 2023: Synthesis Report. Contribution of Working Groups I, II and III to the Sixth Assessment Report of the Intergovernmental Panel on Climate Change*. Geneva, Switzerland. 2023.

[2] European Commission. *Communication from the Commission to the European parliament, the European council, the European economic ans social committee and the committee of the regions : The European Green Deal*. Brussels. 11 December 2019. Available at: `https://eur-lex.europa.eu/legal-content/FR/TXT/?uri=CELEX:52019DC0640`. Consulted on 11 May 2025.

[3] United Nations. *The Paris Agreement*. UNFCC. Available at: `https://unfccc.int/process-and-meetings/the-paris-agreement`. Consulted on 13 June 2025.

[4] Pascal Faucompré. *Autonomie, sobriété, low tech, résilience, frugalité, définitions et applications dans l'habitat : Low tech, une démarche systémique*. BuildGreen. November 2022. Available at: `https://www.build-green.fr/autonomie-sobriete-low-tech-resilience-frugalite-definitions-et-applications-dans-lhabitat/`. Consulted on 13 June 2025.

[5] Low-Tech Lab. *C'est quoi une low-tech : La définition*. Available at: `https://lowtechlab.org/fr/la-low-tech`. Consulted on 13 June 2025.

[6] Eurostat. *Energy statistics - an overview : Final energy consumption*. May 2025. Available at: `https://ec.europa.eu/eurostat/statistics-explained/index.php?title=Energy_statistics_-_an_overview`. Consulted on 15 May 2025.

[7] Eurostat. *Energy consumption in households : Highlights*. June 2024. Available at: `https://ec.europa.eu/eurostat/statistics-explained/index.php?title=Energy_consumption_in_households`. Consulted on 15 May 2025.

[8] David Mercereau. *Logiciel open source d'étude thermique pour poêle de masse*. AFPMA. 2025. Available at: `https://www.afpma.pro/2025/10/04/logiciel-open-source-detude-thermique-pour-poele-de-masse/`. Consulted on 4 May 2025.

[9] Austrian Tiled Stove Association. *Kachelofen-service*. Available at: `https://kachelofenverband.at/en/kov-service/`. Consulted on 4 May 2025.

[10] M-A Perea-Moreno, E. Samerón-Manzano and A-J. Perea-Moreno. *Biomass as Renewable Energy: Worldwide Research Trends*. February 2019.

[11] Dewallef Pierre. Master 1 course, *Renewable energy system design : biomass*. University of Liège. 2024.

[12] IEA Bioenergy. *Implementation of bioenergy in Belgium – 2024 update*. p.4. December 2024. Available at: https://www.ieabioenergy.com/wp-content/uploads/2024/12/CountryReport2024_Belgium_final.pdf. Consulted on 16 June 2025.

[13] REN21. *Renewables 2024 : Global status report : energy demand*. p.33. 2024. Available at: https://www.ren21.net/wp-content/uploads/2019/05/GSR2024_Demand_Full_Report.pdf. Consulted on 16 June 2025.

[14] C. Tagliaferri, S. Evangelisti, R. Clift and P. Lettieri. *Life cycle assessment of a biomass CHP plant in UK: The Heathrow energy centre case*. March 2018.

[15] F. Patuzzi, D. Prando, S. Vakalis, A. Maria Rizzo, D. Chiaramonti, W. Tirler, T. Mimmo, A. Gasparella and M. Baratieri. *Small-scale biomass gasification CHP systems: Comparative performance assessment and monitoring experiences in South Tyrol (Italy)*. June 2016.

[16] ADEME. *Rénovation: Adopter le chauffage au bois* . October 2024. Available at: https://librairie.ademe.fr/index.php?controller=attachment&id_attachment=5265&preview=1. Consulted on 16 June 2024.

[17] A. Rahman, O. Farrok and M. Haque. *Environmental impact of renewable energy source based electrical power plants: Solar, wind, hydroelectric, biomass, geothermal, tidal, ocean, and osmotic*. 2022.

[18] R. Laleman, L. Balduccio and J. Albrecht. *The Role of Biomass in the Renewable Energy System*. University of Ghent. 2012.

[19] Brunner. *Tiled stove and masonry heater*. 2023. Available at: https://www.brunner.com/en/tiled-stoves-fireplaces/water-bearing-devices. Consulted on 18 June 2025.

[20] Anciaux Bertrand. 2024. *Le poêle de masse comme solution écologique : sélection de matériaux, impact environnemental et aspects socio-techniques*. Polytechnic school of Louvain, Catholic University of Louvain. Available at: http://hdl.handle.net/2078.1/thesis:48746. Consulted on 18 May 2025.

[21] Brussels Institute for Environmental Management (IBGE). *Info fiches-énergie : le chauffage au poêle de masse*. February 2009. Available at: https://document.environnement.brussels/opac_css/doc_num.php?explnum_id=3869. Consulted on 21 June 2025.

[22] G. Calender. *L'histoire d'un chauffage moderne, performant, économique et écologique*. Debriel. 2025. Available at: https://www.debriel.com/histoire-chauffage-bois-inertie-accumulation/. Consulted on 22 June 2025.

[23] Stovemason. *Grundofen*. Available at: https://stovemason.com/grundofen/. Consulted on 22 June 2025.

[24] Oxalis. *Poêle de masse : accessible à tous*. 2019. Available at: https://www.oxalis-asso.org/wp-content/uploads/SUPPORT-DE-FORMATION_04-2019.pdf. Consulted on 22 June 2025.

[25] Thermasse. *Les différents types de poêles de masse*. 2025. Available at: https://thermasse.fr/poele-de-masse/les-differents-types-de-poeles-de-masse/. Consulted on 22 June 2025.

[26] O. grelier and P. Bourgoin. *Les poêles de masse artisanaux en France*. ADEME. 2016. Available at: https://librairie.ademe.fr/index.php?controller=attachment&id_attachment=250&preview. Consulted on 21 June 2025.

[27] Stovemason. *Kachelofen*. Available at: https://stovemason.com/kachelofen/. Consulted on 22 June 2025.

[28] J. Schneider. *Tile stoves : elegant and efficient woodburners*. Popular science. vol.214 p.98. 1979. Available at: https://books.google.be/books?id=kQEAAAAAMBAJ&pg=PA98&redir_esc=y#v=onepage&q&f=false. Consulted on 22 June 2025.

[29] Tobias Rutz. *Storage heaters*. Holzoefe. Available at: https://holzoefe.ch/speicheroefen/antik/. Consulted on 22 June 2025.

[30] A.E. Shkolnik. *Russian stove of the 20th century*. 2003. Available at: https://n-t.ru/nj/nz/1988/0107.htm. Consulted on 22 June 2025.

[31] Russian Mayolica. *History of Russian tiled stoves*. 2020. Available at: https://www.russian-mayolica.com/articles/russian-tiled-stoves/. Consulted on 22 June 2025.

[32] : A. Svensson. *History of the Swedish tiled stove*. Keramic & Kakelugnar. 2021. Available at: https://www.keramik-kakelugnar.com/history-of-the-swedish-tiled-stove/. Consulted on 22 June 2025.

[33] Nettitakka. *Pot oven Cozy 76*. Available at: https://nettitakka.fi/tuote/pontouuni-76/. Consulted on 22 June 2025.

[34] Low-Tech Lab. *C'est quoi une low-tech : La définition*. Available at: https://lowtechlab.org/fr/la-low-tech. Consulted on 13 June 2025.

[35] UZUME. *UZUME: poêles de masse*. Available at: https://www.uzume.fr/. Consulted on 21 June 2025.

[36] F. Incropera, D. Dewitt, T. Bergman and A. Lavine. *Incropera's principles of heat and mass transfer*. 8th edition. J. Wiley and Sons. 2017.

[37] P. Dewallef and V. Terrapon. Bachelor 2 course, *Heat transfer*. University of Liège. 2021.

[38] D. Byakatonda. *An overview of numerical and analytical methods for solving ordinary differential equations*. University of Kisubi. 2020. Available at: https://arxiv.org/pdf/2012.07558. Consulted on 15 June 2025.

[39] R. Szymkiewickz. *Numerical Modeling in Open Channel Hydraulics*. Chapter 3. Springer. 2010. Available at: file:///C:/Users/RNJ/Downloads/978-90-481-3674-2.pdf. Consulted on 15 October 2025.

[40] E. Hairer, S. P. Norsett and G. Wanner. *Solving Ordinary Differential Equations I: Nonstiff Problems*. Springer. 1987.

[41] P. Michalak. *Thermal - electrical analogy in dynamic simulations of buildings: comparison of four numerical solution methods*. Journal of Mechanical and energy engineering. 2020. Available at: https://www.jmee.tu.koszalin.pl/ojs/index.php/jmee/article/view/169/127. Consulted on 11 may 2025.

[42] E. Hairer and G. Wanner. *Solving Ordinary Differential Equations II: Stiff and Differential-Algebraic Problems*. Springer. 1991.

[43] J.R. Cash. *On the Integration of Stiff Systems of O.D.E.s Using Extended Backward Differentiation Formulae*. 1980. Available at: https://link.springer.com/content/pdf/10.1007/BF01396701.pdf. Consulted on 11 May 2025.

[44] A. Erchegyi and E. rackz. *Heat Conduction Model Based on the Explicit Euler Method for Non-Stationary Cases*. MDPI. 2025. Available at: https://www.mdpi.com/1099-4300/27/10/994. Consulted on 15 May 2025.

[45] M. Rozali. *Lecture notes: Tutorial 11: Partial Differential Equations: Stability*. November 2017. University of British Columbia. Available at: https://phas.ubc.ca/~rozali/410_tutorial_12.pdf. Consulted on 15 May 2025.

[46] T. Driscoll and R. Braun. *Upwinding and stability*. 2023. Available: https://tobydriscoll.net/fnc-julia/advection/upwind.html. Consulted on 15 may 2025.

[47] J. Cooper. *Lecture notes: Numerical integration of differential equations*. University if Maryland. Available at: https://math.umd.edu/~jcooper/amsc460/DE.pdf. Consulted on 15 May 2025.

[48] MIT (Massachusetts Institute of Technology). *Lecture notes: Forward and Backward Euler Methods*. Available at: https://web.mit.edu/10.001/Web/Course_Notes/Differential_Equations_Notes/node3.html. Consulted on 15 May 2025.

[49] P. Sweby, H. Yee and D. Griffiths. *On spurious steady-state solutions of explicit runge-Kutta schemes*. NASA. 1990. Available at: https://ntrs.nasa.gov/api/citations/19900013024/downloads/19900013024.pdf. Consulted on 16 May 2025

[50] D. Smołka-Danielowska and M. Jabłońska. *Chemical and mineral composition of ashes from wood biomass combustion in domestic wood-fired furnaces*. International Journal of Environmental Science and Technology. June 2021. Available at: https://www.researchgate.net/publication/352999269_Chemical_and_mineral_composition_of_ashes_from_wood_biomass_combustion_in_domestic_wood-fired_furnaces. Consulted on 16 July 2025.

[51] S. Vassilev, D. Baxter, L. K. Andersen and C. G. Vassileva. *An overview of the chemical composition of biomass*. ScienceDirect. October 2009. Available at: https://www.sciencedirect.com/science/article/pii/S0016236109004967?ref=cra_js_challenge&fr=RR-1. Consulted on 16 July 2025.

[52] L. Bianchini, A. Colantoni, R. Venanzi, L. Cozzolino and R. Picchio. *Physicochemical Properties of Forest Wood Biomass for Bioenergy Application: A Review*. MDPI. April 2025. Available at: https://www.mdpi.com/1999-4907/16/4/702. Consulted on 16 July 2025.

[53] Maine Department of Agriculture. *Wood heat Maine: Green & Seasoned Firewood Chart*. 2021. Available at: https://www.maine.gov/dacf/mfs/projects/woodheatmaine/heating_w_firewood.html. Consulted on 16 AugustJuly

[54] A. Taylor. *Moisture Content of 'Seasoned' Firewood*. Forest Products center. University of Tennessee. 2007. Available at: https://utia.tennessee.edu/publications/wp-content/uploads/sites/269/2023/10/W179.pdf. Consulted on 16 July 2025.

[55] M. Holubcík, N. Cajová Kantová, J. Jandacka and A. Caja. *The Performance and Emission Parameters Based on the Redistribution of the Amount of Combustion Air of the Wood Stove*. MDPI. August 2022. Available at: https://www.mdpi.com/2227-9717/10/8/1570. Consulted on 20 July 2025.

[56] Lemort Vincent. 2024. *Cooling and low-temperature heating systems*. Master 1 course, Lecture 8. University of Liège.

[57] O. Skreiberg and L. Georges. *Transient Heat Production and Release Profiles for Wood Stoves*. AIDIC. 2018. Available at: https://www.aidic.it/iconbm2018/programma/79skreiberg.pdf. Consulted on 20 July 2025.

[58] L. Schwarzer, A. M. FRey, M.G. Warming-Jespersen. *Design of Low Emission Wood Stoves*. IEA Bioenergy. October 2022. Available at: https://www.ieabioenergy.com/wp-content/uploads/2022/11/IEA-Bioenergy-Task-32_Report-D1-2_Low-emission-wood-stove-design_final.pdf. Consulted on 20 July 2025.

[59] M. Bugge, N. Haugen and O. Skreiberg. *Transient CFD Simulations of Wood Stoves with Varying Heat Storage Capacity* . AIDIC. 2019. Available at: https://www.pvv.ntnu.no/~nilshau/Own_Papers/2019_Bugge_etal.pdf. Consulted on 20 July 2025.

[60] R. Scharler, J. Kelz, T. Gruber and R. Bardar. *Transient CFD simulation of wood log combustion in stoves*. ResearchGate. June 2019. Available at: https://www.researchgate.net/publication/333801606_Transient_CFD_simulation_of_wood_log_combustion_in_stoves. Consulted on 20 July 2025.

[61] C. Chen and OL. Mangasarian. *Smoothing methods for convex inequalities and linear complementarity problems*. 1994. Available at: https://link.springer.com/content/pdf/10.1007/BF01592244.pdf. Consulted on 21 July 2025.

[62] Y. Zhao, H. Zhang E. Arens and Q. Zhao. *Thermal sensation and comfort models for non-uniform and transient environments, part IV: Adaptive neutral setpoints and smoothed whole-body sensation model*. ScienceDirect. August 2013. Available at: https://www.sciencedirect.com/science/article/pii/S0360132313003181. Consulted on 21 July 2025.

[63] M. Qu and Y. Sun. *Sigmoid-modified topology optimization for minimizing PCM melting time and enhancing heat transfer efficiency in thermal management systems*. March 2025. Available at: https://papers.ssrn.com/sol3/papers.cfm?abstract_id=5163970. Consulted on 21 July 2025.

[64] A.R. Lespinard, P.R. Salgado and R.H. Mascheroni. *Sigmoid model: Application to heat transfer in vegetable preserves sterilized in glass jars*. ResearchGate. July 2018. Available at: https://www.researchgate.net/publication/262760719_Sigmoid_model_Application_to_heat_transfer_in_vegetable_preserves_sterilized_in_glass_jars#fullTextFileContent. Consulted on 21 July 2025.

[65] Z. Yang and A. Gopan. *Improved global model for predicting gas radiative properties over a wide range of conditions*. ScienceDirect. 2021. Available at: https://www.sciencedirect.com/science/article/pii/S2451904921000184?ref=pdf_download&fr=RR-2&rr=9a8d15e44abe17f1. Consulted on 4 August 2025.

[66] D. Tree, J. Tobiasson, S. Egbert and B. Adams. *Measurement of radiative gas and particle emissions in biomass flames*. ScienceDirect. November 2017. Available at: https://www.sciencedirect.com/science/article/pii/S1540748918304073?ref=pdf_download&fr=RR-2&rr=9a8d19455c0a17f1. Consulted 4 August 2025..

[67] IRM. *Statistiques climatiques des communes belges: Liège (ins 62063)*. Available at: https://www.meteo.be/resources/climateCity/pdf/climate_INS62063_LIEGE_fr.pdf. Consulted on 4 August 2025..

[68] R. K. Shah, M. S. Bhatti. In S. Kaçak, R. K. Shah and W. Aung. *Handbook of Single-Phase Convective Heat Transfer*. New York: Wiley-Interscience. 1987.

[69] C. V. Madhusudana, *Thermal Contact Conductance: Second edition*. Springer. 2014. Available at: https://link.springer.com/content/pdf/10.1007/978-3-319-01276-6.pdf. Consulted on 22 May 2025.

[70] J.P. Holman. *Heat transfer: 10th edition*. McGraw-Hill. 2010.

[71] Q. Louveaux, O. Bruls and F. Nguyen. Bachelor 1 course, *Méthodes numériques et projet*. University of Liège. 2021.

[72] UZUME. *Les plans de nos poêles: dossier partagé*. Available at: https://acloud5.zaclys.com/index.php/s/rAGK6YYznLHisD2. Consulted on 12 September 2025.

[73] Poêle-cuisinière. *Un poêle de masse, comment ça chauffe?*. 2023. Available at: https://poele-cuisiniere.fr/un-poele-de-masse-comment-ca-chauffe/. Consulted on 12 September 2025.

[74] UZUME. *UZUME: poêles de masse*. Available at: https://www.uzume.fr/plans-poeles-de-masse/medi-batchblock. Consulted on 12 September 2025.

[75] Bol. *PARKSIDE Thermomètre infrarouge*. Available at: https://www.bol.com/be/fr/p/parkside-thermometre-infrarouge-compteur-de-surface-max-12-m-le-thermometre-infrarouge-indique-les-pertes-de-chaleur-des-fenetres-des-portes-ou-de-l-isolation/9300000067511257/. Consulted on 11 August 2025.

[76] Teledyne FLIR. *FLIR C5*. Available at: https://www.flir.fr/products/c5/?vertical=condition%20monitoring&segment=solutions. Consulted on 11 August 2025.

[77] KLIUM. *FLUKE 51-2 thermomètre digital 50Hz à 1 canal - 1281142*. Available at: https://www.klium.be/fr/fluke-51-2-thermometre-digital-50hz-a-1-canal-1281142-73239. Consulted on 11 December 2025.

[78] Weather Spark. *Average temperagture in Liège*. Available at: https://weatherspark.com/y/52398/Average-Weather-in-Li%C3%A8ge-Belgium-Year-Round#Figures-Temperature. Consulted on 11 August 2025.

[79] AccuWeather. *Weather in Liège*. Available at: https://www.accuweather.com/en/be/liege/29306/may-weather/29306. Consulted on 11 December 20255.

[80] G. Giuffrida, L. Ibos, A. Boudenne and H. Allam. *Exploring the integration of bio-based thermal insulations in compressed earth blocks walls*. ScienceDirect. 2024.

Available at: https://www.sciencedirect.com/science/article/pii/S0950061824005531?fr=RR-2&ref=pdf_download&rr=96e88ae6c8bbb709. Consulted on 21 July 2025.

[81] N. Oudhof. *Fiche technique: BTC*. Isol'en paille. Available: https://www.isolant-paille.com/images/Fiche_Technique_-_BTC.pdf. Consulted on 21 July 2025.

[82] TerreHabitat. *briques de terre crue*. Available: https://www.terrehabitat.be/wp/construction/gros-oeuvre/briques-dargile-crue/. Consulted on 21 July 2025.

[83] H. Gehrmann, H. Matzing, P. Nowak, D. Baris, H. Seifert, C. Dupont, Defoort, M. Peyrot and F. Castagno. *Waste wood characterization and combustion behaviour in pilot lab scale*. ScienceDirect. February 2020. Available at: https://www.sciencedirect.com/science/article/pii/S1743967120300258. Consulted on 13 August 2025.

[84] Forest Research. *Typical calorific values of fuels*. 2025. Available at: https://www.forestresearch.gov.uk/tools-and-resources/fthr/biomass-energy-resources/reference-biomass/facts-figures/typical-calorific-values-of-fuels/. Consulted on 13 August 2025.

[85] The Enginnering ToolBox. *Wood-Combustion Heat Values*. 2003. Available at: https://www.engineeringtoolbox.com/wood-combustion-heat-d_372.html. Consulted on 13 August 2025.

[86] Y. Gach. *Medi Batchblock: Fiche technique*. UZUME. May 2023. Available at: https://www.uzume.fr/plans-poeles-de-masse/medi-batchblock. Consulted on 26 June 2025.

[87] I. Dukic. *Specific Heat Capacity of Wood*. ResearchGate. June 2024. Available at: https://www.researchgate.net/publication/272905720_Specific_Heat_Capacity_of_Wood/link/595352fc458515a20701aa54/download?_tp=eyJjb250ZXh0Ijp7InBhZ2UiOiJwdWJsaWNhdGlvbiIsInByZXZpb3VzUGFnZSI6bnVsbH19. Consulted on 13 August 2025.

[88] W.P. Goss and R.G. Miller. *Thermal Properties of Wood and Wood Products*. Available at: https://web.ornl.gov/sci/buildings/conf-archive/1992%20B5%20papers/028.pdf. Consulted on 13 August 2025.

[89] R. Hrčka and M. Babiak. *Some non-traditional factors influencing thermal properties of wood*. August 2011. Available at: https://www.woodresearch.sk/wr/201203/03.pdf. Consulted on 13 August 2025.

[90] ASHRAE. *ASHRAE Handbook : Fundamentals : SI Edition*. Chapter 9-13. 2013.

[91] NBN ISO. *Ergonomics of the thermal environment - Analytical determination and interpretation of thermal comfort using calculation of the PMV and PPD indices and local thermal comfort criteria (ISO 7730:2005)*. December 2005.

[92] NBN ISO. *Energy performance of buildings - Ventilation for buildings - Part 1: Indoor environmental input parameters for design and assessment of energy performance of buildings addressing indoor air quality, thermal environment, lighting and acoustics - Module M1-6*. May 2019.

[93] NBN ISO. *Ergonomics of the thermal environment - Instruments for measuring physical quantities (ISO 7726:1998)*. October 2001.

[94] NBN ISO. *Ergonomics of the thermal environment - Determination of metabolic rate (ISO 8996:2021)*. December 2021.

[95] NBN ISO. *Ergonomics of the physical environment - Subjective judgement scales for assessing physical environments (ISO 10551:2019)*. July 2019.

[96] Y. Allab. *Thèse : Evaluation expérimentale des performances des systèmes de ventilation dans le bâtiment : efficacité de ventilation et confort thermique*. Chapter 2. Ecole nationale supérieure d'arts et métiers. 2017. Available at: `https://pastel.hal.science/tel-01708316`. Consulted on 22 March 2025.

[97] B. Moujalled. *Thèse : Modélisation dynamique du confort thermique dans les bâtiments naturellement ventilés*. Institut des Sciences Appliquées de Lyon. 2007. Available at: `https://theses.insa-lyon.fr/publication/2007ISAL0005/these.pdf`. Consulted on 22 March 2025.

[98] M. Le Bohec. *Thèse : Contribution du rayonnement au confort thermique et aux économies d'énergie dans l'habitat*. p.87-105. Ecole nationale supérieure de mécanique et d'aérotechnique. 2016. Available at: `https://theses.hal.science/tel-01699156`. Consulted on 22 March 2025.

[99] N. Djongyang, R. Tchinda and D. Njomo. *Thermal comfort: A review paper*. SCienceDirect. Renewable and Sustainable Energy Reviews 14. 2010. Available at: `https://www.sciencedirect.com/science/article/abs/pii/S1364032110002200`. Consulted on 22 March 2025.

[100] Dr R.Cantin, B. Moujalled and Dr HDR G. Guarracino. *Complexité du confort thermique dans les bâtiments*. p.1-4. 6th European Congress of Systems Science Paris. September 2025. Available at : `https://www.afscet.asso.fr/resSystemica/Paris05/cantin.pdf`. Consulted on 23 March 2025.

[101] M. Abdellatif. *Thèse de doctorat: Optimisation dynamique du confort thermique et de la consommation énergétique, approche guidée par les données*. p.25-27. Université d'Artois. september 2021.

[102] G. Kiki et al. *Improving the energy efficiency of an office building by applying a thermal comfort model*. Journal of Physics: conference series. 2021. Available at: `https://iopscience.iop.org/article/10.1088/1742-6596/2069/1/012172/pdf`. Consulted on 25 March 2025.

[103] G. Kiki, C. Kouchadé, A. Houngan, S. Junior Zannou-Tchoko and P. Andréa. *Evaluation of thermal comfort in an office building in the humid tropical climate of Benin*. p.1-4. ScienceDirect : Building an environment. 2020. Available at: `https://www.sciencedirect.com/science/article/abs/pii/S036013232030648X`. Consulted on 26 March 2025.

[104] J. Richard de Dear and S. Gail Brager. *Thermal comfort in naturally ventilated buildings: revisions to ASHRAE Standard 55*. ScienceDirect. July 2002. Available at: `https://www.sciencedirect.com/science/article/abs/pii/S0378778802000051`. Consulted on 26 March 2025.